Synthesis and Characterization of Monolayer Molybdenum Disulphide

Shanshan Wang

Supervised by Professor Jamie H. Warner

Submitted in conformity with the requirements for the degree of DPhil in Materials Science

Department of Materials

Oriel College

University of Oxford

March 2017

Copyright © 2017 by Shanshan Wang

Declaration

The material contained within this thesis has not previously been submitted for a degree at the University of Oxford or any other university. The research reported within this thesis has been conducted by the author unless indicated otherwise.

Copyright Notice

The copyright of this thesis rests with the author. No quotation from it should be published without the prior written consent of the author, and any information derived from it should be acknowledged.

Abstract

Synthesis and Characterization of Monolayer Molybdenum Disulphide

by Shanshan Wang

Oriel College

In pursuit of DPhil Degree, Hilary Term, 2017

Monolayer molybdenum disulphide (MoS_2) is a semiconductor with a direct bandgap of ~1.9 eV. Much research attention has been attracted to its potential applications in nanoelectronics and optoelectronics recently, all of which are based upon a scalable production of high-quality monolayer MoS_2 and the in-depth comprehension of its fundamental properties. The PhD project focused on developing chemical vapour deposition (CVD) methods to grow monolayer MoS_2 and its related two-dimensional (2D) vertical heterostructures with an understanding of the growth mechanism. Subsequently, a range of characterizations were conducted to investigate the structural, vibrational, optical and mechanical properties of as-grown samples.

An atmospheric-pressure CVD (APCVD) approach was first developed to grow monolayer MoS_2 crystals on silicon substrates with a 300 nm oxide layer (SiO_2/Si) by using molybdenum trioxide (MoO_3) and sulphur (S) as precursors. A sharp gradient of MoO_3 was intentionally created, which induced a location-dependent shape evolution of MoS_2 domains. A qualitative explanation was proposed, attributing this phenomenon to local changes in the Mo:S ratio of precursors and its influence on the kinetic growth dynamics of edges. Subsequently, the CVD setup was improved in both the precursor loading manner and the substrate orientation to achieve centimetre-scale monolayer MoS_2 films with large domain sizes of 10-20μm. Finally, 2D MoS_2/hexagonal boron nitride (*h*-BN) vertical heterostructures were fabricated *via* an all-CVD method. Raman and photoluminescence (PL) spectroscopy were applied to show its merits of smaller lattice strain, lower doping level and better interlayer contact compared with CVD-grown MoS_2 on SiO_2/Si substrates and mechanically stacked samples.

Aberration-corrected transmission electron microscopy (AC-TEM) was carried out to study the defect structure and fracture mechanics of monolayer MoS_2 at a single atom level. Subtle lattice reconstructions of line defects in various lengths and widths were resolved. Density functional theory (DFT) predicted a reduction of the bandgap as the line defects broaden, which eventually makes them behave as metallic channels embedded in the semiconducting MoS_2. Another joint experimental and theoretical study was conducted to track the real-time crack propagation in monolayer MoS_2. The atomically sharp crack tip went through the preferential lattice direction with least energy release. Increasing defect density was found to induce an enhanced fracture toughness and a fracture mechanism transition from brittle to ductile.

Acknowledgements

This PhD project would not have been accomplished without the guidance, support and advice of my supervisor, colleagues, families and friends. My first acknowledgement must be to my supervisor, Prof Jamie H. Warner. His rigorous attitude and inexhaustible passion for science has deeply influenced me and shaped my understanding on the scientific research, *i.e.*, pursuing the truth. Moreover, he has provided me with patient guidance and tuition on both fundamental knowledge and practical skills about material synthesis and electron microscopy throughout my 3.5-year study at Oxford. He also generously supplied me financial support during my last half-a-year extension, which ensures the systematicness and completeness of my whole PhD research.

I would also like to express my gratitude to my collaborators and colleagues, who contributed their knowledge and expertise on certain facilities and theoretical calculations. Dr Youmin Rong contributed enormously in building the CVD system for the growth of two-dimensional (2D) transition metal dichalcogenides (TMDs), which provided me with a basic and flexible platform to further study and modify the synthesis strategy of monolayer MoS_2. Dr Kuang He and Dr Alex Robertson selflessly trained me on the TEM operation skills of Oxford's JEOL-2200 and JEOL-2100 as well as image analysis methods. Dr Mercè Pacios in Prof Harish Bhaskaran's group and Dr Ye Fan were constantly genial and supportive to assist with characterization using atomic force microscopy (AFM). Mr Xiaochen Wang supplied me with high-quality, continuous *h*-BN films, which is the cornerstone for the CVD fabrication of 2D MoS_2/h-BN heterostructures. The rest of my colleagues, Dr Zhengyu He, Dr Chuncheng Gong, Mr Haijie Tan, Mr Thomas Samuels, Mr Yuewen Sheng, Ms Yingqiu Zhou, Ms Sha Li, Ms Qu Chen, Ms Wenshuo Xu, Mr Hefu Huang, Mr Martin Tweedie, Mr Ren-Jie Chang, Mr Si Zhou and Mr Tongxin Chen,

generously supplied their opinions during discussion, which broadened my horizon and improved my research. In terms of the support from theoretical calculations, I would like to sincerely thank Mr Sungwoo Lee, Professor Gun-Do Lee and Prof Euijoon Yoon from Seoul National University for performing density functional theory (DFT) calculations on the electronic structure of line defects in monolayer MoS_2. In addition, special gratitude goes to Dr Zhao Qin, Mr Gang Seob Jung, Dr Francisco J. Martin-Martinez and Ms Kristine Zhang from Prof Markus J. Buehler's group from Massachusetts Institute of Technology for conducting molecular dynamics (MD) simulations on the study of the fracture mechanics in monolayer MoS_2.

I also want to give my gratitude to China Scholarship Council (CSC), Department of Materials and Oriel College at University of Oxford. CSC provided me with a full scholarship to cover my tuition fee and living expenses over the first 3 years. Department of Materials and Oriel College gave me continuation bursaries and Hardship Fund to partially cover the living expenses in my last 6-month extension.

Finally, I would like to give the most profound gratitude to my parents for their love and moral support, and my beloved boyfriend, who is also pursuing a PhD degree at University of Oxford and doing research on the zero-dimensional fullerene-based material, for his discussion and flashing ideas. Additionally, my thanks go to two lovely pet guinea pigs for their companionship.

Publications

Here presents a list of research accomplished during the course of this project, which has either been published or is in the process of being published. The result chapters in this thesis are based on 5 published first-author publications.

Chapter 4

1. **Wang, S.**; Rong, Y.; Fan, Y.; Pacios, M.; Bhaskaran, H.; He, K.; Warner, J. H. Shape Evolution of Monolayer MoS_2 Crystals Grown by Chemical Vapor Deposition. *Chem. Mater.* **2014**, *26*, 6371–6379.

2. **Wang, S.**; Pacios, M.; Bhaskaran, H.; Warner, J. H. Substrate Control for Large Area Continuous Films of Monolayer MoS_2 by Atmospheric Pressure Chemical Vapor Deposition. *Nanotechnology* **2016**, *27*, 85604–85611.

Chapter 5

3. **Wang, S.**; Wang, X.; Warner, J. H. All Chemical Vapour Deposition Growth of MoS_2:*h*-BN Vertical van Der Waals Heterostructures. *ACS Nano* **2015**, *9*, 5246–5254.

Chapter 6

4. **Wang, S.**; Lee, G.-D.; Lee, S.; Yoon, E.; Warner, J. H. Detailed Atomic Reconstruction of Extended Line Defects in Monolayer MoS_2. *ACS Nano* **2016**, *10*, 5419–5430.

Chapter 7

5. **Wang, S.** *; Qin, Z.*; Jung, G. S.; Martin-Martinez, F. J.; Zhang, K.; Buehler, M. J.; Warner, J. H. Atomically Sharp Crack Tips in Monolayer MoS_2 and Their Enhanced Toughness by Vacancy Defects. *ACS Nano* **2016**, *10*, 9831–9839.

First-Author

6. Li, H.*; **Wang, S**.*; Samuels, T.; Ggoch, G.; Han, D.; Allen, C. S.; Kirkland, A. I.; Grossman, J. C.; Jamie, H. Atomic Structure and Dynamics of Single Pt Atom Interactions with Monolayer MoS_2. *ACS Nano* **2017**, *11*, 3392–3403.

7. **Wang, S.**; Li, H.; Sawada, H.; Allen, C. S.; Kirkland, A. I.; Grossman, J. C.; Warner, J. H. Atomic Structure and Formation Mechanism of Sub-Nanometer Pores in 2D Monolayer MoS_2. *Nanoscale*, **2017**, *9*, 6417-6426.

* These authors contribute equally.

8. **Wang, S.**; Li, H.; Zhang, J.; Guo, S.; Xu, W.; Grossman, J. C.; Warner, J. H. Epitaxial Templating of Two-Dimensional Metal Chloride Nanocrystals on Monolayer Molybdenum Disulfide. **2017**, *11*, 6404–6415.

9. **Wang, S.**; Sawada, H.; Allen, C. S.; Kirkland, A. I.; Warner, J. H. Orientation Dependent Interlayer Stacking Structure in Bilayer MoS_2 domains. *Nanoscale*, **2017**, *under review*.

10. **Wang, S.**; Sawada, H.; Chen, Q.; Allen, C. S.; Kirkland, A. I.; Warner, J. H. *In-situ* Atomic Scale Study of the Formation of Epitaxial Pt Nanocrystals on Monolayer MoS_2. *ACS Nano* **2017**, *under review*.

Second-Author

11. Li, S.; **Wang, S.**; Salamone, M. M.; Robertson, A. W.; Nayak, S.; Kim, H.; Tsang, S. E.; Pasta, M.; Warner, J. H. Edge-Enriched 2D MoS_2 Thin Films Grown by Chemical Vapor Deposition for Enhanced Catalytic Performance. *ACS Catal.* **2017**, *7*, 877–886.

12. Koh, A. L.; **Wang, S.**; Ataca, C.; Grossman, J. C.; Sinclair, R.; Warner, J. H. Torsional Deformations in Subnanometer MoS Interconnecting Wires. *Nano Lett.* **2016**, *16*, 1210–1217.

13. Zhou, S.; **Wang, S.**; Li, H.; Xu, W.; Gong, C.; Grossman, J. C.; Warner, J. H. Atomic Structure and Dynamics of Defects in 2D MoS_2 Bilayers. *ACS Omega* **2017**, *2*, 3315–3324.

Co-Author

14. Robertson, A. W.; Lin, Y.; **Wang, S.**; Sawada, H.; Allen, C. S.; Chen, Q.; Lee, S.; Lee, G.; Han, S.; Yoon, E.; *et al.* Atomic Structure and Spectroscopy of Single Metal (Cr, V) Substitutional Dopants in Monolayer MoS_2. *ACS Nano* **2016**, *10*, 10227–10236.

15. Rong, Y.; Fan, Y.; Koh, A. L.; Robertson, A. W.; He, K.; **Wang, S.**; Tan, H.; Sinclair, R.; Warner, J. H. Controlling Sulphur Precursor Addition for Large Single Crystal Domains of WS_2. *Nanoscale* **2014**, *6*, 12096–12103.

16. Wang, X.; Hooper, T. N.; Kumar, A.; Priest, I. K.; Sheng, Y.; Samuels, T. O. M.; **Wang, S.**; Robertson, A. W.; Pacios, M.; Bhaskaran, H.; *et al.* Oligomeric Aminoborane Precursors for the Chemical Vapour Deposition Growth of Few-Layer Hexagonal Boron Nitride. *CrystEngComm.* **2017**, *19*, 285–294.

17. Sawada, H.; Allen, C. S.; **Wang, S**.; Warner, J. H.; Kirkland, A. I. Aberration Measurement of the Probe-Forming System of an Electron Microscope using Two-Dimensional Materials. *Ultramicroscopy*, **2017**, *182*, 195-204.

18. Chang, R.-J.; Wang, X.; **Wang, S**.; Sheng, Y.; Porter, B.; Bhaskaran, H.; Warner, J. H. Growth of Large Single-Crystalline Monolayer Hexagonal Boron Nitride by Oxide-Assisted Chemical Vapor Deposition. *Chem. Mater.* **2017**, *accepted*.

Table of Contents

Chapter 1 Introduction **1-1**
1.1 Project Aims 1-1
1.2 The Scope of this Thesis 1-1
Chapter 2 Literature Review **2-5**
2.1 Introduction 2-5
2.2 Structure of 2D MoS_2 2-7
2.2.1 Crystal Phases 2-7
2.2.2 Point Defects 2-10
2.2.3 One-Dimensional Defects 2-13
2.3 Properties of 2D MoS_2 2-16
2.3.1 Fundamental Band Structure 2-16
2.3.2 Photoluminescence Emission Characteristics 2-18
2.3.3 Vibrational Properties 2-21
2.3.4 Mechanical Properties 2-24
2.4 CVD Synthesis of 2D MoS_2 2-24
2.4.1 Route I 2-25
2.4.2 Route II 2-29
2.4.3 Discussion 2-36
2.4.4 MoS_2-Based 2D Vertical Layered Heterostructures 2-40
2.5 Conclusion 2-45
Chapter 3 Methodology **3-47**
3.1 Introduction 3-47
3.2 CVD Synthesis and Transfer 3-47
3.2.1 Preparation and Growth of Monolayer MoS_2 3-49
3.2.2 Transfer of Monolayer MoS_2 3-51
3.3 Scanning Electron Microscopy 3-52
3.4 Raman and Photoluminescence Spectroscopy 3-53
3.5 Atomic Force Microscopy 3-54
3.6 Transmission Electron Microscopy 3-55
3.6.1 Aberration-Corrected Transmission Electron Microscopy 3-55
3.6.2 Image Processing and Simulation 3-56
3.6.3 2D Displacement Maps and Strain Analysis 3-58
Chapter 4 CVD Growth of Monolayer MoS_2 .... **4-60**
4.1 Shape Evolution of Monolayer MoS_2 Crystals 4-60

4.1.1 Introduction 4-60
4.1.2 Results and Discussion 4-62
4.1.3 Conclusion 4-78
4.2 Growing Large-Area, Continuous Films of Monolayer MoS_2 4-79
4.2.1 Introduction 4-79
4.2.2 Results and Discussion 4-80
4.2.3 Conclusion 4-93
Chapter 5 All CVD Growth of 2D MoS_2/h-BN Vertical Heterostructures 5-95
5.1 Introduction 5-95
5.2 Results and Discussion 5-97
5.2.1 Experimental Setup 5-97
5.2.2 Morphology of As-Grown MoS_2 on h-BN Films 5-101
5.2.3 Lattice Strain, Doping and Interlayer Contact 5-102
5.3 Conclusion 5-113
Chapter 6 Line Defects in Monolayer MoS_2 6-115
6.1 Introduction 6-115
6.2 Results and Discussion 6-118
6.2.1 Structure and Dynamics of Sulphur Vacancies 6-118
6.2.2 Lattice Reconstructions of Sulphur Vacancy Lines 6-122
6.2.3 2D Strain Analysis of Sulphur Vacancy Lines 6-130
6.2.4 Band Structure Calculation 6-132
6.3 Conclusion 6-133
Chapter 7 Cracks in Monolayer MoS_2 7-135
7.1 Introduction 7-135
7.2 Results and Discussion 7-137
7.2.1 Fast Fracture in Strained Pristine Monolayer MoS_2 7-137
7.2.2 Slow Fracture in Defective Monolayer MoS_2 7-145
7.2.3 Fracture Toughness Calculation of Defective Monolayer MoS_2 7-153
7.3 Conclusion 7-156
Chapter 8 Conclusion and Outlook 8-157
8.1 Conclusion 8-157
8.2 Outlook 8-160
Appendix A Supporting Information of Chapter 5 163
Appendix B Supporting Information of Chapter 6 167
Appendix C Supporting Information of Chapter 7 177
References 183

Chapter 1 Introduction

1.1 Project Aims

The objective of this doctorate project is to systematically establish, understand and optimize the chemical vapour deposition (CVD) method for the growth of monolayer MoS_2, and subsequently study the structural, vibrational and optical properties of the product by a range of characterization techniques.

1.2 The Scope of this Thesis

The thesis covers the research that has been implemented over the course of 3.5 years of UK PhD degree at the Materials Department, University of Oxford. It unfolds with a literature review, summarizing the recent progress on the study of the structures, properties and CVD synthesis of monolayer MoS_2 (Chapter 2). These contents are the cornerstone for my following investigation, which set up the fundamental knowledge and indicate the gaps needed to be filled in this research field. Subsequently, the basic setup of the CVD system for monolayer MoS_2 growth and a series of characterization techniques with typical data processing methods employed in my research are introduced in Chapter 3. The detailed experimental and theoretical methods used by my collaborators are not included in this part, but they can be found in corresponding published papers.

The general structure of my project results is summarized in **Figure 1.1**. My work starts with the study of the atmospheric pressure CVD (APCVD) growth of monolayer MoS_2 on the Si substrate coated with a thin layer of amorphous SiO_2 (Chapter 4), which has a good compatibility with the current Si-based electronics. The purposes of this work are to establish practical synthesis strategies, which can produce MoS_2 monolayers for further property investigations, and to have a universal and in-depth understanding of the growth mechanism, which has a potential of being expanded to other 2D materials. Two typical methods have been developed. One makes use of the spatial precursor concentration gradient to obtain monolayer MoS_2 with fewer number of experiments and creates a platform to study the shape evolution of as-grown crystals, and the other achieves the centimetre-scale, high-quality monolayer MoS_2 films with domain sizes ranging from 10–20 μm through modifications on both the system setup and the growth recipe. A kinetic growth model has also been proposed to explain the quality improvement of MoS_2.

Subsequently, the study progressed to the fabrication of 2D MoS_2/*h*-BN vertical heterostructures using an all CVD method (Chapter 5), motivated by optimizing the substrate material to a new type that can preserve the intrinsic properties of MoS_2 better and to maintain the overall flexibility of the 2D system. The vibrational and optical properties of CVD-grown monolayer MoS_2 on *h*-BN films have been studied *via* Raman and photoluminescence (PL) spectroscopy, which unveils its advantages on the built-in lattice strain, doping level, and interlayer contact compared with the counterparts fabricated by the mechanical transfer or using the SiO_2 substrate.

The research focus then switches to understanding the atomic structure of CVD-grown monolayer MoS_2 by employing the aberration-corrected transmission electron microscopy (AC-TEM), in which the well-aligned electron beam performs both as an imaging media and controllable external stimuli to modify the intrinsic periodicity of the MoS_2 lattice, thus

tailoring its properties from the bottom level. Line defects were first investigated by introducing a mild concentration of S vacancies, which are prone to migrating and aggregate into vacancies lines (Chapter 6). Both 1D and 2D lattice distortions for line defects in different length and width have been resolved with density functional theory (DFT) calculations conducted to predict the band structure evolution as the line defects extend and broaden. Prolonged focused electron beam irradiation triggers the fracture in suspended monolayer MoS_2, which provides an opportunity to resolve the fine structure of crack tips, torn edges and crack propagation behaviours down to the atomic level (Chapter 7). Large-scale molecular dynamics (MD) simulations were applied to supply theoretical support of the experimental observations and predict the toughness of defective monolayer MoS_2 compared with that of graphene.

The final chapter recapitulate my whole research with significant achievements for each sub-project. A potential future development for corresponding sub-projects is also discussed.

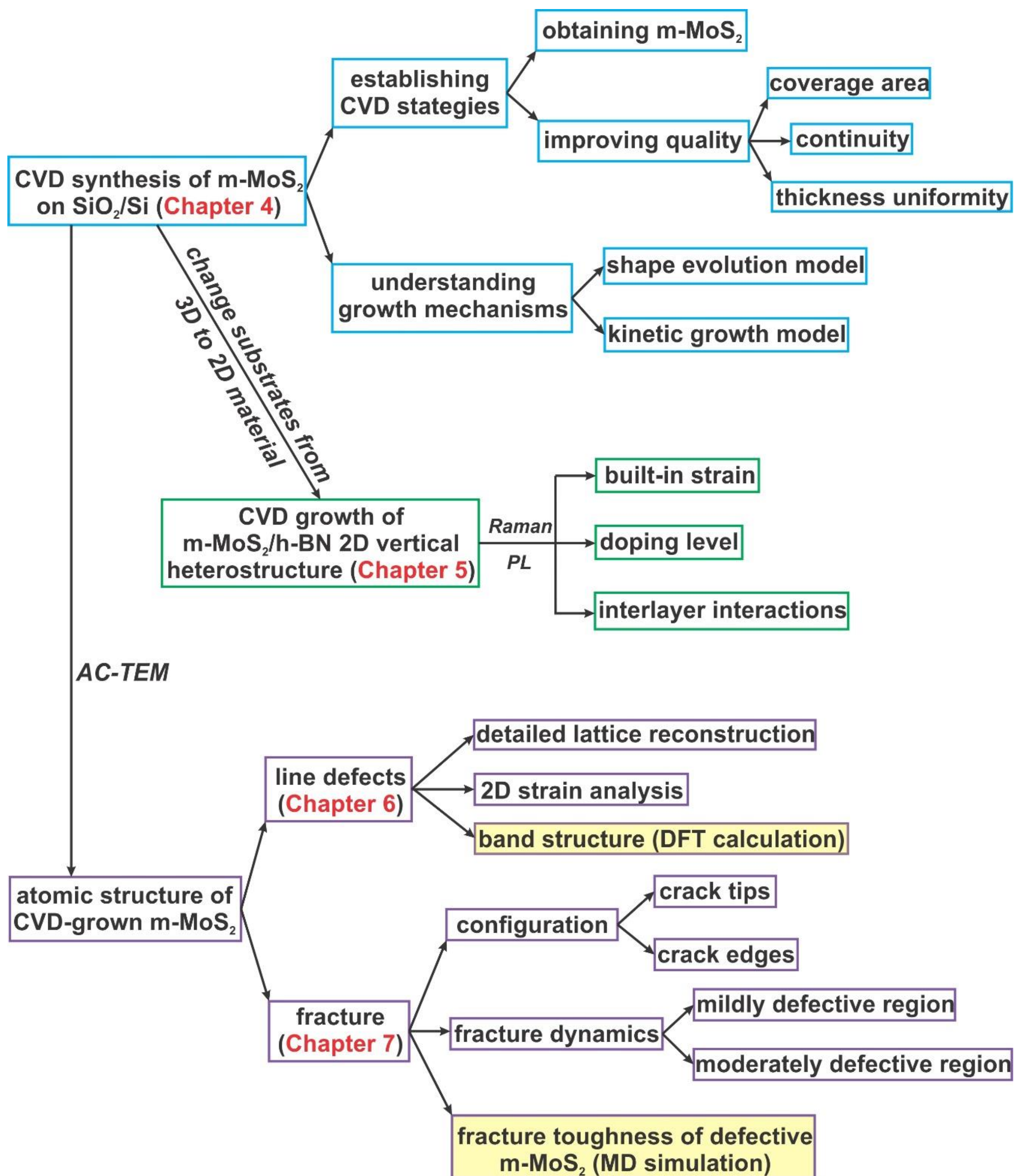

Figure 1.1. Schematic illustration showing the overall structure of my thesis. Those contents highlighted in yellow were accomplished by collaborators. m-MoS_2 represents monolayer MoS_2.

Chapter 2 Literature Review

2.1 Introduction

Graphene is a single-layer two-dimensional (2D) sheet of sp^2-hybridized carbon atoms, which exhibits intriguing condensed matter phenomena that are absent in its bulk counterpart.(*1*) This makes people aware that, apart from the atom arrangement manner and element type, material's property can also be tailored in a third approach, *i.e.* changing the dimensionality. Encouraged by the great progress in graphene and the methodology developed for preparing atomically thin layered materials, research interest was expanded to other kinds of 2D materials, like transition metal dichalcogenides (TMDs).(*2–4*) TMDs, which can be generalized in a formula of MX_2 with M as a transition metal element from group 4 to 10 in its periodic table and X as a chalcogen (S, Se, Te) (**Figure 2.1**), consist of a wide variety of layered materials with diverse electronic properties, ranging from insulators (e.g. HfS_2), semiconductors (e.g. 2*H*-MoS_2 and 2*H*-WS_2), semi-metals (e.g. WTe_2 and $TiSe_2$) to true metals (e.g. NbS_2 and VSe_2).(*5*) The tunable bandgap of different TMDs is derived from the progressive filling of the nonbonding *d* bands of transition metal electrons. In addition, the existence of unsaturated *d* orbitals of transition metals also triggers some exotic properties, including superconductivity, charge density wave (CDW, a periodic distortion of the crystal lattice), magnetism and Mott transition (metal to non-metal

transition).(*5*) Therefore, 2D TMDs offers opportunities for wide applications in catalysis, energy storage, valley electronic applications, nanoelectronics and optical devices.(*6–8*)

Figure 2.1. Period table showing the diversity of TMDs. The transition metals that are fully highlighted predominantly crystalize into layered structures with three chalcogen elements, while those partially highlighted (Co, Rh, Ir and Ni) can form some non-layered structures. The positions of two elements in MoS_2 are marked by red and black boxes, respectively. Reprinted (adapted) with permission from ref.(*5*), © 2013 Macmillan Publishers Limited.

MoS_2 was the first semiconducting TMD obtained in a monolayer form. The band structure of MoS_2 transforms from an indirect bandgap to a direct one when decreasing its thickness from bulk to a single layer, making it complimentary to the zero-bandgap graphene and behave as a promising candidate in nanoelectronic and optoelectronic applications.(*9*) The room-temperature carrier mobility for mechanically exfoliated MoS_2 was measured to be ~100 $cm^2V^{-1}s^{-1}$ with a large switching on/off ratio of $>10^8$.(*10*) In addition, special properties including valley polarization and valley Hall effect can be observed in monolayer MoS_2 due to the lack of inversion symmetry.(*11*, *12*) Moreover, 2D MoS_2 can perform as a low-cost, highly efficient electrocatalyst for hydrogen evolution reaction, which activity can be further promoted by the increase of edge sites and defect density as well as proper heteratom substitutional doping.(*13–17*)

In this chapter, a review of 2D MoS_2 is present to introduce its structure, properties and CVD synthesis approaches. Based on the thesis subject, the focus of the review is arranged on the discussion about different CVD growth strategies, the atomic structures of defects in monolayer MoS_2 as well as its optical and vibrational properties.

2.2 Structure of 2D MoS_2

2.2.1 Crystal Phases

Bulk MoS_2 has a layered structure. Each layer is constructed of three covalently-bonded S-Mo-S' atomic planes, while adjacent layers are coupled by weak van der Waals forces.(*18*) For monolayer MoS_2, there exhibit only two polymorphs due to different coordination manners between the Mo atom and its neighbouring six S atoms. One is trigonal prismatic coordination (D_{3h} point group) and the other is octahedral coordination (D_{3d}), commonly being referred as 1H and 1T, respectively (**Figure 2.2**a,b).(*5*) For multilayer MoS_2, more polymorphs appear due to the diversity of the stacking sequence between each layer. Three intensively investigated polytypisms are 1T, 2H and 3R, where the letters represent different crystal symmetry systems of trigonal, hexagonal and rhombohedral, respectively, and the digits stand for the number of layers in each unit cell (**Figure 2.2**c,d).(*19*) 2H and 3R phases are more energetically favourable compared with the metastable 1T phase and are commonly encountered in natural minerals as well as synthetic products. Both of them have the same intralayer coordination configuration (trigonal prismatic) but with different interlayer coupling manners. In the 2H polytype, two layers are fully eclipsed with Mo (S) atoms of one layer sitting right above S (Mo) atoms of the other layer. For the 3R phase, three layers are staggered with S atoms in the middle layer residing above the Mo atoms in the bottom layer and below the hollow hexagonal centre of the top layer. Two layers in each unit cell of 2H-MoS_2 have a 60° twist in the lattice orientation

between each other, while all three layers in the unit cell of 3R-MoS_2 adopt the same crystal direction.

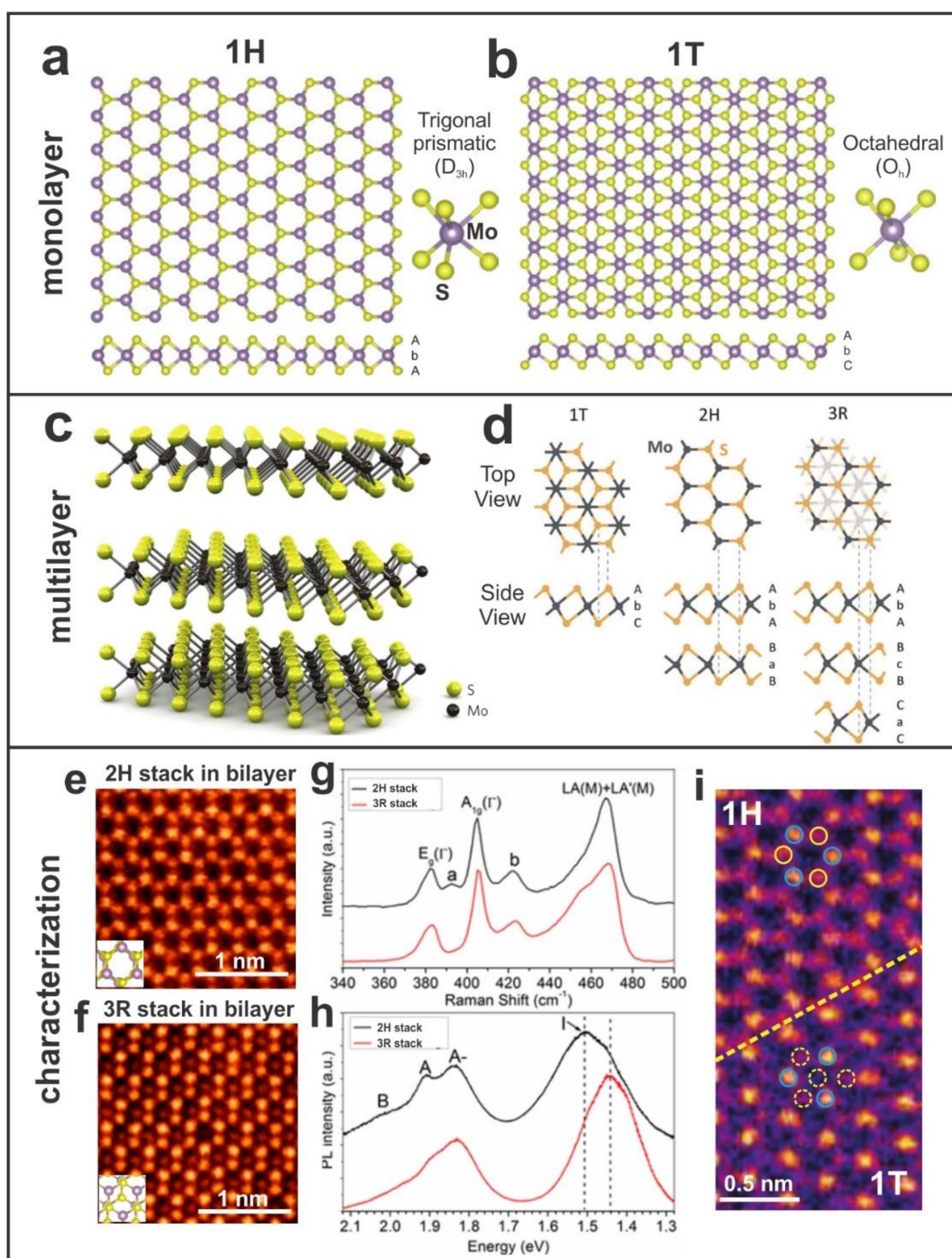

Figure 2.2. Structural models and characterizations of various polymorph phases of MoS_2. (a,b) Atomic models showing 1H and 1T phases of monolayer MoS_2, respectively. (c) 3D schematic illustration of multilayer MoS_2. (d) Atomic models displaying three different phases, 1T, 2H and 3R, in multilayer MoS_2, respectively. (e,f) ADF-STEM images of bilayer MoS_2 exhibiting 2H and 3R stacking sequences, respectively, where an atomic column corresponding to a pair of stacked sulphur

atoms in the centre of each hexagonal ring can be seen in (f) as a distinct feature of 3R polytype. (g,h) Resonance Raman and PL spectra displaying distinguishable variations between 2H and 3R stacked bilayer MoS_2. (i) ADF-STEM image showing an artificial generation of 1T phase in the 1H-phase monolayer MoS_2 by a controllable electron irradiation using *in-situ* scanning electron microscopy. Blue solid circles, yellow solid circles and yellow dashed circles indicate Mo, 2S and 1S atoms, respectively. The yellow dashed line shows the boundary between 1H and 1T phase. Figures reprinted (adapted) with permission from: (a,b), ref.(*5*); © 2013 Macmillan Publishers Limited; (c), ref.(*10*), © 2011 Macmillan Publishers Limited; (d), ref.(*19*), © 2015 Royal Society of Chemistry; (e,f), ref.(*20*), © 2015 American Chemical Society; (g,h), ref.(*21*), © 2015 American Chemical Society; (i), ref.(*22*), © 2014 Macmillan Publishers Limited.

To distinguish different phases of 2D MoS_2, annular dark-field scanning transmission electron microscopy (ADF-STEM) was employed as the most direct and unambiguous characterization tool owning to its atomic resolution as well as a quantitative and proportional relation between the intensity and the atomic number (**Figure 2.2**e,f).(*23*, *24*) Unique fingerprints in Raman and PL spectra were also reported to be capable of identifying different stacking configurations in bilayer and trilayer MoS_2 (**Figure 2.2**g,h).(*20*, *21*) Apart from resolving pristine structures of various phases, conversions between them are also studied (**Figure 2.2**i),(*22*, *25*) especially for 2H and 1T phase of multilayer MoS_2, which exhibit entirely different electronic and magnetic properties. 2H-MoS_2 is a diamagnetic semiconductor, while 1T-MoS_2 is a paramagnetic metal.(*19*) Structurally speaking, each layer of the two phases can transform between each other by a transversal gliding of one of the S planes. Practically, people have successfully used approaches including intercalation with alkali metals, rhenium (Re) atom doping and controllable electron beam irradiation to trigger the phase transition from 2H to 1T.(*22*, *26–28*) The reason could be attributed to the change of the *d*-electron count for Mo atoms in MoS_2 through either the intercalated and doped atoms or from the electron beam, which destabilizes the original 2H phase.

2.2.2 Point Defects

Point defects are a type of zero-dimensional structural imperfection that occur only at or around a single lattice point. They are inevitable in any materials at above absolute zero temperature based on the 2nd law of thermodynamics(*29*) and are particularly noticeable in 2D materials due to their ultrasmall thickness. In this section, the most commonly encountered point defects in monolayer MoS_2 are discussed without the inclusion of those having foreign atoms.

Point vacancies in monolayer MoS_2 can generally be classified into three categories: (1) vacancies, having S, Mo or small MoS_x clusters being removed from the pristine lattice; (2) antisite defects, having Mo (S) atoms being substituted by S (Mo) atoms; (3) adatoms, having additional Mo or S atoms sitting on special sites of the MoS_2 surface. According to this classification, different species of point defects with their corresponding atomic configurations characterized by ADF-STEM are listed in **Figure 2.3**.(*29*, *30*) Most defects retain the 3-fold symmetry except a minority of antisite defects like Mo_{S2} and $S2_{Mo.}$

Different point defects have different occurrence frequencies, which derives from distinctions from the sample preparation method and the defect configuration stability.(*29*)(*30*) If comparing monolayer MoS_2 prepared in three different methods, mechanical exfoliation (ME), chemical vapour deposition (CVD) and physical vapour deposition (PVD), V_s was the most frequently observed point defect in ME and CVD samples, while antisite defects Mo_{S2} and Mo_S were dominant in PVD specimen. This could be attributed to the crystal growth environment with different relative abundance between Mo and S elements (S-deficient *vs.* Mo-deficient) for these three preparation approaches, which makes the formation energy of different defects varies. In addition, concentrations of some defects, like V_{Mo} and V_{MoS6} were extremely low. The reason was explained by the detailed formation energy of S vacancies around V_{Mo} and V_{MoS3}. For V_{Mo}, since the S

vacancy formation energy around V_{Mo} is very low (1.1eV per V_s), once a V_{Mo} is created, its neighbouring three S atoms are prone to losing simultaneously, forming V_{MoS3} instead. However, for S vacancies close to V_{MoS3}, such energetic advantage on the vacancy formation does not exist anymore. Therefore, the defect evolution from V_{MoS3} to V_{MoS6} is not energetically motivated (please refer to **Figure 2.3** for details of each point defect).

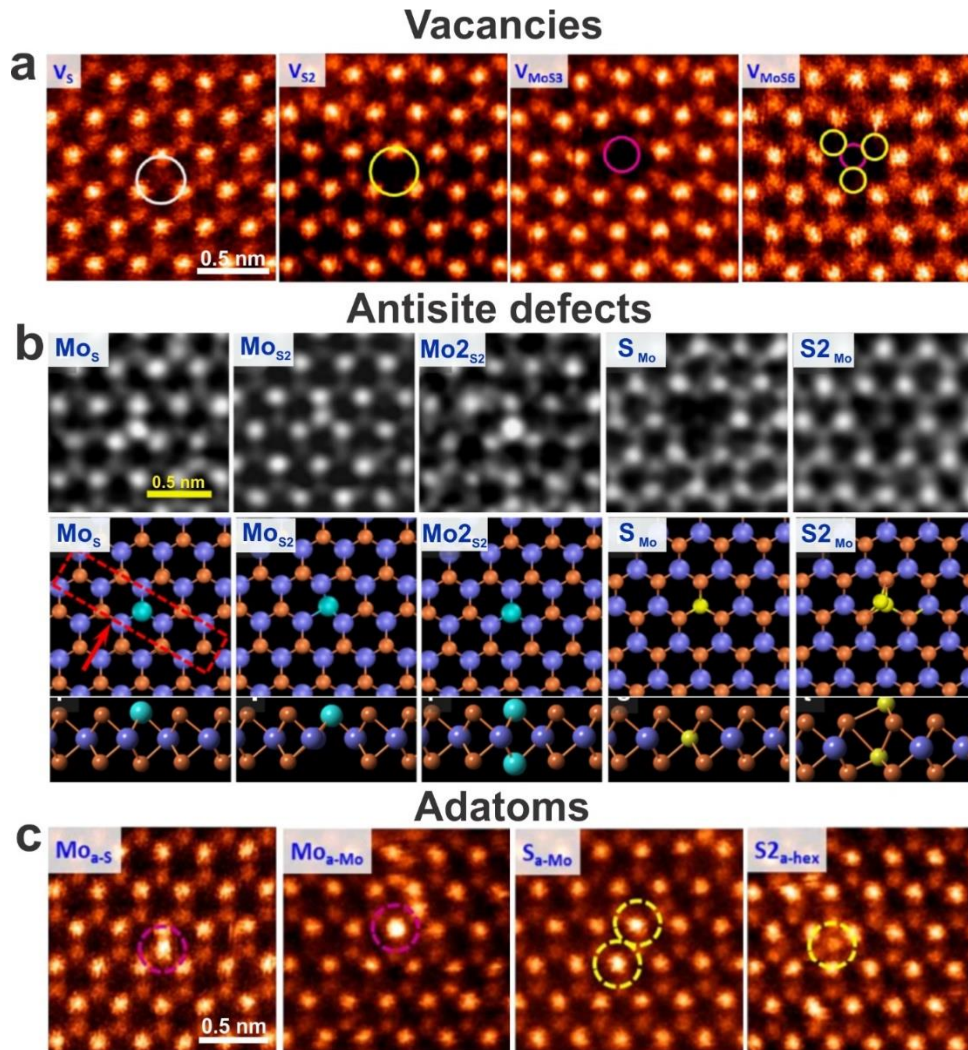

Figure 2.3. Three categories of point defects in monolayer MoS_2. (a) ADF-STEM images showing four types of vacancies. Atoms or clusters in the subscripts are lost. Pink, yellow and white circles indicate the missing single Mo atom, double S atoms and single S atom, respectively. (b) ADF-STEM images of five types of antisite defects with corresponding DFT-relaxed atomic models in both the projected and side views. Atoms in subscripts are substituted by those in the normal size. The former two antisites are dominant in PVD-grown samples. (c) ADF-STEM images of four typical types of adatoms. The subscript represents the atomic site where the atom written in the normal size is absorbed on. 'hex' indicates the centre of the hexagonal ring. Figures reprinted

(adapted) with permission from: (a,c), ref.(*29*), © 2013 American Chemical Society; (b), ref.(*30*), © 2015 Macmillan Publishers Limited.

Point defects in 2D MoS_2 have a significant influence on material's electronic and magnetic properties. Theoretical calculations have shown that S vacancies on the surface of few-layer MoS_2 behave as electron donors, thus inducing localized states in the bandgap.(*29*, *31*) Under a low carrier density, charge transport is dominated by hopping through S vacancy-induced localized states, exhibiting nearest-neighbour hopping and variable-range hopping at high and low temperatures, respectively. Both vacancies and antisite defects perform as strong scattering centres of electrons, which deteriorates the overall carrier mobility of 2D MoS_2 electronic devices. Moreover, antisite Mo_S has been predicted to possess a local magnetic moment of $2\mu_B$, which is distinct in the diamagnetic pristine 2D MoS_2.(*30*)

Point defects do not only inherently exist in 2D MoS_2, but can also be artificially produced using chemical etching or irradiation by high-energy particles, including laser, ion beam and electron beam. This opens the door for defect engineering in 2D MoS_2, providing flexibility to tune electronic, optical and catalytic performances of the material. The electron beam-induced defect generation stems from either a 'knock-on' effect, ionization damage or chemical etching catalysed by hydrocarbon contamination absorbed on the MoS_2 surface. Most of the EB-generated defects are S vacancies. It was calculated that the displacement threshold energy of S atoms in the pristine monolayer MoS_2 is ~6.5 eV, close to the maximum knock-on energy transferred from 80 keV electrons to S atoms.(*32*, *33*) However, electrons having the energy as low as 30 keV can still create S vacancies, indicating a more complicated ionization mechanism.(*34*) In addition, point defects, especially S vacancies, can migrate on the MoS_2 surface under the electron beam illumination, which is supported

by the calculated migration barrier of 2.3eV.(*35*) It endows the defect configuration in MoS_2 with an increased diversity and complexity, which will be discussed in the next section.

2.2.3 One-Dimensional Defects

One-dimensional (1D) defects can be defined as a series of linearly extended atoms whose arrangement is deviated from the normal periodicity in the pristine lattice. In terms of monolayer MoS_2, its commonly encountered 1D defects can be classified into two types depending on whether the lattice occurs an orientation change when going through the 1D defect. The first type has the same crystal directions on two sides of the 1D defect, denoted as common line defects (c-LDs) here, while the crystal orientations on two sides of the second type of 1D defects have a difference, which are widely defined as grain boundaries (GBs).

As mentioned in 2.2.2, the migration barrier of S vacancies is relatively low. With the vacancy concentration increase due to the continuous bombardment of high-energy particles on MoS_2, they are prone to migrating and agglomerate linearly rather than to be distributed in isolation, as it may obtain superiority in the overall surface energy.(*35*) This is the dominant formation mechanism for c-LDs. The linearly aggregated S vacancies will experience subtle structure reconstructions according to their aggregation length, width and the surrounding environment and form a diversity of c-LDs (**Figure 2.4**a). However, limited by the resolution of TEM images,(*35*) their detailed atomic configurations, formation dynamics, lattice strain and band structure evolution have not been thoroughly investigated. This gap is filled by results in Chapter 6.

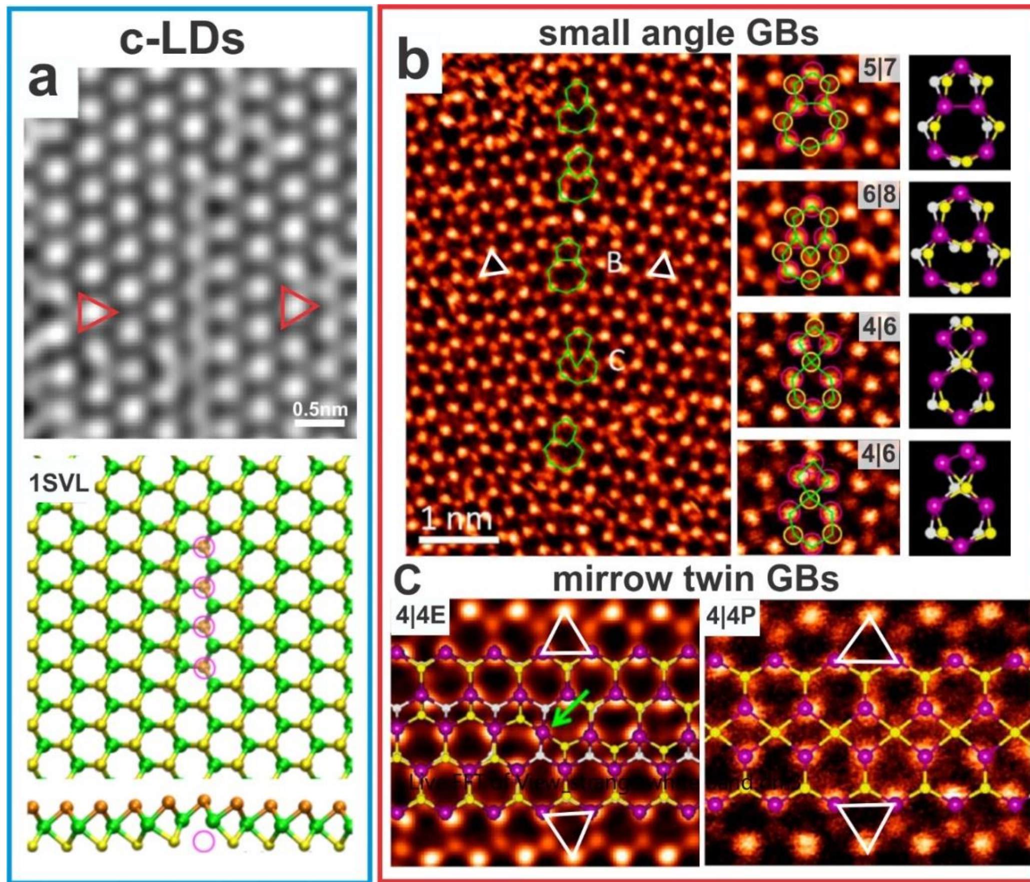

Figure 2.4. Two categories of 1D defects in monolayer MoS_2. (a) HRTEM image and the corresponding DFT-calculated atomic model of a typical common line defect (c-LD), which loses a single row of S atoms (1SVL). The lattice orientation on both sides of the c-LD is the same, which are marked by red triangles determined by using S vacancies as references. (b,c) ADF-STEM images showing two types of GBs, small angle GBs composed of a series of dislocation cores (b) and mirror twin GBs having the grain orientation twist of 60° (c). DFT-relaxed atomic models are either given separately or overlapped on the image. Grain orientations on two sides of the GBs are marked by white triangles. Kinks exist as indicated by the green arrow in (c). Figures reprinted (adapted) with permission from: (a), ref.(*35*), © 2013 American Physical Society; (b,c), ref. (*29*), © 2013 American Chemical Society.

GBs are formed by the atomic stitching between two grains having an orientation variation. The most commonly observed GBs in MoS_2 monolayers can be divided by two categories: small angle GBs and mirror twin GBs. For the former GBs, linearly-aligned dislocation cores composed of 5- and 7-fold (5|7) rings, 6|8 rings, 4|6 rings are observed with slight variations on element types at each lattice point due to the substitution between Mo and S atoms (**Figure 2.4**b).(*29*, *36*) Mirror twin GBs, which can also be named as

inversion domain GBs, appear between two grains twisted by an integral multiple of 60°, being equivalent to swap the position of Mo and S atoms in the hexagonal lattice. A majority of mirror twin GBs extend along the zigzag lattice direction, which adopts the highest structural symmetry. Depending on the relative position between two grains, linear dislocation cores consisting of 4-fold rings with either point sharing (4|4P) or edge sharing (4|4E) are developed (**Figure 2.4**c).(*29*) Due to the diversity in the coordination manner between Mo and S atoms, more complicated GB configurations, such as a recurring 8|4|4 motif, can be formed, which follows the zigzag lattice orientation macroscopically but exhibits an intersection angle of ±20° with respect to the zigzag direction in the nanometre scale.(*37*) Interestingly, mirror twin GBs in monolayer MoS_2 can also be artificially created through the generation of inversion domains by either the electron beam irradiation or thermal annealing.(*38*) The formation mechanism of inversion domains was interpreted by 3 steps: (1) generation of S vacancies induced by the energy obtained from either the electron beam illumination or thermal treatment; (2) aggregation of S vacancies to create c-LDs; (3) displacement of Mo and S sublattice to form triangular inversion domains, which is theoretically explained by the motivation from the lattice strain release.

It is well documented that the overall properties of polycrystalline materials are largely governed by the atomic structure, concentration and distribution of GBs. The influence of GBs in 2D materials may be even more pronounced as they are purely made up of surfaces, and the presence of any defects, like GBs, can alter material's properties dramatically.(*39*) Since GBs in monolayer MoS_2 have a change on both the chemical stoichiometry and the coordination manner between Mo and S atoms, the band structures at GBs evolves compared with the pristine lattice. Based on theoretical calculations, both 4|4P and 4|4E mirror twin GBs exhibit dispersive bands across the Fermi level, making them serve as metallic wires embedded in the semiconducting MoS_2.(*29*) For other types of GBs, calculations reveals the

implantation of mid-gap states.(*29*, *37*) Experimental measurements have also confirmed the significant role of GBs on the electrical transport and photoluminescence emission characteristics (PL peak energy, intensity and width) of monolayer MoS_2.(*37*)

2.3 Properties of 2D MoS_2

2.3.1 Fundamental Band Structure

This section introduces the fundamental band structure of MoS_2, starting from its bulk phase, and then shows its evolution as the thickness decreases down to a monolayer regime. People qualitatively understand the fundamental band structure of bulk MoS_2 from mainly two angles: one is the electron filling states of the compound's molecular orbitals, the other is the lattice configuration. From the first angle, it has been proposed that the diversity of bulk layered TMDs electronic properties predominantly arises from the progressive filling of the non-bonding *d* bands of transition metals. Bulk TMDs exhibit metallic properties when the non-bonding *d* orbitals are partially occupied, and display semiconducting properties when the non-bonding *d* orbitals are fully occupied.(*5*, *40*) **Figure 2.5**a shows the electron occupation states of MoS_2 molecular orbitals, where its non-bonding *d* band, which is also the highest occupied molecular orbital (HOMO), is fully occupied.(*41*) Therefore, bulk MoS_2 is a semiconductor with an indirect bandgap of 1.2-1.3 eV.(*42*) When understanding the fundamental band structure from the second angle, which is the lattice configuration, it can be found that the unit cell of MoS_2 has two different lattice points, one is a single Mo atom and the other is a couple of overlapped S atoms. This is different from the unit cell of graphite, where two lattice points are both carbon atoms. Such configuration difference on the crystal unit cell will eliminate the degeneracy of the electronic structure at the K(K') point in the Brillouin zone, thus opening up an energy bandgap in bulk MoS_2.(*43*)

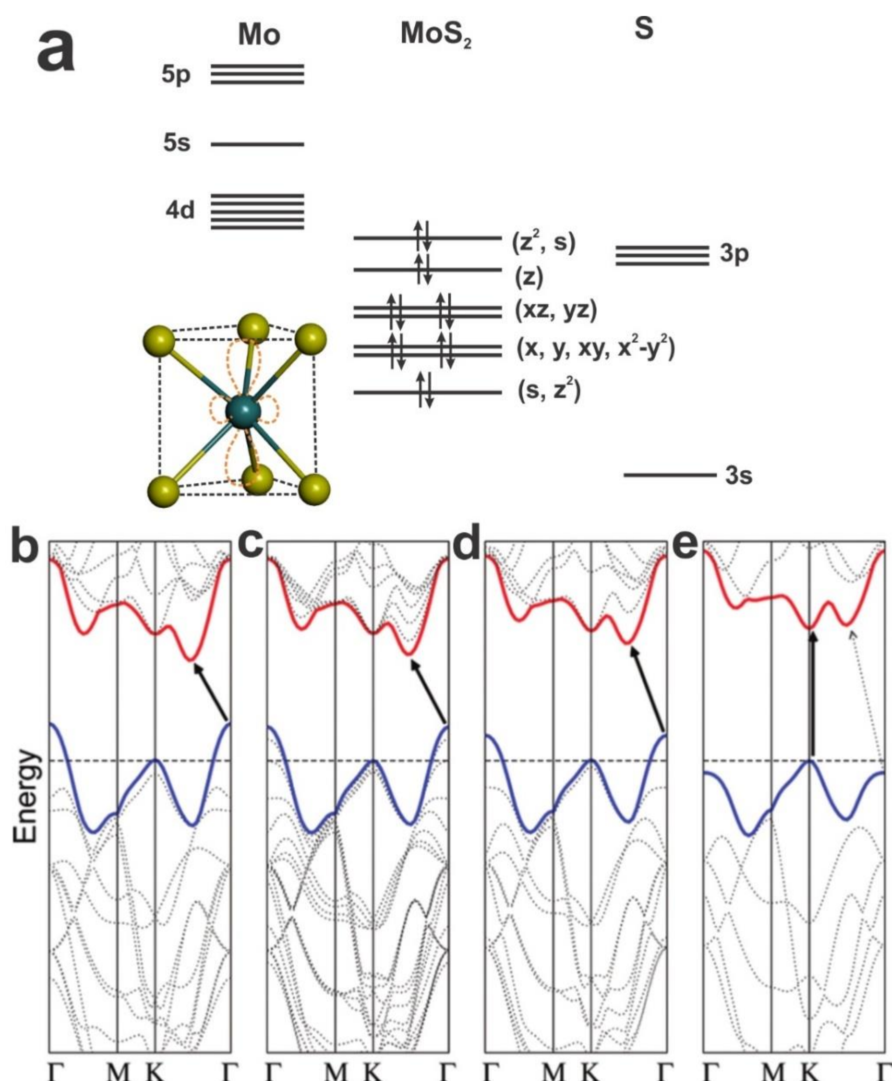

Figure 2.5. Band structure of MoS_2. (a) Diagram showing the energy level of molecular orbitals (MOs) for MoS_6 in 2H-MoS_2. The terms in parentheses (e.g., z^2. s, xz, *etc.*) indicate metal orbitals making primary contributions to the MOs. (b–e) Calculated band structures corresponding to bulk (b), quadrilayer (c), bilayer (d) and monolayer (e) MoS_2. Figures reprinted (adapted) with permission from: (a), ref.(*41*), © 1989 American Chemical Society; (b), ref.(*44*), © 2010 American Chemical Society.

The fundamental band structure of bulk 2*H*-MoS_2 is shown in **Figure 2.5**b, where the valence band maximum is positioned at Γ in the Brillouin zone and the conduction band minimum is located approximately halfway along the Γ-K direction. As the layer number of MoS_2 decreases, its band structure is strongly affected due to quantum confinement, interlayer interaction and long-rang Coulomb effects.(*44–46*) For example, the sensitivity of band states at different points in the Brillouin zone to the change of interlayer interactions

varies, because they stem from orbitals that adopt different spatial distributions.(*44*) The conduction band states at the K point, which are largely contributed by the *d* orbitals of Mo and are highly localized within the S-Mo-S sandwiched layer, are weakly affected by the interlayer interactions. In the contrast, the conduction band states close to the Γ point, which originate from the hybridization between the *d* orbitals of Mo and the antibonding p_z orbitals of S, are susceptible to interlayer interactions. Therefore, as the MoS_2 becomes thinner, lowest conduction band near the Γ point shifts upward remarkably, while the conduction band at the K point barely moves (**Figure 2.5**c–e). When the MoS_2 thickness is reduced to monolayer, the indirect transition gap surpasses the direct bandgap, making the MoS_2 transit from indirect to direct semiconductor. The direct fundamental bandgap value proposed by various theoretical models varies slightly, ranging from 2.8 eV to 3.0 eV.(*47–49*)

2.3.2 Photoluminescence Emission Characteristics

The direct bandgap nature of monolayer MoS_2 triggers the emergence of strong photoluminescence (PL) emission at ~1.8–1.9 eV.(*44*, *50*, *51*) It is worth noting that the energy gap measured by the PL spectroscopy is the optical bandgap, which is the difference between the fundamental bandgap and the exciton binding energy. Even though PL measurements cannot provide the information of fundamental band structure directly, it is the most widely used experimental approach to track the band structure change as well as to verify the validity of the band structure calculated by different theories. In the PL spectrum, two pronounced peaks located at ~677nm and ~627nm, respectively, correspond to the direct excitonic transitions at the K point in the Brillouin zone, which are also known as A1 and B1 transitions (A1 can be denoted as A or X, while B1 can be denoted as B) (**Figure 2.6**a).(*44*) The energy variation is attributed to the strong splitting at the valence band maximum in monolayer MoS_2 due to the spin-orbit effect, which derives from the lack of inversion symmetry in odd-layered MoS_2.(*48*, *52*) The PL quantum yield for monolayer

MoS_2 on the SiO_2/Si substrate was found to be >10^4 higher than its bulk counterparts and ~10^3 greater than multi-layer MoS_2 (**Figure 2.6**b). This is owed to the bandgap evolution from indirect to direct as the MoS_2 thickness decreases, thus promoting the radiative recombination rate drastically.(*44*) If monolayer MoS_2 is negatively doped either by the electron injection through the applied gate voltage or through chemical doping, a split of A1 transition peak appears due to the presence of negative trions (A^-), which can be understood as a quasiparticle composed of a neutral exciton bound with a free electron (**Figure 2.6**c).(*53–55*) The emission peak from negative trions is located at a lower energy (a larger wavelength) than the peak from neutral excitons. Trions were measured to have a large binding energy of ~20 meV at a low temperature of 10 K, making them significant even at room temperature.(*55*)

As mentioned in section 2.3.1, the band structure of MoS_2 is contributed by different spatially distributed atomic orbitals from Mo and S atoms as well as their hybridization states, which can be influenced by crystal structure dimensions and element variations with different sensitivities. Therefore, it is easy to understand why the mechanical strain loading(*56–60*) and chemical/physical doping(*2*, *61*) are two of the most commonly used approaches for bandgap engineering of monolayer MoS_2. In terms of the application of strain, theoretical calculations predict that a small bi-axial strain (~2%) can alter the direct bandgap of monolayer MoS_2 to an indirect gap, while both a relatively large bi-axial tensile (10%) and compressive strain (15%) can transform monolayer MoS_2 from a semiconductor to a metal.(*57*) Experiments also confirm the strain-induced tuning of the bandgap, many of which are probed by PL spectroscopy and reflect the optical bandgap modifications. The optical band gap showed an almost linear change of ~45 meV/% and ~99 meV% under uniaxial tensile strain and biaxial strain (**Figure 2.6**d).(*59*, *62*)

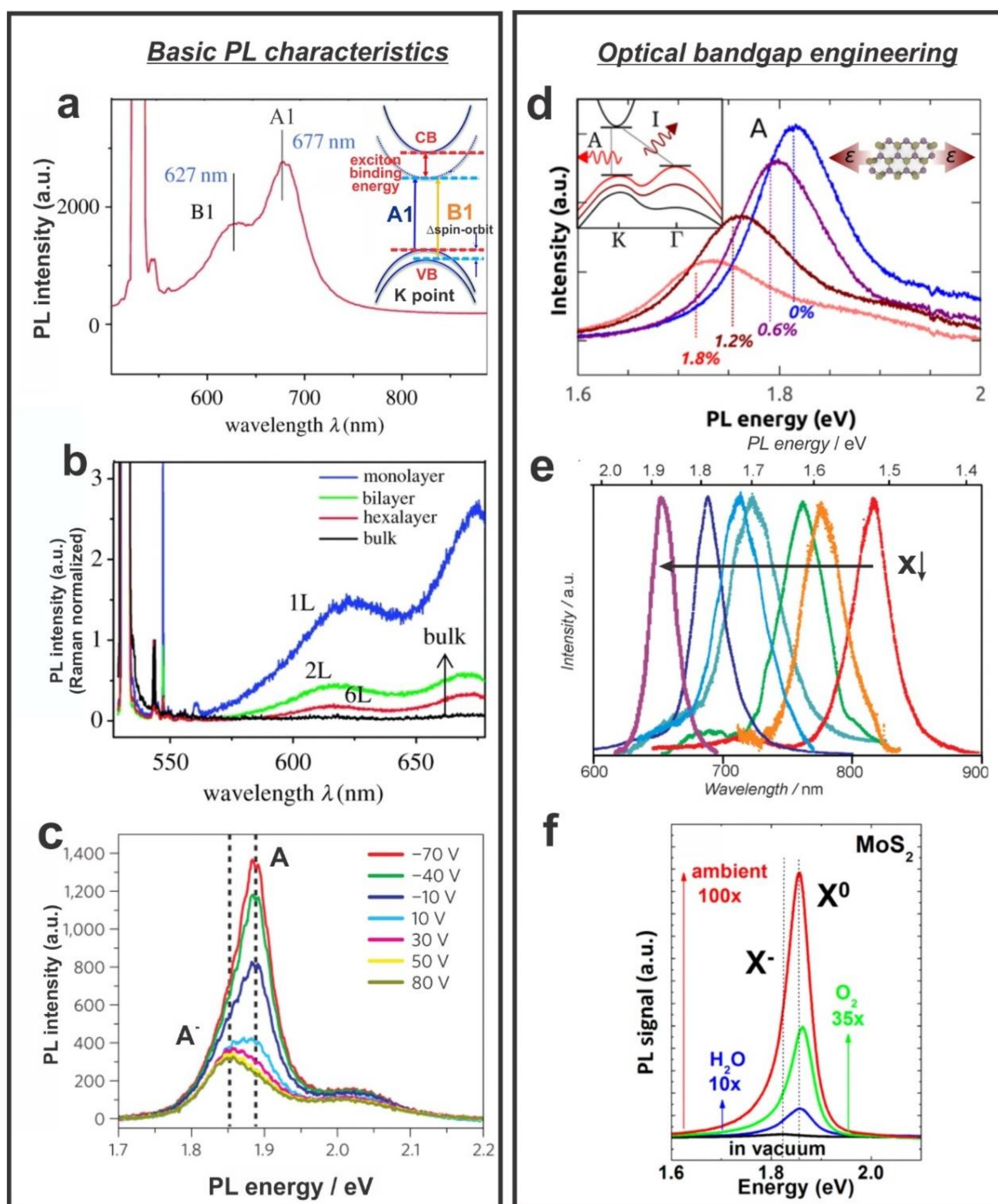

Figure 2.6. Basic PL characteristics and various methods for optical bandgap engineering. (a) PL spectra of monolayer MoS_2. Inset shows the corresponding A1 and B1 neutral exciton transition in the band structure diagram. (b) PL efficiency as a function of the layer number in MoS_2. (c) PL spectra of monolayer MoS_2 at different back-gate voltages at room temperature. The A^- resonance emerges and enhances with an increased negative doping level in monolayer MoS_2. (d) Evolution of PL spectra for monolayer MoS_2 under a uniaxial tensile strain ranging from 0 to 1.8%. (e) Normalized PL spectra for monolayer $MoS_{2(1-x)}Se_{2x}$ with different compositions. (f) PL variations of monolayer MoS_2 upon exposure to H_2O alone (blue curve), O_2 alone (green curve), and ambient (H_2O and O_2) (red curve) compared with its PL measured in vacuum after annealing (black curve). Figures reprinted (adapted) with permission from: (a,b), ref.(*44*), © 2010 American Chemical

Society; inset of (a), ref.(*63*), © 2014 The Royal Society of Chemistry; (c), ref.(*55*), © 2013 Macmillan Publishers Limited; (d), ref.(*59*), © 2013 American Chemical Society; (e), ref.(*64*), © 2013 John Wiley & Sons, Inc.; (f), ref.(*65*), © 2013 American Chemical Society.

Chemical and physical doping tailors the bandgap of MoS_2 predominantly through alloying and surface absorption of foreign molecules. Alloying can be realized by mixing MoS_2 with either metals, such as tungsten (W), or chalcogen atoms, like selenium (Se). Theoretical calculations predict that the bandgap of $Mo_{1-x}W_xS_2$ varies from 1.87 to 2.0 eV with concentration changing from MoS_2 to WS_2, which matches with experimentally measured variation from 1.85eV to 1.99eV well.(*66*, *67*) The bandgap evolution of $MoSe_{2(1-x)}S_{2x}$, which has been theoretically calculated to vary from 1.62eV to 1.86eV, also agrees with experimental results ranging from 1.55eV to 1.87eV, when the stoichiometry changes from $MoSe_2$ to MoS_2 (**Figure 2.6**e).(*64*, *66*) The source of the surface absorption can come from gas molecules or impurities on the substrate.(*65*, *68*) Experiments have shown that charge transfer through the surface-absorbed p-type dopants, which have strong electron affinity and can withdraw electrons from the MoS_2 (*e.g.*, O_2, H_2O, *etc.*), enhances the PL intensity (**Figure 2.6**f), while the n-type dopants reduces the PL intensity.(*54*, *65*) This is explained by the modulation of carrier density which can switch the PL emission between neutral exciton emission and negative trion emission.(*54*)

2.3.3 Vibrational Properties

The vibrational properties of MoS_2 is detected by Raman spectroscopy, which is the widely-used, non-destructive, vibrational spectroscopy that relies on inelastic scattering. The general working principle of Raman spectroscopy can be described as follows. When a monochromatic light source illuminates on a sample, the majority of the light is elastically scattered, which has no energy difference with the excitation source. This is known as Rayleigh scattering. However, a tiny amount of the light is inelastically scattered which has a shift in energy from the excitation source due to interactions between the vibrational

energy levels of the sample and the incident electromagnetic waves. Recording the intensity of this inelastically scattered light and their corresponding frequency shift with respect to the incident light source gives a Raman spectrum which is helpful to sample identification and quantitation.

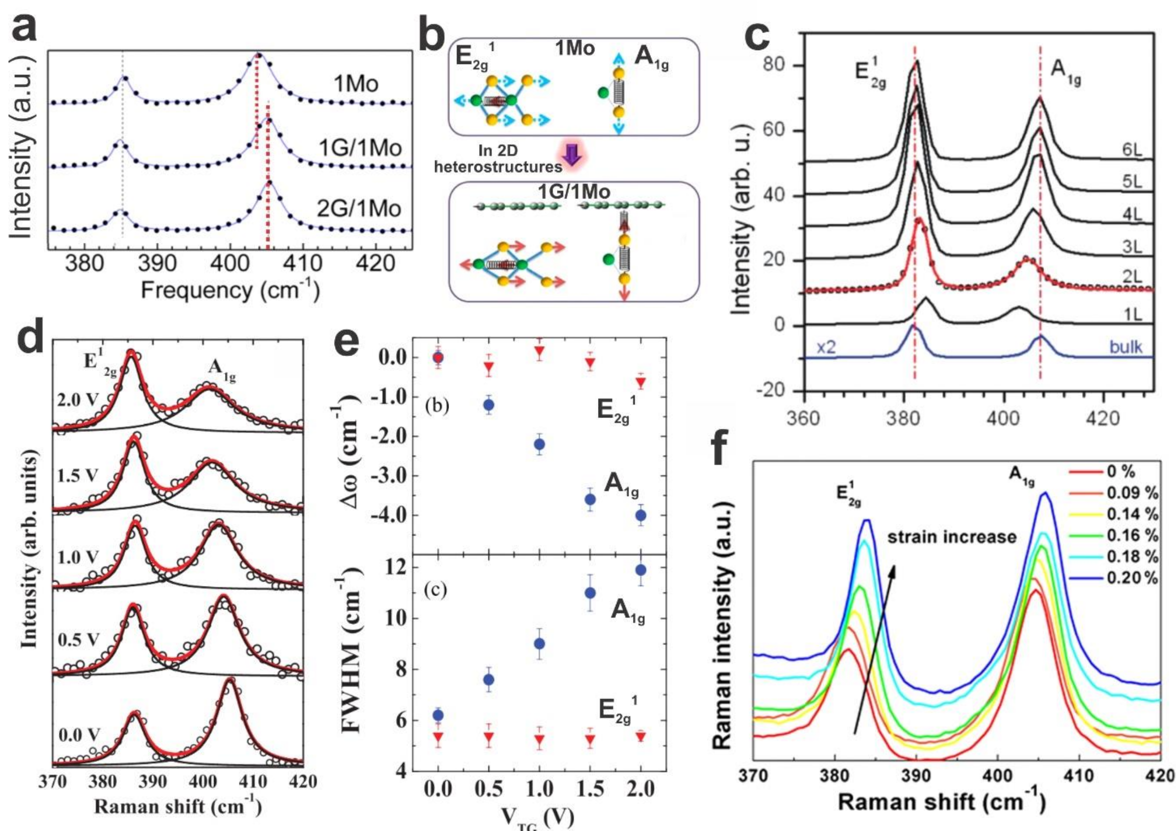

Figure 2.7. Vibrational properties of monolayer MoS_2 characterized by Raman spectroscopy. (a) Shift on the A_{1g} peak position (red dashed lines) as monolayer MoS_2 resides on different substrates. 1Mo indicates that monolayer MoS_2 sits on the SiO_2, while 1G/1Mo and 2G/1Mo represent that monolayer MoS_2 sits on monolayer and bilayer graphene, respectively. (b) Spring model showing two characteristic vibration modes of monolayer MoS_2 (E_{2g}^1 and A_{1g}), which also facilitates to understand the sensitivity of A_{1g} on the interlayer interaction. (c) Evolution on both the E_{2g}^1 and A_{1g} mode dependent on the layer number. (d,e) Variation on the A_{1g} peak position and its full width of half maximum (FWHM) under an increased electron injection dose, conducted by enhancing the top-gate voltages from 0.0 to 2.0 V. (f) Variation on the E_{2g}^1 mode of trilayer MoS_2 under different compressive strains. Figures reprinted (adapted) with permission from: (a,b), ref.(*69*), © 2014 American Chemical Society; (c), ref.(*70*), © 2010 American Chemical Society; (d,e), ref.(*71*), © 2012 American Physical Society; (f), ref.(*72*), © 2013 American Chemical Society.

Raman spectroscopy can provide information about van der Waals interactions (*e.g.* layer number and substrate effect), doping level and lattice strain of MoS_2 mainly through studying the frequency of characteristic peaks. MoS_2 has two most typical vibration modes, E_{2g}^1 and A_{1g}. The E_{2g}^1 mode represents the in-plane opposite vibration of two S atoms with respect to the Mo atom sitting in between them, while the A_{1g} mode is related to the out-of-plane vibration of S atoms in opposite directions, which is believed to be more influenced by the long-range interlayer Coulombic interactions with its neighbouring materials compared with the E_{2g}^1 mode.(*9*, *73*) Therefore, A_{1g} frequency varies remarkably when monolayer MoS_2 resides on different substrates, which alters interlayer interactions, while E_{2g}^1 peak shows negligible shift (**Figure 2.7**a,b).(*69*) As the MoS_2 thickness decreases, A_{1g} undergoes an obvious red shift since the decreased van der Waals forces leads to a smaller restoring forces on atoms. Unexpectedly, E_{2g}^1 shows a blue-shift rather than a commonly expected red-shift. The anomalous behaviour of E_{2g}^1 is speculated to arise from the stacking-induced in-plane configuration change or the Coulombic interlayer interactions (**Figure 2.7**c).(*70*) Practically, the separation between E_{2g}^1 and A_{1g} mode has been widely used to reflect the layer number of MoS_2. Monolayer MoS_2 exhibits a frequency difference ranging from 17.5 to 21 cm^{-1}, and the frequency separation enhances as the MoS_2 thickness increases until the layer number reaches five, where both E_{2g}^1 and A_{1g} mode converge to their bulk values.(*36*, *51*, *70*, *74*) Due to the strong interaction between A_{1g} phonon and electrons, A_{1g} mode is also sensitive to the doping of MoS_2 either from surface adsorbates or the gate-induced electron injection in a transistor. It shows a red shift of the peak position with an increase of the peak width when the doping level enhances (**Figure 2.7**d,e).(*71*, *75*) The Raman spectrum can also unveil the lattice strain predominantly by tracking the evolution of in-plane vibration mode of E_{2g}^1. The E_{2g}^1 peak is red/blue shifted under a tensile/compressive strain, while the A_{1g} peak barely moves (**Figure 2.7**f).(*72*, *76*) Conley

et al. reported a E_{2g}^1 peak split when the mechanically-loaded tensile strain on monolayer MoS_2 is relatively large (>0.8%) and attributed this phenomenon to the strain-induced breaking of the crystal symmetry.(*59*)

2.3.4 Mechanical Properties

2D MoS_2 is reported to possess outstanding mechanical properties by experiments using the AFM probe. Bertolazzi *et al.*(*77*) measured the stiffness and breaking strength of mechanical exfoliated monolayer MoS_2, yielding an in-plane stiffness of 180 ± 60 Nm^{-1}, which corresponds to an effective Young's modulus of 270 ± 100 GPa. Such a high Young's modulus is comparable to that of steel (180 GPa). Fracture takes place when an effective strain reaches between 6% and 11% with an average breaking strength of 15 ± 3 Nm^{-1} (23 GPa). Castellanos-Gomez *et al.*(*78*) measured the elastic properties of suspended MoS_2 nanosheets having thickness variations from 5 to 25 layers and obtained their average Young's modulus as high as 330 ± 70 GPa. In addition, the transistor made up of MoS_2 thin films exhibits remarkably high flexibility, being capable to preserve its carrier mobility at a curvature of 0.75 mm.(*79*) The first-principle calculation can also predict the ideal biaxial tensile strength and elastic modulus, which shows a good agreement with experimental observations.(*80*) These advantages render 2D MoS_2 to become a promising material for flexible electronic and optoelectronic devices.

2.4 CVD Synthesis of 2D MoS_2

In order to meet the demand for fundamental research and the future industrial production, many synthesis methods have been developed, including different types of exfoliation,(*81–83*) hydrothermal synthesis(*84*) and physical vapour deposition(*85*, *86*). However, the growth results are restricted by small lateral size of crystal domains, low yield, poor quality, hard control on the layer number and high requirements of growth conditions. Therefore, a versatile approach of generating high-quality, large area 2D crystalline MoS_2

with controllable thickness and excellent electronic properties are in high demand. Chemical vapour deposition (CVD) approach could hold the answer for this demand. It can generally be categorized into two routes. The first route involves solid phase Mo-based precursors participating in the reaction. Usually, the Mo-based precursors are pre-coated on the substrate surface followed by a sulphurization or decomposition process to convert them into MoS_2. The second route is realised through the vapour reaction, where all precursors are first vaporized and then transported into the reaction zone to form MoS_2. In this section, two routes with different precursors will be introduced followed by a discussion on various synthesis parameters on the growth results.

2.4.1 Route I

One of the early attempts for monolayer MoS_2 growth *via* Route I was done by Zhan *et al.* They deposited the Mo thin films on the SiO_2/Si substrate followed by a sulphurization process.(*87*) The coating of Mo layers was through the e-beam evaporation, while the vapour-phase sulphurization was conducted at a temperature of ~750 °C in an atmospheric pressure CVD system (APCVD) (**Figure 2.8**a). The method can produce single- and few-layered polycrystalline MoS_2 with grain sizes ranging from 10-30 nm (**Figure 2.8**b–d). The small grain sizes could be attributed to the high melting point of Mo (~2623°C), which is much higher than the growth temperature of MoS_2 using Mo and S (~750 °C), and the initial polycrystalline nature of the deposited Mo atomic layer. The high melting point of Mo restricts the migration ability of Mo atoms during the MoS_2 growth, thus being detrimental to the grain size expansion. The size and thickness of MoS_2 layers was only limited by the substrate size and the thickness of the pre-deposited Mo. The devices based on as-grown few-layer MoS_2 with a high density of grain-boundaries displayed p-typed behaviour with relatively low field effect mobility between 0.004 to 0.04 $cm^2V^{-1}s^{-1}$. Laskar *et al.*(*88*) also applied this method but changed the substrate to crystalline sapphire and increased the

sulphurization temperature up to 1100°C. It was found that a higher sulphurization temperature can enhance the MoS_2 crystallinity, evidenced by the increased relative ratio between E^1_{2g} and A_{1g} peak in Raman spectroscopy, as the in-plane vibration mode (E^1_{2g}) is subject to the nanoscale and randomly distributed grains of the intralayer structure. Apart from the growth temperature, the choice of the substrate also crucially impacts the crystal quality of MoS_2 films. A high temperature sulphurization of pre-deposited Mo film on (0001) oriented sapphire produced large area (0001) oriented MoS_2 multilayer films. Their devices fabricated with this 2D MoS_2 showed n-type behaviour with significantly improved mobility of 10-14 $cm^2V^{-1}s^{-1}$.

In addition to the metal Mo, molybdenum oxides (MoO_x) is also a choice of pre-coated materials. Lin *et al.* selected MoO_3 (melting point: ~795°C) as the deposition material on the *c*-phase sapphire substrate (**Figure 2.8**h).(*89*) Then a two-step process was employed. The first anneal was conducted at 500 °C in a reducing environment of mixed argon and hydrogen (Ar/H_2) under a pressure of 1 Torr, while the second anneal took place at 1000 °C in a sulphur atmosphere under 600 Torr. Large-area, polycrystalline multi-layer MoS_2 films (2-3 layers) were uniformly grown on the entire sapphire substrate (**Figure 2.8**i–k) with a grain size of ~160 nm, yielding n-type MoS_2 field effect transistor (FET) devices with an on/off ratio of ~ 10^5 and a field effect-mobility of 0.8 $cm^2V^{-1}s^{-1}$. The film thickness was found to rely on the amount of pre-coated MoO_3. Wang *et al.* deposited rhomboidal MoO_2 microplates on the SiO_2/Si substrate as a starting material (**Figure 2.8**e). It was realised by reducing the evaporated MoO_3 through sulphur vapour at 650-850°C, leading to the MoO_2 nucleation on the substrate surface.(*74*) MoO_2 microplates were further sulphurized at 850-950 °C under the atmospheric pressure for 0.5-6 hours, forming controllable layer numbers of MoS_2 depending on the annealing duration (**Figure 2.8**f). The MoS_2 thin layers can be peeled off from the MoO_2 microplates by spin-coating poly(methyl methacrylate) (PMMA)

thin films (**Figure 2.8**g), owning to a relatively weak adhesion between MoS_2 and MoO_2. The obtained 2D MoS_2 have an average domain size is of ~10 μm, exhibiting n-type behaviour in a bilayer FET device with an on/off ratio of ~10^6 and a carrier mobility of ~0.3 $cm^2 V^{-1}s^{-1}$.

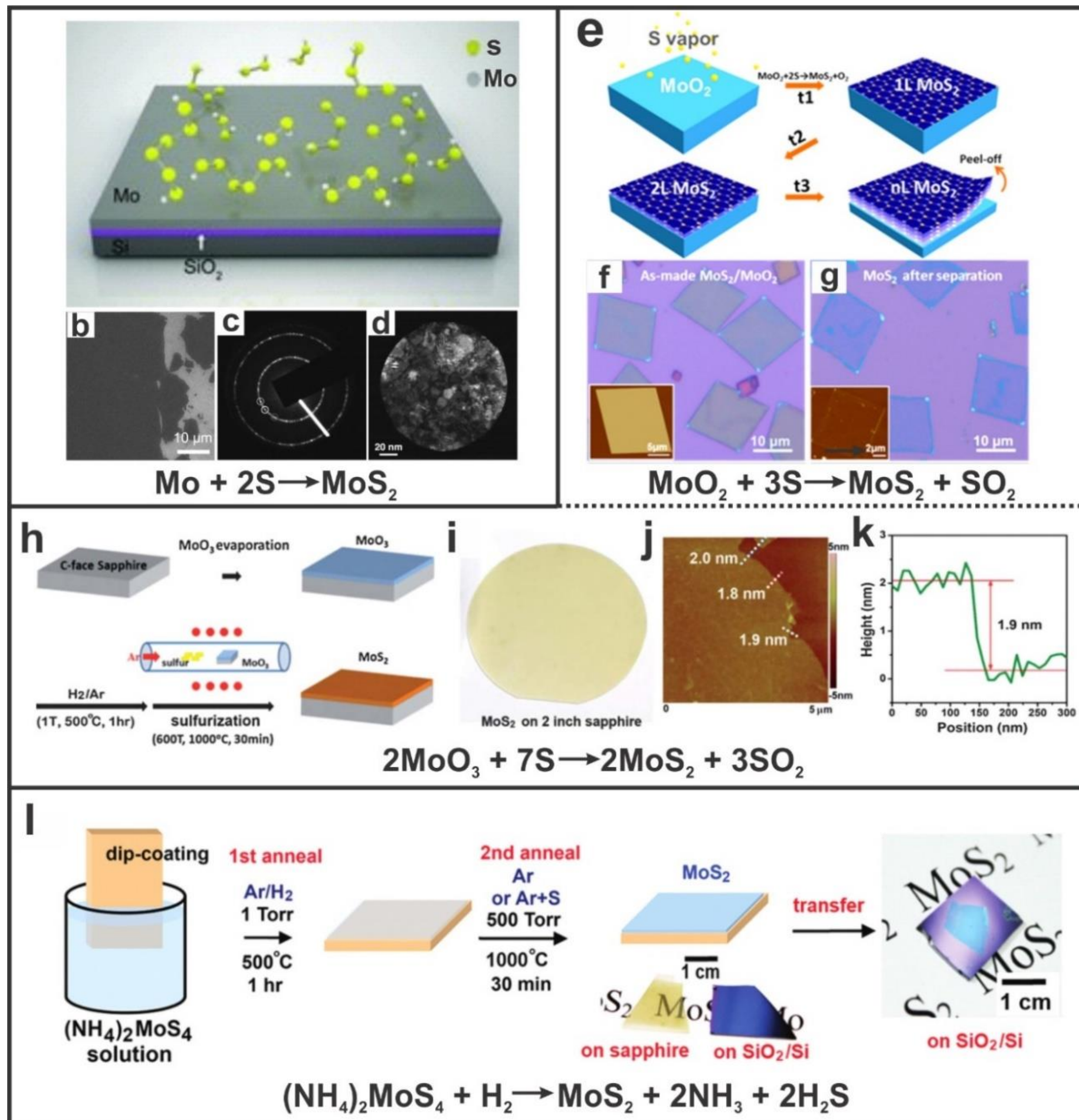

Figure 2.8. CVD synthesis methods *via* route I. (a–d) Sulphurization of the pre-coated Mo layer to obtain MoS_2 thin films (a). SEM image (b), diffraction pattern (c) and dark-field TEM image (d) of as-grown MoS_2 films. (e–g) Layer-by-layer surface sulphurization of MoO_2 microplates to achieve thickness controllable MoS_2 (e). Optical images show as-made MoS_2/MoO_2 (f) and transferred MoS_2 (g) after being peeled off, respectively, with corresponding AFM images in insets. (h–k) Sulphurization of a MoO_3 layer pre-deposited on the c-phase sapphire (h) to obtain 2-inch sized multilayer MoS_2 films, verified by the optical image (i) and AFM (j,k). (l) Decomposition of a

pre-coated ammonium thimolybdate layer. Figures reprinted (adapted) with permission from: (a–d), ref.(*87*), © 2012 John Wiley & Sons, Inc.; (e–g), ref.(*74*), © 2013 American Chemical Society; (h–k), ref.(*89*), © 2012 The Royal Society of Chemistry; (l), ref.(*90*), © 2012 American Chemical Society.

Ammonium thimolybdate ($(NH_4)_2MoS_4$) is the third type of pre-deposited Mo-based material in route I (**Figure 2.8**l). Liu *et al.*(*90*) dissolved $(NH_4)_2MoS_4$ in the dimethylformamide (DMF) solution, dipped the substrate in it followed by a vertical pull of it out of the solution at a constant low rate to ensure the uniform coating of the precursor layer. Subsequently, the pre-treated substrate was annealed twice. The first anneal was carried out at a temperature of 500°C under a low pressure of 1 Torr in the flowing Ar/H_2, which realized the chemical conversion of $(NH_4)_2MoS_4$ to MoS_2 and removed residual NH_3 and other by-products. The reaction can be simplified as $(NH_4)_2MoS_4 + H_2 \rightarrow 2NH_3 + 2H_2S + MoS_2$. The second anneal was at 1000°C under a pressure of 500 Torr in Ar. Adding S in the second anneal brought several benefits, including protecting the MoS_2 film from oxidation, enhancing the crystallinity and increasing the grain size (hundreds *versus* tens of nanometres). This approach can grow large-area, uniform, multi-layer MoS_2 films (2-3 layers) on both SiO_2/Si and sapphire substrates. However, the as-grown MoS_2 on sapphire showed a better crystal quality and electrical performance compared with those grown on SiO_2/Si. They had a grain size of ~160 nm and exhibited n-type behaviour with an on/off ratio of ~10^5 and electron mobility up to 6 $cm^2V^{-1}s^{-1}$. This was attributed to a higher chemical stability of sapphire at high temperature than that of SiO_2, which effectively suppressed the oxygen doping in the MoS_2 lattice.

To sum up, route I, which is realized by the sulphurization or decomposition of pre-deposited solid-state Mo-based precursors, is a straightforward and universal way to synthesize few-layer MoS_2. The choice of the pre-coated Mo-based materials evolved from metal Mo to MoO_x to $(NH_4)_2MoS_4$, showing a decreased melting point (increased vapour

pressure under the same growth temperature), a better solubility and a lower chemical conversion temperature to MoS_2, which enhances the controllability of the deposition amount and thickness on the substrate as well as mitigating the reaction condition. Moreover, route I has advantageous in producing wafer-scale continuous MoS_2 thin films, as the growth area is only restricted by the substrate scale. However, its weaknesses lie in the difficulty of obtaining monolayer MoS_2, a poor thickness uniformity, small grain sizes and the cockamamie multi-step fabrication processes. They originate from the harsh requirements of pre-depositing an ultrasmall amount of Mo-based precursors with atomic-level homogeneity, the limited free diffusion path of atoms in a solid-phase reaction and a potential incomplete sulphurization of the precursor layers. Therefore, new methods possessing a more precise layer number control, a better reaction uniformity and concise steps are demanding.

2.4.2 Route II

Route II is a one-step vapour-phase reaction developed from route I, where all precursors are thermally evaporated and transported to the reaction zone simultaneously to form MoS_2 on the substrate. The pioneering work was done by Lee *et al.*(*91*), who loaded MoO_3 and S powder in the heating zone with a substrate (either SiO_2/Si or sapphire) face-down covered on the crucible containing MoO_3 (**Figure 2.9**a,b). The substrate was pre-treated by aromatic molecules (*e.g.* reduced graphene oxide (rGO)), as seed crystals can enhance the wettability of the substrate surface. The reaction underwent at a relatively low temperature of 650°C in the flowing nitrogen (N_2) under atmospheric pressure. Star-shaped MoS_2 crystals with a lateral grain size of ~160 nm grew around the seed crystals which coalesced to form monolayer to few-layer areas. The seed crystals performed as the nucleation sites and promoted the layer-by-layer lateral growth of MoS_2. FET devices fabricated based on the as-prepared MoS_2 crystals showed n-type behaviour with an on-off

ratio of ~10^4 and a field effect mobility of 0.02 $cm^2 V^{-1}s^{-1}$. This seed-promoted synthesis strategy was further developed by Lee *et al.* and Ling *et al.* by developing seeding promoters to larger aromatic systems with high sublimation/decomposition temperatures and proper concentrations. These modifications facilitate the growth of monolayer MoS_2 on various substrates, including both three-dimensional (3D) corrugated substrates (quartz, sapphire, Si particles, TiO_2 aggregates, *etc.*) and 2D substrates (graphene, hexagonal boron nitride (h-BN), *etc.*).(*92*, *93*) The typical growth results with proper seeds were isolated triangular domains with lateral sizes of ~50 μm and small regions of continuous films on SiO_2/Si substrates.

Van der Zande *et al.* optimized the CVD technique reported by Lee *et al.*(*91*) through not using seeds to realize the layer-by-layer growth of MoS_2 on SiO_2/Si substrates. It excludes the potential contamination effects from seeding.(*37*) They obtained monolayer MoS_2 triangular isolated islands with an average crystal size varying between 20 and 100 μm, and the largest single crystal reached an edge length up to ~120 μm. An ultraclean substrate surface before the growth and a protection of precursors from the air during storage were demonstrated as keys for growth success. However, as the substrate was still mounted face down on the crucible loading MoO_3, non-uniformity in nucleation density and crystal size is an obvious limitation, which is due to the sharp MoO_3 concentration gradient on the substrates.

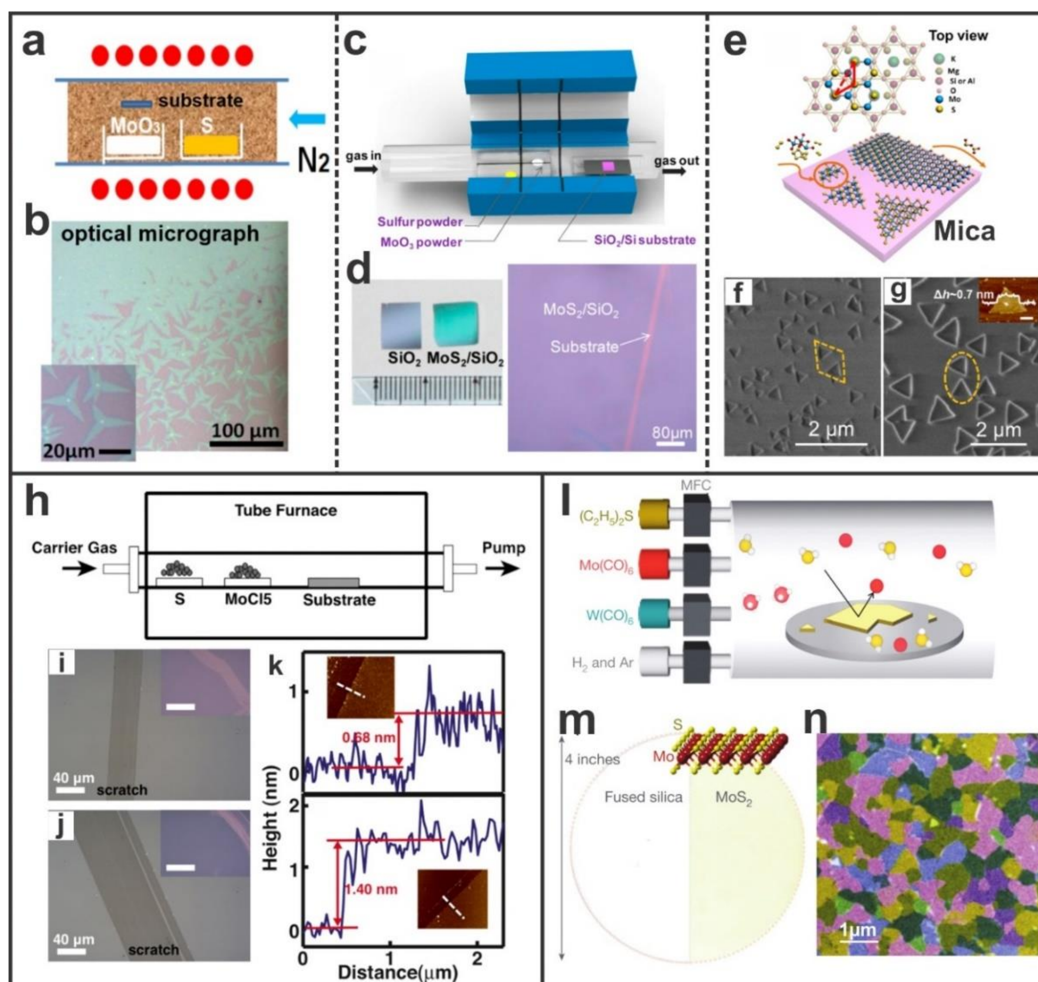

Figure 2.9. CVD synthesis strategies *via* route II. (a–g) Three different setups for monolayer MoS_2 growth by the reaction between the MoO_3 and S vapour. The first approach pre-treated the substrate with the chemical seeds of rGo and loaded the substrate facedown at the crucible containing the MoO_3 powder (a), growing inhomogeneously distributed star-shaped monolayer MoS_2 domains, as shown by the optical image in (b). The second approach separated MoO_3 and S precursors by utilizing two mini-tubes and was conducted under low pressure (c), achieving centimetre-scale uniform monolayer films, as shown by optical images in (d). The third approach selected the layered mica as the substrate (e) and realized the epitaxial growth of monolayer MoS_2 domains, confirmed by SEM images in (f,g). (h–k) CVD growth of MoS_2 by the gas-phase reaction between $MoCl_5$ and S (h), Optical images (i,j) and AFM (k) show the obtain of mono- and bi-layer continuous films. (l) Schematic illustration of the setup for metal-organic CVD growth method, applicable for both MoS_2 and WS_2 synthesis. MFC represents the mass flow controller. (m) Photo of monolayer MoS_2 films grown on the 4-inch fused silica substrate. (n) False-colour dark field TEM image showing a continuous MoS_2 monolayer film with an average grain size of ~ 1 µm. Figures reprinted (adapted) with permission from: (a,b). ref.(*91*), © 2012 John Wiley & Sons, Inc.; (c,d), ref.(*94*), © 2013 American Chemical Society; (e-g), ref.(*95*), © 2013 American Chemical Society; (h–k), ref.(*96*), © 2013 Macmillan Publishers Limited; (l-n), ref.(*97*), © 2015 Macmillan Publishers Limited.

Najmaei *et al.* systematically studied the fundamental mechanism of this approach by varying the precursor concentration, chamber pressure, reaction temperature and substrate surface roughness.(*36*) Rather than using the powder-state MoO_3, they prepared it into dispersed highly-crystalline nanoribbons through hydrothermal reactions on a SiO_2/Si substrate and placed another two bare SiO_2/Si chips with face-up beside it for MoS_2 growth. A stage-heating was conducted with the main reaction occurring at 850°C, which produced primarily sharp-edged triangular monolayer MoS_2 single crystals with a side length of ~10 µm. It was found that the S concentration governs the morphology and size of the single crystalline domains, while the MoO_3 concentration determines the nucleation density and the coverage ratio of MoS_2 on the substrate. In terms of the total chamber pressure, as it interrelated to the S concentration (S partial pressure), which further changed the concentration ratio between gaseous MoO_3 and S, both the nucleation density and the crystal morphology were impacted by this parameter. Moreover, MoS_2 triangular domains and films showed preference to nucleate in the vicinity of edges, scratches, dust particles or rough surfaces. It inspires the spatial-controlled growth strategy by patterning the substrate with a uniform distribution of rectangular SiO_2 pillars, thus promoting the MoS_2 nucleation density at designated locations and enabling the continued film growth. The FET devices fabricated with the as-grown MoS_2 films showed n-type behaviour with an average mobility of 4.3 ± 0.8 $cm^2V^{-1}s^{-1}$ and a maximum on/off ratio of 6×10^6.

Growing large-are uniform monolayer MoS_2 films is a pivotal precondition for industrial applications. To realize this goal, a stable and controllable introduction of gaseous MoO_3 and S into the reaction zone is essential. However, all previous methods cannot avoid the gradual quench of the MoO_3 precursor by S vapour as the reaction proceeds, which induces a decreased and uncontrollable evaporation amount of MoO_3. Zhang *et al.* improved the CVD setup by separately loading MoO_3 and S precursor in two different mini-tubes

(**Figure 2.9**c). It avoided their cross-contamination and ensured a stable supply of both gaseous precursors to the reaction region.(*94*) The SiO_2/Si substrate was horizontally loaded at the downstream of the quartz tube with faces up. The growth proceeded under a low pressure of 0.67 Torr with typical temperatures of 120-130°C, 450-600°C and 750-800°C for S, MoO_3 and substrates, respectively. Centimetre-scale, continuous polycrystalline monolayer MoS_2 film were obtained over the entire substrate surface (**Figure 2.9**d) with a tunable grain size from ~20 nm to ~1 μm. Bilayer or multilayer was rarely seen, indicating a self-terminated growth mechanism under such condition. FET fabricated based on as-grown MoS_2 films with a typical grain size of ~ 600 nm showed n-type behaviour with a field mobility of ~ 7 $cm^2V^{-1}s^{-1}$ and an on/off ratio of ~ 10^6.

In addition to the requirement of large-area, monolayer growth with thickness uniformity, an ordered crystal orientation alignment on the substrate is another concern in MoS_2 synthesis. Ji *et al.*(*95*) reported the epitaxial growth of monolayer MoS_2 on mica ($KMg_3AlSi_3O_{10}F_2$) (**Figure 2.9**e) at a low reaction temperature of ~ 530 °C under a pressure of 30 Pa. Mica has a good lattice match with MoS_2. Uniform triangular MoS_2 monolayers were achieved with two primary crystal orientations having 180° twist (**Figure 2.9**f). They were intrinsically strained due to a small lattice mismatch (~ 2.7%) between MoS_2 adlayers and the mica substrate.

Apart from the most frequently used precursors, MoO_3 and S, there also exist other types of precursors in route II. Yu *et al.*(*96*) reported using molybdenum chloride ($MoCl_5$) and sulphur powder as precursors. The reaction was at ~850°C under a low pressure of ~ 2 Torr. Uniform and high quality monolayer and bilayer MoS_2 films were deposited on the substrates of SiO_2/Si and sapphire (**Figure 2.9**h–k). It was found that the MoS_2 layer number can be adjusted accurately by the control of the $MoCl_5$ amount, the chamber pressure and the growth temperature. Moreover, the synthetic process was demonstrated to be self-limited

controlled by the balance between the equilibrium pressure of MoS_2 thin films and the partial pressure of MoS_2 species in the vapour phase (Note that whether the growth mechanism of 2D MoS_2 *via* route II is the ‘absorption-surface reaction’ process or the ‘gas phase reaction-precipitation’ process is still controversial. This work supports the latter. More information is given at the end of this section). Therefore, the partial pressure of MoS_2 species and the interaction of MoS_2 films with substrates played key roles in this self-limiting mechanism.

The most recent progress was done by Kang *et al.*, who applied the metal-organic Mo-based precursor, $Mo(CO)_6$, and $(C_2H_5)_2S$ to form 4-inch wafer-scale homogeneous MoS_2 monolayer films with an average grain size of ~ 1 μm on SiO_2/Si substrates (**Figure 2.9**l–n). The electrical performance is outstanding, showing an electron mobility of 30 $cm^2V^{-1}s^{-1}$ at room temperature and 114 $cm^2V^{-1}s^{-1}$ at 90 K, being comparable with that from exfoliated samples. The gaseous precursors were slowly injected into the chamber, and the reaction was conducted at a low temperature of 550 °C under a low pressure of 7.5 Torr in the flowing H_2/Ar for a long time (~ 26 hrs). The growth mode is governed by the partial pressure of Mo vapour (P_{Mo}) supplied by the thermal decomposition of $Mo(CO)_6$. A low P_{Mo} in a $(C_2H_5)_2S$ sufficient atmosphere promoted the layer-by-layer growth mode, resulting in a uniform monolayer MoS_2 film formation, while a higher P_{Mo} led to an island growth mode having a mixture of monolayer, multilayer and no-growth areas.(*98*) This could be attributed to a low density of Mo active species absorbed on the substrate under a low P_{Mo}, which ensures the edge attachment to the as-formed monolayer MoS_2 nuclei as the dominant growth mechanism. The grain size, morphology and intergrain stitching are sensitive to the concentration of $(C_2H_5)_2S$, H_2 and residual water in the CVD system. A high concentration of these three constituents, which links to an enhancement of S vapour concentration, led to an increase of the nucleation density and a decrease of the grain size. In addition, the intergrain boundaries did not remarkably degrade the electrical transport properties of their

monolayer MoS_2 films, which was presumably due to a good lattice stitching with less defects at grain boundaries.

To conclude, route II is a more feasible and controllable way to grow large-area, high quality uniform monolayer MoS_2 domains and films with big grain sizes compared with route I. Its advantages come from: (1) the nature of the vapour phase reaction, which provides a better mixture between reactants, a more thorough sulphurization process and a larger mean free diffusion path of species on the substrate, which enhances product's crystallinity and grain sizes; (2) a more accurate control on the injection amount of precursors, as precursors are vaporized and diluted in the inert carrier gas, giving a better tunability on their concentrations; (3) more adjustable parameters, such as the independent temperature control on S, Mo-based precursor and the growth substrate, the chamber pressure, seeds coated on the substrate, *etc.*, which increases the flexibility of the MoS_2 growth; (4) a more time-effective, one-step fabrication process. However, the increased controllability and flexibility also indicate an enhanced complexity in the growth mechanism. Until now, the detailed mechanism of route II has not been fully understood. There are two possible processes. One supports an 'absorption-surface reaction' process, where both the Mo-based (MoO_{3-x}) and S-based (S or H_2S) precursor species first absorb on the substrate followed by a surface migration/reaction process between them to form 2D MoS_2. The other indicates a 'gas phase reaction-precipitation' process, where both precursors first react directly in the gas phase to form gaseous MoS_2, which then precipitates from the gas, nucleate and grow 2D MoS_2 on the substrate. To realize a full control of 2D MoS_2 growth in route II, an in-depth understanding of its growth mechanism is highly desirable, which relies on the careful study of key synthesis parameters. I will discuss them in the next section.

2.4.3 Discussion

Even though hundreds of different recipes in route II have been reported, there exist some fundamental factors of growth, which are of universality and govern the synthesis results. In my perspective, three factors are of great significance. The first is the growth temperature (T_{growth}), which is often close to the substrate temperature ($T_{substrate}$) in most CVD designs. It predominantly determines the reaction rate and the complete degree, as well as the surface migration ability of adsorbates on the substrate. It also impacts the density of absorbed active species (Mo-based, S-based precursor molecules and as-formed MoS_2) on the substrate ($D_{surface}$). The second key factor is the density of gas molecules in the growth system (D_{gas}), which is commonly tailored by the total chamber pressure ($P_{chamber}$). D_{gas} influences the volatilization and diffusion of precursors. More significantly, it dominates the mean free path of the gas molecules, thus impacting the rate of the mass transport procedure in the gas phase. Therefore, an alteration on D_{gas} is frequently applied to kinetically switch the rate-limiting step between the mass transport process and the surface reaction/diffusion process,(*99*) which influences the thickness uniformity of MoS_2. That is why APCVD and low pressure CVD (LPCVD) usually have distinct growth mechanisms and results. The third factor is the density of active species absorbed on the substrate surface, defined as $D_{surface}$. $D_{surface}$ influences the nucleation density and the grain size of as-grown MoS_2. A decrease in $D_{surface}$ will reduce the nucleation density and enlarge the grain size. Furthermore, at a suitable T_{growth}, $D_{surface}$ governs the average distance travelled by an active particle before collisions with another active particle on the surface, defined as mean free migration length ($L_{surface}$). The lower the $D_{surface}$ is, the longer the $L_{surface}$ will be. A longer L_{surfce} triggers the MoS_2 growth to be thermodynamically controlled rather than kinetic controlled. Therefore, it gives rise to an enhanced crystallinity and facilitates the layer-by-layer growth of MoS_2, because absorbed active species are capable of migrating and binding to energetically

favourable sites (edges and corners of the as-formed MoS_2 monolayer nuclei) to expand pristine monolayer lattice. Unfortunately, $D_{surface}$ is not a parameter that can be directly controlled in experiments. It is determined by $T_{substrate}$ and the partial pressure of gas precursors based on the adsorption law. The partial pressure of precursors can further be controlled by those experimental parameters, including the heating temperature for the Mo-based and S-based precursors (T_{Mo} and T_S), their usage amounts, the flow rate of the carrier gas and even the $P_{chamber}$ when the chamber pressure is pumped below the equilibrium partial pressure of the precursor at its heating temperature. I will discuss these experimental parameters in the following paragraphs.

In principle, a good $T_{substrate}$ should ensure a thorough sulphurization of the Mo-based precursor, a relatively low $D_{surface}$, and supply enough energy for absorbed active species on the substrate to overcome the surface migration barrier. The ideal growth temperature when using MoO_3 and S as precursors was reported to be 800-850°C, and increasing the growth temperature is widely found to be beneficial for the MoS_2 crystallinity improvement.(*36*) T_{Mo}, and T_S directly influence the partial pressure of Mo-based and S-based precursor vapours, denoted as $P_{gas\text{-}Mo}$ and $P_{gas\text{-}S}$, respectively. The growth is commonly conducted in a S-sufficient atmosphere ($P_{gas\text{-}S} >> P_{gas\text{-}Mo}$) with a low $P_{gas\text{-}Mo}$ for the purpose of a complete sulphurization process and suppressing the nucleation density, especially when using MoO_3 and S as precursors.(*36*) The MoS_2 domain morphology was found to be sensitive to the ratio between $D_{gas\text{-}Mo}$ and $D_{gas\text{-}S}$ (see section 4.1).(*100*) The usage amount of precursors can also impact their corresponding partial pressure in the system under a certain heating temperature. However, since the evaporation of the solid precursors is directly related with their surface area rather than the weight. It is necessary to keep the surface area of precursor powder to be roughly the same between each experiment as well when the usage amount

does not change, so that the partial pressure of the precursor vapour can remain stable in each attempt.

In terms of the carrier gas, if it is fully composed of inert gases (N_2, Ar, *etc.*), its effect predominantly lies in the dilution of the gaseous precursors, transporting reactants to the reaction zone and removing by-products out of the CVD system. However, if the carrier gas contains active ingredients, such as H_2 when utilizing $Mo(CO)_6$ and $(C_2H_5)_2S$ as precursors, it plays a more complicated role. H_2, on the one hand, promotes the decomposition of $(C_2H_5)_2S$ to release active S-based species for MoS_2 nucleation and growth, and on the other hand, etches the as-grown MoS_2 and prevents the intergrain connection. Therefore, a proper ratio between H_2 and the inert gas should be determined to reach a good balance between the above competing effects. In addition, some commonly-encountered impurity gases, such as H_2O and O_2, may also play an important role in the MoS_2 growth and influence the reproducibility. Water vapour can convert MoO_3 to a volatile mono-hydroxide ($MoO_2(OH)_2$) at elevated temperatures, hence the sublimation amount of the Mo-based precursor vapour would increase at a certain temperature if there is residual water in the growth system or the MoO_3 is stored in the humid atmosphere.(*101*) A small amount of oxygen (2 sccm oxygen and 100 sccm Ar) has been reported to be conducive to the large-area (side length: ~350μm), single-crystalline monolayer MoS_2 growth, as oxygen can suppress the nucleation density of MoS_2 due to its etching of unstable MoS_2 nucleus.(*102*) However, as oxygen may also etch MoS_2 domains and induce defects, the introduction amount needs to be carefully controlled.

$P_{chamber}$ is powerful to alter the kinetic process of the MoS_2 synthesis. A low $P_{chamber}$ induces a small D_{gas}, which leads to a long mean free path of gaseous molecules, so that the evaporation of solid precursors speeds up. It also promotes the mass transport procedure, making molecules easier to diffuse through the bulk gas phase to attach on the substrate

surface. That is why most LPCVD is controlled by the surface reaction procedure, rather than the mass transport one, which is opposite to the APCVD.(*98*, *99*, *103*, *104*) The advantages of a low $P_{chamber}$ involve (1) making the rate-limiting step to be surface reaction instead of mass transport, so that the thickness homogeneity of MoS_2 is less affected by the uniformity level of gaseous precursors around the substrate surface; and (2) generating a low partial pressure of precursor vapours, which gives rise to a small nucleation density and a mild growth rate of MoS_2. The first merit is particularly critical when using the precursor with a high melting point (low vapour pressure), e.g. MoO_3 powder, as it is difficult to realize a homogenous dispersion of it in the gas phase. However, since LPCVD requires pumps and higher energy consumption, it deserves to investigate a proper APCVD design, which can alleviate the negative gradient effect of gaseous precursors on the MoS_2 layer uniformity (see section 4.2).

Apart from the aforementioned parameters, there exist other key factors, including the substrate material and the seed crystals. SiO_2/Si is the most widely used substrate due to its good compatibility with Si-based electronics. However, both its relatively low chemical inertness and a high charged impurity on the surface are detrimental to preserve the intrinsic property of monolayer MoS_2, leading the as-grown product to be seriously doped. In addition, as SiO_2 lacks a periodic lattice configuration, it cannot realize the epitaxial growth of MoS_2. Compared with SiO_2/Si, sapphire performs better due to its increased chemical stability, making MoS_2 less oxygen doped after experiencing a high temperature synthesis procedure and display a higher crystallinity. However, in comparison with 3D-structured SiO_2 and sapphire, 2D substrate (graphene (graphite), *h*-BN, mica, *etc.*), inherently possessing atomically flat surface with no dangling bonds and less charged impurites, could be a better choice as substrate materials (see section 2.4.4).(*95*, *105–107*) Their periodic lattice structures coupled with weak van der Waals interactions at interlayers are

advantageous for the alignment of MoS_2 domains, even when there exists a poor lattice commensurability between MoS_2 and the underlying 2D substrate.(*105*, *106*, *108*) It is noteworthy that a low growth temperature is commonly considered beneficial to the epitaxial growth of MoS_2, since a greater thermal energy promotes a random alignment of the nuclei.

In the initial attempts of monolayer MoS_2 growth, seeds were widely used, among which aromatic molecules with a high sublimation temperature and a superior chemical stability were manifested as the best. The assistant effect of seeding promoters is demonstrated to arise from their wettability, which reduces the surface energy for the nucleation and growth. Therefore, the growth temperature for 2D MoS_2 with the presence of seeds on the substrate is commonly lower than that on the bare substrate. It has also been reported that seeds impact whether the growth mode is layer-by-layer or island growth, as the surface adhesive force between seed molecules and MoS_2 varies with the seed species. When the surface adhesive force between monolayer MoS_2 and seeds surpasses the cohesive force between two layers of MoS_2, layer-by-layer growth dominates.(*93*) Otherwise, island growth is preferred. However, since seed-promoted MoS_2 growth requires an extra pre-coating procedure on substrates and introduces impurites which might deteriorate material's property, it is less prevalent now.

2.4.4 MoS_2-Based 2D Vertical Layered Heterostructures

In parallel with the progress of growing monolayer MoS_2 with large area and better quality, the fabrication of 2D vertical layered heterostructures (van der Waals heterostructures) incorporating monolayer MoS_2 with other 2D layered materials emerges, including graphene, *h*-BN and tungsten disulphide (WS_2). The feasibility and the application prospect of this idea derive from the structural feature of 2D layered crystals. On the one hand, each type of 2D layered crystals displays a high periodicity of atom arrangement in-plane through strong covalent bonds, which gives them special electrical, optical and

mechanical properties distinctive from amorphous materials due to crystal's anisotropy. On the other hand, they have weak van der Waals forces at interlayers, a large surface area and an ultrasmall thickness. Therefore, highly disparate 2D layered crystals can be vertically assembled without a strict constraints of lattice commensurability. The newly generated heterostructures will adopt a novel lattice periodicity, which empowers the tunability and creation of material's fundamental properties. Moreover, such construction of new hybrid materials goes deeply into changing the unit cell configuration, being totally different from the traditional stacking of various 3D-structured thin films, in which the modification is only limited at the interface.

There are two prevalent fabrication methods of vertical layered heterostructures, the mechanical top-down technique and the direct-growth bottom-up approach. The first method is carried out by sequentially transferring and restacking different mechanically exfoliated or CVD-grown 2D layered materials on top of each other. The second one is primarily completed by CVD growth. Both two methods have advantages and weaknesses. The mechanical assemble method is less limited by the synthesis process of different 2D materials and has greater freedom on tailoring the crystal orientation alignment between different layers. However, it suffers from a poor scalability, a high requirement on the accurate position control when stacking two layers, and a more serious contamination problem at interfaces, which could spoil the interlayer contact and the whole periodic structure of the vertical heterostructures. In contrast, the CVD method is more scalable and time-effective. It also can create clean and atomically sharp interfaces, and implement the large-area growth of vertical heterostructures with ordered crystal orientation alignment. Nevertheless, more attention needs to be paid to finding an appropriate synthesis condition. In this section, typical CVD growth strategies about MoS_2/graphene, MoS_2/h-BN and WS_2/MoS_2 will be introduced.

Shi *et al.* reported the epitaxial growth of multilayer MoS_2 flakes on metallic graphene, which was CVD-synthesized on the copper (Cu) foil.(*105*) The precursor, $(NH_4)_2MoS_4$, was dissolved into the organic solution and transported into the reaction zone through bubbling. The growth occurred at a low temperature of ~ 400 °C in the flowing Ar under a low pressure of ~ 10 mTorr, forming hexagonal or quasi-hexagonal MoS_2 flakes with a lateral size ranging from several hundred nanometres to several micrometres and a thickness between ~ 2 and ~ 5 nm. The fast Fourier transform of the STEM image showed a relatively narrow orientation distribution of as-grown MoS_2 with respect to the graphene template (from -11 to 18°), indicating an epitaxial tendency. Next, Lin *et al.* grew monolayer to multilayer MoS_2 using epitaxial graphene on silicon carbide (SiC) as the template (**Figure 2.10**a).(*106*) The synthesis was carried out at 670 °C utilizing MoO_3 and S as precursors in route II under a low pressure of 5 Torr in the pure Ar flowing gas. The 2D MoS_2 films expanded through a combination of layer-by-layer growth and island growth. Miwa *et al.* also reported the epitaxial growth of monolayer and bilayer MoS_2 sheets on the graphene/SiC substrate under ultrahigh vacuum condition. The growth was conducted through a cycled procedure of Mo deposition and sulphurization in route I at a temperature of ~ 777 °C under 10^{-10} mbar.(*109*) The common discoveries in the above three papers can be summarized as follows: (1) even though there exists a large lattice mismatch (~ 28%) between MoS_2 and graphene, it can be largely relaxed through a weak van der Waals interaction at interfaces, which is conducive to the formation of MoS_2/graphene heterostructures; (2) those structural imperfection regions on graphene, such as wrinkles and terraces, are prone to becoming nucleation sites for MoS_2, which might also be detrimental to the thickness uniformity of the as-grown MoS_2; (3) graphene does not perturb the intrinsic electronic structure of 2D MoS_2 and can even improve its photoresponsivity; (4) graphene performs as a robust substrate for MoS_2, being able to survive in a high growth temperature without obvious quality degradation and being

tolerant to various precursors; (5) there exists a strong epitaxial tendency between MoS_2 and graphene, which could originate from the symmetry match between two crystals.

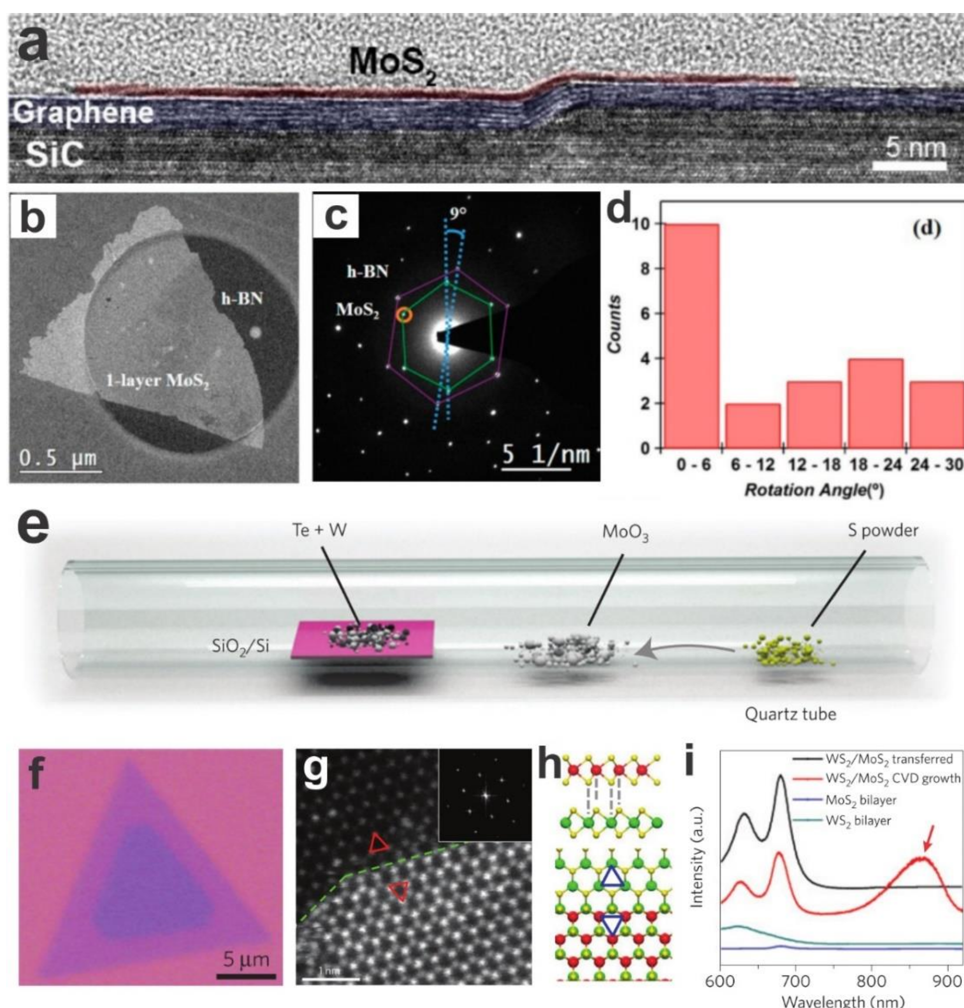

Figure 2.10. CVD growth of MoS_2-related 2D vertical layered heterostructures. (a) Cross-sectional HRTEM image of MoS_2/graphene vertical heterostructures. (b) Dark filed TEM image showing monolayer MoS_2 grown on an exfoliated h-BN flake by selecting a diffraction spot (orange circle) in (c). (c) Selected area electron diffraction (SAED) pattern of as-grown monolayer MoS_2 on *h*-BN. The green and purple hexagon represents diffraction spots from MoS_2 and h-BN, respectively, showing a rotation angle of ~ 9°. (d) Histogram showing the distribution of the rotation angle between MoS_2 and *h*-BN at 22 different locations similar to the growth in (b). (e) CVD setup of vertical heterostructures of WS_2/MoS_2 monolayers. (f) Optical image of vertically stacked WS_2/MoS_2 heterostructures. (g,h) ADF-STEM image of the step edge of WS_2/MoS_2 bilayer (g) with corresponding atomic models (h). The green dashed line marks the step edge. Two red triangles indicate the lattice orientation of monolayer MoS_2 (top part) and WS_2 (bottom part), respectively. Inset is the Fast Fourier transform of (g). (i) PL spectra showing an emerging peak at 875 nm for the

CVD-grown WS_2/MoS_2 sample, which is absent in transferred WS_2/MoS_2 heterostructures, MoS_2 bilayer and WS_2 bilayer samples. Figures reprinted (adapted) with permission from: (a), ref.(*106*), © 2014 American Chemical Society; (b-d), ref.(*108*), © 2015 American Chemical Society; (f-i), ref.(*110*), © 2014 Macmillan Publishers Limited.

Wang *et al.* was one of the pioneers to synthesize monolayer MoS_2 on *h*-BN films without the help of seeds (see Chapter 5).(*111*) The reaction was conducted at ~ 800 °C under ambient pressure using MoO_3 and S as precursors in route II, and the substrate was CVD-grown multilayer h-BN films, which was transferred onto the SiO_2/Si chip. Truncated three-point-star-shaped monolayer MoS_2 domains were obtained with a side length of ~ 3 μm. Raman and PL spectroscopy were applied to manifest the merits of CVD-grown MoS_2 monolayers on 2D *h*-BN films compared with mechanical transfer method and those grown SiO_2/Si substrate, including smaller lattice strain, lower doping level, sharper interfaces and better interlayer contact. Next, Yan *et al.* grew single- and multi-layer MoS_2 on exfoliated *h*-BN flakes using MoO_3 and S precursors as well (**Figure 2.10**b).(*108*) Monolayer MoS_2 was found to exhibit a narrow rotation angle distribution (< 5°) with respect to the underlying *h*-BN (**Figure 2.10**c,d). In general, *h*-BN is an ideal insulating 2D substrate for MoS_2, which has a high chemical inertness and less trap states on the surface, thus maintaining the intrinsic property of 2D MoS_2 effectively.

Gong *et al.* realized the vertical growth of WS_2/MoS_2 heterostructures, in which both layered materials are direct bandgap semiconductors in a monolayer regime.(*110*) Tungsten (W), MoO_3 and S were utilized as the source of the elements of W, Mo and S. Importantly, W was scattered directly on the growth substrate of SiO_2/Si with an addition of tellurium (Te), which facilitates the formation of WTe alloy having a much lower melting point than that of W (**Figure 2.10**e,f). Hence, the diffusion of W atoms on the substrate surface was accelerated for monolayer WS_2 growth. The reaction was conducted at ~ 850 °C under atmospheric pressure, rendering the epitaxial growth of monolayer WS_2 on top of monolayer

MoS_2, following 2D stacking perfectly (**Figure 2.10**g,h). The absence of contaminations due to the *in situ* growth gives a sharp interface, thus allowing the emergence of a novel direct bandgap deriving from the type-II band alignment between vertically stacked WS_2 and MoS_2 monolayers (**Figure 2.10**i). The formation of vertical layered heterostructures rather than $Mo_xW_{1-x}S_2$ alloy was attributed to the different nucleation and growth rate between MoS_2 and WS_2.

To sum up, the vertical heterostructures having 2D MoS_2 assembled with metallic (graphene), insulating (*h*-BN) and semiconducting (WS_2) atomic layers can all be fabricated by CVD with proper recipes. Apart from these layered materials as the 2D building block for the fabrication of vertical heterostructures, researchers are dedicated to stabilizing more non-layered materials into a 2D form by exploiting suitable layered materials as templates,(*112*, *113*) which can dramatically enrich the library of 2D vertical heterostructures and improve our ability to tailor materials' properties.

2.5 Conclusion

Compared with graphene consisting of only one layer of carbon atoms, 2D MoS_2, which has an increased element diversity and structural complexity, possesses more tunability on properties. To make the 2D MoS_2 applicable, developing cost-effective and environment-friendly synthesis strategies to produce wafer-scale, high-quality, continuous MoS_2 films with uniform and controllable thickness as well as large grain sizes is the first target. Many approaches with disparate recipes have been reported. However, an in-depth understanding of the dominant factors and the growth mechanisms hidden behind a diversity of experimental parameters are still lacking. Secondly, since the 2D MoS_2 is susceptible to the environment, surface adsorbates from the air or the substrate and the tiny lattice strain introduced either due to the artificial substrate bending or in the growth procedure can alter the electrical and optical properties of MoS_2 remarkably. This leads to the actual

performance of the 2D MoS_2 to be closely linked with its application condition, making the comprehension of the environmental influence, such as surface adsorbates and substrate effect, on the 2D MoS_2 properties to be significant. Thirdly, thanks to the structural diversity of 2D MoS_2 in both the crystal phases and the defective configurations, it provides much freedom to tailor the material's property from the bottom level by artificially changing the periodicity of the pristine MoS_2 lattice. This target can be better accomplished with the help of the state-of-the-art (S)TEM, which can manipulate the atomic structure of 2D MoS_2 with a high spatial controllability and a real-time imaging. Finally, much development potential in 2D materials is hidden in 2D vertical heterostructures, which opens up a door for customizing materials with desired properties simply by choosing suitable 2D fundamental building blocks from a big material library and assembling them together. Many of these important aspects in the 2D MoS_2 research will be touched in my following investigations.

Chapter 3 Methodology

3.1 Introduction

The purpose of this chapter is to introduce the specific experimental setup and characterization techniques utilized in my research project, which are achieved by an understanding of previous work combined with my practical experience based on existing experimental conditions in our lab. Detailed information including the design of the CVD system, growth recipes, operating procedures of various analytical apparatus and typical data processing methods employed in my work will be covered.

3.2 CVD Synthesis and Transfer

The CVD system used for monolayer MoS_2 preparation is composed of four parts: (1) a 1-inch-diameter quartz tube; (2) two independent tubular furnaces; (3) a gas delivery system; and (4) a gas exhaust system (**Figure 3.2**). The quartz tube acts as a reactor. Both two precursors, MoO_3 and S powder, and the substrate are placed at different locations in the quartz tube. The tube is inserted through the centres of two tubular furnaces during the reaction. Furnace 1 is responsible for the heating of S powder, while furnace 2 controls the temperature of MoO_3 powder and the substrate. The separate temperature setting on MoO_3 and the substrate is implemented by tuning their positions in furnace 2, which makes use of the existing temperature variation as a function of the horizontal position in the tubular

furnace open both ends (**Figure 3.1**). The purpose of applying two furnaces is to give an independent temperature control on both two precursors and the substrate, thus facilitating the free adjustment on two fundamental growth parameters, which are the growth temperature (T_{growth}) and the density of active species (Mo-based and S-based) absorbed on the substrate ($D_{surface}$), respectively (see section 2.4.3). The gas delivery and exhaust system are connected to two ends of the quartz tube, respectively. The gas delivery system involves a mass flow controller (MFC) for a precise manipulation on the flow rate of pure Ar gas, which is used as the inert carrier gas of MoS_2 growth. The gas exhaust system consists of a relatively long plastic pipeline linked with a bubbler. Since the redundant S vapour is prone to solidifying in the exhaust pipeline, it is necessary to monitor the bubbling rate in the bubbler before and during the reaction to avoid the overpressure in the quartz tube, and replace the congested pipeline in time. The detailed design about the loading manner and loading positions of both precursors and the substrate based on different research targets will be introduced in Chapter 4 and Chapter 5.

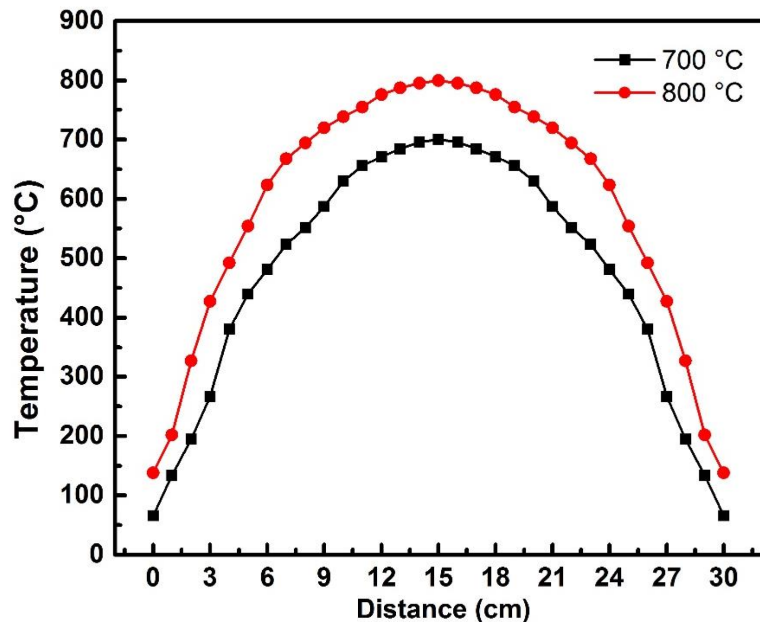

Figure 3.1. Plot showing the temperature gradient as a function of the horizontal position in furnace 2, when the temperature in the centre of the furnace are 700°C and 800°C, respectively. The temperature gradient from 14 cm to 16 cm is mild, having less than~4.5°C difference, which ensures

a uniform heating temperature for substrates loading in the furnace centre. The temperature gradient close to the end of the furnace is relatively sharp, providing flexibility to adjust the heating temperature of the MoO_3 powder by switching its horizontal position close to the furnace end.

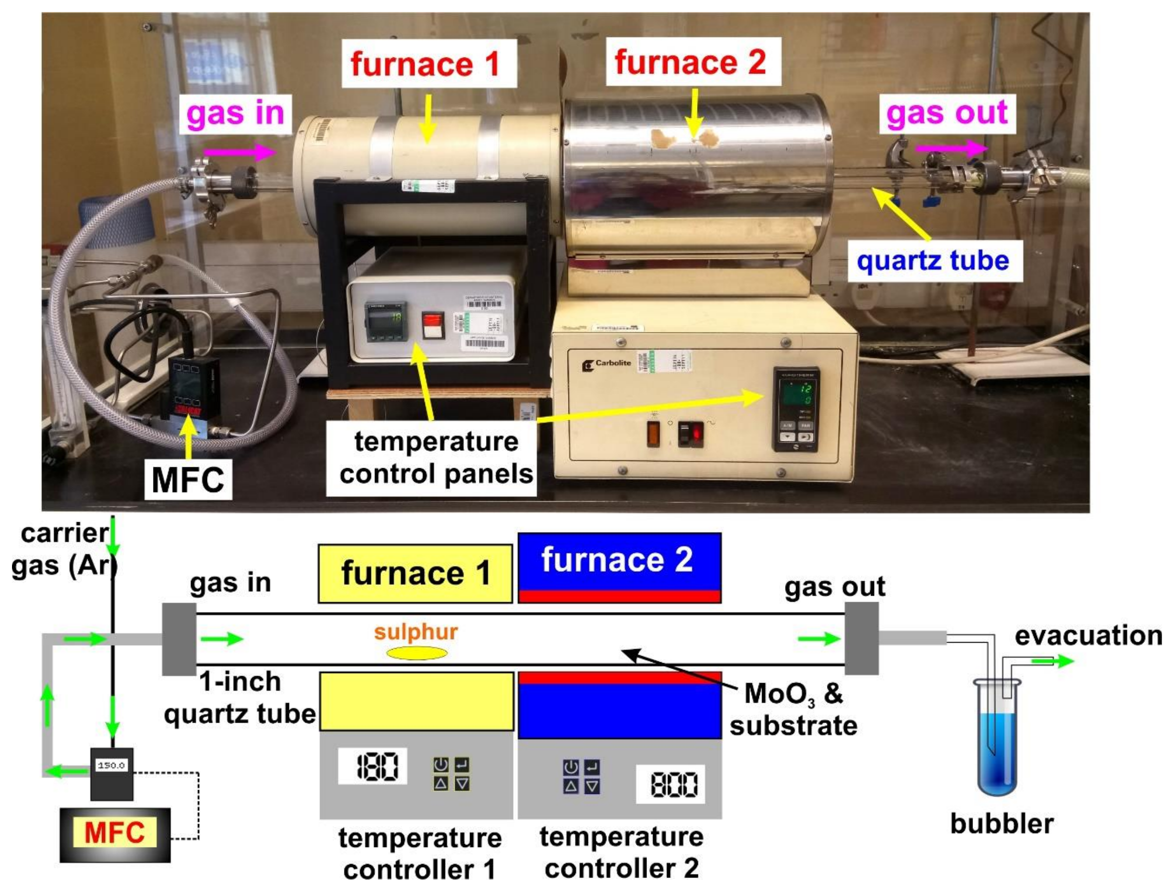

Figure 3.2. Photograph and schematic diagram showing the general CVD experimental setup for monolayer MoS_2 growth.

3.2.1 Preparation and Growth of Monolayer MoS_2

If the monolayer MoS_2 was directly grown on bare silicon substrates coated with a 300 nm oxide layer (SiO_2/Si), the substrates need to be cleaned thoroughly before the growth to avoid the unfavourable heterogeneous nucleation during the reaction. Substrates were cleaned in acetone for 30 min and then 2-propanol for 15 min *via* ultrasonic bath, followed by a treatment of O_2 plasma for 5 min. All the recipes employed in the thesis for monolayer MoS_2 growth were hydrogen-free CVD approaches in atmospheric pressure with precursors of MoO_3 (≥99.5%, Sigma-Aldrich, melting point: 795 °C, particle size: 100nm) and S (≥99.5%, Sigma-Aldrich, melting point: 115 °C, boiling point: ~ 445 °C) powder. Since the

detailed technical parameters of recipes for different study purposes vary, only their common points are included in this section, while their features will be highlighted in corresponding chapters of results. After loading the precursors and the substrate at designed locations, the CVD system was flushed by ultra-high purity Ar gas in a high flow rate of 500 sccm (standard cubic centimetres per minute) for ~ 90 min at room temperature to eliminate O_2 in the growth system. During the reaction, S powder was heated at a temperature ranging from150-180 °C and its usage amount exceeded that of MoO_3 greatly. This is to generate a general S sufficient atmosphere, thus ensuring a thorough sulphurization of MoO_3 to convert into MoS_2. However, the temperature at the substrate was maintained above the heating temperature of S even at the S vapour pre-introduction stage to avoid any deposition of S on the substrate, as it may contaminate the surface cleanness and spoil the homogeneous nucleation and layer-by-layer growth of MoS_2. The reaction was conducted at ~ 700-800 °C, which is consistent with the suitable growth temperature demonstrated by literatures when using MoO_3 and S as precursors (see section 2.4.3). The flow rate of Ar gas was decreased to generate a proper concentration of gaseous precursors during the MoS_2 growth. After the reaction, the residual S in furnace 1 was quickly exhausted by setting the temperature of furnace 1 up to ~ 400 °C for ~ 5 min with a high Ar flow rate of 500 sccm. Subsequently, a fast cooling process was applied by shifting the substrate region out of furnace 2 rapidly and using an electric fan to speed up the cooling process. The purposes of these actions are to (1) prohibit any S deposition on the substrate after the reaction; (2) accurately control the reaction time; and (3) avoid the sublimation and potential oxidation of as-grown MoS_2 monolayers in a slow cooling process. All the growth strategies can be completed within 90 min.

3.2.2 Transfer of Monolayer MoS_2

The as-grown monolayer MoS_2 on the SiO_2/Si substrate can be transferred onto an arbitrary substrate, such as Si_3N_4 TEM grids, for further characterizations using a polymer-assisted method (**Figure 3.3**). Its surface was first spin-coated with a thin film of poly-methyl-methacrylate (PMMA, 8% wt. in the anisole, 495 molecular weight) as a supportive scaffold. The rotation speed of the main spin-coating stage was programmed to 4500 rpm (round per minute) for 50 seconds with an initialization stage and an ending stage, both having a slow spin speed of 500 rpm for 5 seconds. Therefore, the deposited PMMA droplets can first wet the surface well at a low spin speed stage and then be spread into a uniform thin film at a high spin speed stage with the droplets being spun off the edges and the solvent being evaporated. After this, the sample was heated at 180 °C in the air on a hot plate for 90 seconds to remove the residual solvent thoroughly and strengthen the interlayer contact between MoS_2 and the PMMA layer. Subsequently, the PMMA/MoS_2/SiO_2/Si specimen was floated on a 1 mol/L potassium hydroxide (KOH, Sigma-Aldrich reagent grade 90%) solution, so that the PMMA/MoS_2 layer can detach from the substrate after SiO_2 being etched away. It is worth noting that, since the PMMA also covered the edges of the SiO_2/Si substrate when it was spread by the centrifugal force, all the edges of the SiO_2/Si substrate were rubbed by a diamond file before floating the sample on a KOH solution. This is to remove the coated PMMA layer on edges such that the SiO_2 can be exposed to contact directly with the KOH solution. After the PMMA/MoS_2 film peeled off, it was then transferred to the deionized water for several times to wash off any residual contamination from the etching process. The rinsed PMMA/MoS_2 film was then scooped up by a holey Si_3N_4 TEM grid (Agar Scientific AG21580) or other substrates, air-dried for overnight and baked at 180 °C for 15 minutes to ensure a strong interface contact between MoS_2 monolayers and the new substrate. Finally, the PMMA scaffold was removed by submerging

the new sample in the acetone solution for 8 hours. It is worth mentioning that, if the transfer was aimed at releasing the built-in strain of the MoS_2 directly grown on the SiO_2/Si substrate (see Chapter 5), all the baking processes involved should be avoided, as they could introduce new strain due to the difference on the thermal expansion coefficient between MoS_2 and the new substrate.

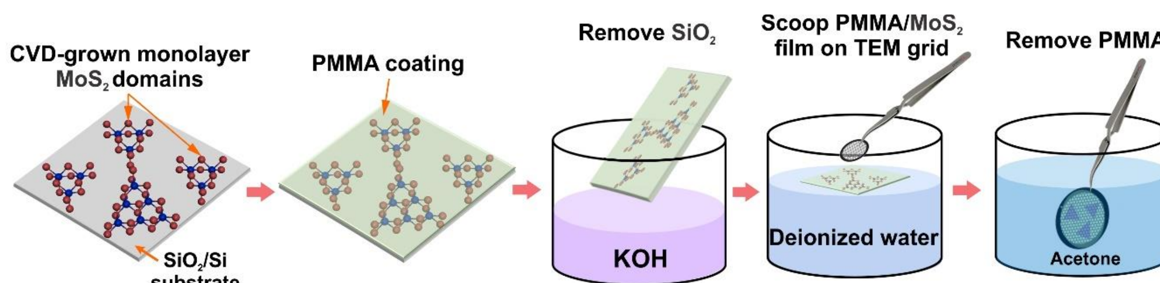

Figure 3.3. Schematic illustration showing the transfer process of monolayer MoS_2 from the growth substrate to a TEM grid.

3.3 Scanning Electron Microscopy

Scanning electron microscopy (SEM) is a powerful tool to characterize material's surface topography. This stems from its image generation mechanism, where the contrast originates from the secondary electrons (SEs) excited by the incident beam on the sample surface and only those SEs generated within a few nanometres of the surface can escape. In this project, Hitachi S-4300 field emission scanning electron microscope was operated to characterize micrometre-scale features of the as-grown 2D MoS_2 and MoS_2/h-BN heterostructures, including the nucleation density, domain size and shape, layer number and film continuity. All 2D specimens were on SiO_2/Si substrates. The SEM sample was mounted onto the sample stub firmly using carbon sticky pads, which can diminish unwanted charge-up. The accelerating voltage was set to be 3 kV coupled with a beam current of 10 μA. The choice of such a low accelerating voltage is for gaining clearer surface structures with less electron charging and irradiation damage to samples.

3.4 Raman and Photoluminescence Spectroscopy

Raman and photoluminescence (PL) spectroscopy were employed in this research project to investigate the layer number, lattice strain, doping level and interlayer contact of as-grown 2D MoS_2 (see section 2.3.2 and 2.3.3). The spectra were captured by a JY Horiba LabRAM ARAMIS imaging confocal Raman microscope, which couples a Raman spectrometer with a standard optical microscope. Therefore, a high magnification visualization of the sample and the Raman/PL signal acquisition using a micrometre-sized laser spot can be conducted simultaneously. The excitation light was a 532 nm laser with an estimated laser spot size of ~1 µm. Before the measurements, the Raman spectrometer was calibrated by a standard silicon chip (520.7 cm^{-1}) to exclude any instrumental error introduced into the collected data. Two types of grating can be selected, being 600 g/mm (600 grooves per mm grating) and 1800 g/mm, respectively. The density of grooves is proportional to the resolving power of the spectrometer, but is inversely proportional to the wavelength coverage. Upon using Raman mode, 1800 g/mm was selected to give a better spectral resolution without a concern about the relatively narrow wavelength coverage this type of grating can cover, because all the characteristic vibrational modes of monolayer MoS_2 are located within a small frequency range (see section 2.3.3). The spectrum was normally taken from 300 to 600 cm^{-1} with an acquisition time of ~2 seconds and an accumulation number of ~2, which can supply a good signal-to-noise ratio and avoid any sample damage by the thermal effect from the laser. The PL spectrum was normally captured from 500 to 750 nm using the coarse resolution 600 g/mm grating with the same acquisition time and accumulation number as those used in Raman spectra. The PL spectral range covered not only PL peaks but Raman peaks as well, as the latter was used to normalized the PL spectrum to show the quantum efficiency of 2D MoS_2, which links with the layer number.(*44*) To investigate the thickness homogeneity of as-grown MoS_2, a Raman/PL

mapping was employed by conducting multi-point spectra collection across lateral dimensions (XY coordinates) in a fixed step size. Thanks to the SWIFT^{TM} mapping mode embedded in the HORIBA Raman system, the acquisition time at each spot can be decreased to 0.1 second without compromise in characterization quality. The step size was set to be 1 μm, being similar as the diameter of the laser spot. A step size smaller than the laser spot diameter causes an obvious convolution effect especially on the MoS_2 edges, while a larger step size degrades the spatial mapping resolution.

3.5 Atomic Force Microscopy

Atomic force microscopy (AFM) is the most unambiguous characterization method to provide information about the sample thickness and surface morphology of 2D MoS_2. The as-grown MoS_2 on either a SiO_2/Si substrate or a *h*-BN/SiO_2/Si substrate can be directly used for AFM measurements due to a good surface flatness and rigidity. The AFM characterization was performed by Asylum Research MFP-3D in a tapping mode (AC mode) with a silicon AC-160TS cantilever (Olympus, spring constant of ~42 N/m and resonant frequency of ~300 kHz) (*i.e.*, data was collected by Dr Merce Pacios). Various imaging modes can be recorded simultaneously, including the topological imaging mode and the phase mode. The first was used to characterize the thickness of monolayer MoS_2 on the SiO_2/Si substrate, as this mode commonly displays the height change of material surface. However, when monolayer MoS_2 was grown on *h*-BN films, it was invisible in the topological mode, which could arise from an increased surface roughness of transferred CVD-grown *h*-BN films that covered up the height alteration at MoS_2 regions. In this case, the phase imaging mode, which is sensitive to the elasticity variation between different materials, was employed, thus differentiating monolayer MoS_2 areas with bare *h*-BN films clearly. The 'Gwyddion' software were applied to generate AFM mappings and height/phase profiles.

3.6 Transmission Electron Microscopy

3.6.1 Aberration-Corrected Transmission Electron Microscopy

The aberration-corrected transmission electron microscopy (AC-TEM) was conducted using Oxford's JEOL JEM-2200MCO field emission gun TEM (OJ2200 MCO) under an accelerating voltage of 80 kV. The microscope is remotely controlled, thus ensuring an extremely stable environment for image acquisition. The base pressure in the specimen chamber is ~10^{-4} Pa. The aberration correctors consisting of pairs of hexapoles are designed by CEOS, which are capable of correcting aberrations up to the third order. The spherical aberration (C_S) is corrected by running a Zemlin tableau on a thin amorphous area within a predefined range for the beam tilt angle at a magnification of ~500K. A series of diffractograms corresponding to different beam tilt angles are automatically recorded, which are used to solve and correct C_s based on the wave aberration function by the software (**Figure 3.4**a, b). After C_s being corrected, the resolution of the ACTEM system can reach ~1.2 Å. Images were recorded using a Gatan Ultrascan 4k × 4k CCD camera with 1-2 s acquisition time, 2 pixel binning. The electron dose used for imaging was ~10^5 e^-/nm^2. **Figure 6.6**d was captured with an additional use of a double Wien filter monochromator with a 7 µm slit (*i.e.*, data was collected by Dr Kuang He), which reduced the energy spread of the electron beam to ~0.21 eV, thus further improving the resolution to ~0.8 Å. The general sample preparation procedure is outlined in section 3.2.2. However, exposing TEM samples in the air induces the amorphous contamination accumulated on the surface of monolayer MoS_2, which blocks the direct observation of its pristine atomic configuration under TEM. Therefore, a dry-clean method was employed one day before the TEM characterization,(*114*) where samples were buried in the activated carbon powder and baked at ~200 °C in the air for ~ 60 min to remove adsorbates thoroughly. **Figure 3.4**c shows the surface of monolayer MoS_2 after the dry-clean treatment, where an area exceeding 120 nm^2

is absent of contamination, which provides a large window to image the pristine lattice of monolayer MoS_2. The contamination only occupies a small region marked by yellow dashed lines in **Figure 3.4**d. White spots in the central area of panel d correspond to the locations of vacancy defects.

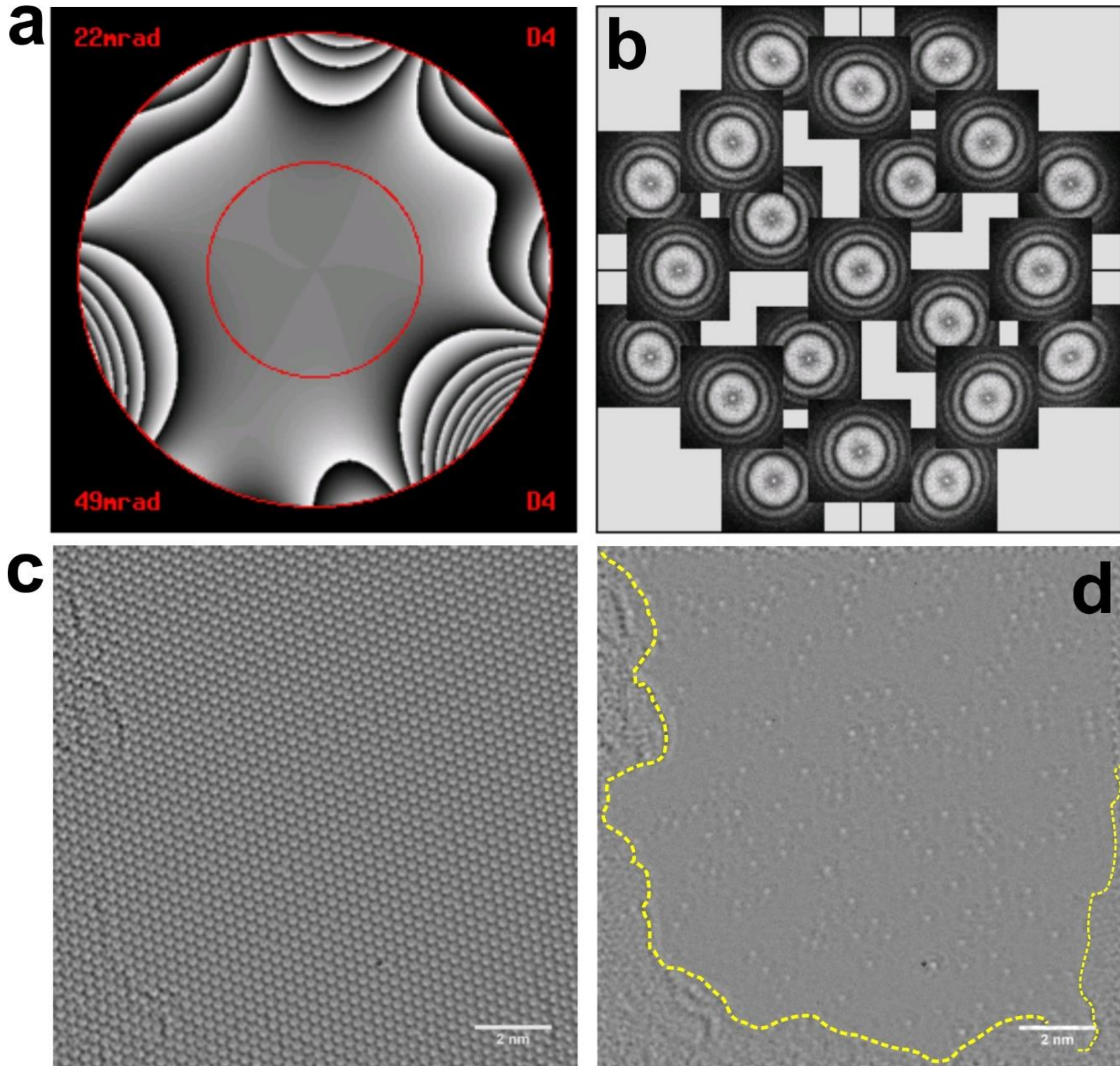

Figure 3.4. (a,b) Zemlin tableau taken with an outer tilt angle of 24 mrad on the OJ2200 MCO. (c) AC-TEM image showing the surface of monolayer MoS_2 after the dry-clean treatment. (d) Reconstructed AC-TEM image after removing the MoS_2 lattice by applying a fast Fourier transform (FFT) filter. The contaminated area is marked by yellow dashed lines.

3.6.2 Image Processing and Simulation

Images were processed using the software of ImageJ. They were initially adjusted with a band-pass filter (between 100 and 1 pixel), which primarily cut out signals from low spatial

frequencies to mitigate the beam stigmatism effects, thus improving the long-range non-uniformity on the illumination intensity. A Gaussian blur filter (2-4 pixels) was subsequently applied to smooth images. Mathematically, it equals to convolving the AC-TEM image with a Gaussian function in the real space, which intuitively can be understood as using the weighted average of a spot's neighbourhood as the new value for this spot. Since the Fourier transform of a Gaussian function is still a Gaussian function, this convolution operation corresponds to multiply the Fourier transform of this image with another Gaussian function in the reciprocal space. Therefore, the effect of a Gaussian blur filter is to remove noises from high spatial frequencies and at the same time perverse the edge features better than other uniform blurring filters. The Gaussian blur applied on **Figure 6.3**a-c in is 8, which is for the specific purpose of highlighting locations of vacancies and line defects in the low magnification AC-TEM images. The original grayscale images with black atom contrast were inverted and then a fire false colour look up tables (LUT) was used to improve the visual contrast. The magnifications of AC-TEM images were calibrated using the reflexes from {100} of monolayer MoS_2 as a reference (zigzag lattice directions, see **Figure 2.2**a), whose lattice spacing is ~ 0.27 nm.

Atomic models were established *via* the software of Accelrys Discovery Studio Visualizer. Those models calculated by density functional theory (DFT) were conducted by Prof Gun-Do Lee, Mr Sungwoo Lee and Prof Euijoon Yoon. The coordinate value of each atom in the atomic model was then converted into a suitable format, which is readable by the image simulation software, using a Python script written by Dr Christopher S. Allen. Multislice TEM image simulations based on corresponding atomic models were generated using JEMS software (programmed by Dr P. A. Stadelmann), where multislice approximation is applied by dividing specimen into many thin slices in order to imitate the multiple scattering as the electrons propagate through the specimen. The simulated TEM

images were used as a comparison with experimental images to manifest the validity of the configuration deduction. Many parameters can be adjusted to match different alignment qualities of the equipment and the specific imaging conditions. The most frequently adjusted parameters include defocus and defocus spread. Defocus indicates the distance between the sample plane and the ideal focal plane. It varies from one image to another, because each image was captured at a different z height. Defocus spread relates to the intrinsic energy spread of the electron gun, as well as the fluctuation of the accelerating voltage and the objective lens current. The defocus spread of OJ2200 MCO without a monochromator is ~6 nm. The other simulation conditions were set to an accelerating voltage of 80 kV, chromatic aberration (C_c) of 0.591, C_s of 0.005, energy spread of -0.32 and a lens stability of 0.

3.6.3 2D Displacement Maps and Strain Analysis

The precondition of constructing 2D displacement and strain maps using a real space method is the high resolution of a TEM image, where the position of each atom can by unambiguously resolved, and my data in Chapter 6 meet this requirement. I first identified the positions of atoms from the AC-TEM images having sulphur vacancy lines and subtracted them from their expected locations in a periodic pristine MoS_2 lattice. This approach was previously applied to resolve the strain in carbon nanotubes.(*115*) For 2D displacement maps, I rotated the TEM image to align the S vacancy line's length in the vertical direction (y-axis), and chose one set of Mo atoms as the reference point (indicated by the black arrow in the line of Mo atoms marked by white circles in **Figure 6.8**(i)a and **Figure 6.8**(ii)a, respectively). This is used to accurately align the corresponding Mo atom in a pristine lattice. The magnitude of each atom displacement is separately expressed by two directions, x and y. Atoms undergoing displacement to right (up) are in positive values, while those moving to left (down) are in negative. To resolve the 2D local lattice strain, I initially used scattered interpolation with a proper step-size on the displacement map, and

then calculated the displacement value difference divided by their location variations along certain directions between each two interpolated spots to form 2D gradient maps of $\partial Ux/\partial x$, $\partial Uy/\partial y$, $\partial Ux/\partial y$ and $\partial Uy/\partial x$. These calculations were completed by writing a code in the 'Matlab' software. More detailed will be described in section 6.2.3.

Chapter 4 CVD Growth of Monolayer MoS_2

This chapter introduces two strategies for monolayer MoS_2 growth directly on the silicon substrate coated with a thin oxide layer, which was developed in my first year of PhD. The first method artificially creates a sharp spatial concentration gradient of MoO_3 vapour on the substrate, which both facilitates the achievement of MoS_2 monolayer domains with the least experimental trials and provides a platform to study the shape evolution of as-grown crystals depending on the precursor concentration gradient. The second approach makes several improvements on the basis of the first method for the purpose of improving the coverage area, thickness uniformity and continuity of the product. A kinetic growth model is established to interpret the quality improvement of the as-grown MoS_2 *via* the modified method.

4.1 Shape Evolution of Monolayer MoS_2 Crystals

4.1.1 Introduction

As discussed in section 2.4, CVD has been one of the most promising methods of producing large area and high quality MoS_2 thin films. Many kinds of domain shapes have been synthesized in the CVD method, such as triangles, hexagons, truncated triangles, three-point stars and six-point stars.(*36*, *37*) However, the understanding about the shape evolution of MoS_2 domains is still limited. For graphene, significant attention has been paid to the

study of morphology control, since many of graphene's mechanical and electrical properties are highly dependent on how differently shaped domains interconnect within the polycrystalline film.(*116*) Depending on their shape and size, graphene films exhibit a wide variety of microstructures characterized by domain sizes, shapes, crystal orientation and lattice defects.(*117*) Thus, as an analogue of graphene, it is important to study the shape evolution of 2D MoS_2 in chemical vapor deposition.

In this section, I present an experimental method to study the shape evolution of CVD-grown MoS_2 domain (**Figure 4.1**). Scanning electron microscopy (SEM), Raman spectroscopy, photoluminescence (PL) and atomic force microscopy (AFM) techniques are employed to comprehensively study the crystal structure of MoS_2 on the Si substrates with 300nm SiO_2 surface (SiO_2/Si) after growth. I explain the different shapes using simple principles of crystal growth and present a qualitative shape transformation model with dependence on the Mo:S atom ratio.

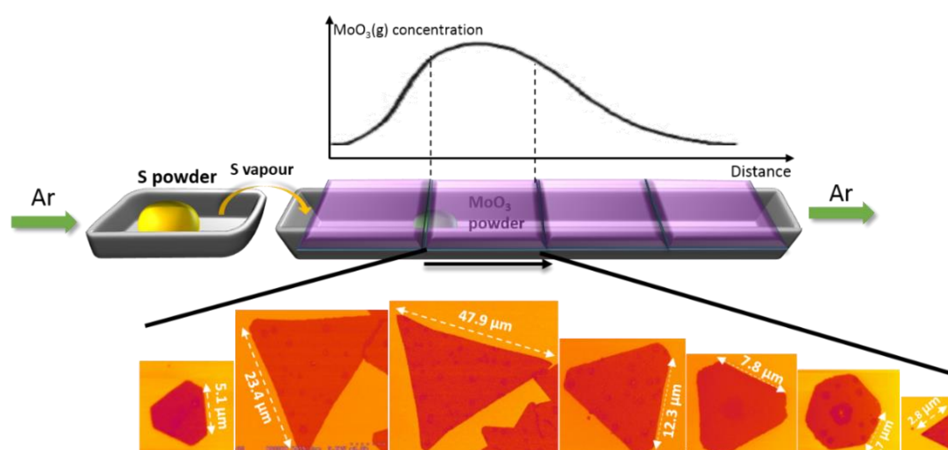

Figure 4.1. Schematic illustration showing the shape evolution of monolayer MoS_2 domains as a function of their spatial locations on the SiO_2/Si substrate. The MoO_3 concentration gradient with respect to the location is a schematic plot.

4.1.2 Results and Discussion

4.1.2.1 Experimental Setup

Figure 4.2a–c shows an illustration of the CVD setup for MoS_2 growth, along with the main steps of the growing method, and the temperature curves for both precursors (MoO_3 and S powder), for the whole experimental procedure. Briefly, the samples were grown by CVD with solid MoO_3 and S using the recipe similar to the previous report.(*37*) In contrast to the previous work,(*37*) I used two separate furnaces to provide accurate control of the temperature of MoO_3 and S separately. Fifteen milligram MoO_3 powder (particle size: 100nm) was put in an aluminium oxide ceramic boat, where it is directly below the gap of the first and the second substrate. The boat has a greater length along the gas flow direction, creating a growth condition with a wider change of MoO_3 concentration gradient. This ceramic boat was placed in the second furnace and the MoO_3 powder was located in the furnace centre. Also, 80 mg of sulphur powder (vapour pressure: 1mmHg at 183.8°C) was put in another aluminium oxide ceramic boat and the boat placed close to the downstream of the first furnace. Four pieces of SiO_2/Si substrates were tightly aligned on the boat, being face down to the MoO_3 powder, and only leaving one small gap (~0.3cm) between the boat head and the first substrate for Ar gas and S vapour in and another small gap (~0.2cm) between the boat tail and the last substrate for gas out. The distance between the two ceramic boats is 18 cm. This long distance is to ensure that the S vapours concentration gradient on the SiO_2/Si substrates can be ignored, compared with the MoO_3 concentration gradient. An ultralow Ar flow rate (10sccm) is also helpful for the gradient generation. The S powder was heated 15 minutes after increasing the temperature of MoO_3. The growth temperature was set to 700°C. **Figure 4.2**d shows the deposition pattern of pure MoO_3 on the second SiO_2/Si substrate when S is not introduced, revealing the MoO_3 concentration variation on the SiO_2/Si substrate. This resulted in the deposition pattern after reacting with S (**Figure 4.2**e).

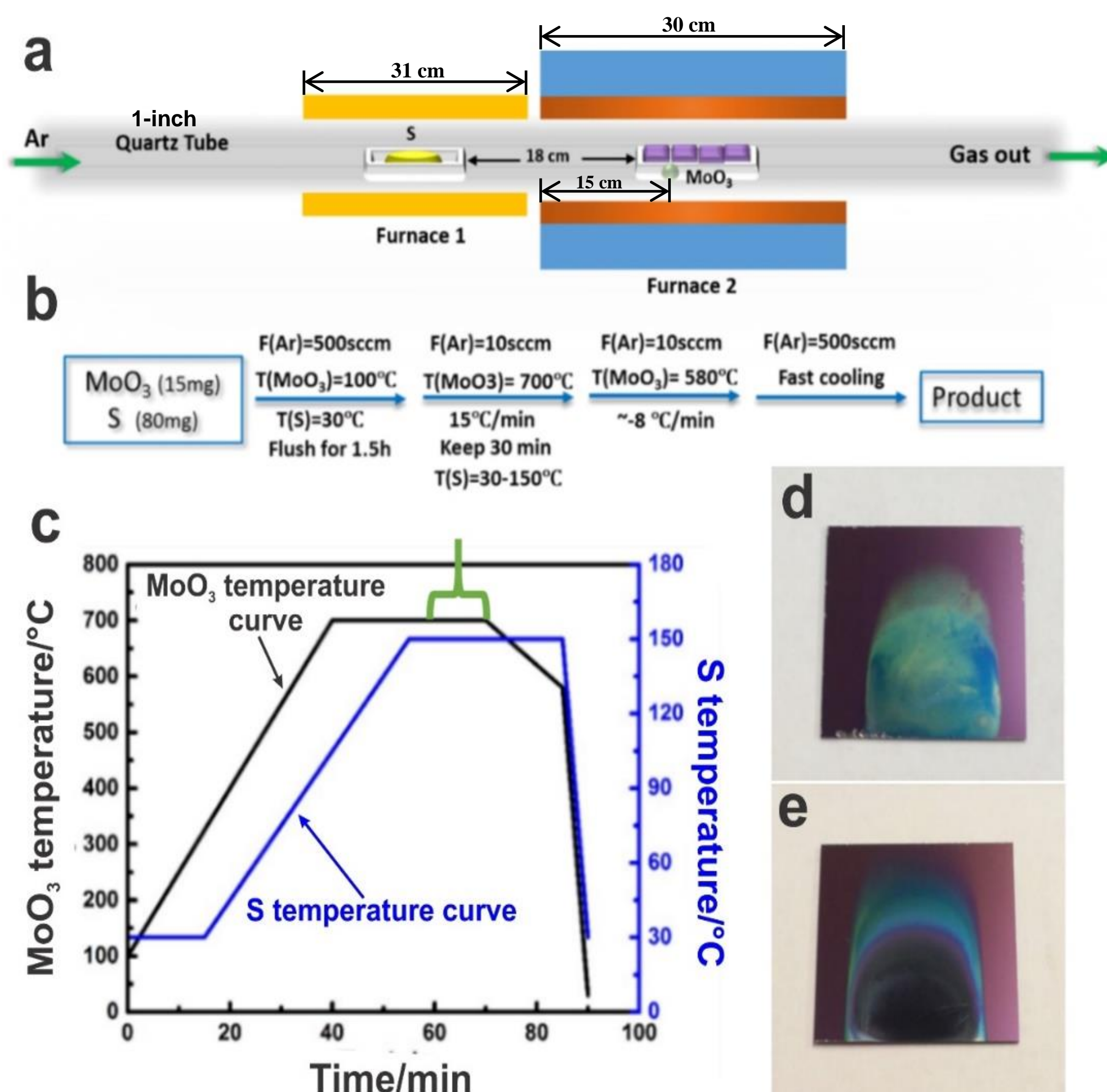

Figure 4.2. (a) Schematic illustration of the MoS_2 CVD system. The plot showing the temperature gradient as a function of the horizontal position in furnace 2 is given in **Figure 3.1**, indicating a relatively uniform heating temperature for the MoO_3 precursor and the substrates placing in the furnace centre. (b) Flowchart showing the main steps of the MoS_2 growing method. (c) Temperature programming process of MoO_3 and S precursors. (d) Pattern of deposition of MoO_3 on the SiO_2/Si substrate without introducing S. (e) Pattern of deposition of MoS_2 on the SiO_2/Si substrate after growth. The side length of the SiO_2/Si substrate is 2 cm.

4.1.2.2 Characterization on Morphological, Vibrational and Optical Properties of as-grown MoS_2

Figure 4.3 presents a schematic illustration of how the second growth substrate is spatially sectioned into six parts with corresponding SEM images from those sections shown

below. Toward the edge of the deposited material, as shown by the dashed yellow oval, isolated MoS_2 islands with edge lengths ranging from 2 to 47.9 μm were observed. The islands merge into a continuous film toward the inner region of the deposited film. Surprisingly, a regular shape change along the flow direction was observed. To clearly show the dependence of the shape change on the distance from the MoO_3 precursor, the second Si substrate was divided into six regions (1–6) along the gas flow direction (**Figure 4.3**). The exact location of the MoO_3 powder precursor in the experiment was directly underneath the left side of the second Si substrate. The MoS_2 domain morphology in each region is shown by the SEM images (**Figure 4.3**). It can be seen that, with the increase in the distance between the precursor and the growth location, MoS_2 domains experience a regular morphology transformation as well as a size change. Section 1 is dominated by ~6 μm truncated triangles. However, as the deposition location moves further from the MoO_3 powder, the length of the truncated sides becomes shorter, and the morphology finally changes to triangular with sharp edges and smooth sides. Also, the domain is obviously enlarged and reaches a peak at ~50 μm. Then the domain shape gradually transforms back to truncated triangles. Within section 4, the truncated sides become longer, which results in a hexagonal shape in section 5, ~10 mm from the MoO_3 powder. In the last region in the downstream part of the substrate, the morphology of MoS_2 is mainly ~2–3 μm small triangles. In general, the morphology of MoS_2 along the gas flow direction on the surface of the second Si substrate experiences a transformation from medium-sized truncated triangles to large triangles, then back to medium-sized truncated triangles followed by decreasing sizes of hexagons, and finally very small triangles. The small dark regions on the flakes and films are secondary layers that form during CVD growth.

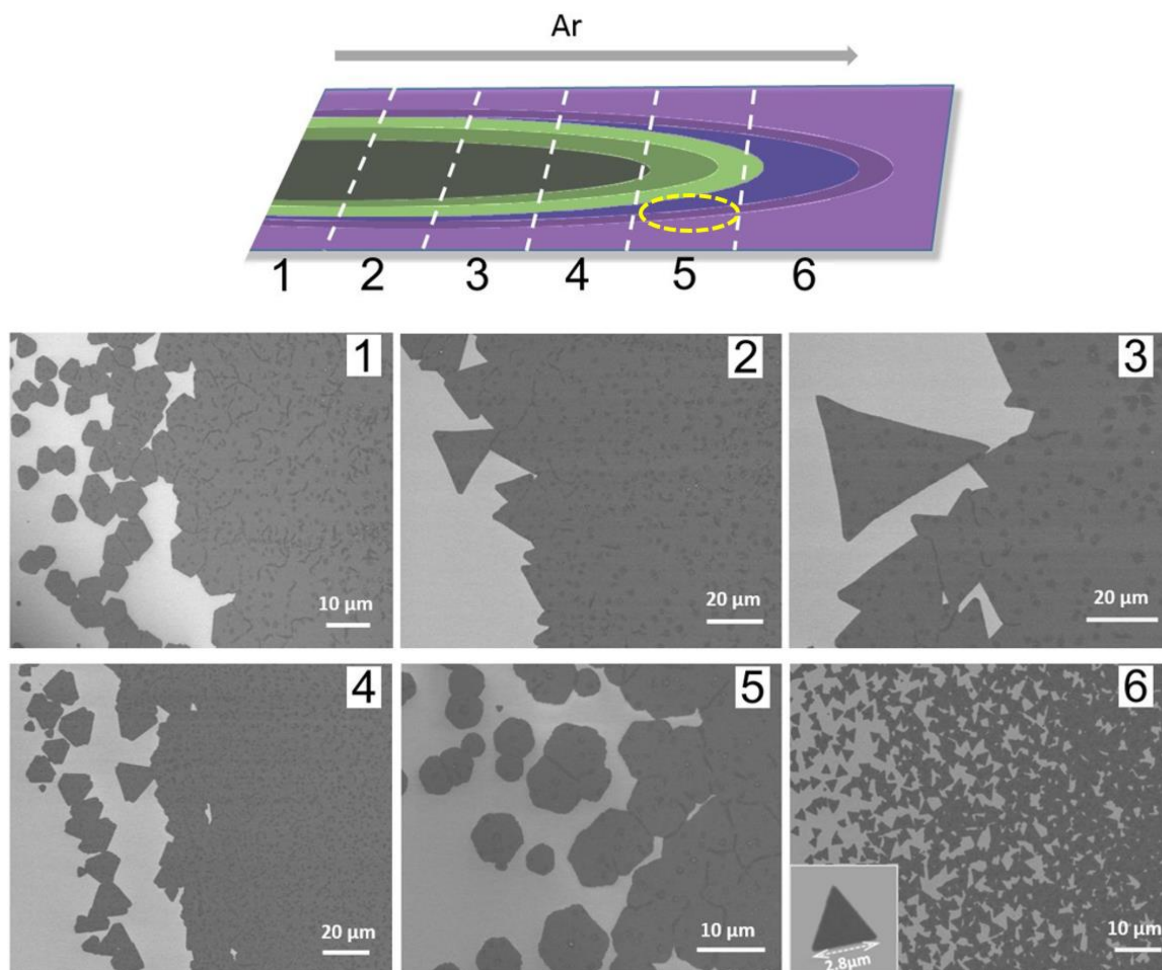

Figure 4.3. Schematic illustration showing the spatial sectioning of the growth substrate into sections 1-6 and the corresponding SEM images from the edge of those sections. The dashed yellow oval indicates the typical region within a section examined by SEM, where individual domains can be found. Each section of sections 1-5 has a width of 2–3mm, and section 6 has a width of ~5 mm.

To be sure that the domains imaged by SEM in **Figure 4.3** were indeed monolayer MoS_2, they were characterized by Raman spectroscopy and AFM (**Figure 4.4**). Two characteristic Raman vibration modes can be seen in the spectra in **Figure 4.4**a, the E_{2g}^1 mode representing the in-plane vibration of molybdenum and sulphur atoms and the A_{1g} mode related to the out-of-plane vibration of sulphur atoms.(*51*) The frequency difference between these two modes depends on the number of layers of MoS_2. Here, the fitting results show that these two modes are located at 384.7 and 405.0 cm^{-1}, respectively, giving a frequency difference Δk of 20.3 cm^{-1}. This matches well with the frequency difference of CVD-grown monolayer MoS_2 in previous work.(*36*, *93*, *96*) The full width at half maximum

(FWHM) of the E_{2g}^1 peak is 3.8 cm^{-1}, which is close to that of the exfoliated monolayer MoS_2, 3.7 cm^{-1}, suggesting good crystalline quality of the CVD-synthesized monolayer domains.(*96*) Raman mapping was also performed on a large triangle MoS_2 domain by plotting the 2D spatial variation of the magnitude of the frequency difference between the A_{1g} and E_{2g}^1 peaks in order to show the thickness uniformity of a large area (**Figure 4.4**b). More than 95% of the domain region has a Δk of < 20.5 cm^{-1}, confirming a homogeneous monolayer. Interesting, an obvious increasing of the frequency difference can be observed at the edge of the triangle domain. Panels c and d of **Figure 4.4** give a typical AFM measurement, showing the thickness of the domain is ~ 0.6 nm. This layer thickness is not only in the range of single-layer MoS_2 film on the bare substrates (0.6–0.9 nm),(*70*) but also consistent with the 0.6–0.7 nm value typically quoted for exfoliated monolayer films, indicating that the MoS_2 monolayer is of high quality without the presence of large scale absorbents or other interactions between the film and the oxide substrate surface(*118*).

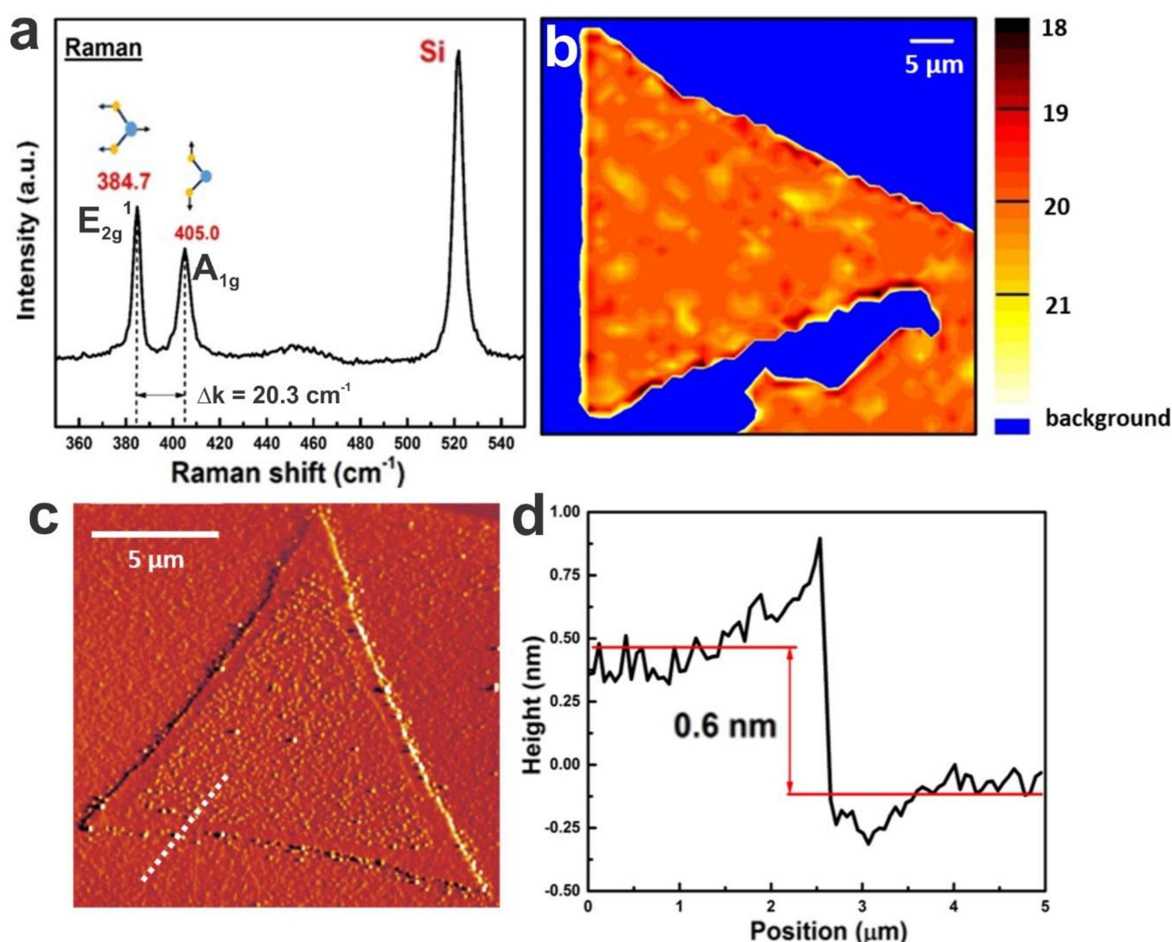

Figure 4.4. (a) Raman spectrum and (b) Raman map of the MoS_2 domain, plotting the spatial variation of the magnitude of the frequency difference between A_{1g} and E_{2g}^1. Laser excitation of 532nm was used. (c,d) AFM image and height profile for MoS_2 domains taken across the dotted white line in (c).

Photoluminescence from differently shaped MoS_2 domains was characterized. **Figure 4.5**a shows the typical PL spectra from a synthesized MoS_2 domain. All three domains showed a similar spectral profile in terms of peak position and FWHM. A strong PL signal is located at 681 nm, which can be correlated to the A1 excitation of MoS_2, and another broad peak is located at about 625 nm, which is known as the resonance of B1 excitation.(*44*) The intensity ratio between the A1 excitation and Raman is around 2.7, indicating that the as-grown MoS_2 domains are monolayer with high quality. 2D images of the PL intensity for different domain shapes have also been measured by stepping a focused excitation laser (532nm) across the sample and integrating the PL signal from each point. Panels b-d of

Figure 4.5 show corresponding PL intensity maps for a large triangle, medium truncated triangle and a small hexagonal MoS_2 domain, suggesting high crystallinity and uniformity of the MoS_2 monolayer. Additionally, for all kinds of shapes, there is a clearly visible increase of PL intensity at the centre of domains and no edge enhancement.

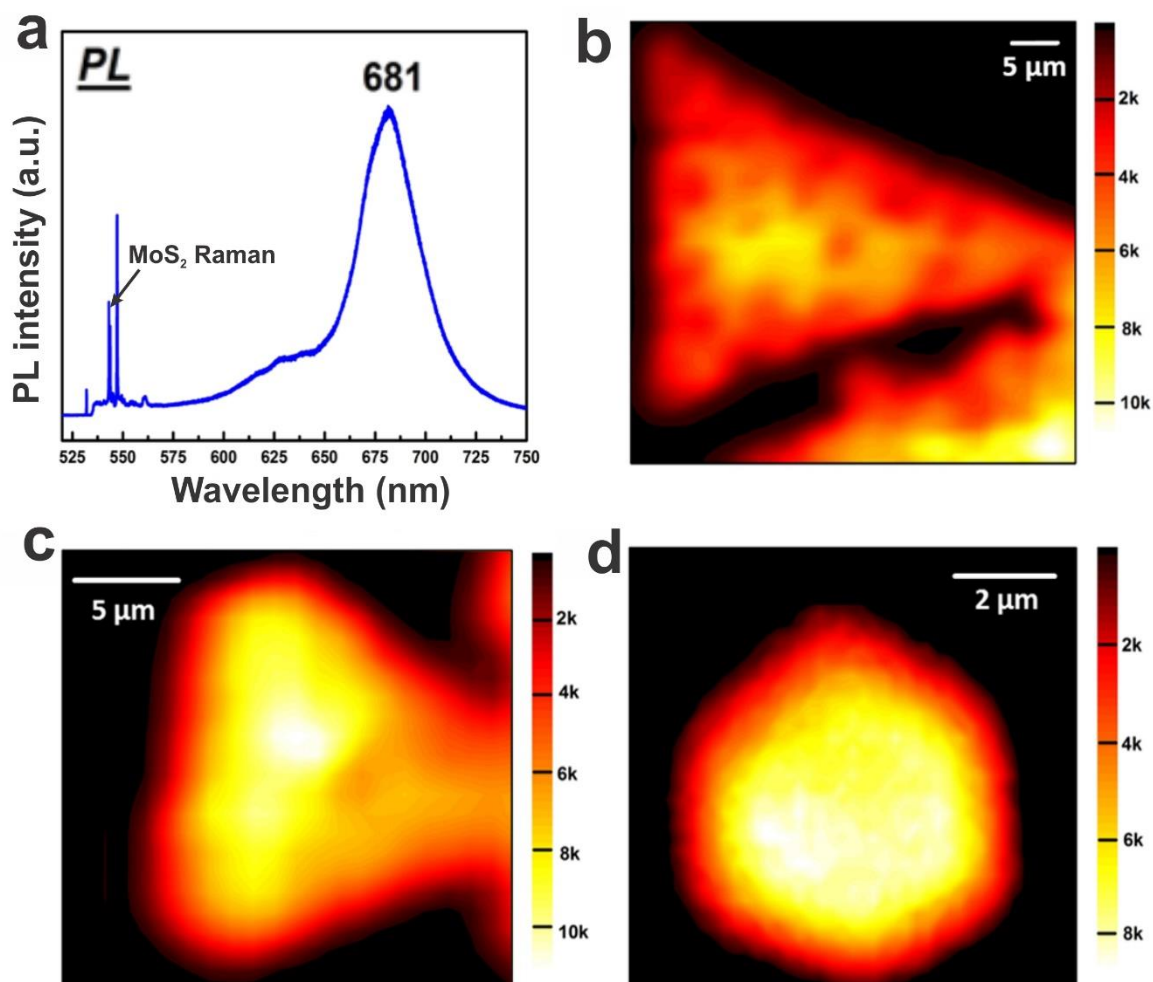

Figure 4.5. (a) Photoluminescence (PL) spectrum of a synthesized MoS_2 domain. (b–d) 2D images of the PL intensity of triangle, truncated triangle and hexagon MoS_2 domains, respectively. The excitation wavelength is 532 nm.

4.1.2.3 Qualitative Model for the Shape Evolution of MoS_2 Domains

Here, I establish a qualitative model to explain the change in the morphology of MoS_2 along the gas flow direction. The main reason for this shape change phenomenon is the change in the Mo:S atom ratio along the SiO_2/Si substrate surface. Before the explanation,

it is worthwhile to note that all the aforementioned characterized monolayer MoS_2 domains were grown in the last 10 min of the main reaction session, which is marked by the green bracket in **Figure 4.2**c, because if reducing the heat preservation time by 10 minutes, only a minority of MoS_2 crystals with size of several hundred of nanometers can be seen in the same area, where large domains with lateral size of tens of microns were observed in **Figure 4.3** (**Figure 4.6**). During this period, the S precursor has been in the heat preservation stage at 150 °C for 5 min. Associated with considering the long distance between S and MoO_3, the S vapor gradient on one SiO_2/Si substrate during the growth of monolayer MoS_2 can be negligible. On the other hand, because the distance between the substrate and the MoO_3 is very small, there will be an obvious concentration gradient on the surface of substrates.

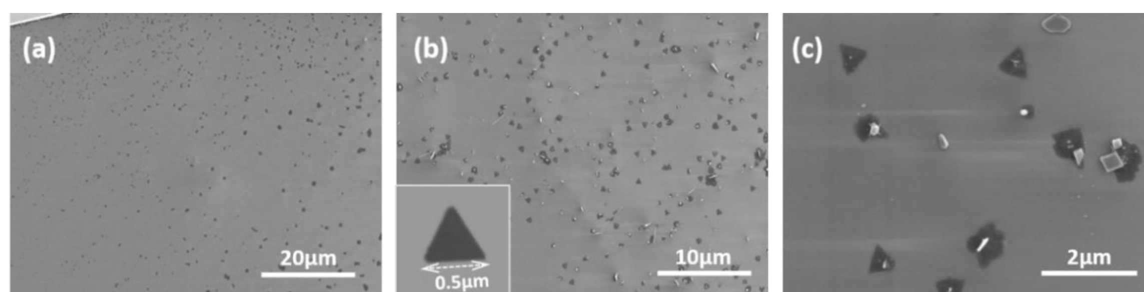

Figure 4.6. SEM images of MoS_2 domains on the second SiO_2/Si substrate when reducing the heat preservation time from 30 min to 20 min under the temperature of 700°C.

On the basis of the principles of crystal growth,(*119*, *120*) the shape of a crystal is determined by its growing rate of different crystal faces. The slowest growing facets become the largest, and the rapidly growing facets either become smaller or disappear altogether. The growing rate of facets commonly depends upon the surface free energy, and in 2D crystals, this corresponds to the edge free energy. Not surprisingly, the low-energy facets tend to be those that grow slowly. For monolayer MoS_2, its final shape will be related to the growing rate of different edge terminations. The most commonly observed edge structures are Mo zigzag (Mo-zz) terminations and S zigzag (S-zz) terminations, which are supposed to be the most energetically stable structures.(*37*) These two kinds of terminations are both

zigzag edges; however, for S-zz edges, the S atoms are exposed to the outside and each S atom has only two bonds with two Mo atoms (the saturated S in the MoS_2 should have three bonds with three different Mo atoms), while for Mo-zz edges, the Mo atoms are exposed to the outside and each has only four bonds with S atoms (the saturated Mo in the MoS_2 should have six bonds with six different S atoms). This structural difference gives them different levels of chemical activity under different Mo:S ratio conditions, which may impact the growing rate and finally influence the domain shape. Generally, this problem can be discussed by separating the Mo/S ratio on the growth substrate into three possible simplified conditions: Mo/S>1:2; Mo/S=1:2 and Mo/S<1:2.

It is assumed that all shapes of domains start growing from a hexagonal nucleus with three sides of Mo-zz terminations and another three sides of S-zz terminations (in fact, this hypothesis is not necessary, just for simplifying the explanations). Under the first condition, S-zz terminations grow faster than the Mo-zz terminations, because in Mo sufficient atmosphere, S-zz terminations with unsaturated S atoms exposed to the outside are more energetically unstable than the Mo-zz terminations and have higher probability of meeting and bonding with free Mo atoms. In **Figure 4.7** under the first condition, it can be seen that if S-zz terminations grow faster than the Mo-zz terminations, the domain shape will change from a hexagon to a triangle with three sides of Mo-zz terminations. Under the second condition, where the Mo:S ratio corresponds to the stoichiometric ratio of MoS_2, the termination stability and the probability for two types of terminations meeting corresponding free atoms are similar, which results in similar growing rates. In this case, the final shape of the domains will be hexagonal. Under the third condition with a S rich atmosphere, the analysis is similar to that of the first condition. The domain shape will also transform to triangular but having three sides of S-zz terminations. To be more detailed, the exact ratio between Mo and S atoms on the substrate will influence the energetic stability of Mo-zz and

S-zz terminations, causing the growth rate difference. If the Mo:S ratio is ≫1:2, the rate of growth of S-zz terminations will increase much faster than that of Mo-zz, making crystal domains transform to a triangular shape in a very short period of time. However, if the Mo:S ratio is slightly above 1:2, the difference in the rate of growth between two types of terminations will be small, resulting in the formation of truncated triangles within the same period of growing time.

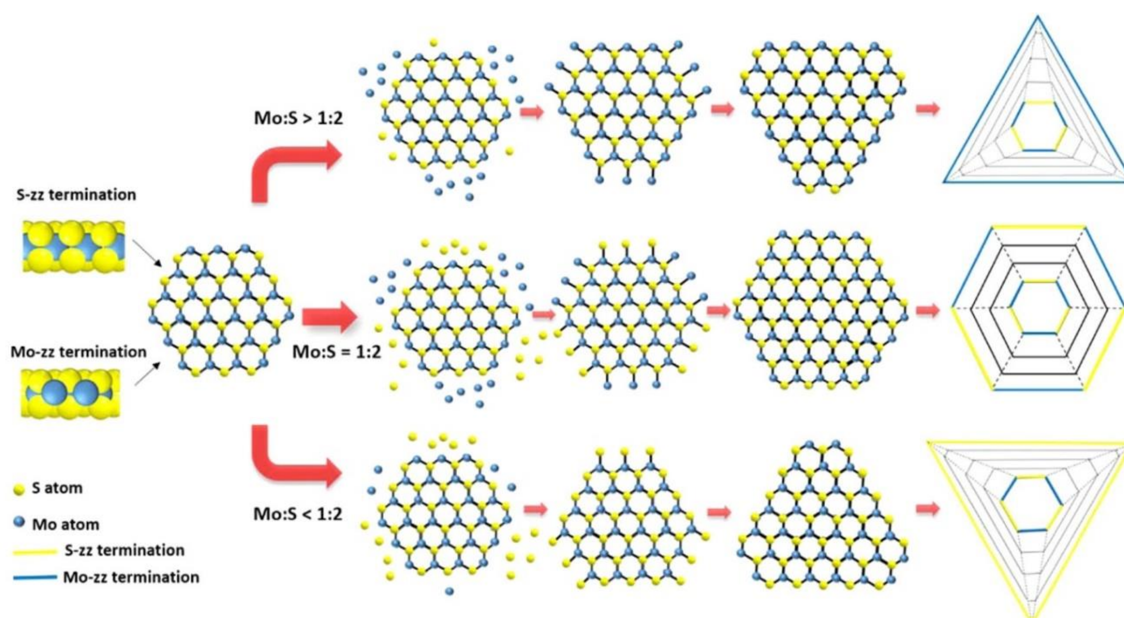

Figure 4.7. Schematic illustration of the relationship between Mo:S atom ratio and the domain shape. The ball-and-stick models in the central part show the top view microstructure of the monolayer MoS_2 crystal in different shapes, while the ball models on the left shows two kinds of MoS_2 termination structures. The schematic diagram on the right illustrates the domain shape changing procedure depending on the growing rates of two different terminations.

There are several reasons to support the hypothesis described above. The first is that, in the previous work,(*36*, *37*, *92*) different shapes of MoS_2 domains were synthesized by adjusting the ratio between MoO_3 and S precursor amount. The relationship between the domain shape and the Mo:S ratio fits the above hypothesis well. Lee *et al*. used 0.03 g MoO_3 and 0.01 g S (Mo:S ratio of 1:1.5>1:2) to produce monolayer triangle MoS_2 domains.(*92*) Najmaei *et al.* synthesized triangle monolayer MoS_2 crystals in S sufficient atmosphere, and when they decreased the S precursor amount, hexagonal and truncated triangles were

observed.(*36*) Another study claims that Mo-zz triangles have sharper, straighter edges than S-zz triangles.(*37*) This morphological difference can be clearly seen for truncated triangles in section 4 of **Figure 4.3**, where three short sides are much rougher than the other three long sides. Based on the SEM characterization results, these truncated triangles grow between large triangles and small hexagonal domains. On the basis of the model described above, it should grow at a Mo:S ratio of >1:2, meaning that the S-zz terminations grow faster than the Mo-zz terminations, so that S-zz terminations should be shorter than the Mo-zz one. The greater roughness of shorter sides supports its S-zz edge structure and corresponds to the analysis well. The third reason is that, this regular shape changing phenomenon not only exists along the gas flow direction, but is also observed in the direction perpendicular to the gas flow direction on the substrate. As shown in **Figure 4.8**a, the MoO_3 concentration decreases along the white arrow as the deposition location becomes further to the MoO_3 powder precursor, but the S concentration keeps constant. This results in the reduction of Mo:S atom ratio along the white arrow direction. **Figure 4.8**b shows clearly the MoS_2 crystal shape transformation process from truncated triangles to hexagons and finally back to triangles with a decrease of the domain size. The reason of observing truncated triangles rather than triangles at the left beginning may be that the triangles have merged into uniform layers. The observation of the similar shape transformation process along the direction vertical to the Ar gas flow indicates that the Mo:S ratio change is the main cause of shape transformation, because, in this direction, all conditions including the reaction temperature and the S concentration, are uniform, except the concentration of MoO_3, which makes the Mo:S ratio to be the only changing parameter. All the factors mentioned above indicate that the Mo:S ratio change is the most important reason for the shape change. Despite the shape evolution, the crystal size also experiences a regular change. This may relate to the concentration gradient of the gas phase MoO_3 along the gas flow direction, which impacts

the average growing rate of the MoS_2 crystals. The aforementioned qualitative model to explain the spatial evolution on crystal's shape and area has been strongly supported and further developed by the theoretical work done by Rajan *et al*.,(*121*) in which a generalized mechanistic model using a Kinetic Monte Carlo (KMC) simulation has been established based on my experimental data. The simulation results are consistent with my observations. It is worth mentioning that the shape evolution model proposed here simplified the MoS_2 growth process, especially on the procedures about how Mo(S)-based active species migrate to the as-formed nuclei, react with the corresponding S(Mo)-terminated edges and finally attach on them to expand the grain. Several hypotheses were made, including assuming the single-crystallinity of each individual domains imaged in **Figure 4.3** and the zigzag configuration of edges. Moreover, the reaction rate between S active species and the Mo-zz terminations was assumed to be equal with the reaction rate between Mo active species and the S-zz terminations. The reaction order was assumed to be one, indicating that the growth rate of Mo(S)-zz edges is linearly dependent on the concentration of S(Mo) active species on the substrate surface. Further quantitative experiments are required to check the validity of these hypotheses and modify this shape evolution model.

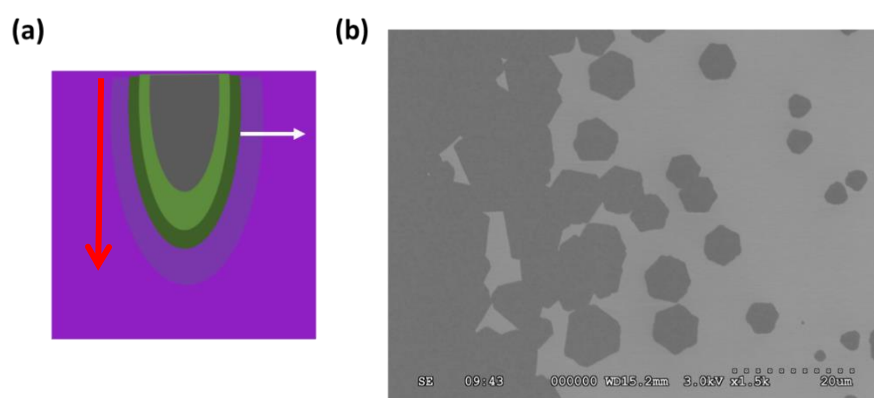

Figure 4.8. (a) Schematic diagram of deposited pattern of MoS_2 on the second SiO_2/Si chip after growth. The red arrow shows the direction of the Ar gas flow, and the white arrow represents that there is also crystal shape evolution along this direction perpendicular to the red arrow. (b) SEM image showing the MoS_2 morphology transformation along the white arrow direction.

4.1.2.4 Impacts of the MoO_3 Precursor Heating Temperature and the Ar Flow Rate

The effect of MoO_3 precursor temperature on the MoS_2 shape change has also been investigated, and it was found that this morphology transformation phenomenon widely exists. However, as the temperature influences the evaporation amount of MoO_3, leading to a different MoO_3 concentration gradient in the gas phase, the location of the deposition showing this crystal shape changing process slightly moves. **Figure 4.9** shows the MoS_2 shape transformation along the Ar gas flow direction at 750 °C on the third SiO_2/Si chip. The crystal morphology evolution is similar to that at 700 °C, indicating that this phenomenon commonly exists in the MoS_2 growth process.

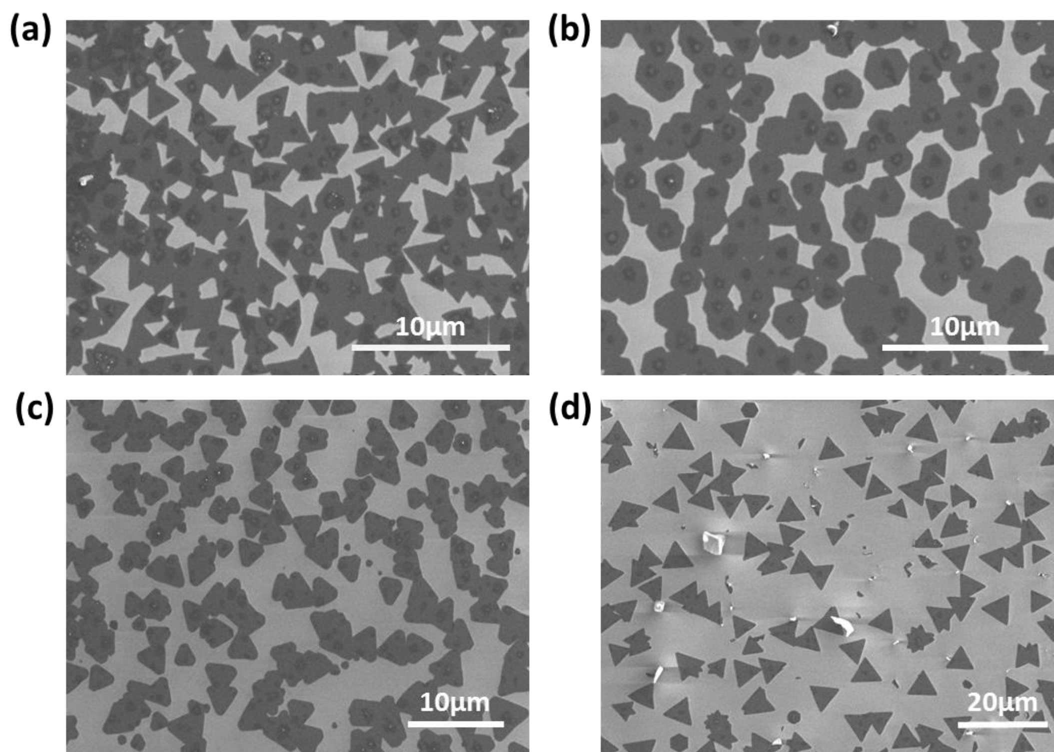

Figure 4.9. SEM images of MoS_2 shape changing process under the reaction temperature of 750°C on the third SiO_2/Si chip. The observation direction is along the red arrow shown in **Figure 4.8**.

When the MoO_3 temperature was decreased to 650 °C, except the aforementioned shape changing trend, the domain shape ended up with three-point stars instead of triangles (**Figure 4.10**a–e). This is possibly because the decreasing temperature reduces the evaporation amount of MoO_3, resulting in a Mo:S ratio even lower than that under 700 °C,

which makes the difference in growing rate between Mo-zz terminations and S-zz terminations larger. The growth of S-zz edges cannot catch up with that of Mo-zz edges, so that S-zz edge is able to form only a curved side instead of a straight one (**Figure 4.10**f), which looks like a three-point star. This shape is very easy to transform into several-point stars, because the curved crystal edge is not perfectly S-zz structure anymore. During the slow growing process of the curved side, when a defect emerges with a Mo-zz structure on it, the Mo-zz structure will grow with high speed and form a sharp point within a short period of time. This is why many several-point stars can be observed. Panels a to c of **Figure 4.10** show two different sized domains have formed, large 10 μm domains and smaller sub-micrometre domains.

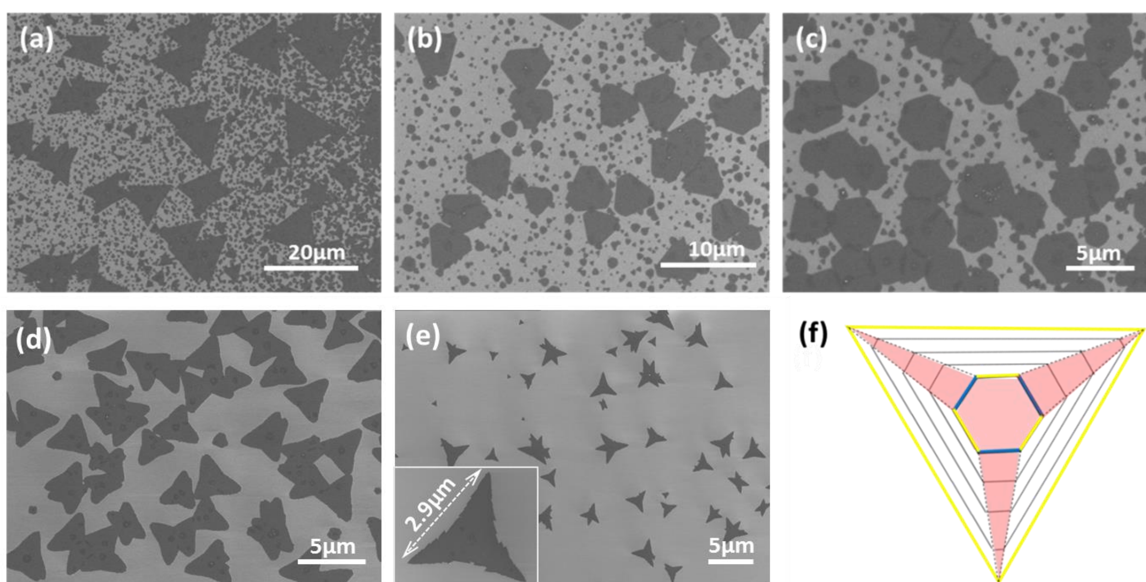

Figure 4.10. (a–e) SEM images indicating the MoS_2 shape evolution along the red arrow direction in **Figure 4.8** under the reaction temperature of 650 ^{o}C on the second SiO_2/Si chip. (f) Schematic illustration of the three-point star formation.

The effect of Ar gas flow rate on MoS_2 crystal growth has also been investigated. **Figure 4.11** shows the SEM images of MoS_2 domain morphologies in different areas marked by red spots in the central schematic diagram on the first Si chip, with an increase in Ar gas flow rate from 10 to 100 sccm. In general, the loss of stability during crystal growth can be

clearly observed, because the smoothness of the domain sides is severely reduced, and the crystal shape becomes dendritic-like in some areas. The high flow rate may promote the mass transfer process, which contributes to the increase in the crystal growth rate. In this case, instability may occur as atoms absorbed on the substrate surface do not have enough time to move into the right lattice locations, where crystal domains could have the lowest surface free energy, and the probability of defect formation may increase. Therefore, under the high-flow rate condition, the MoS_2 crystals are more likely to grow under "kinetic" conditions, in which the rate limiting step is the surface migration ability of absorbed atoms on the substrate, rather than the chemical reaction between precursors, which is typical for colloidal nanocrystals with high precursor feedstock. However, the regular shape domains with smooth sides and sharp edges can still be seen in some locations, as shown in section 3 in **Figure 4.11**. This is because the direction from section 1 to 3 is perpendicular to the Ar gas flow direction and there is a decrease in the concentration of MoO_3 on the substrate surface, as the distance from the MoO_3 powder precursor to each spot increases.

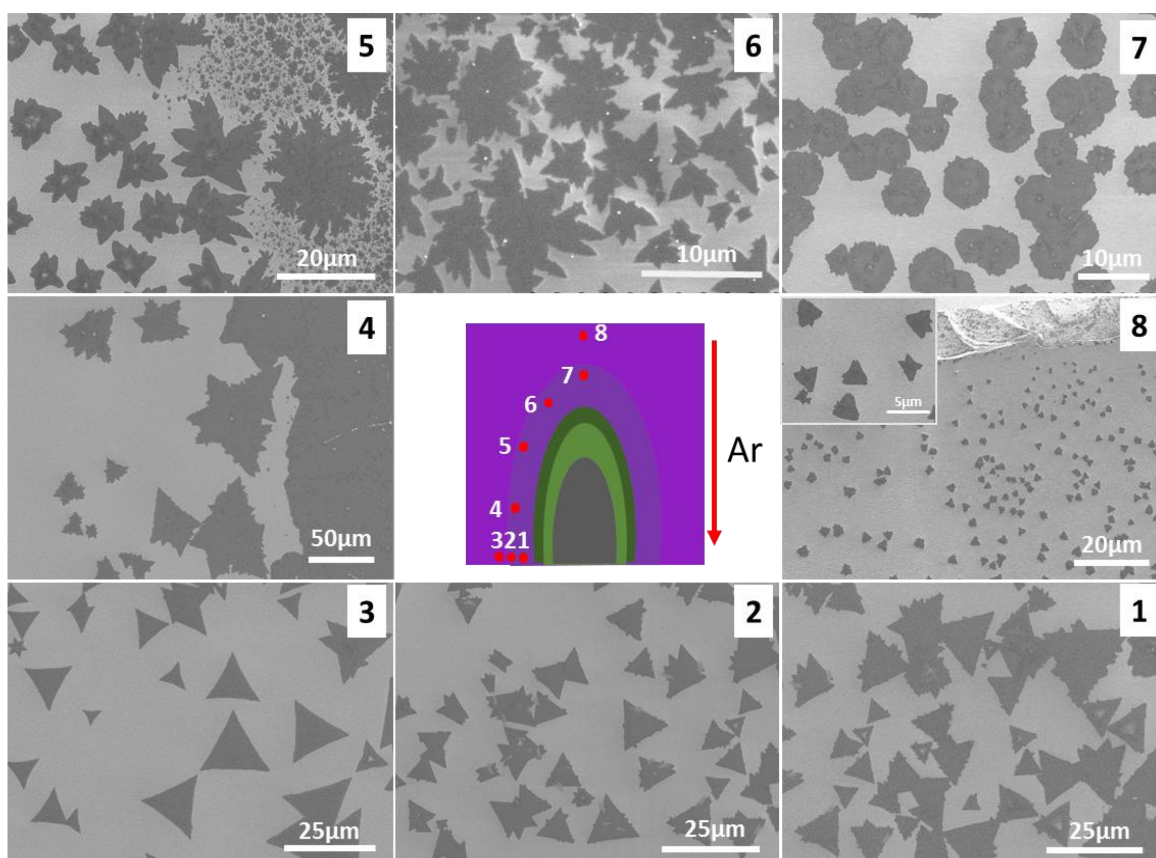

Figure 4.11. SEM images showing the MoS_2 shape evolution under the Ar flow rate of 100 sccm. on the first SiO_2/Si chip. Each SEM image with a number on the top right corner corresponds to the location having the same number on the schematic illustration in the centre.

The decrease in precursor concentration has an effect of slowing the crystal growth rate, which can balance the positive influence from the high flow rate, thus leading to stable crystal growth under thermodynamic control. Furthermore, in the direction parallel to the gas flow, the MoO_3 concentration on the first substrate decreases as the sections of investigation move farther from the MoO_3 powder. This is why in section 8 in **Figure 4.11**, crystal domains transform back into more regular shapes compared to those before it. However, as the MoO_3 concentration in the central area of the substrate is too high, it is not able to achieve isolated monolayer domains there, making the direct comparison of crystal shape along the gas flow direction not feasible. From these studies, it can be found that the increase in Ar flow rate could turn the control of crystal growth from the thermodynamic to kinetic regime, resulting in the formation of dendritic morphologies, which are not

favourable for the production of high-quality 2D crystal. However, with a decrease in the precursor concentration, a new balance can be achieved to stabilize the crystal growth and shift the growing conditions to the thermodynamic control.

4.1.3 Conclusion

In conclusion, I developed a hydrogen-free, atmospheric-pressure CVD approach to grow monolayer MoS_2 domains on the SiO_2/Si substrate. MoO_3 and S precursors were designed to locate in different furnaces, which gave independent heating profiles and provided greater flexibility in the growth recipe. The microstructure and properties of the MoS_2 crystals were measured by SEM, Raman spectra, AFM, and PL spectra, confirming that the MoS2 domain was a uniform, single layer with high crystallinity. I intentionally established a sharp gradient of MoO_3 precursor concentration on the growth substrate to explore its sensitivity to the resultant MoS_2 domain growth within a relatively uniform temperature range. I found that the shape of MoS_2 domains was highly dependent upon the spatial location on the SiO_2/Si substrate, with variation from triangular to hexagonal geometries. The shape change of domains has been attributed to local changes in the Mo:S ratio of precursors (1:>2, 1:2, and 1:<2) and its influence on the kinetic growth dynamics of edges. In addition, the effects of MoO_3 precursor temperature and Ar gas flow rate on MoS_2 crystal shape were also investigated. It is anticipated that these studies will allow the shape-controllable synthesis of MoS_2 and improve the ability to discover of more shape-dependent properties.

4.2 Growing Large-Area, Continuous Films of Monolayer MoS_2

4.2.1 Introduction

After realizing the growth of monolayer MoS_2 domains and having insights into some important experimental parameters on the synthesis quality, the next target is to modify the CVD method for the production of continuous, large-scale, high-quality MoS_2 monolayer films, which is conducive to the industrial application of this novel material. The main difficulties arise from either the layer number control or the large-area continuity. There have been a few reports about the realization of large-scale growth of continuous monolayer MoS_2 films *via* the sulphurization to either MoO_3(*94*, *122*, *123*) or $MoCl_5$,(*96*) or through a metal-organic CVD (MOCVD) technique with precursors of $Mo(CO)_6$ and $(C_2H_5)_2S$.(*97*) However, all the reactions occur under the low pressure, which increases the requirement of the experimental equipment. Moreover, the MOCVD method suffers from using precursors with relatively high toxicity. Therefore, proposing a feasible approach, which is simple, safe and low-cost is challenging and highly desirable.

Before the modification, I need to know the characteristics of my old CVD system clearly, especially those weaknesses that hinder the product's wide coverage, continuity and thickness homogeneity. As shown in the top panel of **Figure 4.12**a, this is my CVD setup used for the MoS_2 domain growth in section 4.1.2.1. Its major drawbacks can be summarized into three points. Firstly, S vapour can contact and react with the MoO_3 powder directly, thus gradually decreasing the amount of the MoO_3 powder and leading to an uncontrollable decay of the evaporated MoO_3 in the gas phase during the MoS_2 growth. Secondly, both the MoO_3 powder and the growth substrates are placed in the centre of the second furnace, making the independent temperature control of them impossible. Thirdly, since the substrates are loaded with faces closely towards the MoO_3 powder, there exists a sharp concentration gradient of MoO_3 on the substrate, which is detrimental to the growth

uniformity. Therefore, the modification of the CVD system should aim at solving the three problems listed above, *i.e.*, (1) avoiding the cross-contamination between S and MoO_3 precursors to ensure a stable feedstock of both precursors in the gas phase; (2) realizing the separate temperature control of MoO_3 and the growth substrate, thus expanding the control dimensionality further; (3) optimizing the concentration uniformity of gaseous MoO_3 on the substrate. In this section, I demonstrate a novel CVD synthesis strategy, which has realized the above three optimization goals and led to the growth of continuous and high-quality monolayer MoS_2 films in the order of centimetres directly on a SiO_2/Si substrate under atmospheric pressure.

4.2.2 Results and Discussion

4.2.2.1 Experimental Setup

As shown by the bottom panel of **Figure 4.12**a, two key modifications were made for the new CVD system compared with the old one. One is to add a mini inner quartz tube into the 1-inch quartz tube outside and place MoO_3 powder in it, thus avoiding the gradual quench of MoO_3 powder by the S vapour during the reaction. The independent temperature control on the MoO_3 powder can also be conveniently achieved by adjusting the MoO_3 location relative to the left open of the second furnace. The other modification is to make the growth substrate orientation vertical to the mass flux of precursors, which eliminates the

precursor concentration gradient on the substrate. The detailed growth strategy is described as below (**Figure 4.12**b).

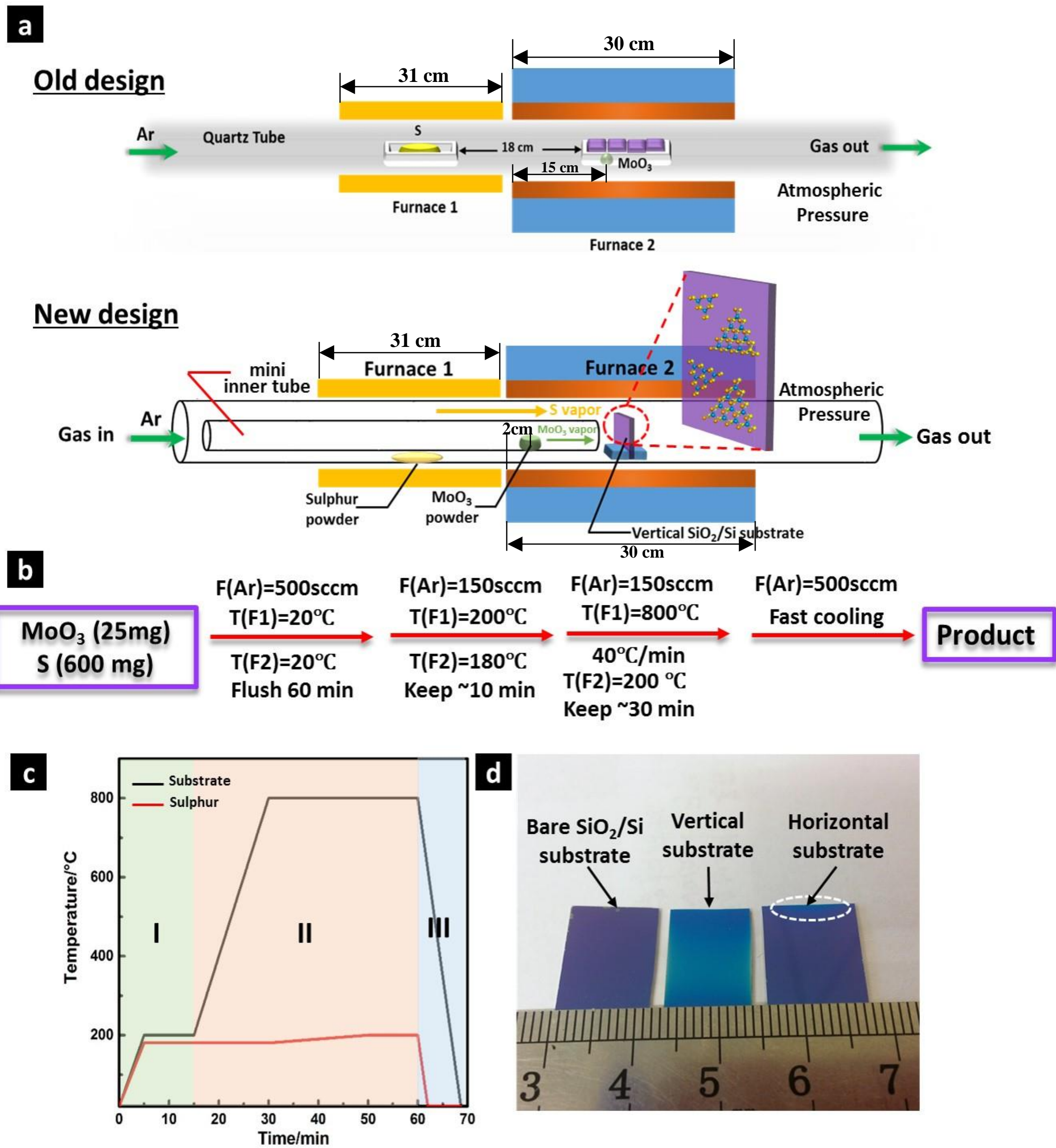

Figure 4.12. (a) Schematic illustration showing a comparison of the CVD synthesis setup of MoS_2 between an old design used in section 4.1.2.1 and the new one applied in this section. (b) Flowchart showing the main steps of the growth of the large-area, continuous monolayer MoS_2 films. (c) Temperature programming process of MoO_3 and S precursors. (c) Optical images showing the contrast difference of the bare SiO_2/Si substrate, the vertical substrate and the horizontal substrate after experiencing the same MoS_2 growth recipe.

MoO_3 (25 mg) and sulphur powder (600 mg) were used as precursors, loaded separately into two furnaces, 1 and 2, to provide independent temperature controls. A bare SiO_2/Si substrate (300 nm thick amorphous SiO_2 coated on the p-doped Si from University Wafer), was inserted into a homemade holder (made by three pieces SiO_2/Si chips stuck up by fire cement) to keep it vertical, and was placed in furnace 2. This places the substrate surface to be perpendicular to the gas flow direction, decreasing the precursor concentration gradient on the SiO_2/Si and reducing the influence of the geometric effects from the gas flow by promoting the mass transport of precursors through the boundary layer above the substrate surface, which will be discussed in more detail afterwards. The sulphur precursor and the vertical substrate were both positioned in the central area of two furnaces, respectively, while the MoO_3 powder was loaded at the upstream of the second furnace in order to produce a mild evaporation temperature for MoO_3. Since the nucleation density of MoS_2 is dominated by the MoO_3 gas concentration,(*36*) such design enables better control over the nucleation density with flexibility of temperature adjustment by simply shifting the loading position of the MoO_3 powder. One of the MoO_3 locations for the best growth results was 2 cm away from the left open end of furnace 2 (see **Figure 3.1**). The reaction occurred under atmospheric pressure with argon used as carrier gas. I separated two solid precursors by placing the MoO_3 into an inner quartz tube (diameter ~1 cm) inside the outer 1-inch tube with its inlet far exceeding the sulphur position. This avoids the gradual sulphurization of MoO_3 powder by sublimated sulphur, stabilizing the supply amount of both gaseous precursors to the reaction area around the substrate during the whole synthesis. The distance between the substrate surface and the outlet of the inner tube was 1.5 cm, which gives enough time for the even mixing of gaseous sulphur and MoO_3 and at the same time limits the formation of MoS_2 compounds in the gas phase that produce the three-dimensional MoS_2 flakes on the substrate. The growth can be divided into three sections: 1. Pre-introduction of

S vapour to fill up the whole system by heating the sulphur powder up to 180°C for 15 minutes with an Ar flow rate of 150 sccm, creating a sulphur sufficient atmosphere (**Figure 4.12**c section I); 2. A main growth section with the typical temperatures for sulphur, MoO_3 and substrate to be ~180–200°C, ~300°C and ~800°C, respectively, without changing the Ar flow rate (**Figure 4.12**c section II). 3. A fast cooling process with a 500 sccm Ar to quickly stop the reaction and accurately control the growth time (**Figure 4.12**c section III).

To investigate the impact of the substrate loading on the final growth results, a direct comparison experiment was conducted by placing the substrate horizontally without changing any of the parameters. **Figure 4.12**d shows that, compared with a bare SiO_2/Si chip, the vertical substrate surface was uniformly covered by a MoS_2 film on the centimetre scale, showing green optical contrast different from the purple one from the bare substrate. For the horizontal substrate, the MoS_2 covered only a small top region on the substrate oriented to the gas inlet direction, which is marked by the dashed white ellipse, indicating a sharp precursor concentration decay on the substrate surface, when loading the SiO_2 surface to be parallel to the gas flow direction.

4.2.2.2 Impacts of the Substrate Temperature and the MoO_3 Precursor Temperature

To gradually narrow down the range of growth parameters and optimize the MoS_2 film quality, several modifications were investigated, including the heating temperature of the precursor, MoO_3, and the growth temperature (temperature for the substrate), which were found to be the key factors for synthesis. **Figure 4.13** shows the MoS_2 growth dependence on these two parameters from a series of SEM images of the as-grown MoS_2 with their corresponding MoO_3 temperature and the growth temperature. In **Figure 4.13**c,f,i, for the growth temperature of 750 °C, when increasing the heating temperature of MoO_3 from 200°C to 400°C, the MoS_2 nucleation density goes up with a deterioration in the uniformity of the layer thickness, leading to island-like structures with smaller grain sizes. In contrast,

when the MoO_3 temperature is fixed with a rise in the growth temperature, the nucleation density decreases with improved homogeneity in the layer thickness and higher crystallinity, evidenced by flatter surface morphology and the formation of larger triangular-shaped monolayer domains (**Figure 4.13**f,e,d). The reason for such a growth mode transition could be attributed to the change of the mean free migration length ($L_{surface}$) of Mo-based active species (MoO_{3-x}/MoS_2) absorbed on the substrate surface, which is influenced by both the MoO_3 heating temperature and the growth temperature (see section 2.4.3). With higher MoO_3 temperature, the supply of gaseous MoO_3 will be more sufficient, leading to a larger amount of Mo-based clusters on the substrate surface, which initiates new nuclei rather than making them attach to the existing nuclei already formed. That is why the nucleation density increases with smaller grains grown when the MoO_3 temperature rises. In contrast, with higher growth temperature, the mean free migration length of Mo-based molecules could be longer due to a reduction of the amount of Mo-based species absorbed on the substrate surface, leading to their attachment to preformed nuclei and expanding the crystal size rather than forming new nuclei. This results in a decrease of the nucleation density with larger domain sizes as the growth temperature increases. In addition, the increased growth temperature is expected to enhance the crystallinity of MoS_2, evidenced by an improvement on the domain shape faceting. It is also worth noting that the best growth recipe is a combination of both the temperatures of the MoO_3 and the substrate, respectively. It is possible to obtain similar mean free migration length of absorbed Mo-based species with different combinations of these temperatures, thus obtaining uniform full coverage of monolayer MoS_2 for two different parameters (**Figure 4.13**e,g).

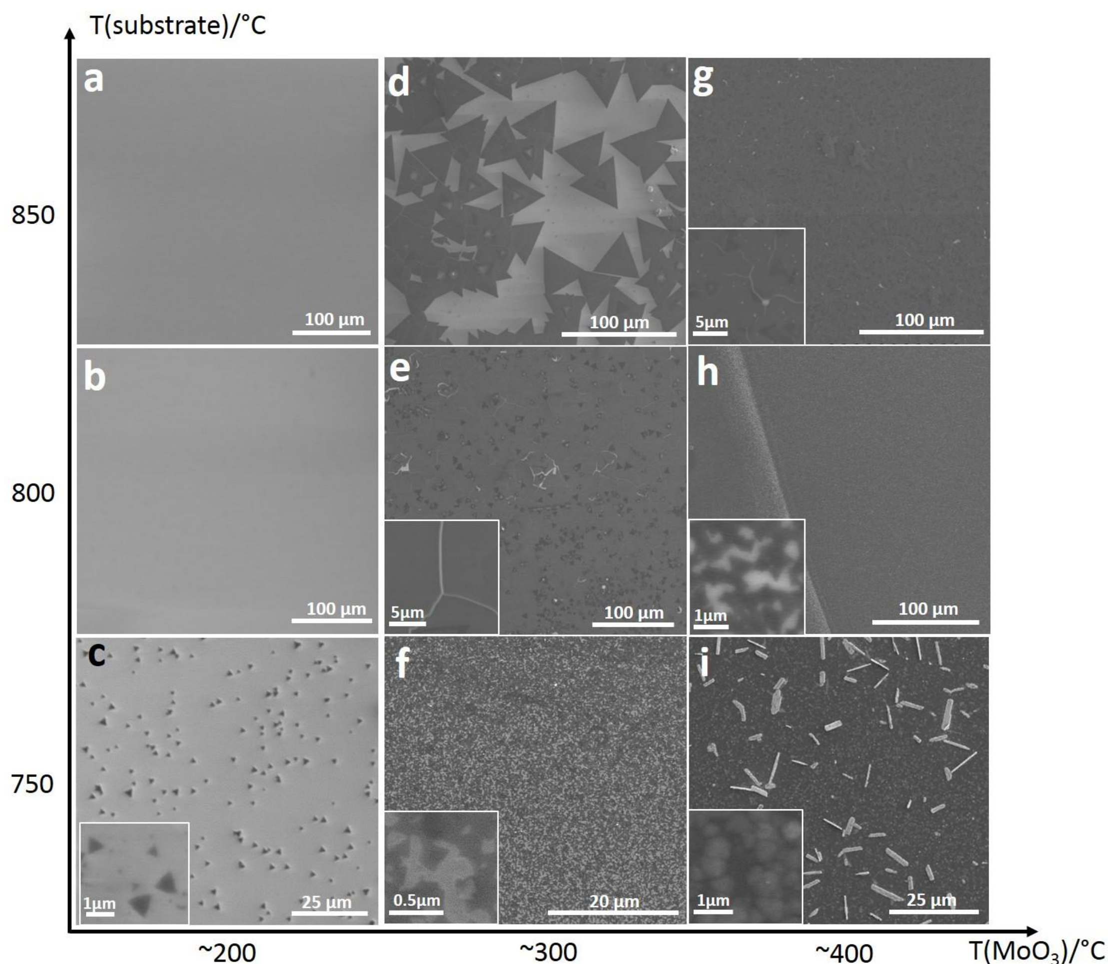

Figure 4.13. SEM images showing how the growth results depend on the parameters of the MoO_3 heating temperature and the substrate temperature (growth temperature), with magnified images as insets to highlight the detailed domain size and morphologies in panels (c) and (e)–(i), respectively. Panels (a) and (b) show that there is nothing grown on the substrate under these conditions.

4.2.2.3 Characterization on the Quality of As-Grown MoS_2 Films

Figure 4.14a shows a low-magnification optical image of a typical MoS_2 film grown on the SiO_2/Si substrate with an intentional scratch introduced to show the optical contrast difference between the MoS_2 film and the bare substrate. **Figure 4.14**b shows more detailed information, indicating that most of the area is uniformly covered by a continuous monolayer MoS_2 film, with only a very small portion of multilayer regions with brighter optical contrast (the proof of the MoS_2 thickness uniformity will be given by the following PL and Raman characterization in **Figure 4.15**). The scanning electron microscopy (SEM) images in

Figure 4.14c,d are consistent with the optical images, confirming the large-area and continuous growth of monolayer MoS_2 films. The presence of micro-cracks or winkles was potentially induced by the fast-cooling step because of the thermal expansion coefficient difference between the monolayer MoS_2 and SiO_2. When choosing an area close to the substrate boundary, where the substrate surface is not fully covered by MoS_2, the continuous films are formed by the gradual merger of isolated monolayer triangular MoS_2 domains with sizes of 10-15 μm (**Figure 4.14**e,f). To better evaluate the grain size of the MoS_2 membrane, an oxidation treatment was carried out at a temperature of 300°C in air, which has been previously shown to reveal the grain boundaries in TMDs films under an optical microscope.(*94*, *124*) As shown in **Figure 4.14**i–k, the grain boundaries were gradually etched out after oxidizing for 70 and 100 min, respectively, and the crystal size was confirmed to be around 10 to 20 μm, which is larger than that of the MoS_2 monolayer films obtained by other low pressure CVD techniques(*94*, *97*) and is in agreement with the observations in **Figure 4.14**e,f. I have also characterized the growth results when loading the SiO_2/Si substrates horizontally. As shown in **Figure 4.14**g, large amounts of nanometre-sized, isolated and irregular-shaped MoS_2 domains were densely distributed in the top region of the substrate (white dashed ellipse in **Figure 4.12**d). When taking the SEM image ~300μm away from the location in **Figure 4.14**g to the downstream of the substrate, the nucleation density of the MoS_2 domains dramatically decreases (**Figure 4.14**h) indicating a sharp precursor concentration gradient on the SiO_2 surface, which hinders the production of large-area and homogeneous MoS_2 films.

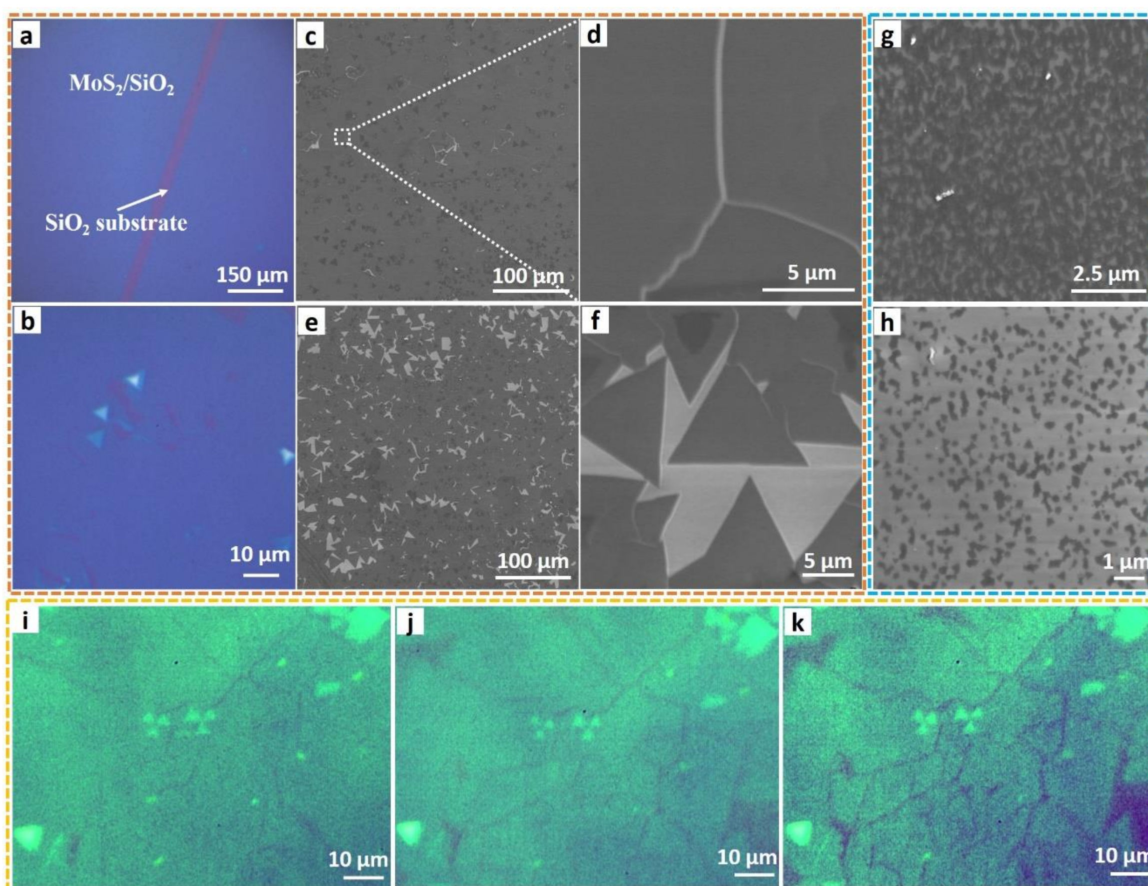

Figure 4.14. (a,b) Low-magnification and high-magnification optical images of an as-grown continuous MoS_2 film, respectively. (c) Low-magnification SEM image of the MoS_2 continuous film, where MoS_2 domains fully merge. (d) Higher magnification SEM image of the area marked in the white dashed box in (c), showing the uniformly grown MoS_2 film with micro-cracks or wrinkles potentially induced by the fast-cooling process. (e) Low-magnification SEM image of a growth area near the substrate boundary, where triangular MoS_2 domains nearly merge into a continuous film. (f). High-magnification SEM image of the same area as (e), showing the coalescence of triangular MoS_2 domains with a side length of 10-15µm. (g,h) SEM images of MoS_2 in the top region of the horizontal substrate using the same recipe. (i–k) Optical images of the MoS_2 continuous thin film before (i) and after the oxidation treatment in the air for 70 min (j) and 100 min (k), respectively, at a temperature of 300 °C to reveal grain boundaries.

Raman and photoluminescence (PL) spectroscopy, as well as atomic force microscopy (AFM) were utilized to evaluate the thickness, quality and uniformity of the as-grown MoS_2 films. **Figure 4.15**a–c provides the optical image together with the Raman and PL spectra from the spots marked with the corresponding coloured circles shown in panel a. There are two characteristic Raman peaks for MoS_2, E_{2g}^1 and A_{1g}, which represent the in-

plane vibration of Mo and S atoms and the out-of-plane vibration of S atoms, respectively.(*44*) The frequency difference between these two peaks is dependent on the layer number, which is used to determine the MoS_2 thickness.(*51*, *125*) The fitting results show that MoS_2 from the black spot has the E_{2g}^1 and A_{1g} modes located at 384.1 and 401.6 cm^{-1}, respectively, with a peak spacing of ~17.5 cm^{-1}, consistent with the exfoliated monolayer MoS_2.(*126*) The full width of half maximum (FWHM) of E_{2g}^1 is ~4.6 cm^{-1}, suggesting good crystallinity of the CVD-grown MoS_2.(*96*) The Raman spectra of MoS_2 with a lighter green contrast (red spot) and a bright white contrast (blue spot) show an increased frequency difference (Δ) between E_{2g}^1 and A_{1g} peak, having Δ to be ~ 21.6 and ~23.6 cm^{-1}, respectively, indicating thickness of bilayer and multilayers (>3 layers). I have also characterized the PL spectra from the same three spots, and normalized the MoS_2 PL signal by its Raman intensity to better reveal the PL quantum efficiency dependence on the MoS_2 layer number, because such a normalized PL can cancel out the influence from many external effects, such as laser excitation intensity, quantity of materials, and local electric field factors.(*44*) As shown in **Figure 4.15**c, the PL spectra from monolayer MoS_2 (black spot) exhibits the highest PL intensity, with two pronounced emission peaks at ~681 and ~627nm, respectively, corresponding to the A1 and B1 direct excitonic transitions. The emission intensity obviously reduces for bilayer and multilayer regions, due to the bandgap shifting from direct to indirect transitions with the increase of the MoS_2 thickness. 2D Raman mapping was performed over an area of 100×100 μm in the continuous MoS_2 film (marked by the dashed purple square in panel a) by plotting the spatial variation of the magnitude of the frequency difference between A_{1g} and E_{2g}^1 peaks (**Figure 4.15**d). The thickness distribution correlates well to the contrast on the optical image in panel a, having more than 90% of the area with a frequency difference to be less than ~19 cm^{-1} and only a small fraction of bilayer or multilayer flakes, which confirms the growth of large area

uniform monolayer MoS_2 films on the SiO_2/Si. The AFM measurements in the topological mode is a more direct way to determine the MoS_2 layer number and uniformity. The height profile of an almost fully-merged region was provided to evaluate the layer thickness across the area marked by a white dotted line in **Figure 4.15**e, as shown by the upper part of **Figure 4.15**g. A thickness of 0.75 nm is obtained, in agreement with the MoS_2 monolayer thickness.(*92*, *96*, *122*) Since the thickness of monolayer MoS_2 is quite small, to better distinguish the coverage region of MoS_2 films from the bare SiO_2/Si substrate, phase mode mapping is shown in **Figure 4.15**f, where the visibility of partially merged MoS_2 monolayers increases because of the elasticity difference between MoS_2 and SiO_2. The phase profile in the lower part of **Figure 4.15**g shows that the phase change of the AFM tip vibration when moving from the surface of monolayer MoS_2 to SiO_2 is ~2 degrees.

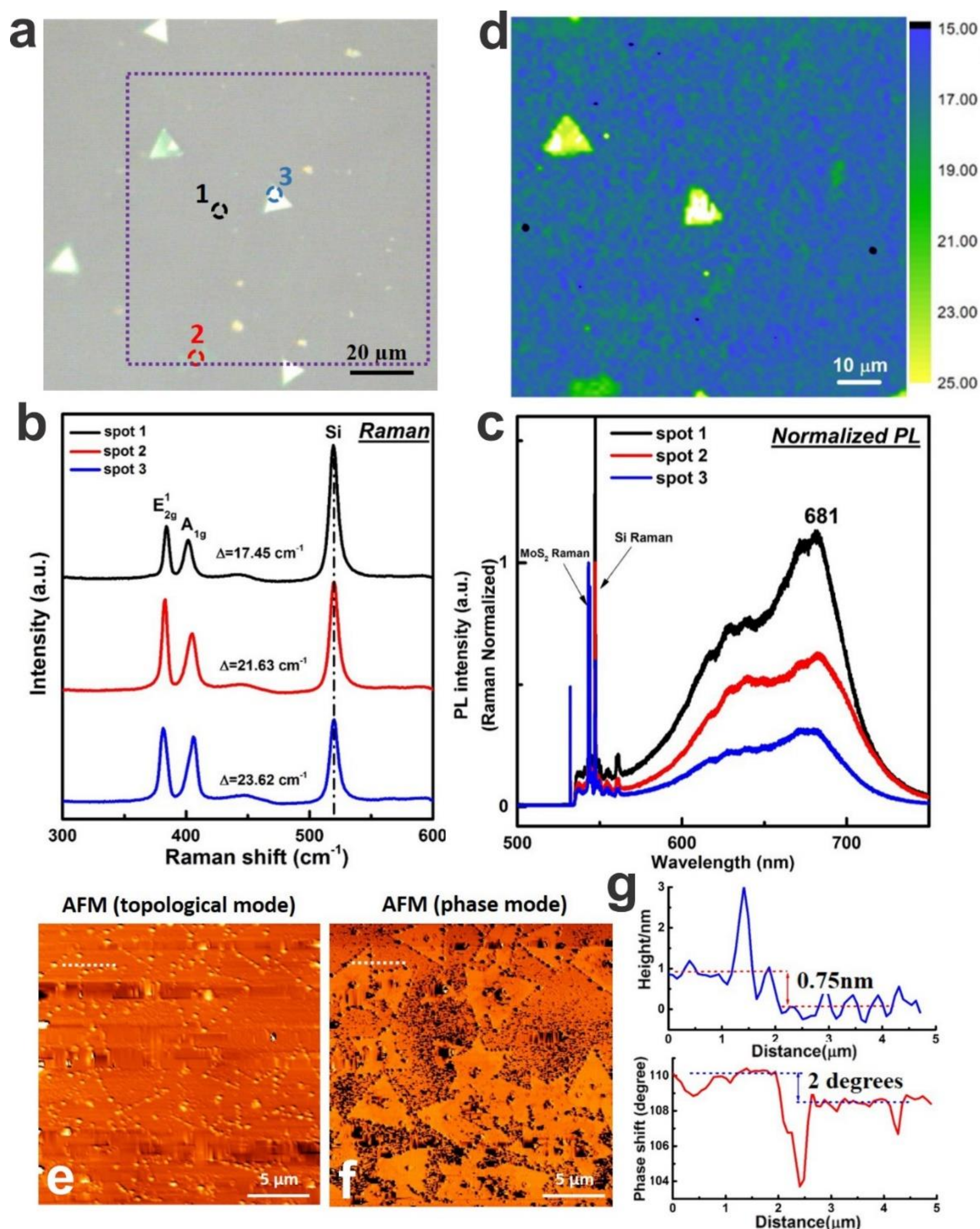

Figure 4.15. (a) Optical images of the MoS_2 continuous film, showing monolayers in most areas with only a small percentage of multi-layer regions. (b) Raman and normalized photoluminescence spectrum from the marked spots with corresponding coloured circles in (a). (d) Raman maps of the MoS_2 film in the square marked by a dashed purple outline in (a), plotting the 2D spatial variation of the magnitude of the frequency difference between A_{1g} and E_{2g}^{1}. Laser excitation of 532 nm was used. (e-f) AFM images in the topological and phase mode, respectively, of a nearly fully-merged MoS_2 growth region. (g) Height and phase profiles taken across the same MoS_2 edge marked by dotted white lines in (e) and (f), respectively.

4.2.2.4 *Kinetic Growth Model*

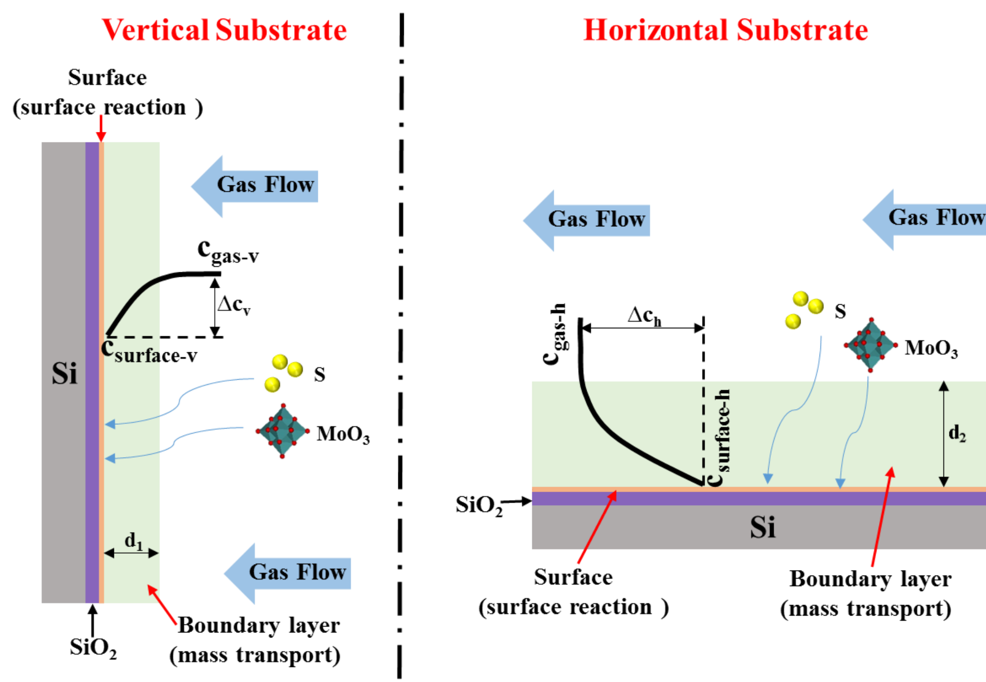

Figure 4.16. Schematic illustration showing how the loading orientation of the substrate could influence the MoS_2 growth kinetics. c_{gas-v} and c_{gas-h} represent the precursor concentrations in the bulk gas flow when putting the substrate in a vertical and a horizontal orientation, respectively. They equal to each other at the same growth condition. $c_{surface-v}$ and $c_{surface-h}$ represent the precursor concentration on the substrate surface of a vertical and a horizontal substrate, respectively.

I now discuss the influence of the substrate orientation on the MoS_2 growth by establishing a kinetic growth model (**Figure 4.16**). Briefly, the 2D MoS_2 growth can be divided into two procedures: (1) the mass transport of gaseous precursors through the boundary layer to reach the substrate surface, and (2) the chemical reaction for precursors on the substrate surface, primarily involving the absorption/desorption and migration of Mo-based and S-based active species on the surface and their reactions with each other to form MoS_2. In the CVD growth of graphene under atmospheric pressure at a high temperature, mass transport is usually the rate-limiting step, which means that the boundary layer above the substrate surface is thick so that the synthesis progress is governed by the diffusion speed of the active species through the boundary layer to reach the substrate surface.(*98*, *99*, *103*,

104) Therefore, factors such as the geometry of the precursor gas flow can easily impact the overall synthesis, because the precursor spatial concentration gradient in the bulk gas phase varies the concentration of the active species absorbed at different locations on the substrate. This will eventually result in thickness non-uniformity of the as-grown materials. For the APCVD synthesis of 2D MoS_2 utilizing two solid-state precursors (MoO_3 and sulphur), the uniformity level of two types of physically-mixed precursor vapours significantly influences the growth scale and thickness uniformity. Unfortunately, it is more challenging to achieve homogeneously mixed gaseous precursors for MoS_2 growth than the case of graphene, which commonly uses gaseous methane as the precursor. This makes the geometric effect of the precursor gas flow on the growth uniformity even more remarkable. Two routes can be applied to solve this problem. One is to enhance the concentration uniformity of gaseous precursors close to the substrate surface. The other is to decrease the thickness of the boundary layer so that the rate-limiting step can be switched from the mass transport process to the surface reaction process, making the growth results not be dominated by the mixability between two precursors in the gas phase. Loading the substrate vertically with its surface perpendicular to the gas flow direction can simultaneously realize these two optimization goals. It achieves a more uniform precursor spatial concentration on the substrate surface, since the concentration gradient mainly exists in the horizontal direction. Moreover, the thickness of the boundary layer could also be drastically decreased and the penetration of active species through the boundary layer is much faster, because precursor species directly bombard the substrate when the substrate orientation is perpendicular to the gas flow direction. On the contrary, for the horizontal substrate under the same growth conditions, the boundary layer is thicker than the vertical substrate, which leads to a sharp precursor concentration reduction when going through the boundary layer, thus decreasing the amount of precursor species absorbed on the substrate surface and limiting the large-area growth of

2D MoS_2. The MoS_2 grown on the top edge of the horizontal substrate could be attributed to the flow disturbance when the gas flow initially meets the edge of the substrate, which reduces the boundary layer thickness around that region. However, as the migration distance for active species on the surface is limited, the surface precursor concentration will decay sharply along the gas flow direction. This helps explain why the MoS_2 coverage percentage dramatically decreases when moving further downstream along the horizontal substrate. Moreover, even though the precursor concentration in the gas phase can be increased so that the amount of the active species absorbed on the substrate surface can reach the nucleation and growth threshold of MoS_2, the concentration gradient along the horizontal direction is unavoidable and will induce the growth non-uniformity, which has been confirmed by previous reports.(*36*)

4.2.3 Conclusion

In conclusion, I report a simple approach for growing centimetre-scale, high-quality and predominantly monolayer MoS_2 films with large domain sizes, directly on the SiO_2/Si substrate in CVD at atmospheric pressure. The achievement is realized by applying vertically orientated substrate, an additional use of an inner quartz tube to separate MoO_3 with S powder, and an independent temperature control for the growth substrate and the MoO_3 powder, respectively. The film microstructure, thickness homogeneity and quality were characterized by optical microscopy, SEM, Raman spectra, AFM and PL spectra. A systematic study about the nucleation density, thickness uniformity, coverage areas and the crystallinity of the as-grown MoS_2 as a function of the temperature of the MoO_3 powder and the growth substrate, respectively, were conducted. A qualitative kinetic model explaining the merits of loading the substrate vertically was also proposed. This approach has potential to scale up further by increasing the diameter of the reaction quartz tube in the furnace to reach the 4-inch size. By avoiding the use of highly toxic metal organic precursors, our

approach has the potential for industrial compatibility in scale up and easily meets safety requirements for commercial implementation. These results show how sensitive the growth of monolayer materials is to minor variations in the CVD geometry and that drastic improvements can be easily achieved by simple optimizations.

Chapter 5 All CVD Growth of 2D MoS_2/h-BN Vertical Heterostructures

In Chapter 4 I have introduced two APCVD methods to grow isolated domains and continuous films of monolayer MoS_2 directly on the SiO_2/Si substrate, which is the most prevalent substrate due to its great compatibility with the current Si-based electronics. However, its surface is constructed by the 3D-structured amorphous SiO_2, having a relatively low chemical inertness, high charged impurities and inevitably possessing dangling bonds, all of which could degrade the intrinsic properties of monolayer MoS_2 (see section 2.4.3). This inspired me to select a better substrate. At this moment, the insulating 2D hexagonal boron nitride (h-BN), which has the atomic thinness, good flexibility, dangling-bond-free surfaces and high chemical stability, came into my view.

5.1 Introduction

Rapid progress in the research of 2D atomic crystals, such as graphene, monolayer and multilayer h-BN and transition metal dichalcogenides (TMDs), has extended to the fabrication of vertical heterostructures with different types of 2D crystals stacking on top of each other. The flexible and transparent heterostructures compiled by van der Waals stacking of various 2D materials produces novel heterojunctions that have great potential in

electronic and optoelectronic applications.(*127–131*) The layer-by-layer heterostructures were first created by stacking different types of materials through sequential mechanical transfer techniques.(*127*) However, this method is complicated with several disadvantages, such as the contamination at the interface, the low quality of interlayer contact, the high requirements on the position control for different 2D crystals stacking on top of each other, and the lack of future scalable production for large area coverage.(*110*, *127*, *132*, *133*) The direct growth of vertical layered heterostructures *via* chemical vapour deposition (CVD) is much more promising in terms of scalability. Recent advances have demonstrated that vertical heterostructures, such as graphene/h-BN,(*134*) MoS_2/graphene,(*105*) $MoSe_2$/graphene,(*135*) MoS_2/h-BN,(*93*) WS_2/h-BN(*107*), MX_2/SnS_2 (M = Mo, W; X = S, Se),(*136*) and WS_2/MoS_2,(*110*) can be grown by CVD. Growing 2D materials on h-BN exploits the advantage that h-BN has an atomically flat surface without dangling bonds and charged impurities, as well as being chemically inert, which lead to improvements in the device performance and optical properties.(*137*, *138*) However, for CVD-grown TMDs heterostructures on h-BN substrates, there still exist challenges in utilizing CVD grown h-BN, rather than mechanically exfoliated h-BN.

h-BN obtained by mechanical exfoliation has small flake size and therefore is not possible to create large millimetre or centimetre scale heterostructured materials that could be used in large area opto-electronics like solar cells, photodetectors and 2D imaging arrays. Prior work on direct growth of MoS_2/h-BN heterostructures by CVD used organic seeding promoters to help nucleate the MoS_2 on exfoliated h-BN,(*93*) which might remain at the interface between MoS_2 and h-BN after growth and have some influence on the properties of this heterostructures. Ideally, a scalable approach for directly growing seed-free MoS_2 on CVD grown h-BN is needed.

There are several challenges that must be overcome in order to successfully grow a TMD on h-BN by an all-CVD approach. Firstly, the h-BN grown on Cu by CVD needs to be transferred to an alternative substrate, because the S will react the Cu. The transfer of CVD grown h-BN films from Cu to substrates compatible to TMDs growth like SiO_2/Si or sapphire must be clean, with the polymer scaffold used for transfer removed to leave an exposed h-BN surface for direct growth of TMDs. The growth temperature should not be too high, because this will increase the decomposition of the h-BN film before the TMD has been grown. The process should be hydrogen-free, as the introduction of H_2 gas at high temperature will decompose the h-BN film. Residual oxygen in the CVD system, and oxygen species available from the metal-oxide precursor commonly used to grow TMDs is likely to also etch the h-BN during the CVD growth of TMDs.

5.2 Results and Discussion

5.2.1 Experimental Setup

2D MoS_2 crystals are grown on the substrate of CVD-grown h-BN film under atmospheric pressure using MoO_3 (molybdenum trioxide) and sulphur powder as precursors. When attempting to grow MoS_2 on monolayer h-BN films, it was found that the h-BN had been substantially decomposed by the growth process and led to poor samples. This could be due to the oxidation effect from either the oxygen atom in the MoO_3 vapour or the residual oxygen gas in the growth system. Alternatively using few-layer h-BN films (2-4 layers) was ideal because the films were more robust against degradation during the growth and enabled successful deposition of precursor and ultimately the growth of MoS_2 domains on a continuous few layer h-BN film. The steps of A, B and C in **Figure 5.1**a present the fabrication process of the MoS_2/h-BN vertical heterostructures by CVD. The few-layer h-BN film was initially grown on the Cu substrate by CVD using an ammonia borane precursor, and then transferred onto the central area of a bare SiO_2/Si chip by a PMMA-assisted method,

leaving four corners of the substrate as bare SiO_2 surfaces. The PMMA was removed by acetone to leave a relatively clean h-BN (Synthesis and transfer of h-BN was done by Mr. Xiaochen Wang. **Figure A1.** The potential hydrocarbon contamination can desorb from the h-BN surface when heating the h-BN/SiO_2/Si substrate for MoS_2 growth). The substrate with h-BN was subsequently loaded into the CVD system designed for the growth of 2D MoS_2 on the top of both h-BN film and SiO_2. In order to compare the differences between directly growing MoS_2 on h-BN by CVD method with those fabricated by a transfer process, as seen in the steps of A, D, E and F in **Figure 5.1**a, I also did MoS_2/h-BN heterostructures *via* a two-step PMMA-assisted transfer approach. This involved replacing the direct CVD synthesis of MoS_2 (step C) with another transfer process of the CVD-grown 2D MoS_2 crystals from the original SiO_2/Si chip to a new SiO_2/Si substrate having h-BN film covered in the centre and SiO_2 exposed at four corners (step E and F). For the CVD system of MoS_2 growth (**Figure 5.1**b), it mainly inherited the design introduced in section 4.2.2.1, avoiding the cross-contamination between two precursors by adding an inner quartz tube and providing an independent temperature control on MoO_3, S and the growth substrate, respectively. The typical heating temperatures for S, MoO_3 and the substrate were also unchanged, being ~180, ~300 and 800 °C, respectively. Two modifications were made, including (1) loading the face-up substrate horizontally rather than vertically in the tube for reaction (red arrow in **Figure 5.1**b), and (2) adjusting the Ar gas flow rate program by separating the flow rate into two stages, a high flow rate stage (F(Ar) = 150 sccm) and a low one (F(Ar) = 10 sccm). The high flow rate stage was to introduce two gaseous precursors to the reaction zone and make their gaseous concentration approach the nucleation threshold of MoS_2. At the low flow rate stage, the precursor concentration in the gas phase could experience a spontaneous 'ascent-descent' variation procedure. The initial ascent stage may arise from a reduction of the gas flow rate without changing the heating temperature of both

precursor powders, thus making gaseous precursors be less diluted by the carrier gas. However, since the gas flow rate is so small, it cannot fully prohibit the S vapour in the outer quartz tube from diffusing into the inner tube, which led to the gradual quench of the MoO_3 powder. This was consistent with my observation on the colour of the MoO_3 powder after the reaction, which changed from light green to black, indicating a conversion to MoS_2. Therefore, the precursor concentration decreased due to an inactivation of the MoO_3 powder. In brief, the purpose of these two modifications is to generate a concentration gradient of gaseous precursors as a function of both the growth time and the spatial location on the substrate surface, as it facilitates the achievement of monolayer MoS_2 grown on h-BN within the least experimental trials. Such concept of experiment design was also applied in exploring the growth strategy of monolayer MoS_2 on SiO_2/Si substrates (see section 4.1.2.1). A suitable spatial or temporal concentration variation is an advantage at the exploration stage of growing a novel material, as it opens up a wide window which could cover a suitable condition for the synthesis of this material, thus speeding up the progress and making the researcher become one of the pioneers to achieve this novel material. However, such a wide growth window, which, on the other hand, indicates an uncertainty about the best growth condition, should be gradually narrowed and replaced with a stable and uniform growth environment so that a large-area, high-quality and homogenous material can be produced (see section 4.2.2.1). In summary, this simple, scalable CVD growth approach can realize the direct fabrication of a relatively large-area MoS_2/h-BN heterostructures with a clean interface and good interlayer contact, which is advantageous over mechanical transfer method, which will be manifested by comprehensive characterizations.

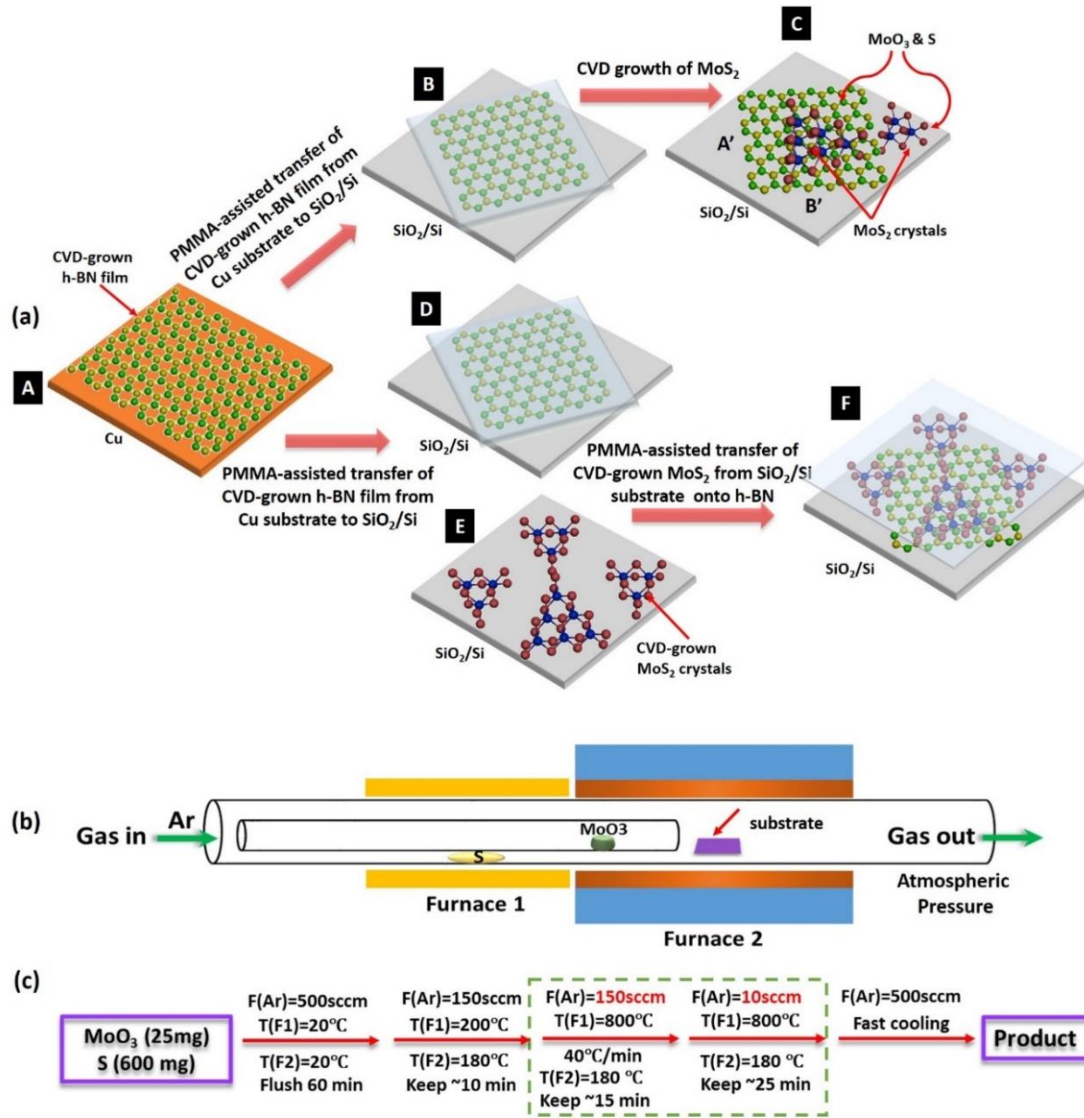

Figure 5.1. (a) Schematic illustration of two fabrication processes of MoS_2/h-BN heterostructures. The first method is initially transferring the CVD-grown h-BN film from a copper foil to the centre of a SiO_2/Si chip, leaving four corners of the substrate to be bare SiO_2 surface. This substrate is then loaded face-up into the CVD system to grow MoS_2 on it. The MoS_2 domains will cover both h-BN and SiO_2 areas. The second approach is through a two-step PMMA-assisted transfer process. The CVD-grown h-BN film was still first transferred onto the centre of a SiO_2/Si chip surface, followed by stacking another layer of CVD-grown MoS_2 domains on the whole substrate surface, obtaining transferred MoS_2 domains on h-BN in the central area and on SiO_2 at four corners. Two of the transfer boundaries of the h-BN film on the SiO_2 surface in the first fabrication method are labelled by the letters of A' and B', respectively. (b) Schematic illustration of the CVD system for MoS_2 growth. The substrate was loaded horizontally rather than vertically with face up in this experiment, as indicated by the red arrow. (c) Flow chart showing the operation steps of growing monolayer MoS_2 on h-BN films. The green dashed box highlights the main differences between this method and the strategy discussed in section 4.2.2.1.

5.2.2 Morphology of As-Grown MoS_2 on h-BN Films

Figure 5.2a,b are optical microscope (OM) images around the transfer boundary of h-BN on SiO_2 showing 2D MoS_2 growth occurs over a large area. The homogeneous colour contrast of MoS_2 domains indicates the thickness uniformity. The 2D MoS_2 crystals grown on the h-BN film exhibit a pronounced higher nucleation density and smaller domain size, compared to those grown on the SiO_2, which may result from the higher roughness of transferred h-BN films on SiO_2 (**Figure A1**c). The small optical contrast from the h-BN film on SiO_2 can be attributed to its negligible opacity in the visible spectrum arising from its large band gap (>5 eV), making it hard to be detected.(*139*) However, the existence of h-BN under 2D MoS_2 has been confirmed by Raman spectroscopy, which will be discussed afterwards. The SEM images (**Figure 5.2**c–j) displays more detailed information, such as the variations of MoS_2 crystal morphology on different substrates. It can be seen that, MoS_2 crystals grown on SiO_2 are not exact triangles with sharp edges as normally observed, but rather are three-pointed star shaped with an average domain size of ~5 µm. For those grown on h-BN, the crystal shape transforms to truncated three-point stars with a flake size decrease to ~3 µm. I interpret the formation of three-point-star-shaped instead of triangular domains of MoS_2 on SiO_2 to the ultra-low Mo:S ratio of precursors absorbed on the substrate, and attribute the crystal shape and size difference between MoS_2 on h-BN and on SiO_2 to the growth rate and time variations arising from different interactions between precursor species and two types of substrate surface.(*100*)

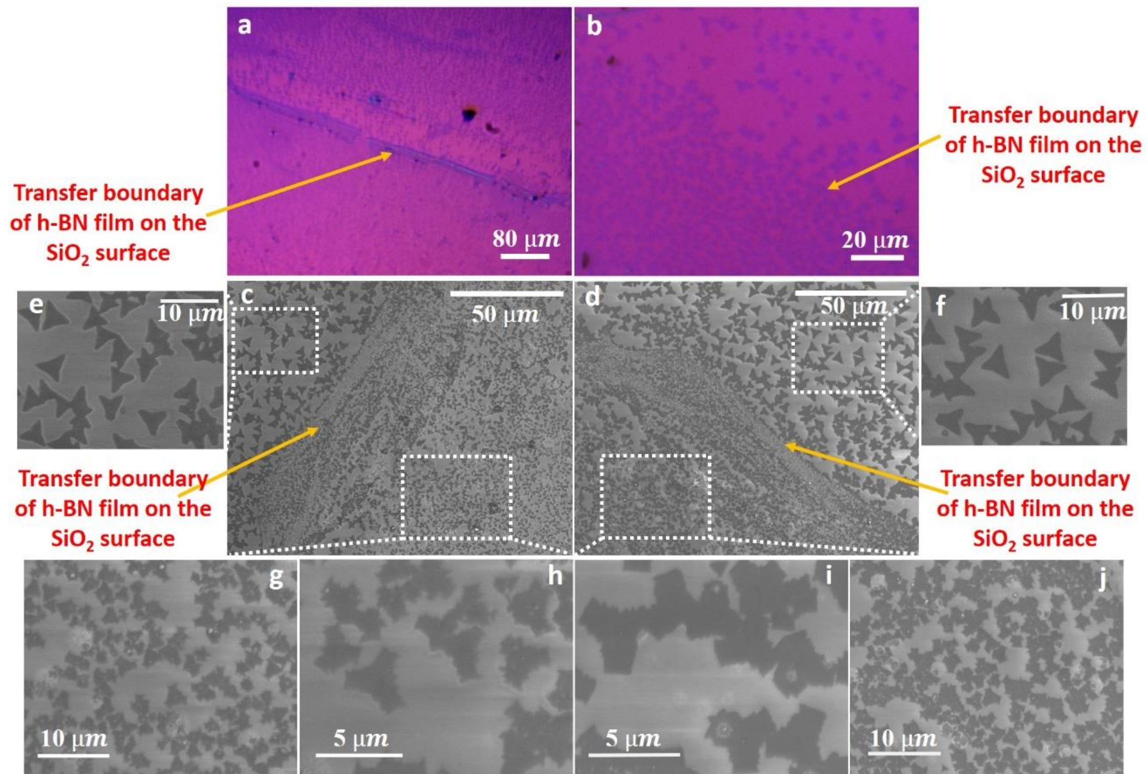

Figure 5.2. (a,b) Optical microscopy images of the edge region of the h-BN film on the SiO_2 surface, showing MoS_2 crystals grown by CVD both on and off the h-BN film. (c,d) SEM images of CVD-grown MoS_2 crystals around the edge region of the h-BN film on the SiO_2 surface marked by letters of A' and B', respectively, in step C of **Figure 5.1**a. (e,f) Zoomed-in SEM images of MoS_2 crystals grown on the SiO_2 in the region of white boxes shown in panels c and d, respectively. (g-j) Zoomed-in SEM images of MoS_2 crystals grown on the h-BN film in the region of white boxes shown in panels c and d, respectively.

5.2.3 Lattice Strain, Doping and Interlayer Contact

Raman spectroscopy is a very useful technique to determine the layer number of MoS_2 by measuring the frequency difference between two characteristic vibration modes, E_{2g}^1 and A_{1g}.(*44*, *51*) The E_{2g}^1 mode represents the in-plane vibration of molybdenum and sulphur atoms, while the A_{1g} mode is related to the out-of-plane vibration of sulphur atoms.(*51*) **Figure 5.3**a shows the Raman spectra of the direct-grown MoS_2 on CVD-grown h-BN film and on SiO_2, respectively, with an excitation wavelength of 532nm. The fitting results show that, for MoS_2 grown on h-BN, these two modes are centred at ~380.6 cm^{-1} and

401.2 cm^{-1}, respectively, while those MoS_2 domains grown on SiO_2 have these two vibration modes located at ~382.4 cm^{-1} and ~402.9 cm^{-1}, respectively, both giving a frequency difference of ~20.5 cm^{-1}. This is compatible with the CVD-grown monolayer MoS_2 in previous works.(*36*, *74*, *93*) **Figure 5.3**b is the measured characteristic Raman peak of CVD-grown h-BN under MoS_2 domains, which is located at ~1372 cm^{-1}, confirming the existence of the h-BN film after experiencing the growth process of MoS_2. A line scan was also carried out, measuring the Raman spectrum point-by-point for the characteristic h-BN vibration mode across a transfer boundary of h-BN film on SiO_2, marked by the dashed black line in **Figure 5.3**c. **Figure 5.3**d shows a plot of the integrated h-BN Raman peak as a function of distance, and it rapidly disappears in the central region. It confirms that this region is the edge of the transferred h-BN film on SiO_2 and **Figure 5.3**e,f shows examination of the boundary region.

The peak location variations of both modes were also observed, when MoS_2 were grown on different substrates. In **Figure 5.3**a, compared to the Raman spectra of MoS_2 grown on SiO_2, a pronounced phonon mode stiffening reflected with the blue-shift of both E_{2g}^1 and A_{1g} peaks can be observed for MoS_2 grown on h-BN. The variations are measured to be ~1.8 cm^{-1} and 1.7 cm^{-1} for E_{2g}^1 and A_{1g} mode, respectively. I also performed Raman mappings around the region of a transfer boundary, where half of the mapping area had the monolayer MoS_2 grown on the h-BN film and another half had MoS_2 on SiO_2 (**Figure 5.3**c). By plotting the 2D spatial variation of the magnitude of E_{2g}^1 and A_{1g} peak frequency separately (**Figure 5.3**e,f), it can be found that the frequency difference for these two characteristic vibration modes depending on the growth substrate is ubiquitously observed on the sample. Furthermore, I also investigated the substrate effect on transferred CVD-grown MoS_2 domains on these two types of material, h-BN film and SiO_2, *via* a two-step PMMA-assisted transfer method (steps A, D, E and F in **Figure 5.1**a). It was found that the

MoS_2 on h-BN and on SiO_2 had the E_{2g}^1 peak centred at almost the same wavenumber, while the A_{1g} mode of MoS_2 on h-BN appeared a slight blue-shift in a value of ~0.7 cm^{-1}, compared to that of MoS_2 on SiO_2 (**Figure 5.4**a). This phenomenon can also be commonly observed on the sample by comparing the Raman mapping of frequencies for these two characteristic modes of MoS_2 on h-BN and on SiO_2, respectively (**Figure 5.4**c–f). **Figure 5.4**b shows the characteristic Raman vibration mode of the h-BN film lying underneath the transferred MoS_2 domains, which is measured to be at ~1368 cm^{-1}.

In addition to distinguishing the number of layers, Raman spectra can also be utilized to investigate other effects such as lattice strain, doping levels and the van der Waals interaction at the interface for 2D crystals.(*59*, *68*, *69*, *72*, *76*, *140*, *141*) The in-plane Raman mode, E_{2g}^1, is sensitive to the built-in strain of 2D MoS_2,(*59*, *72*, *76*, *142*) and therefore, the E_{2g}^1 peak position variation of ~1.8 cm^{-1} observed in **Figure 5.3**a can be attributed to the different strain effect in monolayer MoS_2 grown on h-BN and on SiO_2. In order to determine the MoS_2 lattice strain on these two types of substrates, I used the same growth method to produce MoS_2 on a bare SiO_2 substrate followed by measuring its Raman spectra, and then transferred these MoS_2 domains onto another SiO_2 substrate, and measured the Raman spectra again. The transfer process is aimed at releasing the potential strain existing in the direct-grown MoS_2 crystals. It was found that the E_{2g}^1 mode of transferred MoS_2 crystals showed a blue-shift of 1.7-2.0 cm^{-1}, compared to the direct-grown ones on SiO_2, while the A_{1g} peak position remained unchanged (**Figure 5.5**).

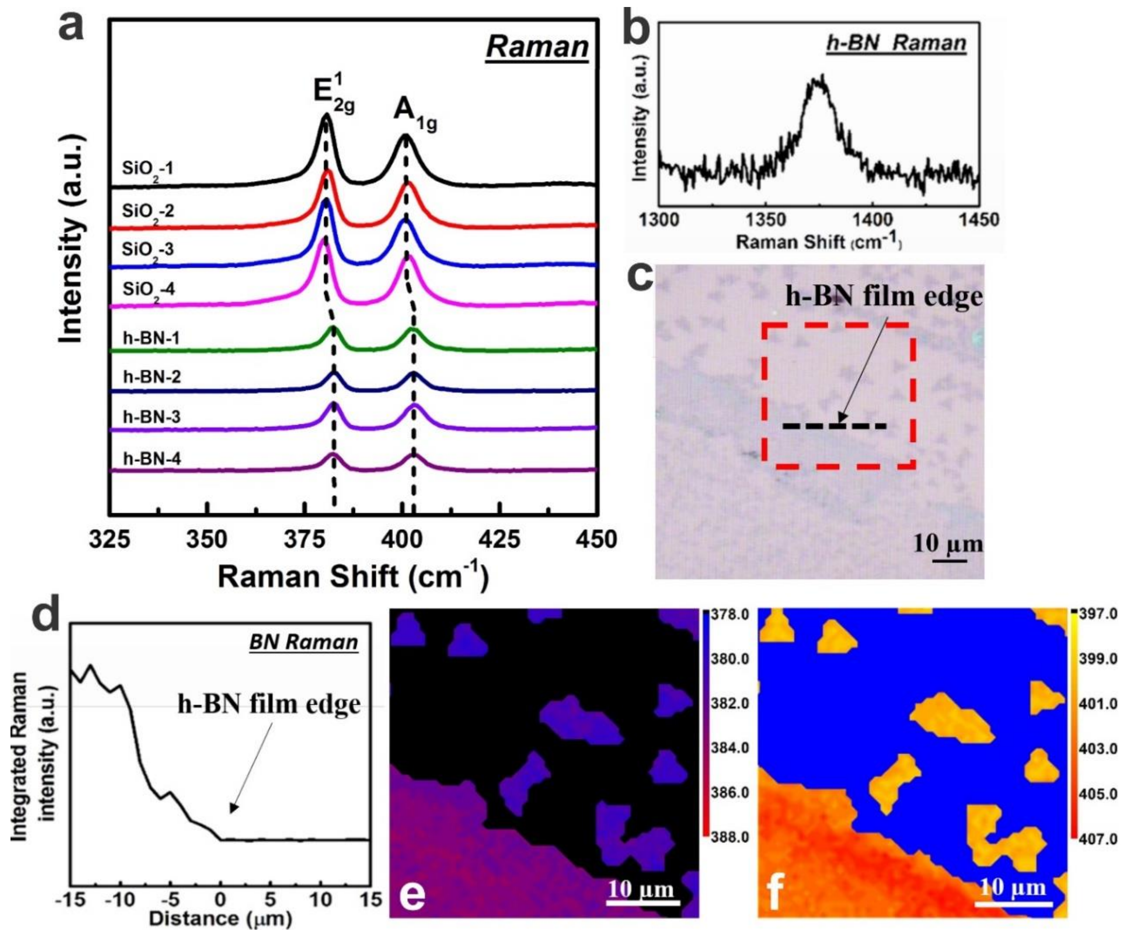

Figure 5.3. (a) Raman spectra collected from eight different MoS_2 domains grown on two types of substrate, four of which are grown on the SiO_2 surface, another four are grown on the h-BN film. (b) Raman spectra measured from the h-BN film under the directly grown MoS_2 crystals. (c) Optical image showing the MoS_2 crystal growth around the region of the transferred h-BN film edge. (d) A plot of the integrated h-BN Raman peak intensity as a function of distance, which was measured across the edge of the h-BN film, marked by a black dashed line in panel c. The point on the curve which is indicated by a black arrow corresponds to the location of the h-BN film edge in panel c, as the integrated h-BN Raman peak disappears from this point. (e,f) Raman maps of direct-grown MoS_2 domains on different substrates, plotting the spatial variation of the peak position for $E_{2g}{}^1$ and A_{1g} mode, respectively, in the area of the red box marked in panel c, where the upper right region has the substrate of SiO_2 and the left bottom area has the substrate of h-BN.

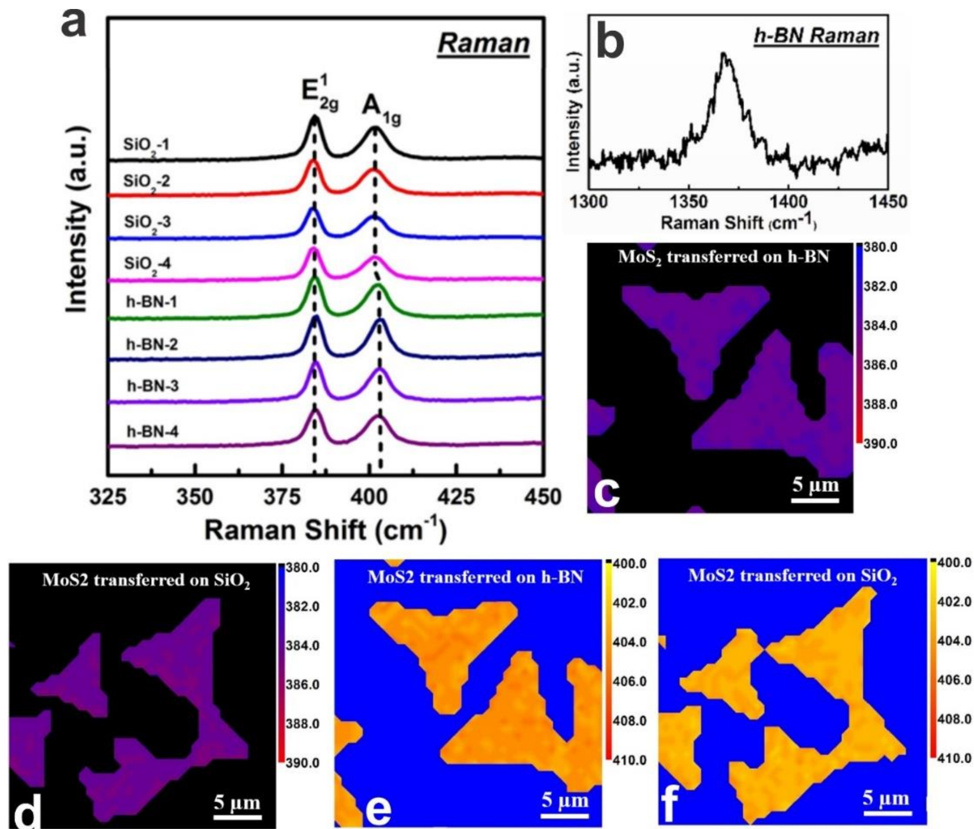

Figure 5.4. (a) Raman spectra collected from eight different MoS_2 domains transferred on two types of substrates, four of which are transferred on the SiO_2 surface, another four are transferred on the h-BN film. (b) Raman spectra measured from the h-BN film under the transferred MoS_2 crystals. (c–f) Raman maps of the peak position for E_{2g}^1 and A_{1g} mode, respectively, of transferred MoS_2 domains on different substrates, h-BN and SiO_2.

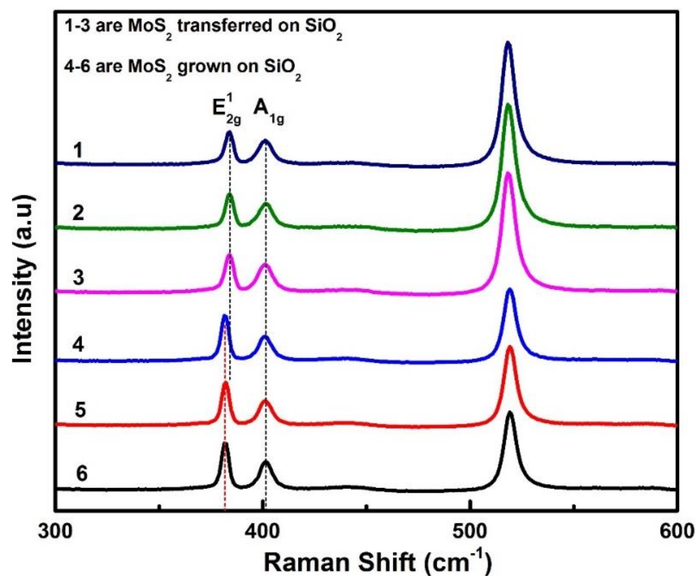

Figure 5.5. Raman spectra collected from six different MoS_2 domains on the substrate of SiO_2/Si. Spectra 1-3 were measured from the transferred crystals, while spectra 4-6 were obtained from direct-grown ones on the SiO_2/Si chip.

The biaxial lattice strain in the direct-grown MoS_2 domains can be calculated by applying the equation of $\varepsilon = \frac{\omega - \omega_0}{2\gamma w_0}$,(*69*, *143*, *144*) where ω and ω_0 are the Raman wavenumber at finite strain and zero strain, respectively, γ is the Gruneisen parameter of E_{2g}^1, and ε is the biaxial strain. Given that the Gruneisen parameter of E_{2g}^1 mode is 0.54(*145*) and the initial wavenumber of 383.8 cm^{-1}, I determined that the monolayer MoS_2 crystals grown on SiO_2 suffered a biaxial lattice tensile strain of ~0.45%, in agreement with the previous reports on CVD-grown monolayer MoS_2 on the same substrate.(*76*, *146*) Considering that the monolayer MoS_2 grown on h-BN has a ~1.8 cm^{-1} blue-shift of E_{2g}^1 mode, which is quite similar to the frequency variation (1.7-2.0 cm^{-1}) between the strain-free transferred MoS_2 and the direct grown MoS_2 on SiO_2, it indicates that using the CVD-grown h-BN film as a substrate can lead to a much smaller lattice strain in monolayer MoS_2 grown above, which may arise from the weak van der Waals force at the interface of MoS_2/h-BN heterostructures, making the lattice strain easier to release. This conclusion is further supported by the negligible frequency difference of E_{2g}^1 mode between transferred monolayer MoS_2 located on h-BN and on SiO_2, indicating that E_{2g}^1 mode is barely affected by other factors, such as substrate materials, doping levels, interlayer contact, *etc*., except for the built-in strain. In terms of A_{1g} mode, which is associated with the doping level, a stiffening of it in a value of ~1.7 cm^{-1} for MoS_2 grown on h-BN film, compared with that on SiO_2 can be attributed to the reduced electron density in monolayer MoS_2.(*71*, *147*) Compared with SiO_2, h-BN is known to have a much lower degree of charged impurities, which can decrease the doping level of the above 2D MoS_2, since there will be less charge transfer from the substrate to MoS_2 through the interface, consistent with recent studies.(*65*, *148*, *149*) The A_{1g} peak frequency difference between MoS_2 on h-BN and on SiO_2 drastically decreases from ~1.7 cm^{-1} to ~0.7 cm^{-1}, when this contact mode is realized by the transfer process instead of direct growth. As aforementioned, there is no change on the A_{1g} peak

position between the direct-grown and the transferred monolayer MoS_2 on SiO_2. This means that, through the transfer process, the blue-shift magnitude of A_{1g} mode for MoS_2 on h-BN obviously reduces. This could result from two reasons, one is the contamination from different kinds of solvents used during transfer, which spoil the clean interface and increase the doping effect,(*147*) another possible reason is the lower quality of interlayer interaction between monolayer MoS_2 and the h-BN film underneath, which may arise from the higher surface roughness of CVD-grown h-BN film transferred on SiO_2, compared with the bare SiO_2 surface.(*69*)

However, as the laser-induced thermal effect can change the anharmonicity in the lattice potential energy of MoS_2, having an influence on both E_{2g}^1 and A_{1g} mode, (*69*, *150*, *151*) one may argue that, in our experiment, the shift could also be produced by a laser-induced temperature contribution. In order to exclude any thermal effects, all the experimental conditions used in each Raman measurement was set to be constant, so that the thermal effect would be approximately the same for different samples. Furthermore, I did a comparison experiment by decreasing the acquisition time from 2s to 0.5s accompanied by a reduction on the number of spectra averaged for signal-to-noise enhancement from 2 to 1, it was found that there was no obvious shift on the position of both E^1_{2g} and A_{1g} peak (**Figure 5.6**), which indicates that the laser-induced thermal perturbation in our experiment can be ignored.

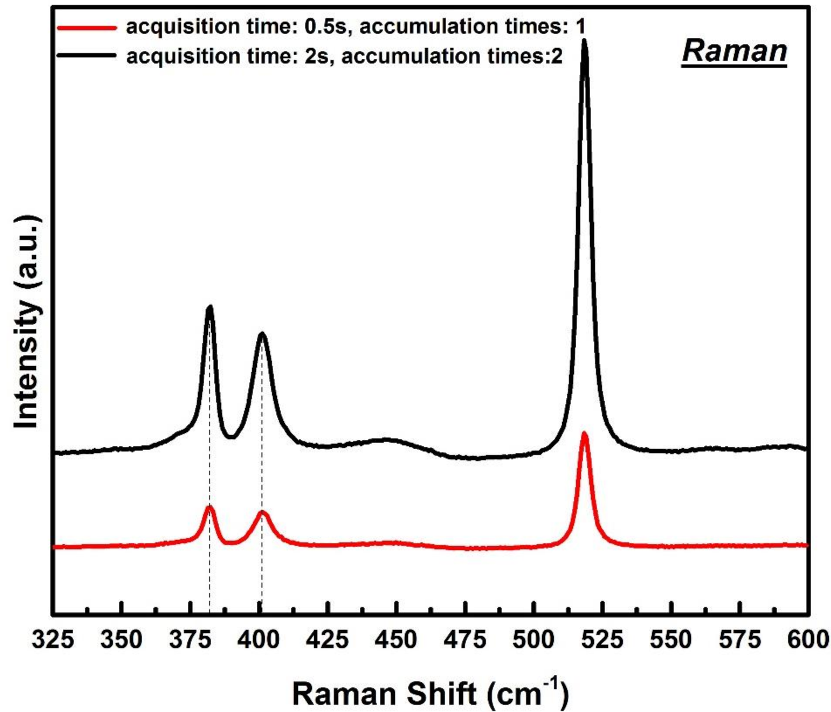

Figure 5.6. Raman spectra of transferred MoS_2 domains on the SiO_2 with different acquisition time and the number of spectra averaged, defined as 'accumulation times' in the figure.

The peak intensity as well as the intensity ratio between A_{1g} and E_{2g}^1 also shows slight differences for MoS_2 on different substrates. For transferred samples, the Raman intensity for both vibration modes of MoS_2 on h-BN appears stronger with a slightly higher intensity ratio of A_{1g}/E_{2g}^1, compared to that of MoS_2 on SiO_2 (**Figure 5.4**a). This could arise from the substrate-induced interference effects, as the absorption and the emission intensities can be strongly modulated by the interference within different types of substrates.(*68*) However, for the direct-grown MoS_2 on h-BN, even though the A_{1g}/E_{2g}^1 intensity ratio is still higher than that of the direct-grown MoS_2 on SiO_2, in agreement with the phenomenon observed in the transferred samples, the intensities of both characteristic modes decrease drastically (**Figure 5.3**a). This could possibly be due to two reasons. One is the smaller MoS_2 domain size, which makes the precise focus of laser spots onto MoS_2 crystals under optical microscope to be more difficult. The other reason is the higher roughness of monolayer MoS_2 domains grown on h-BN film, since the contact quality

between the direct-grown MoS_2 and h-BN film is higher than the transferred one, making the directly grown MoS_2 conform to the rougher landscape of the transferred h-BN film underneath. The lower quality of the laser beam focus as well as the fluctuation of the domain surface could both result in the decrease of the signal intensity for a confocal Raman apparatus.

Next, I investigated the photoluminescence (PL) of monolayer MoS_2 in different conditions. The PL spectra are normalized against the Raman intensity to show the relative luminescence quantum efficiency between different samples.(*44*) As depicted in **Figure 5.7**a, for the PL spectra of transferred MoS_2 on either h-BN or SiO_2 and the direct-grown MoS_2 on h-BN, which have been proved to be almost strain-free in the lattice, there are mainly three sub-peaks, located at ~625 nm (1.98eV), ~670 nm (1.85eV) and ~680 nm (1.82eV), respectively, which constitute the whole PL spectra of MoS_2. The peak at ~670 nm is contributed by the neutral exciton emission from the direct transition at the K point (denoted as A or A1 excitation in different literatures), while the peak at ~625 nm arises from exciton emission from another direct transition between the conduction band and a lower lying valence band (denoted as B or B1 excitation in different literatures).(*44*, *59*) However, the MoS_2 is easy to be unintentionally negatively doped, when it is contaminated with some types of solvent, or is just placed on SiO_2, which provides a relatively high level of trapped donors on the surface.(*42*, *147*) Then, a third peak, located at lower energy than A peak, emerges, and it can be associated with the recombination of negatively charged excitons of A (trions, A^-), that is, a free electron bound to a neutral exciton *via* Coulomb interaction. Compared with the literature data, the observed three sub-peaks in our PL for strainless MoS_2 correspond to the aforementioned B, A and A^- excitonic transition modes, respectively.(*55*, *65*, *68*, *152*) The energy difference between A and A^- at room temperature, which is ~30–40 meV, arises from the large binding energy of the second electron in A^-. (*55*)

I further extract quantitative information of three types of strainless MoS_2 by fitting the data to Lorentzian or Voigt functions with three peaks located at photon energy corresponding to B, A and A^- excitonic species (**Figure 5.7**c–e). Since the detailed peak shape could be determined by various factors, including lifetime broadening, thermal effect, collision and dopants, which lead to different spectral line shapes, various fitting functions, including Gaussian, Lorentzian and Voigt were applied to find the best fitting results. The results show a difference in integrated PL intensity ratio between A and A^- (A/A^-), indicating that the relative populations of neutral to charged A excitons is affected by the doping level of MoS_2. The higher the doping level is, the lower this ratio will be. It was found that the MoS_2 directly grown on h-BN has the highest A/A^- (~ 6.7), followed by transferred MoS_2 on h-BN (~ 2.4) with transferred MoS_2 on SiO_2 (~ 1.3) being the lowest. This observation further reveals the high degree of charged impurities for SiO_2, in agreement with the study on Raman A_{1g} mode above, and the contaminations introduced *via* transfer process, which can also increase the doping level of MoS_2, making the transferred MoS_2 have a significantly lower A/A^- than the direct grown one even on the same substrate material of h-BN film. Moreover, in **Figure 5.7**a, for direct-grown MoS_2 on SiO_2, its PL peak corresponding to the direct transition at the K point experiences a redshift to ~686 nm, leading it to be in an even lower energy than the A^- transition mode of the strain-free MoS_2. The PL softening phenomenon has been interpreted as a signature of the tensile strain existence in MoS_2 lattice, which is well compatible with the analysis of Raman E_{2g}^1 mode aforementioned and other recent studies, because it has been reported that both the tensile strain can not only affect Raman modes but also reduce the band gap of monolayer MoS_2, leading to a redshift on its A excitonic transition mode.(*59*, *143*)

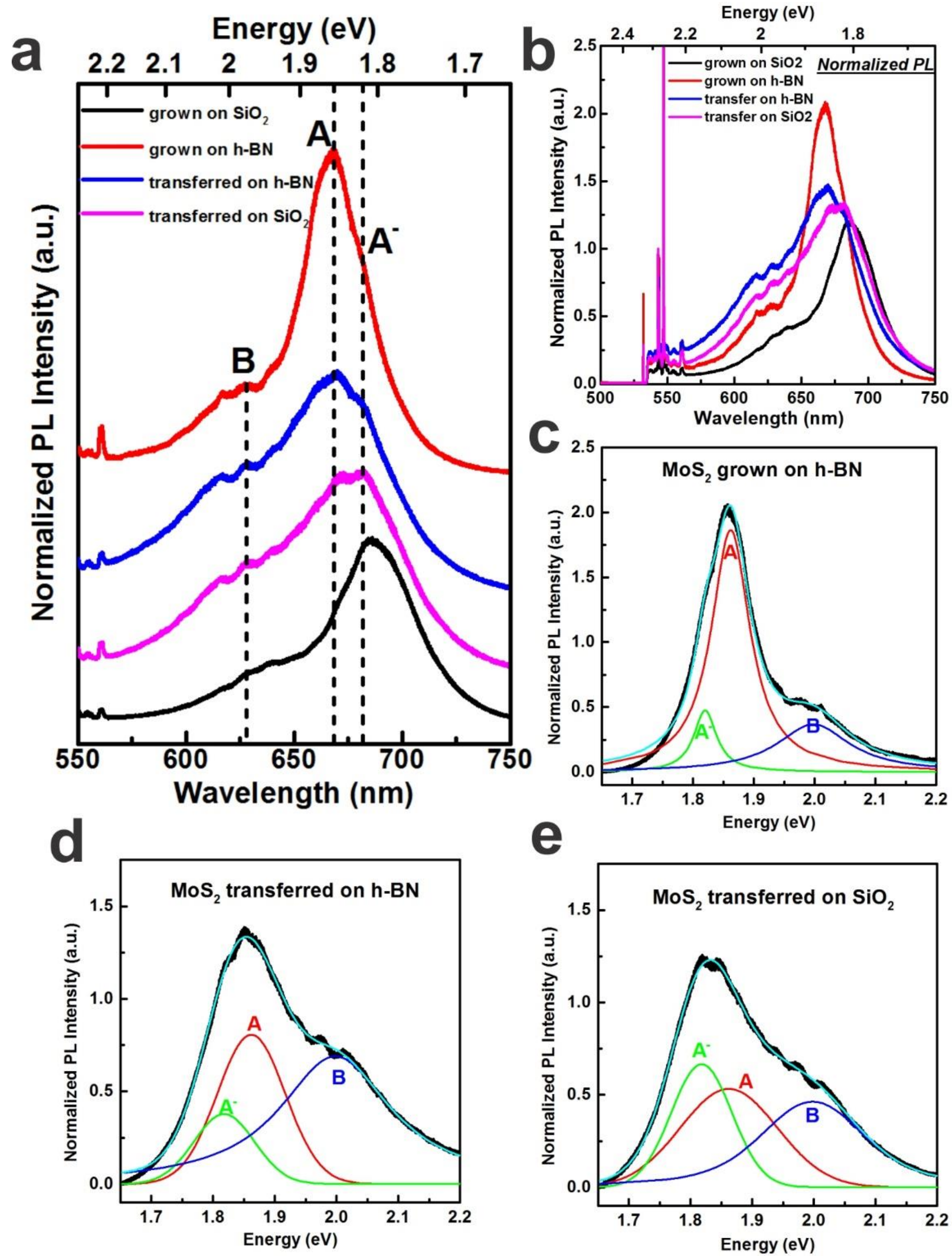

Figure 5.7. (a) PL spectra of the direct-grown and transferred MoS_2 on h-BN and SiO_2, respectively, which highlights the peak shape and location variation. Both the wavelength and the photon energy of peaks are given, as shown in the bottom and top x axis, respectively. The dashed black lines indicate the positions of three main peak emissions, B excitonic transition (B), the neutral excitonic transition of A (A) and the charged excitonic transition of A (A^-), which can be easily found in the PL of strain-free MoS_2 domains, including the direct-grown MoS_2 on h-BN and the transferred MoS_2 on either h-BN or SiO_2. (b) PL spectra of the direct-grown and transferred MoS_2 on h-BN and on SiO_2, respectively, normalized by the MoS_2 Raman intensity to highlight the PL intensity variation. (c–e) Fits to the PL peak of strain-free MoS_2 with three sub-peaks corresponding to A, A^- and B, respectively.

As seen in **Figure 5.7**b, the direct-grown MoS_2 on h-BN has a stronger PL intensity with narrower FWHM (full width at haft maximum) than both transferred samples and direct-grown MoS_2 on SiO_2, indicating the higher crystallinity of the direct-grown MoS_2 on h-BN with a clean interface and a lower level of charged impurities. It is worth noting that the PL intensity of transferred MoS_2 on h-BN and on SiO_2 is similar, which means the substrate of h-BN does not show obvious advantage to SiO_2 when the contact between MoS_2 domains and substrates is realized through the transfer process instead of direct CVD growth. This could be due to the heavy doping effects on MoS_2 from solvent contaminations in the transfer, which covers up the superiority of the low charged impurity level of h-BN compared with SiO_2. This phenomenon further highlights the merits of using CVD approach to fabricate such MoS_2/h-BN heterostructures.

5.3 Conclusion

In summary, I have demonstrated the fabrication of high quality MoS_2/h-BN vertical van der Waals heterostructures through the direct CVD growth of monolayer MoS_2 on h-BN films. The large area h-BN films grown by CVD on copper was utilized, which were then transferred onto the SiO_2/Si substrates. Based on the analysis of Raman and PL spectra, I found that the direct CVD-grown MoS_2 crystals on the h-BN film suffered smaller lattice strain and lower doping levels than those directly grown on SiO_2 (**Figure 5.8**). This led to a higher percentage of exciton recombination compared to trion recombination. In addition, this direct vapour phase growth of MoS_2/h-BN heterostructures also had reduced contamination and led to better interlayer interactions at the interface, compared to those obtained *via* layer-by-layer polymer-assisted transfer methods. This direct and versatile fabrication approach of MoS_2/h-BN heterostructures may have potential in electronic and optoelectronic applications and open up the possibility to create other types of TMDs/h-BN ($MoSe_2$/h-BN, $MoTe_2$/h-BN, WSe_2/h-BN, ReS_2/h-BN, *etc.*) heterostructures.

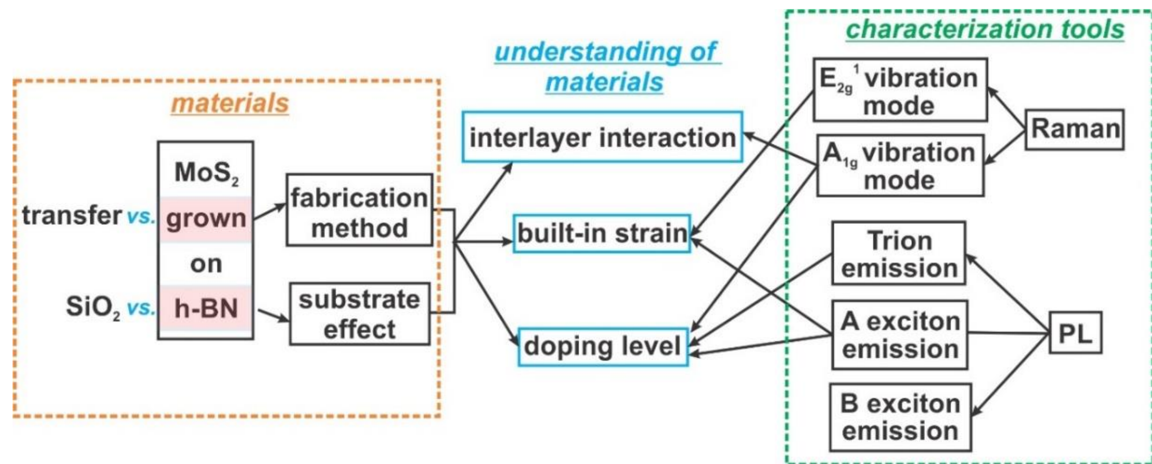

Figure 5.8. Schematic illustration showing how to build a bridge between the synthesized material and their properties through proper employment of characterizations in this work.

Chapter 6 Line Defects in Monolayer MoS_2

Over the preceding two chapters I have systematically investigated the CVD growth strategies of monolayer MoS_2 domains/films on 3D amorphous SiO_2 substrates and 2D h-BN films, respectively. By studying and comparing the optical and vibrational properties of MoS_2 on various substrates using Raman and PL spectroscopy, it helps me comprehend some commonly encountered factors, such as doping and lattice strain, which can impact the intrinsic properties of MoS_2.(*54*, *59*, *153*, *154*) However, a direct observation of the structure of monolayer MoS_2, which provides the most intuitionistic knowledge of this material and opens the door for its property engineering from the bottom level, is still lacking in this project. Therefore, from this chapter, I will fill this gap by employing the aberration-corrected TEM (AC-TEM) to observe the lattice configuration of monolayer MoS_2 down to the atomic level and utilizing the electron beam in the TEM as an ultrafine probe to change the pristine lattice periodicity of this 2D crystal, thus manipulating its properties.

6.1 Introduction

It is known that structural imperfections in graphene, such as point defects, dislocations, edges and grain boundaries, can impact its chemical, mechanical, optical and electronic properties. The effects can be beneficial, such as providing active bonding sites for absorbed atoms and molecules in controlled chemical reactions, or detrimental, such as

decreasing the charge carrier mobility for graphene-based field-effect transistors.(*39*, *155*) There have also been several reports concerning defects in monolayer MoS_2 and the TMDs family in general. For example, a unique class of trefoil-like point defects formed by 60° rotations of metal-chalcogen bonds has been recently discovered, which could give rise to p-type doping and local magnetic moments.(*156*) In addition, due to the flexibility of coordination characteristics for both transition metal and chalcogen atoms, a variety of grain boundaries composed of a series of dislocation cores having 5|7, 4|4, 4|6, 4|8, and 6|8 fold rings have been discovered. Some of these defect structures are predicted to be one-dimensional conductive channels embedded in the intrinsic trigonal prismatic lattice, providing exciting opportunities to tailor local properties of monolayer MoS_2.(*29*, *37*, *157*) All these examples offer successful paradigms of adjusting monolayer MoS_2 properties through defect engineering (see section 2.2.2 and 2.2.3).

Electron beam irradiation can create defects in 2D materials, due to either a 'knock-on' effect, ionization or beam-induced chemical etching, facilitating the sculpting of 2D membranes with high spatial accuracy and flexible pattern design.(*158*, *159*) A recent study showed that 60° grain boundaries around vacancy-induced inversion domains on TMD monolayers can be generated artificially by a proper dose of electron irradiation.(*38*) The electron beam in the (scanning) transmission electron microscope can be utilized not only as an imaging tool but also as a probe for precise nanostructure fabrication. Theoretical calculations reported that the displacement threshold of S atoms in a pristine MoS_2 lattice is ~ 6.5 eV, similar to the maximum knock-on energy transferred from 80 keV electrons to S atoms.(*32*, *34*) Therefore, a prolonged electron beam illumination on monolayer MoS_2 under 80kV can produce large amounts of S vacancies. In contrast, bond rotations similar to Stone–Wales defects in graphene, need much higher formation energy and are not favourable in MoS_2 under this imaging condition at room temperature.(*156*) The isolated S vacancies are

prone to agglomerating into line defects of various geometries, which are different from the defect structures produced in graphene.(*35*, *160*) Although line defects in transition metal dichalcogenides have been imaged before by AC-TEM, the spatial resolution was not sufficient to accurately resolve the positions of all S atoms within the defect structure and provide direct insights into the detailed S bond lengths and reconstructions.(*35*) The details of subtle lattice reconstructions in line defects in monolayer MoS_2, such as the bond length changes and S atom positions are needed for precise theoretical predictions of its electronic and magnetic properties.

In this chapter, a combination of atomic resolution imaging by AC-TEM and density function theory (DFT) calculations is used to systematically study the lattice reconstructions associated with line defects in MoS_2 (**Figure 6.1**). I provide detailed information about bond length changes and 2D strain field variations for line defects as a function of their length and width, as well as a prediction on the band structure evolution from semiconducting to metallic as the line defect broadens in width.

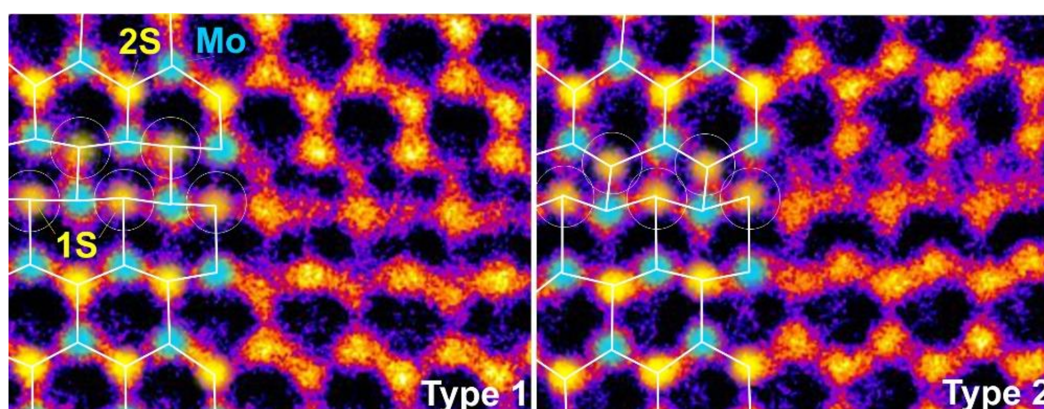

Figure 6.1. AC-TEM images showing two typical kinds of lattice reconstructions in double sulphur vacancy lines (2SVL) of monolayer MoS_2.

6.2 Results and Discussion

6.2.1 Structure and Dynamics of Sulphur Vacancies

Monolayer MoS_2 is produced by chemical vapour deposition growth using my previously reported method in Chapter 5. Samples are transferred to Si_3N_4 TEM grids with 2 μm holes using a polymer support layer that is removed to leave suspended monolayer MoS_2 regions. AC-TEM imaging is performed using an accelerating voltage of 80kV, which has sufficient energy to produce S vacancies. The spherical aberration of the electron beam is corrected, which provides a high spatial resolution of the TEM image and increases the ability to resolve the position of atoms (see **Figure 3.4**c). Single S vacancies (SV) and double S vacancies (DV) are the two simple point defects produced in monolayer MoS_2 under electron beam irradiation, shown in **Figure 6.2**a-d.

Bond length measurements in the SV region were obtained using boxed line profiles along three armchair directions starting from one SV site in **Figure 6.2**e, spanning four atoms in projection as S-Mo-2S-Mo, which is schematically illustrated in **Figure 6.2**i. The distance between atoms is determined by fitting double Gaussians and measuring the distance between Gaussian peak positions(*161*), with the distance scale calibrated by measuring Mo-S bonds in a pristine region of MoS_2 lattice. The distances measured between atoms in the AC-TEM image are the 2D projected distances of MoS_2. The deviations of bond lengths between S-Mo and 2S-Mo in three armchair directions for the SV are almost negligible and are close to the standard 2S-Mo distance measured in 2D projection (~1.8 Å). Small fluctuations in the distance are attributed to the influence of other SVs around the area and are within the noise level of the measurement (labelled by white circles in **Figure 6.2**e).

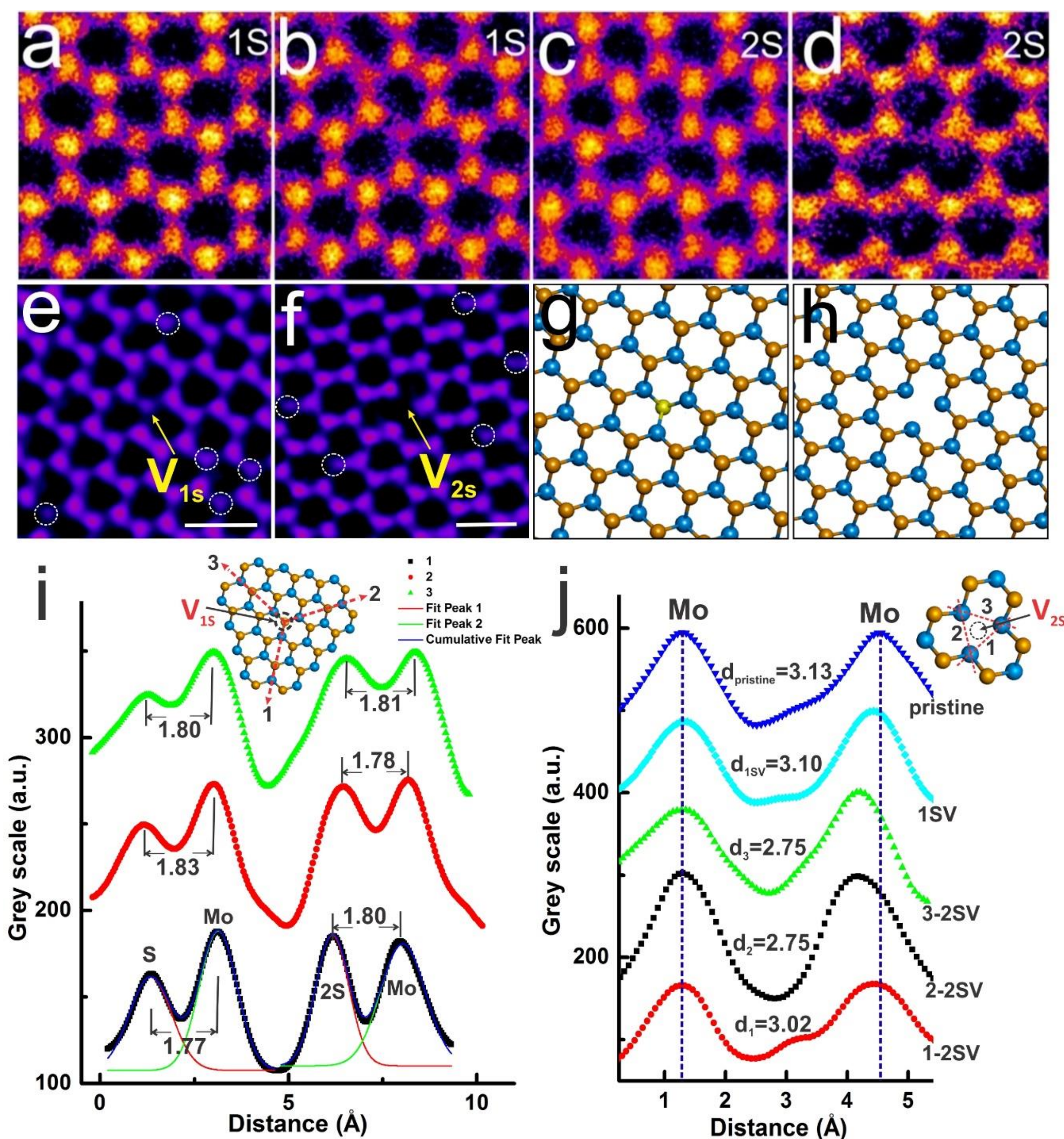

Figure 6.2. (a,b) Typical AC-TEM images of SV in MoS_2. (c,d) Typical AC-TEM images of DV in MoS_2. (e-f) AC-TEM images of SV and DV, represented as V_{1S} and V_{2S}, respectively. The typical examples that are used to conduct bond length measurements in (i,j) have been highlighted by yellow arrows. The distribution of other single S vacancies around are marked by white circles. (g, h) DFT-calculated atomic models for SV and DV, respectively, in a pristine monolayer MoS_2 lattice. (i,j) Intensity line profiles at SV and DV shown in (e,f), respectively, along directions indicated by red arrows in the schematic diagrams in each panel. Scale bar corresponds to 0.5nm in all panels.

For the DV in **Figure 6.2**f, the loss of two S atoms causes the distance between the three neighbouring Mo atoms to be reduced by 12% from a value of 3.13 Å in the pristine lattice to 2.75, 2.75 and 3.02 Å, (labelled 1, 2 and 3, respectively) (**Figure 6.2**j). The Mo-

Mo bond contraction along three zigzag directions in the DV is not purely isotropic and I attributed this to the random distribution of other SVs around DV (marked by white circles in **Figure 6.2**f), exerting anisotropic influence on the lattice configuration at the DV site. This effect is supported by the DFT calculations (**Figure B1**). In comparison, the Mo-Mo bond lengths around the one missing S atom in the SV were all measured as ~3.10 Å, which is close to the pristine value and indicates negligible compression.

Prolonged electron beam irradiation causes the concentration of point defects to increase, with a tendency to initially aggregate into small clusters and then form extended line defect networks (**Figure 6.3**a–c). **Figure 6.3**d shows the detailed lattice structure corresponding to the early stage of vacancy agglomeration, where isolated point defects begin to migrate and gather into small clusters and short lines in different geometries, indicated by white circles and lines. As the size of the vacancy cluster grows, the amount of bond reconstruction increases, as shown in the red and yellow circles in **Figure 6.3**d. The defect clusters primarily adopt linear geometry, which is different to graphene defect clusters at room temperature. These line defects have a certain length along the zig-zag direction determined by the number of missing S atoms, but can also grow across more than one zig-zag lattice line to obtain width in the armchair direction. The width of a line defect is essentially the number of adjoining parallel S vacancy lines (n), and denoted as nSVL. Some S point defects agglomerate into ultra-short 1SVL, 2SVL and 3SVL, as shown in **Figure 6.3**e–g, respectively, and become the nucleation of future extended line defects.

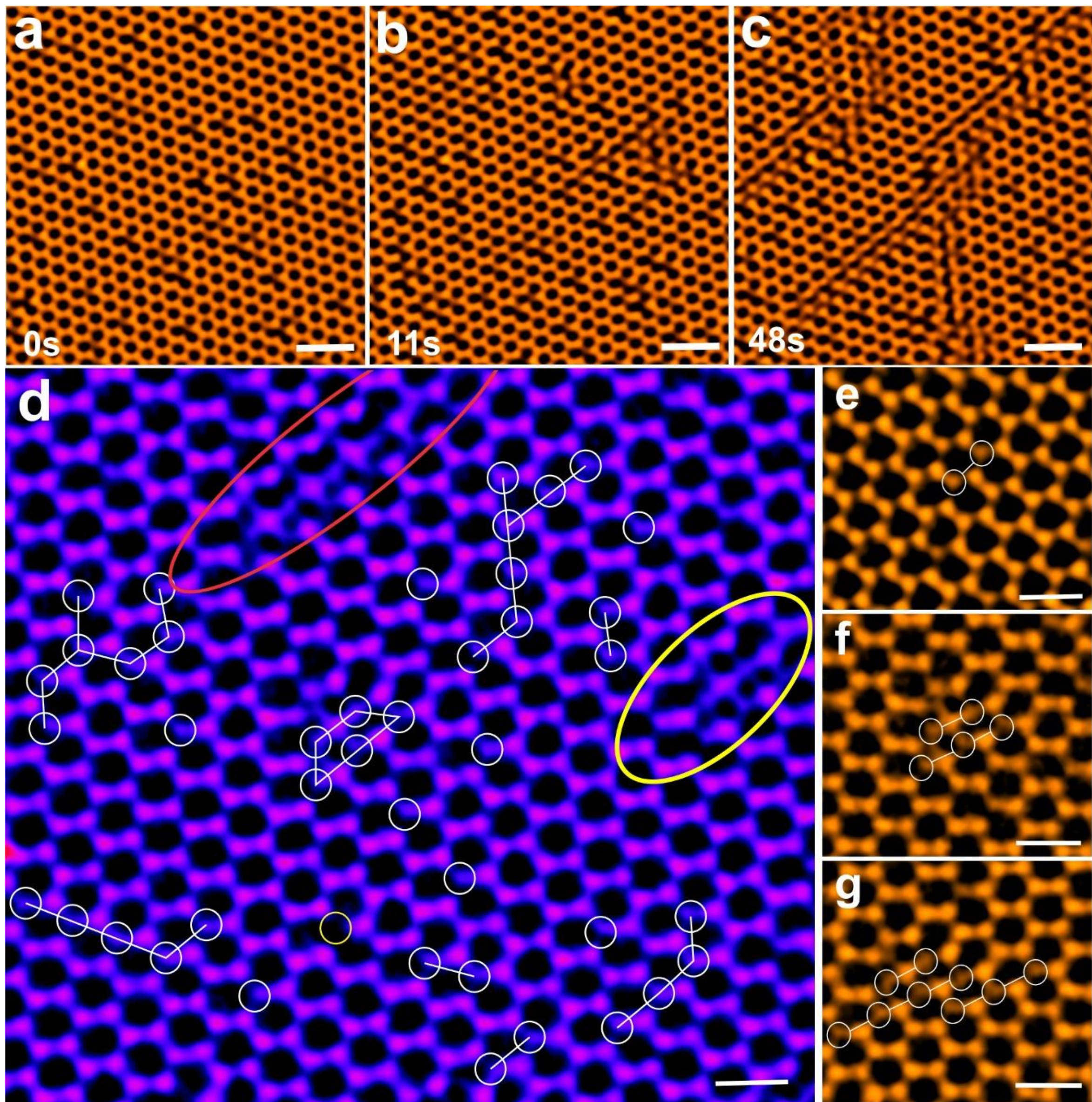

Figure 6.3. (a-c) Sequence of AC-TEM images showing isolated S vacancies aggregating into extended line defects under a continuous electron beam illumination at an accelerating voltage of 80 kV. All scale bars correspond to 1nm. (d) AC-TEM image showing detailed configurations of agglomerated S point defects into lines in different geometries, varying in length and width, which are marked by white circles and lines. The red and yellow ellipses show two line defect examples that both have two parallel S vacancy lines aggregated but in different lengths, which show a detectable variation on the lattice contraction level along the armchair direction. The scale bar corresponds to 0.5nm. (e-g) AC-TEM images of three typical examples of short 1SVL, 2SVL and 3SVL, respectively, which can be seen as the nucleation of extended line defects. All scale bars correspond to 0.5nm.

6.2.2 Lattice Reconstructions of Sulphur Vacancy Lines

In **Figure 6.4**, I examine the changes in bond reconstruction as a function of length for a 1SVL line defect in more detail. **Figure 6.4**a–d are a series of AC-TEM images showing line defects of having only one line of single S vacancies (1SVL) but with lengths varying from 2 to 7 SVs (marked by white circles in **Figure 6.4**a–d). **Figure 6.4**e shows the atomic model obtained from the DFT calculation in both the 2D projection (top-down view) and side view based on **Figure 6.4**d. A multislice image simulation based on the atomic model shown in **Figure 6.4**e is presented in **Figure 6.4**f and matches the experimental image. DFT calculations indicate that having the S vacancies all within the same layer reduces the energy by 1.7eV compared to random distribution across the two layers (**Figure B2**). The formation of 1SVL alters the local stoichiometry from MoS_2 to Mo_3S_4, whereby the coordination of Mo atoms with S atoms at the defect site changes from six-fold to four-fold and S atoms maintain the three-fold coordination with Mo atoms as in a pristine lattice. The DFT calculated atomic model shows the generation of 1SVL triggers a slight out-of-plane distortion (side view), leading to the splitting of double stacked S atoms adjacent to 1SVL in the top-down view (labelled by two black rectangular boxes in **Figure 6.4**e). This results in the slight intensity decrease and blurring at the corresponding 2S sites in the AC-TEM image (marked in white square boxes in **Figure 6.4**d). I measured the lattice contraction in 1SVL line defects of different lengths by taking intensity line profiles along the armchair direction across the middle section (**Figure B3**a–d) spanning 2S-Mo_1-S-Mo_2, **Figure 6.4**g (the subscripts are used to differentiate two Mo atoms measured in the same line). Comparing 1SVL with different lengths to the pristine lattice shows the projected atomic distances between 2S and Mo_1 are the same (**Figure 6.4**g) whereas the distance between the two Mo atoms (Mo_1-Mo_2) has contracted, along with the S atom position moving closer to Mo_1 as the length of the 1SVL extends. The projected atomic distances between Mo_1-S, S-

Mo_2 and Mo_1-Mo_2 were determined by Gaussian peak fitting, and **Figure 6.4**h shows the plot of the relevant interatomic distances as a function of the 1SVL defect length. It shows that the Mo_1-Mo_2 distance has a compression that increases with the 1SVL length, from ~5.3 Å in a pristine lattice to ~4.2 Å when the aggregated number of S vacancies reaches 7 at 1SVL, yielding a shrinkage ratio of 21%. The planar Mo_1-S distance drastically decreases, while the S-Mo_2 distance increases when the aggregated number of single S vacancies increases from 0 to 5, indicating that a single S atom undergoes displacement relative to Mo_1 on its left. Therefore, with the extension of 1SVL, the projected view of the line defect structure shows an increased contraction ratio for Mo sublattice at 1SVL along the armchair direction, indicated by a continuous decrease of Mo_1–Mo_2 distance. In addition, residual single S atoms at 1SVL undergo displacement to Mo_1 atoms, which switches the original zigzag configuration of the Mo-S string to an approximately straight line (indicated by dashed rectangular black and white boxes in **Figure 6.4**e,f, respectively).

I next studied the effect of increasing the width of line defects by examining the 2SVL that has two adjacent parallel sulphur vacancy lines. **Figure 6.5**a,b show two types of extended 2SVL defects, which have slightly different S reconstruction. **Figure 6.5**c shows a 2SVL with a kink that has the two different types of reconstruction present. The fine details of these reconstruction are shown in **Figure 6.5**d–g, highlighting the shifts in the S positions and the impact on the positions of Mo along the line defect (**Figure 6.5**h,i). The S atoms in the type 1 2SVL are further apart compared to the type 2 2SVL and the Mo atoms are spaced further apart in the type 1 2SVL compared to the type 2. **Figure 6.5**i shows the separation distances between Mo atoms along the regions indicated in the AC-TEM image in **Figure 6.5**h, for type 1 and type 2 2SVL structures. The origin of the two types of 2SVL is likely associated with strain effects from the compression occurring in the lattice from the missing S atoms. The kink in the line defect in **Figure 6.5**c results in non-orthogonal strain

components from one line defect impacting on the other section. In general, type 1 2SVL is the most common 2SVL observed in the lattice.

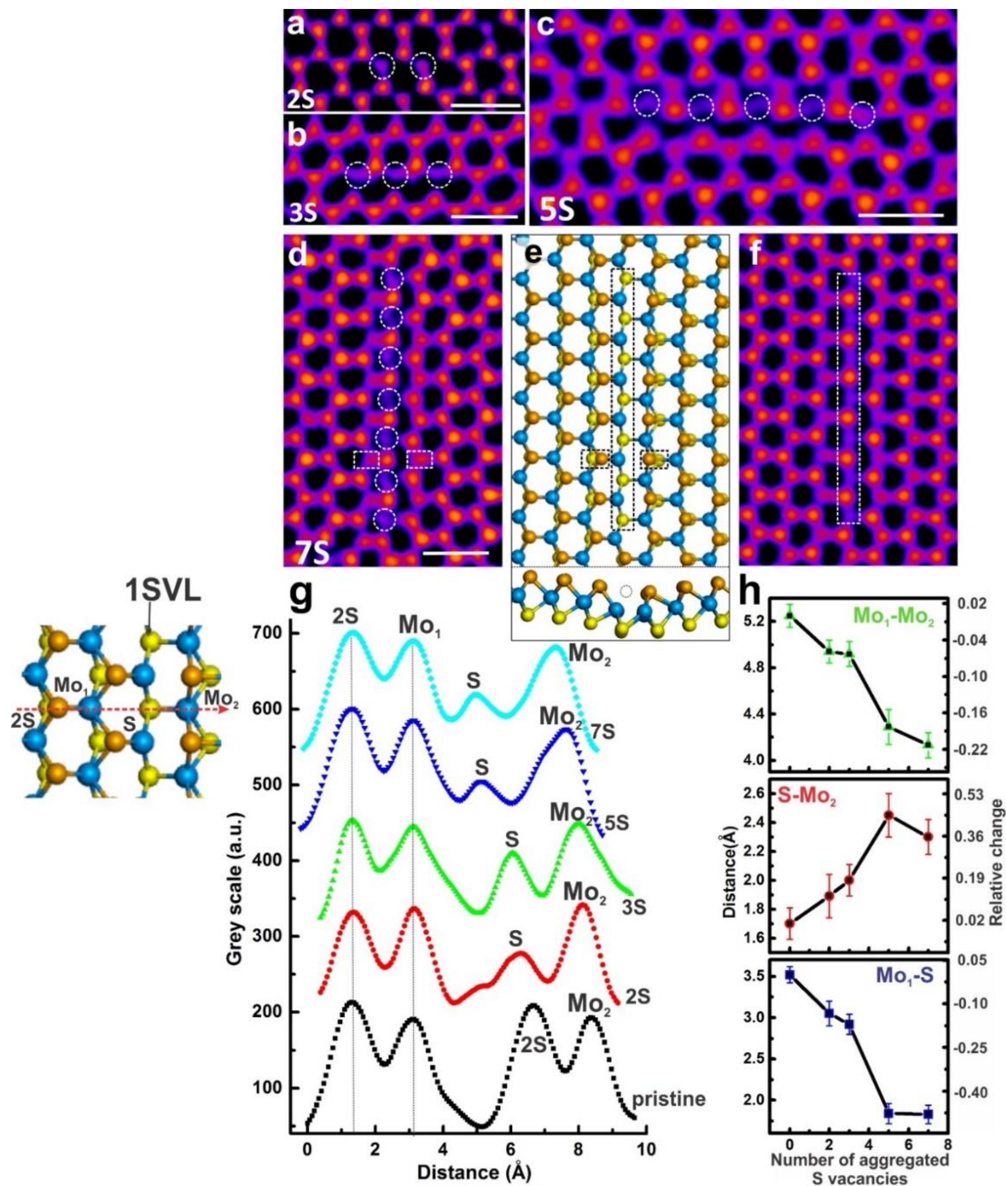

Figure 6.4. (a–d) AC-TEM images showing 1SVL in different lengths, having elevated numbers of single S vacancies aligning in the same line, being 2, 3, 5 and 7, respectively. (e) DFT-calculated atomic model based on (d), with both the projection view and the associated side view. (f) Multislice TEM image simulation corresponding to the atomic model in (e). (g) Intensity line profiles measured across the middle of 1SVL in different lengths, shown in (a–d), along the armchair direction indicated by the red arrow labelled in the schematic diagram, spanning 2S-Mo_1-S-Mo_2 in projection (the subscripts are used to differentiate two Mo atoms measured in the same line). (h) Scattered line graphs showing the distance variations between Mo_1 and Mo_2, S and Mo_2, as well as Mo_1 and S, respectively, when the number of aggregated single S vacancies increases from 0 to 7. Scale bar corresponds to 0.5nm in all panels.

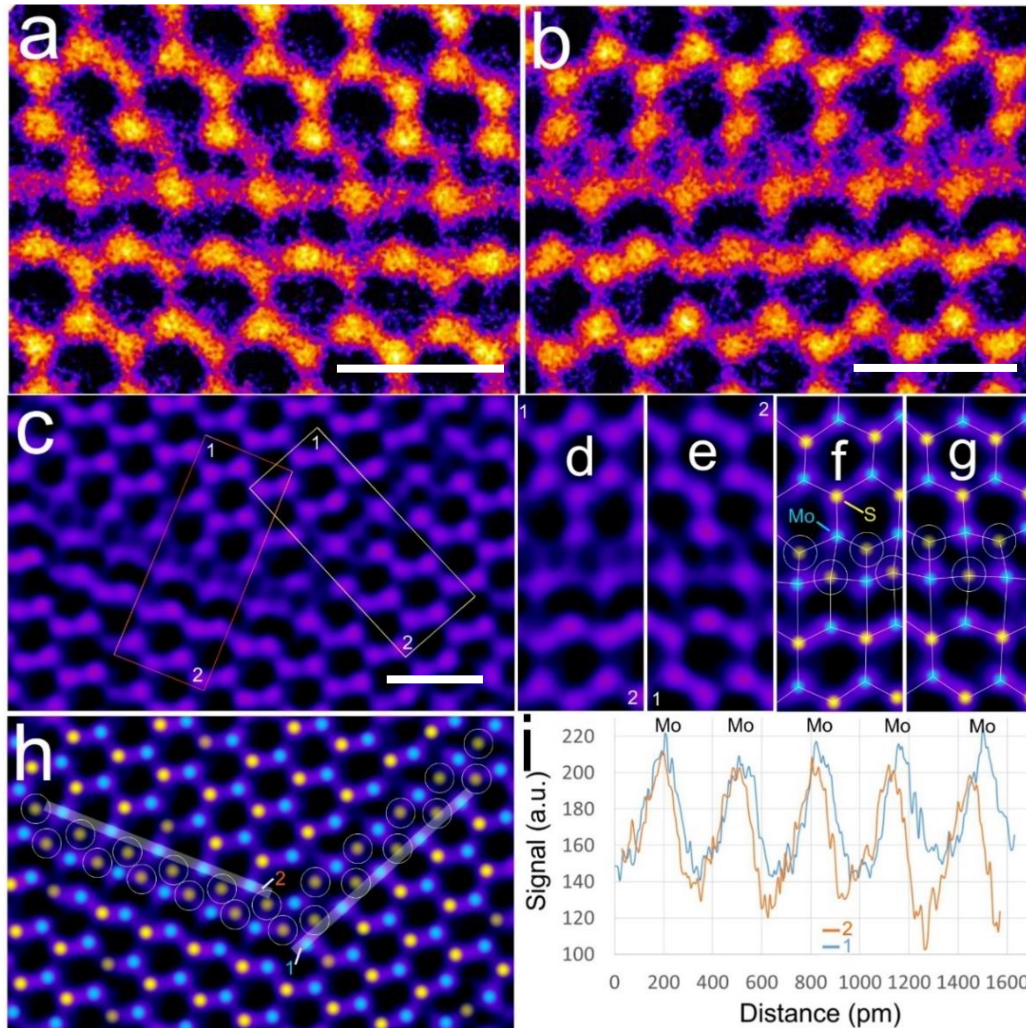

Figure 6.5. AC-TEM image of a 2SVL with (a) type 1 S reconstruction and (b) type 2 S reconstruction. (c) AC-TEM image showing the intersection of type 1 and type 2 2SVL defects. (d) Magnified view of the red boxed region in (c) for a type 2 2SVL. (e) Magnified view of the yellow boxed region in (c) for a type 1 2SVL. (f,g) Schematic atomic model overlaid onto the respective AC-TEM images from (d,e). (h) Positions of Mo and S atomic columns are indicated on the AC-TEM image from (c), with S in yellow and Mo in cyan. White circles indicate the S vacancy sites. (i) Comparison of line profiles taken in the regions indicated with the broad white lines in (h) for the two types of 2SVL. All scale bars correspond to 0.5 nm.

Based on DFT calculations, the low energy configuration for the type 1 2SVL has alternating rows of S vacancies between top and bottom planes, shown in **Figure 6.6**b, agreeing with previous reports.(*35*) Similar to 1SVL, 2SVL also induces a slight out-of-plane distortion at the defect site. The lowest coordination number of Mo atoms with S atoms further decreases from 4-fold for 1SVL to 3-fold for type 1 2SVL (**Figure 6.6**b). The type 2

2SVL has similar S positions to a 1T phase of MoS_2 and in **Figure 6.6**e-h I show its transformation to a type 1 2SVL structure after 10 seconds of electron beam irradiation. This occurs by shifting the single S atom line labelled in yellow circles (**Figure 6.6**e) to right along the armchair direction slightly (**Figure 6.6**h), switching the geometry of the Mo-S string on the right side from zigzag to a straight line. The type 2 2SVL usually occurs when there are other defect structures around, such as the triangular inversion domain shown in **Figure 6.6**d. **Figure 6.6**i–l shows a schematic illustration of the atomic position changes needed to achieve a type 2 2SVL structure. The actual formation pathway of a type 2 2SVL will be more complicated than the process shown in **Figure 6.6**i–l, because the line defects are formed by the agglomeration of point defects that involves multiple bond reconstructions.

The lattice changes for the 2SVL were measured as a function of their lengths and types using line profiles across the middle section spanning Mo_1-S-Mo_2 (**Figure 6.6**m). The short type 1 2SVL is from **Figure 6.3**f, while the longer type 1 2SVL is from **Figure 6.6**a (**Figure B1**e–g). The projected distances between Mo_1-Mo_2, S-Mo_1 and Mo_1-S in 2SVL as a function of their type and length are plotted in **Figure 6.6**n. Compared with the pristine MoS_2 structure, both types of 2SVL have lattice compression along the armchair direction, as depicted in the line chart of Mo_1-Mo_2 (**Figure 6.6**n). However, the contraction for a type 1 2SVL (17%) is larger than for a type 2 (11%), even considering both the short type 1 2SVL and a long type 2 2SVL. The compression is greater for the longer type 1 2SVL compared to short type 1 2SVL, similar to 1SVL and confirms an increased lattice compression in the projected view with an extension of S vacancy lines. The position of single S atoms relative to its two neighbouring Mo atoms also varies for the two types of 2SVL. Compared with the pristine MoS_2 lattice having 2S placed closer to Mo_1, the single S atom tends to locate at approximately the middle of two Mo atoms for type 1 2SVL, whereas the type 2 2SVL has single S positioned closer to Mo_2.

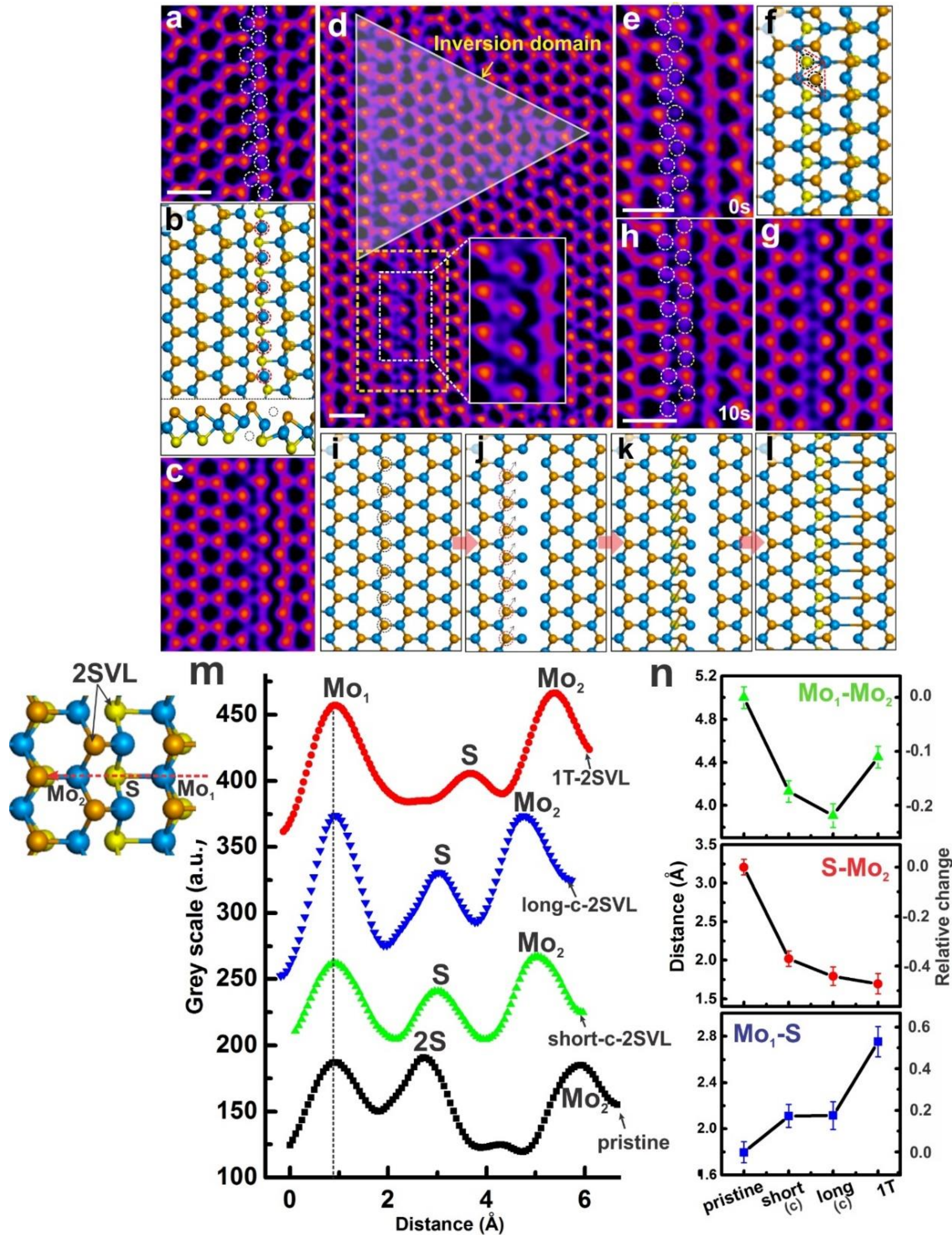

Figure 6.6. (a) AC-TEM image of type 1 2SVL with two adjacent single S vacancy lines highlighted by white circles. (b) DFT-calculated atomic model for the type 1 2SVL shown in (a). The Mo atoms marked by red circles show a three-fold coordination with their neighbouring S atoms. (c) Multislice TEM image simulation based on the atomic model in (b). (d) AC-TEM image showing type 2 2SVL with its surrounding environment included, having a triangular inversion domain on top. The detailed configuration of type 2 2SVL labelled in the white dashed box is magnified as inset. (e) AC-TEM image of the region marked in the orange dashed box in (d), with two single S vacancy lines marked by white and yellow circles from left to right, respectively. (f) Atomic model of type 2 2SVL, with

labels indicating that single S atoms along two S vacancy lines are located in the centre of their triangularly-arranged three Mo atoms. (g) Multislice TEM image simulation based on the atomic model in (f). (h) AC-TEM showing the transformation of a type 2 2SVL to type 1 after 10 seconds. (i-l) Schematic illustration showing atomic position changes from pristine lattice to type 2 2SVL. (m) Intensity line profiles measured across the middle of 2SVL in different types and lengths, along the armchair direction indicated by the red arrow shown in the schematic diagram. The short type 1 2SVL, long type 1 2SVL and type 2 2SVL correspond to the example of the type 1 2SVL in **Figure 6.3**f and this figure's (a) and (e), respectively. (n) Plots showing the distance difference between Mo_1 and Mo_2, S and Mo_2, as well as Mo_1-S, respectively, for 2SVL with the variation of types and lengths. Scale bar corresponds to 0.5nm in all panels.

The 2SVL further increases in width by S vacancies agglomerating along the armchair direction, forming 3SVL and 4SVL, as shown in **Figure 6.7**a–c. These generally have structure similar to the type 1 2SVL in terms of the S bond reconstruction. **Figure 6.7**d shows the AC-TEM image of the region marked with the dashed white box in **Figure 6.7**c, with the DFT-calculated relaxed atomic model and the corresponding multislice simulation shown in **Figure 6.7**e,f, respectively. The energetically stable structure still has staggered arrangements of S line vacancies alternating between the top and bottom S planes, **Figure 6.7**e. In the 2D projected view, the periodical structure at the defect site transforms from hexagonal in the pristine lattice to rectangular, highlighted by the red box in **Figure 6.7**e. Intensity line profiles are measured for the 3SVLs with two different lengths (long and short) from images in **Figure 6.3**g and **Figure 6.7**d (**Figure 6.7**g) (**Figure B3**h,i). Lattice contraction occurs along the armchair orientation and increases with the 3SVL length, agreeing with the observations on 1SVL and 2SVL. A prolonged electron beam irradiation causes the line defects to further expand in both length and width. **Figure 6.7**h,j are two typical examples of nSVL having 5 and 8 extended sulphur vacancy line widths, with corresponding atomic models shown in **Figure 6.7**i,k, respectively. This indicates a large tunable range for line defect geometry, providing flexibility for patterning MoS_2-based 2D nanodevices.

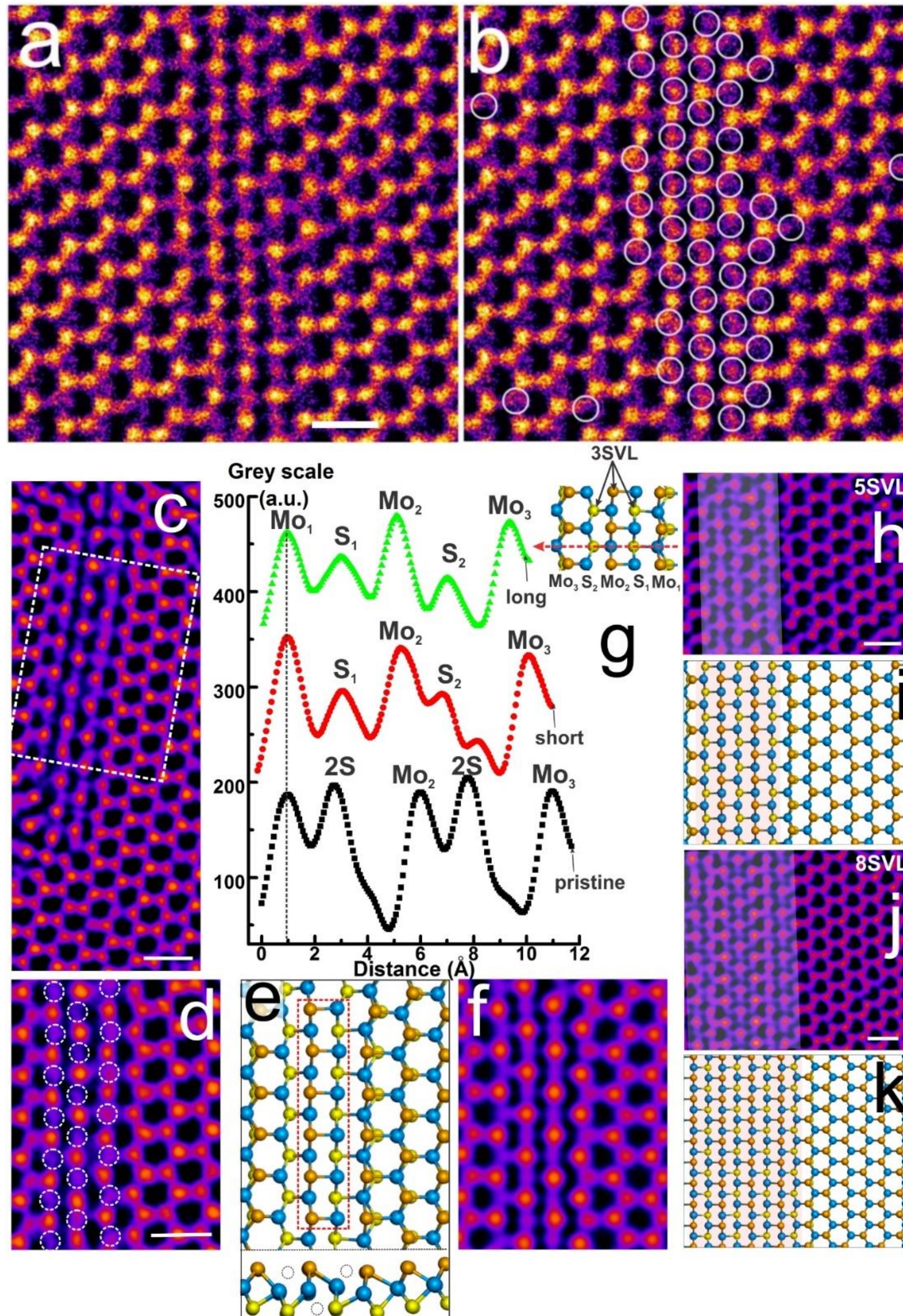

Figure 6.7. (a) AC-TEM image of S line vacancy with increased width, with (b) showing white circles to indicate the 1S vacancy locations. (c) AC-TEM image showing the structure of 3SVL. (d) Magnified AC-TEM image of the region labelled in the white dashed box in (c), showing the detailed lattice reconstruction at 3SVL, with three single S vacancy lines highlighted by white circles. (e) DFT-calculated atomic model of 3SVL corresponding to (d). The lattice marked in the red dashed box indicates a transformation on the periodicity of atom arrangements from hexagons to rectangles in the projection view. (f) Multislice TEM image simulation based on the atomic model in (e). (g) Intensity line profiles measured across the middle of 3SVL in different lengths, along the armchair direction indicated by the red arrow shown in the schematic diagram. The short and long examples

correspond to 3SVL shown in **Figure 6.3**g and (d), respectively. (h, j) AC-TEM images showing two typical examples of nSVL (n > 3), which are 5SVL and 8SVL, respectively. The line defect region has been highlighted by covering a half-transparent white mask, which displays distinct structural difference from the right pristine lattice with an atomically-sharp and straight boundary. (i, k) Atomistic models corresponding to the structure of 5SVL and 8SVL shown in (h) and (j), respectively. Scale bar corresponds to 0.5nm in all panels.

6.2.3 2D Strain Analysis of Sulphur Vacancy Lines

I examine the strain in the lattice resulting from the line defect formation (**Figure 6.8**). 2D displacement and strain maps were constructed for two typical examples of type 1 2SVL and 7SVL using a real space analysis method similar to prior work on carbon nanotubes (see section 3.6.3).(*115*) Measuring changes in atomic positions has also been used to map strain in graphene grain boundaries and divacancies.(*162*)(*163*) The 2D displacement maps of 2SVL and 7SVL show prominent lattice compression towards the line defects in the x direction with an increased magnitude as the line defect broadens (**Figure 6.8**(i)a,(ii)a), whereas the lattice distortion in the y-axis is insignificant (**Figure 6.8**(i)b,(ii)b) (**Figure B4**). The compression or tension of the local lattice in the x-y plane is revealed by maps of $\frac{\partial U_x}{\partial x}$ and $\frac{\partial U_y}{\partial y}$. Interestingly, for type 1 2SVL, strain fields in the x direction are organized into tension-compression dipoles along the S line defects but in large magnitude variations, as indicated by black boxes in **Figure 6.8**(i)c. The contraction strain fields can reach above 50%, while the tension strain fields are only around 20%. This is consistent with the atomic position measurements across the type 1 2SVL (**Figure 6.6**n), where the projected interatomic distance of S-Mo_2 and Mo_1-S for the long type 1 2SVL show a compression and an elongation trend, respectively, with a distinct difference on the relative change. The strain field in the y direction is almost zero, which is due to the negligible displacement along this direction. Because the TEM image is the 2D projection of the 3D

atomic structure, the elongation or shrinkage of the distance between two neighbouring atoms measured in a TEM image can come from two effects: (i) the bond length variation between two atoms, which indicates an in-plane lattice deformation; (ii) an out-of-plane distortion, which can alter the projected distance between two atoms along certain direction in the x-y plane. To confirm the origin of the 2D strain fields in the x direction in line defects, I calculated the Mo-S bond length variation between line defects in DFT-calculated atomic models and a pristine lattice, yielding a compression/tension ratio of less than 5% (**Figure B5**). This indicates that both the contraction and tension fields along x-axis are mainly derived from the out-of-plane distortions of the lattice in line defects, also seen in the side view of atomic models for type 1 2SVL (**Figure 6.6**b). The angle between Mo-S bonds and the x-y plane varies at the defect site compared with the pristine lattice, resulting in a change of the projected distance between Mo and S atoms. The 2D shear strain fields of $\frac{\partial U_x}{\partial y}$ are ordered into positive-negative dipoles as well (marked by black dashed boxes in **Figure 6.8**(i)e), with an approximately balanced magnitude along the line defects, while $\frac{\partial U_x}{\partial y}$ is nearly ignorable, representing a periodically-organized simple shear mode in projection. Both the normal and shear strain fields are highly localized along the 2SVL, with small perturbations to the neighbouring lattice. In terms of strain field maps for 7SVL, they show similar characteristics as 2SVL regarding both the organization manner of strain fields and their magnitudes, as shown in **Figure 6.8**(ii)c–f. The only difference is that the strain fields of $\frac{\partial U_x}{\partial x}$ along different S vacancy lines has small deviations in magnitudes, which could be due to the generation of ripples at line defects (**Figure B6, Figure B7, Figure B8**).

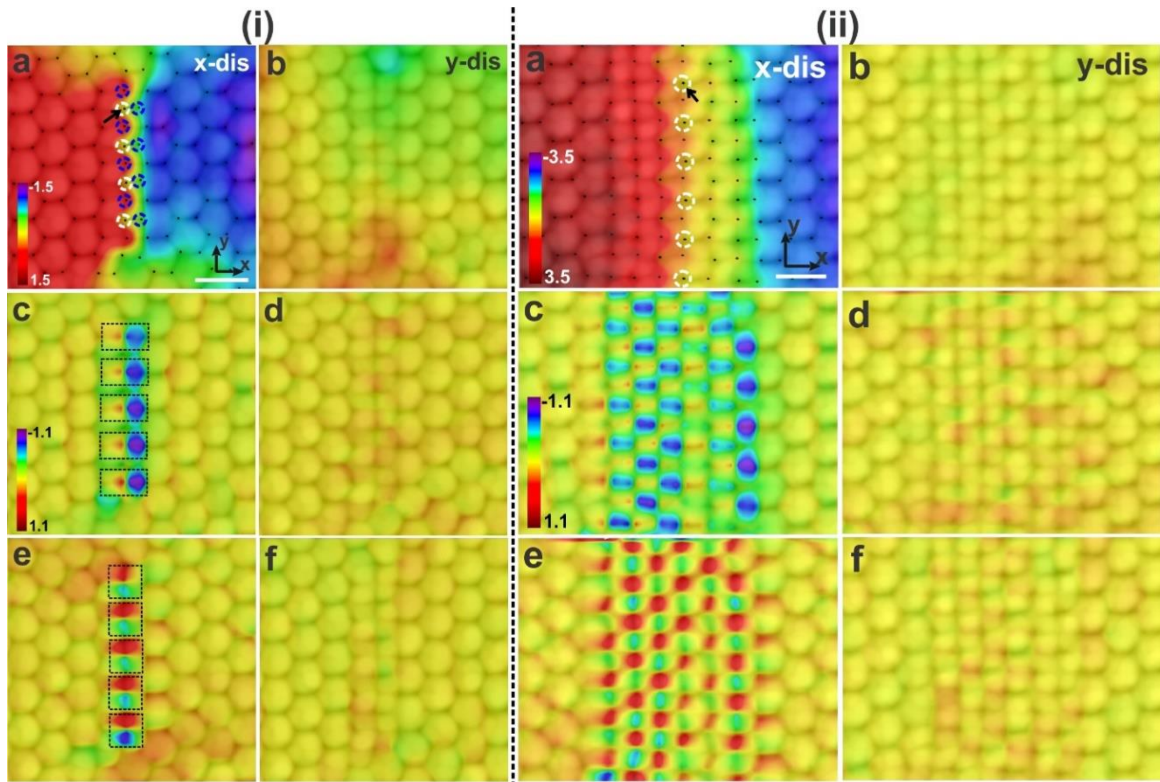

Figure 6.8. (i)(a, b) 2D displacement maps of type 1 2SVL in the x and y direction, respectively, which are overlaid on the corresponding maximum-filtered 2SVL AC-TEM image. The colour scale is ± 1.5Å. The white circles indicate the line of Mo atoms which locate close to its neighbouring two single S vacancy lines, marked by blue circles. The black arrow points out the Mo atom that is chosen as the reference point. (c-f) 2D strain maps of $\partial Ux/\partial x$, $\partial Uy/\partial y$, $\partial Ux/\partial y$ and $\partial Uy/\partial x$. The colour scale is ±1.1 (±110%). The black rectangular boxes marked in panel c show the normal strain fields in the x direction, which are organized into tension-compression dipoles with a large magnitude variation, while the black boxes labelled in panel e displays shear strain fields that are also ordered into pairs but with balanced magnitude along type 1 2SVL. (ii)(a, b) 2D displacement maps of 7SVL along the x and y direction, respectively, which are overlaid on the corresponding maximum-filtered 7SVL AC-TEM image. The colour scale is ± 3.5Å. The white circles indicate one line of Mo atoms which locates in the middle of the defective region. The black arrow indicates the Mo atom that is chosen as the reference point. (c-f) 2D strain maps of $\partial Ux/\partial x$, $\partial Uy/\partial y$, $\partial Ux/\partial y$ and $\partial Uy/\partial x$ for 7SVL. The colour scale is ±1.1 (±110%). Scale bar corresponds to 0.5nm in all panels.

6.2.4 Band Structure Calculation

Finally, DFT has been applied to calculate how the band structures of MoS_2 are impacted by the presence of these line defects (calculated by Prof Gun-Do Lee, Mr Sungwoo

Lee and Prof Euijoon Yoon). In particular, the electronic properties have been studied under the assumption of infinitely long line defects in MoS_2. For the band structure calculations, the infinite line defects are made within a periodic orthorhombic unit cell of the pristine MoS_2 lattice structure. As the width of the line defects increases, the size of the band gap decreases, as shown in **Figure 6.9**. The band gap of pristine MoS_2 without a line defect is found to be 1.68 eV, similar to previous reports.(*164*, *165*) The defect lines introduce new states between the conduction band minimum and the valence band maximum, compared with the band structure of pristine MoS_2. The band structure of 1SVL, 2SVL, and 3SVL shows direct band gaps of 0.546, 0.058 eV, and 0.047 eV, respectively. As the number of defect lines increases over 4SVL, the band gap disappears and it finally becomes metallic (**Figure B9**). From the band structure calculations, the tunability of band gap depending on the number of line defects can be found.

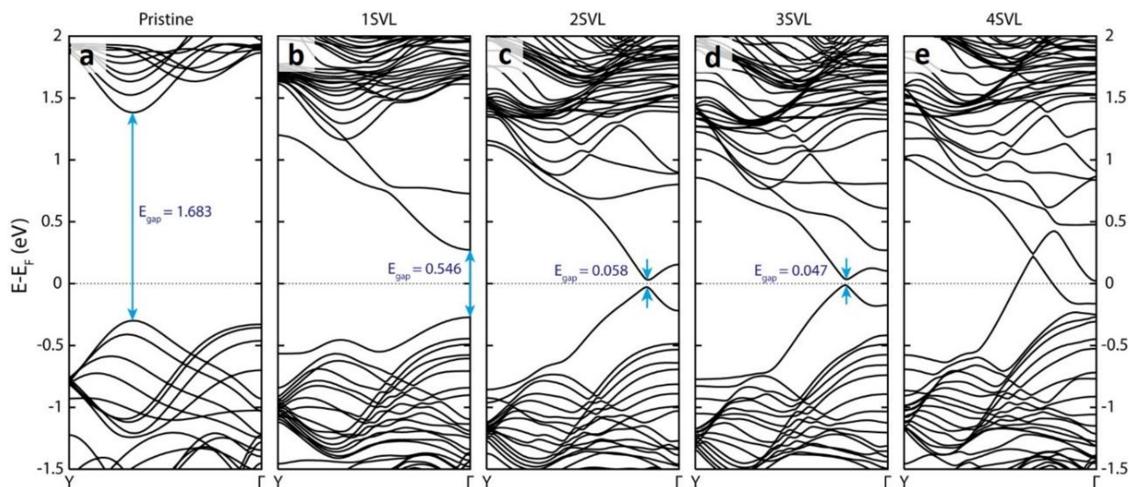

Figure 6.9. DFT calculated band structures of 1SVL, 2SVL, 3SVL and 4SVL, respectively, indicating a gradual band gap decrease as the line defect broadens with the electronic property alteration from semiconductor to metal.

6.3 Conclusion

In this chapter, I study the detailed bond reconstructions that occur in S vacancies within monolayer MoS_2 using a combination of aberration-corrected transmission electron microscopy, DFT calculations and multislice image simulations. Removal of a single S atom

causes little perturbation to the surrounding MoS_2 lattice, whereas the loss of two S atoms from the same atomic column causes a measurable local contraction. Aggregation of S vacancies into linear line defects along the zig-zag direction results in larger lattice compression that is more pronounced as the length of the line defect increases. For the case of two rows of S line vacancies I find two different types of S atom reconstruction with different amounts of lattice compression. Increasing the width of line defects leads to nanoscale regions of reconstructed MoS_2 that are shown by DFT to behave as metallic channels. In addition, 2D strain maps based on displacement maps display the strain field distribution around various line defects, providing a general view of the lattice distortion. This study opens up the opportunity for top-down patterning of semiconducting/metallic interfaces through defect engineering, which has importance for future electronic and opto-electronic devices.

Chapter 7 Cracks in Monolayer MoS_2

In Chapter 6, I studied the fine structures of various line defects, which were formed by the migration and aggregation of S vacancies generated by the electron beam (EB) irradiation. If I went on bombarding the clean, suspended monolayer MoS_2 membrane with an enhanced electron dose *via* focusing the beam, more S atoms were knocked off with Mo atoms agglomerating into nanowires and clusters.(*166*) Since there was also residual mechanical stress in MoS_2 due to the transfer process (baking treatment), the monolayer MoS_2 film lost its continuity quickly, forming holes with expanded sizes followed by cracks generating and emanating from the hole. This is similar as puncturing a drumhead by a needle. It provides a 2D platform to study the facture mechanics of the material, enabling me to image the crack tip configurations and track the real-time crack propagation with the ability of resolving each single atom unambiguously.

7.1 Introduction

Fracture in a material is centred around the mechanical behaviour of cracks and their tips as they develop.(*167–175*) Brittle fracture is associated with rapid clean cleavage of bonds and ductile fracture generally involves some plastic deformation around the tip front that slows down the crack propagation.(*176*) Preventing a crack from brittle propagations can delay mechanical failure and effectively increase the material's fracture toughness.

Crack tips with atomic sharpness are predicted to play a major role at the frontier of crack propagation and therefore it is important to understand their behaviour at the single atom level.(*177*) However, the non-negligible thickness of samples has been a major factor limiting atomic level *in-situ* dynamic studies of crack tip interactions in materials,(*178–180*) which could be overcome by utilizing ultrathin monolayer 2D materials.

Gaining a deep understanding of fracture mechanics requires investigation at the atomic level, due to the nature of bond breakage in crack propagation, the nanoscale size of crack tips, interactions with defects and the plasticity generated in ductile materials under stress. Among different imaging techniques,(*181–184*) TEM can provide single atom resolution, and the recent rise of 2D materials, such as graphene, MoS_2 and BN, provides material samples to image the exact atomic structure of crack tips where the atomic positions can be truly interpreted from their 2D projection.(*29*, *185*) Classical molecular dynamics (MD) simulation represents an efficient tool to investigate the mechanics and fracture of different 2D materials. Fracture in graphene has been heavily investigated in simulations with comparison to experiments,(*186–190*) and there is evidence that defects in graphene do not strongly alter the crack propagation speed.(*191*) However, it is not clear if all the 2D materials fail in the same way.

Here, the structure and dynamics of cracks in suspended single crystals of monolayer MoS_2 have been examined at the atomic level using aberration-corrected TEM (AC-TEM). Cracks were introduced into MoS_2 by popping the strained 2D membrane with a focused EB to cause fractures (**Figure 7.1**a). MD simulations based on first-principles reactive force fields on the same length scale as experiments are used to reproduce the experimental observations and provide insights into the dynamical behaviour (MD simulations were done by Dr Zhao Qin, Mr Gang Seob Jun, Dr Francisco J. Martin-Martinez; Ms Kristine Zhang and Prof Markus J. Buehler.).

7.2 Results and Discussion

7.2.1 Fast Fracture in Strained Pristine Monolayer MoS_2

Figure 7.1b shows a low magnification TEM image of the region where the EB has popped the MoS_2 membrane by sputtering a hole, indicated with the yellow dashed boxed area, and the cracks that emanated into the surround area of the MoS_2 that had not been subjected to EB irradiation. The region of the crack tip is indicated with the white dashed box (**Figure 7.1**b) and the inset shows a magnified view of this area. The cracks were found to have zigzag edge terminations, as shown in **Figure 7.1**c, that are straight and long and indicative of brittle fracture along the crystallographic plane. Large scale MD simulations also predict the presence of cracks propagating from the end of an elliptical hole (**Figure 7.1**d) along the zigzag direction with similar zigzag edge terminations. Snapshots from the MD simulations reveal that the crack can narrow to an apex tip with atomic sharpness and in some cases have reconstructed tips that contain atomic chains bridging the gap (**Figure 7.1**f–h).

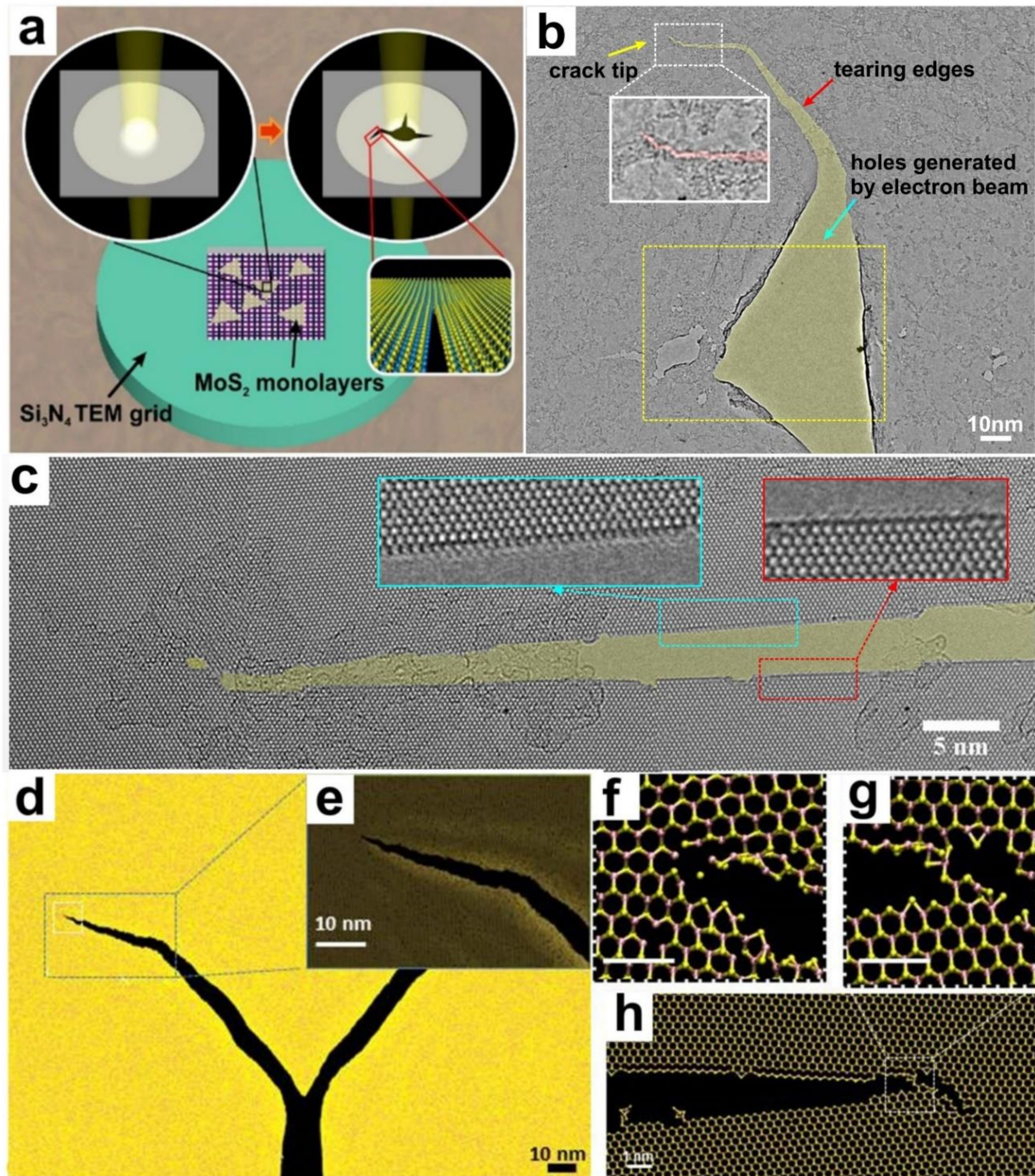

Figure 7.1. (a) Schematic illustration showing CVD-grown triangular-shaped monolayer MoS_2 domains with the size of ~15 μm transferred on to a Si_3N_4 TEM grid with arrays of 2 micron holes. Each domain can completely cover several holes. The zoomed-in image of the circular window shows the crack generation process by the focused EB on the suspended monolayer MoS_2 membrane covered on one TEM hole. (b) TEM image showing the crack microstructure. The crack was developed from a hole created by continuous focused EB irradiation, marked by the yellow box. A typical crack propagated along a certain lattice direction can be seen (masked by a semi-transparent yellow colour), leaving long and straight teared edges, highlighted by the red arrow. The white dashed box shows the crack morphology (highlighted by a semi-transparent red colour) in its final propagation stage including the crack tip with a higher magnification image below as an inset. (c) Montage of AC-TEM images stitched together to show the long range atomic sharpness of the edges

of the crack. The shape of the crack is highlighted in yellow. Insets show magnified AC-TEM image of the edge configurations. (d,e) Snapshot of MD simulation of the crack propagating from the end of an elliptical hole in a piece of MoS_2 model of 200 by 200 nm^2 under mechanical stretching force. The crack tip shows an atomic sharpness feature. (f-h) MD simulation snapshot of a different crack propagation by creating a smooth crack edge before creating a step and breaking bonds in front of an intact Mo-S bond, leaving a residue chain behind the crack tip. Pink and yellow spheres indicate Mo and 2S atoms, respectively.

Analysis of AC-TEM images for several different crack tips showed excellent agreement with the MD calculations (**Figure 7.1**f,g), with the two different types of sharp tips (atomically sharp and reconstructed) observed (**Figure 7.2**a–d). The first type shows the crack narrows all the way down to a single Mo-S bond at its tip by cleavage of bonds directly along a certain zig-zag lattice orientation, with almost no reconstruction at the tip (**Figure 7.2**b). The second type shows reconstructions at the tip, which might help relieve the rotational strain around that region. A schematic illustration based on experimental observations, which indicates a possible movement of atoms required to form the reconstructed tip, is supplied in **Figure 7.2**e–i. Initially, four Mo-S bonds labeled by short red lines are broken (**Figure 7.2**e) due to the stress concentration at the crack tip. Subsequently, the Mo-S bond between atom 4 and 1, marked in a white dashed ellipse, has a clockwise rotation (**Figure 7.2**f) and hangs above the bottom torn edge, making the second and fourth Mo atoms face to two 2S sites labeled in two dashed rectangles (**Figure 7.2**g) and bond with them (**Figure 7.2**h). Some S atoms on the crack edge or dislocation edge dissociated from the MoS_2 lattice during the crack and reconstruction process possibly due to the EB irradiation (**Figure 7.2**i), and finally form the crack tip with dislocation cores situating ahead, consistent with the atomic configuration in **Figure 7.2**d.

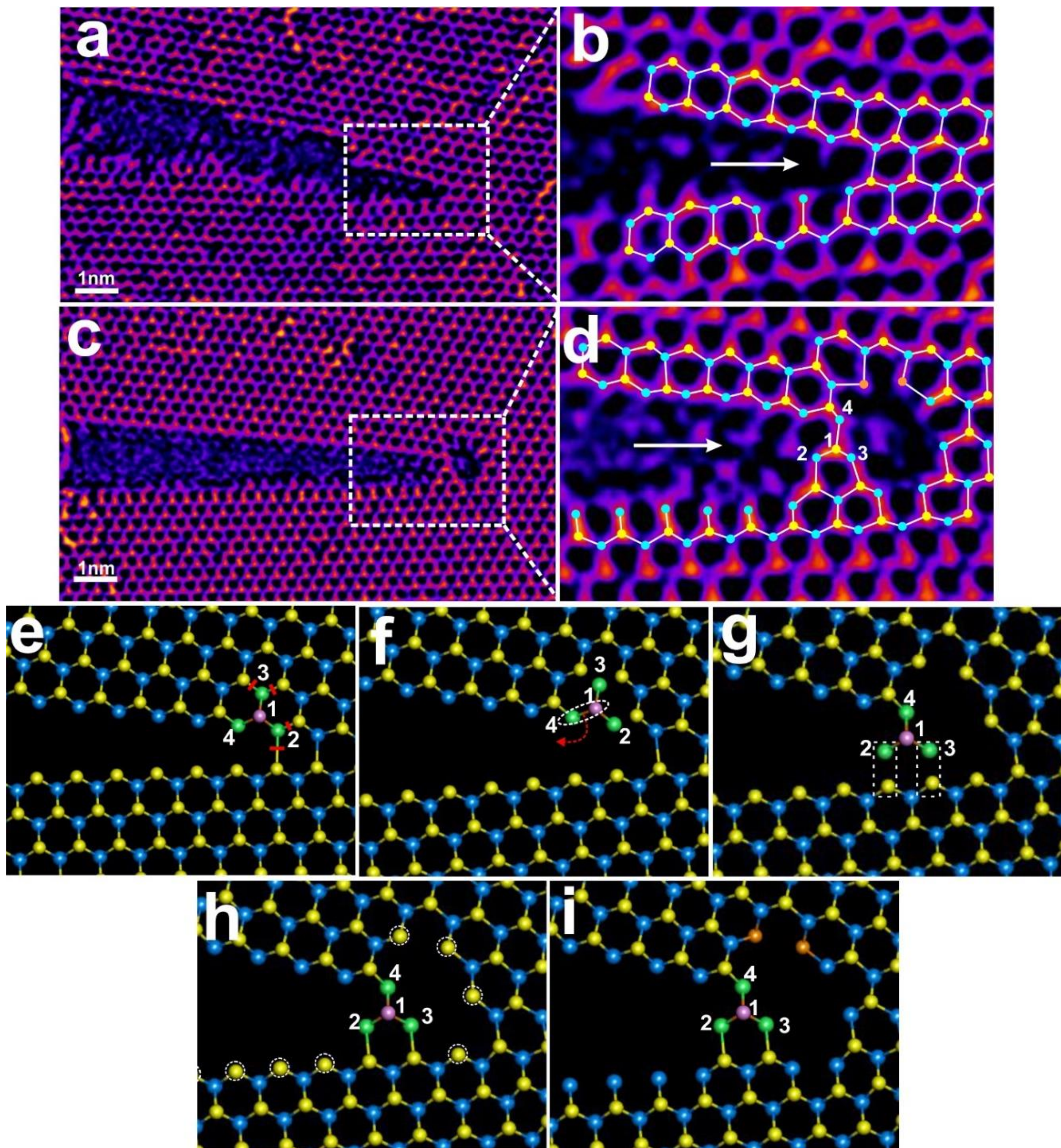

Figure 7.2. Structure of atomically sharp and reconstructed crack tips. (a) AC-TEM image of an atomically sharp crack tip in MoS_2 and (b) magnified image with atomic model overlay. Mo and yellow and orange circles represent Mo, 2S and 1S atoms, respectively. (c) AC-TEM image of a reconstructed sharp tip in MoS_2 and (d) magnified image with atomic model overlay. Atoms that are labelled by numbers from 1 to 4 a pair of stacked S atoms and three Mo atoms, respectively. (e–i) Atomic models showing the possible formation process of the reconstructed tip in panel d. The Mo and 2S atoms of those highlighted ones are coloured in green and pink, respectively, being different from the colour of blue and yellow in a pristine lattice.

Crack propagations in MoS_2 can be straight for up to 1μm, forming atomically smooth edges of over nanoscale distances (**Figure 7.3**a-d). Very tiny (sub-nm) crack

deflections are observed across one or two rows of lattice (**Figure 7.3**a). Interestingly, different from graphene, for which cracks occur along both armchair and zigzag lattice directions,(*190*) in monolayer MoS_2 cracks predominantly occur along the zigzag lattice direction. The cracks have complementary atomic edge terminations, indicative of cleaving the Mo-S bond along the zigzag direction, as shown in **Figure 7.3**b–d (**Figure C1, Figure C2**). The left side is constructed by Mo zig-zag edges, whilst the right side has Mo atoms dangling on S zigzag edges, similar as Klein edges in graphene.(*192*) The outermost S atoms, marked by yellow circles in **Figure 7.3**c, disappeared, which may happen either during the unzipping of bonds as the crack propagated or as the EB irradiation prolonged. Occasional 60° direction changes of the cracks following zigzag orientations were observed (**Figure 7.3**e) and the near-perfect unzipping along all directions demonstrates brittle fracture.

MD simulations show that cracks heading in the zigzag direction have smooth propagation with tiny deflections, while a crack heading in the armchair direction propagates with more deflections of 60° (**Figure 7.4**b,c). The computed energy release from MD simulations along the zigzag direction is 2.09±0.13 eV/Å, lower than the armchair direction of 2.48±0.16 eV/Å, agreeing with previous DFT calculations of 2.21 eV/Å for zigzag directions (**Figure 7.4**d). Such difference in energy release explains the predominant zigzag crack propagation direction in experiments. The ratio of the energy release is very close to the ratio of the total crack length (cos(30°)), suggesting that the increment in the crack path length for the atomic crack tip mainly contributes to the delayed crack propagation along the armchair direction.

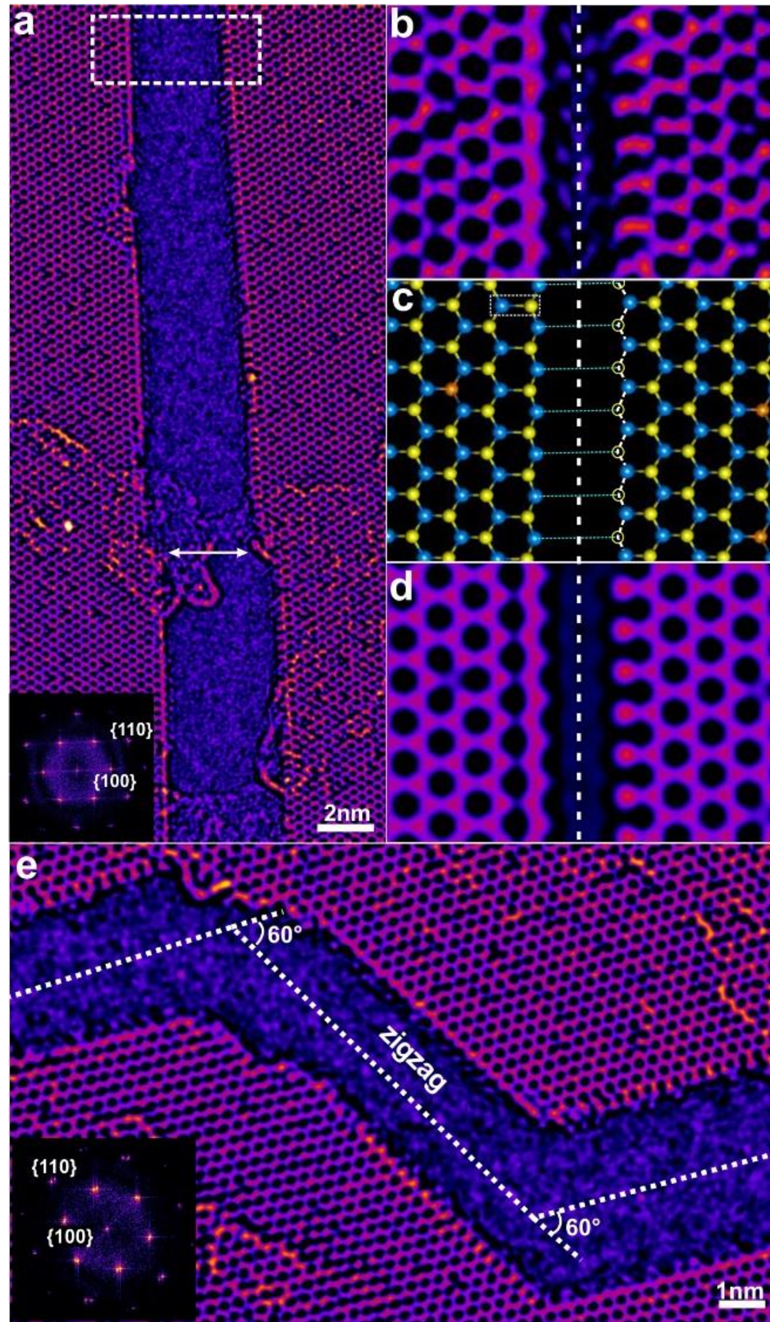

Figure 7.3. AC-TEM images showing edge structures of a brittle fracture on MoS_2. (a) AC-TEM image of long and straight zigzag crack edges. The inset is the Fourier transform of the image with labels of two main families of 2D MoS_2 crystal planes, {100} and {110}. (b) Detailed structure of the MoS_2 edges from the region indicated by the white dashed box in panel a. (c) Atomic model of the edge structure in panel b. The blue, yellow and orange spheres represent the single Mo atom, double S atoms and the single S atom, respectively. The yellow circles represent the missing S atoms, and the series of horizontal blue dashed lines are drawn to help showing the alignment between these two edges. (d) Multi-slice image simulation using the atomic model in panel c in a supercell. (e) AC-TEM image showing direction changes of crack direction along the zigzag lattice direction. The inset is the Fourier transform of the image, confirming the zigzag direction of each edge.

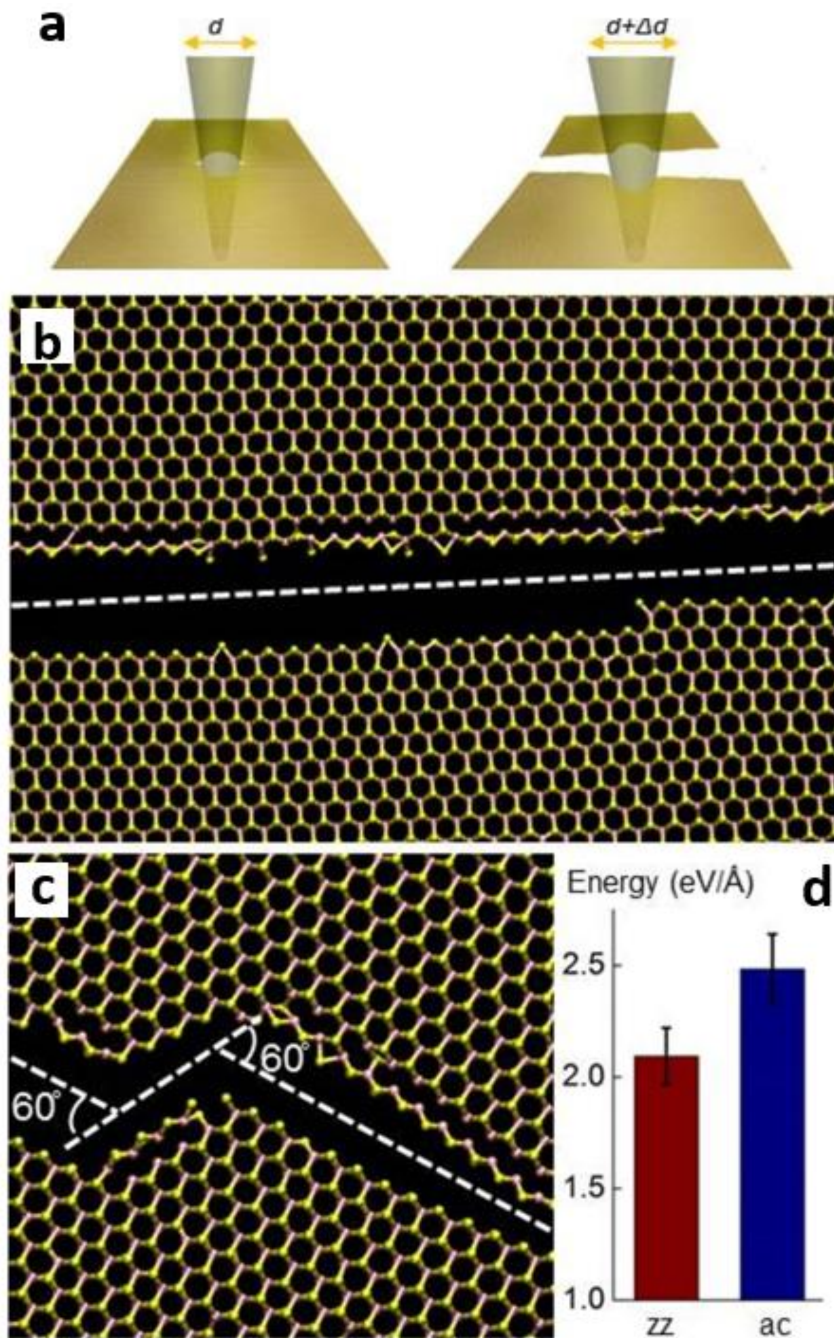

Figure 7.4. MD simulations showing edge structures of a brittle fracture on MoS_2. (a) Simulation snapshots of the MoS_2 model before and after loading by penetrating with a rigid cylindrical beam as schematically shown. Each model is initially built with a circular hole of 10 nm in diameter and two initial cracks with 30° sharpness and 2 nm in length. Increment in the diameter of the beam generates the driving force for the crack to propagate. Models of different lattice directions (zigzag versus armchair) respect to the direction of the initial cracks were tested. Snapshots of the crack edges after rupturing along the zigzag (b) and armchair (c) directions. (d) Energy release after crack propagation in two different directions.

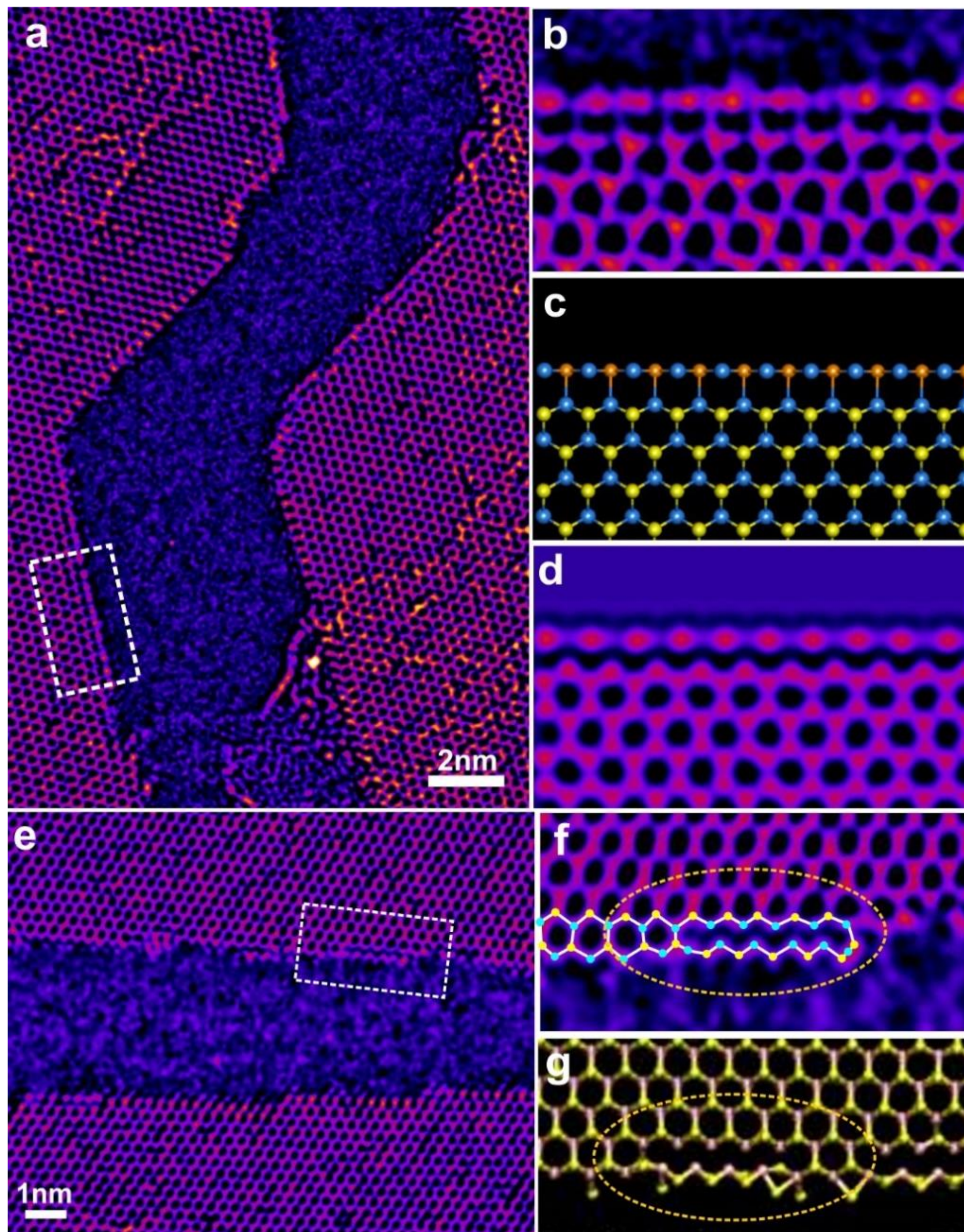

Figure 7.5. Diversity of edge structures. (a) AC-TEM image of the MoS_2 torn edges with a path deflection. (b) Detailed structure of a segment of the MoS_2 edge from the region indicated by the white dashed box in (a), where a configuration reconstruction of the outermost Mo and S atom takes place. (c) Atomic model of the edge structure in (b). The blue, yellow and orange spheres represent the single Mo atom, double S atoms and the single S atom, respectively. (d) Multislice TEM image simulation using the atomic model in (c). (e) AC-TEM image of another typical long and straight MoS_2 zigzag edge. (f) Detailed edge structure from the region marked in the white dashed box in (e) with an atomic model overlaid. (g) Simulation snapshot of the MoS_2 edge structure after performing a penetration test in a MoS_2 model, which is cropped from **Figure 7.4**b. The regions marked by orange ellipses in (f) and (g) show a good match on edge configurations between the AC-TEM image and the simulation results *via* a penetration test.

The zigzag edges do not have only one specific, well-defined configuration, but instead, could slightly vary, showing multiplicity of states with a certain level of flexibility for the detailed locations of the outermost Mo and S atom rows. As shown in **Figure 7.5**a,b, one segment of the edge on a deflected crack path exhibits reconstructions, where the outermost S atoms on a Mo-terminated zigzag edge has only 50% occupancy. In addition, this line of single S atoms is pushed closer to the outermost Mo atoms, showing a straight profile instead of a zigzag geometry. The similar structure of such 50% S-covered Mo-edge has also been reported in other work(*29*), and could be triggered by either the cracking process or the influence from the EB irradiation.

Another edge configuration is depicted in **Figure 7.5**e, on a pair of long and straight zigzag torn edges with small terraces, there is one segment which has the outermost single row of Mo and S atoms mismatch and lose their connection with the rest lattice (**Figure 7.5**f), consistent with the simulated edge configuration after performing a penetration test on the MoS_2 model (**Figure 7.5**b). However, this part of the edge could easily be sputtered by EB irradiation due to its loose connection with the rest of the lattice.

7.2.2 Slow Fracture in Defective Monolayer MoS_2

Exposing the crack tip region to the EB caused propagation within a fixed location. Before analyzing the fracture dynamics, one question needs to be answered, *i.e.*, what is the driving force for the crack propagation in monolayer MoS_2 under EB? In general, cracks in MoS_2 can be separated into two stages: (1) fast crack stage after popping the 2D membrane by the focused EB, and (2) slow crack stage derived from a continuous EB irradiation that allows us to follow and image the crack tip region to learn its dynamics. The driving force for crack propagations in these two stages are different.

In stage 1, the dominant driving force was the residual mechanical stress derived from the transfer process of MoS_2 monolayers from the growth substrate to the TEM grid. Since this PMMA-assisted transfer process includes steps like baking and cooling of the sample. It introduced mechanical stress to MoS_2 films that covers on circular windows of the TEM grid, similar as a tight 'drumhead'. However, the stressed drumhead will not break spontaneously if there is no needle to puncture it. The focused EB can work as a needle to puncture the sample inside the TEM. Once there was a small hole punctured by the EB, cracks quickly formed and propagated over a long distance. At the same time, the residual mechanical stress from the transfer process of the 2D film was largely released, causing the crack propagation to halt. The crack speed in this stage is too fast to be captured by TEM, so I can only study freshly torn edges, which reflects fast crack propagation behaviour shown in **Figure 7.3**.

I tracked the location of the crack tip by following the brittle torn edges to the apex point and imaged the crack tips with a magnification of 1.5 million times in TEM. Surprisingly, it was found that the crack began to propagate further with a very slow velocity during my imaging. If blanking the EB, the crack position did not proceed. Such a EB-induced slow crack propagation is described as stage 2, during which I tracked the crack propagation dynamics and captured images shown in **Figure 7.7** and **Figure 7.8**. In brief, the crack driving force at this stage was triggered by the line-defect-induced lattice contraction and the rolling up of the fresh torn edges, both of which provided small stress at the crack tip and led the lattice to slowly open up. In terms of the first reason, as discussed in Chapter 6, EB at 80kV can generate S vacancies in monolayer MoS_2, which prefer to agglomerate into line defects. Line defects were prone to aligning along zigzag lattice directions, therefore, causing a remarkably lattice contraction in the armchair direction (**Figure 7.6**a,b, Chapter 6). Since I kept imaging along the fracture edges until reaching the

crack tip, many S vacancies were created by the continuous EB irradiation, forming line defects along fracture edges, which can supply small mechanical stress along the armchair direction at the crack tip to pull the lattice apart. As shown by the schematic illustration in **Figure 7.6**c, if assuming line defects were uniformly distributed along three different zigzag directions in the upper half cracked region close to torn edges (represented by three red solid lines), they will induce lattice contraction along three corresponding armchair directions (represented by three pairs of arrows in white, yellow and black, respectively). Since the torn edges are free ends, while other sides of the MoS_2 membrane are fixed because of their attachment to the Si_3N_4 TEM grid, the resultant strain should align in the direction perpendicular to the upper torn zigzag edge. The mechanical stress is in the same orientation as that of strain. The analysis of the stress generated in the region that is below the bottom torn edge due to the line defects formed at the lower half cracked region is similar, and I can get another mechanical stress heading downwards, being perpendicular to the bottom edge. Such stress provides the driving force for the crack propagation in the slow crack stage. In terms of the second reason, it was found that the freshly cracked edges tend to curl up, which could be induced by a decrease of the surface energy. This behaviour also supplies mechanical stress to open up the lattice at the crack front. Therefore, the penetration test applied in the simulation develops a very similar situation as the real fracture happening under TEM and can mimic the crack behaviour. Another thing which is worth mentioning is that the imaging region by the CCD (charge couple device) camera is smaller than the area that is illuminated by EB. The yellow circle in **Figure 7.6**c schematically indicates the imaging region, while the black circle represents the illumination region. In addition, as I tracked the crack tip along the edges (represented by the green arrow), the region that is in the right part of the illumination area, which cannot be imaged, had a longer accumulated irradiation time by the EB than the central imaging area. It facilitated the formation of large

numbers of line defects there and generated enough mechanical stress for the slow crack propagation. That is the reason why in some images (**Figure 7.7**), even though there were only a small number of vacancies being imaged in the near-tip region, the crack can still propagate forward.

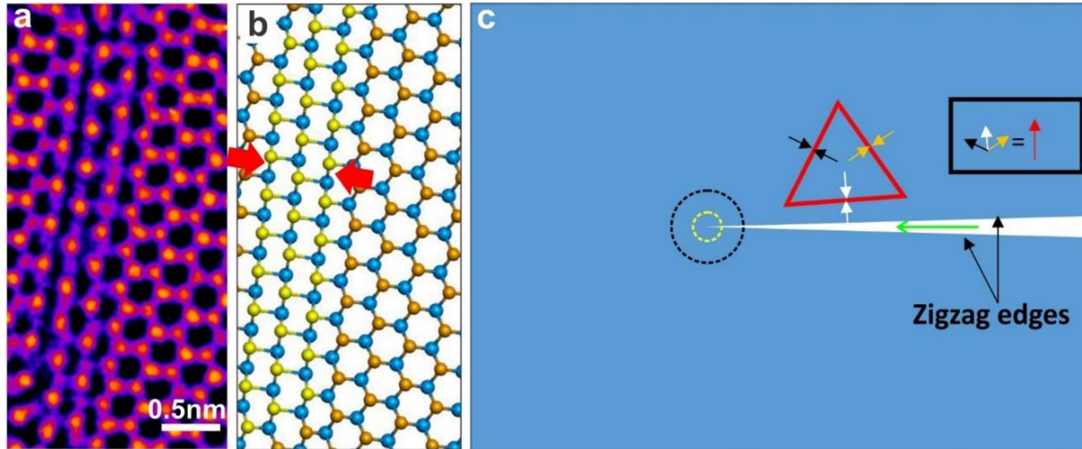

Figure 7.6. Driving force of the crack propagation under the electron beam. (a) AC-TEM image showing the formation of line defects in monolayer MoS_2 due to the missing of three S lines along the zigzag lattice orientation under EB irradiation. (b) Atomic model of the line defect structure. The pair of red arrows shows the lattice contraction along the armchair direction due to the generation of line defects. The blue, yellow and orange spheres indicate the single Mo atom, the single S atom and double S atoms, respectively. (c) Schematic illustration showing the line-defect-induced stress for the slow crack propagation.

A fracture speed of ~ 0.2 nm/s was found under the conditions (**Figure 7.7**a–c) and is slow enough to capture the dynamics with atomic resolution in AC-TEM. Since the EB introduces S vacancies into the MoS_2 lattice, it enabled me to study how the crack propagation was influenced by defects. The crack propagating in the region with a small amount of vacancies encountered more path deflections compared with edges produced in a fast fracture (**Figure 7.1**-**Figure 7.3**), indicating an increased crack instability. The fast crack propagation occurred in pristine regions of the MoS_2 that were not exposed to the EB and therefore had minimal defect density. **Figure 7.7**d shows the crack propagation trajectory with respect to two S vacancies (marked by white circles) that are located close to the crack

tip. **Figure 7.7**e shows that the crack deflection occurred at a region between the two S vacancies, After the crack front passed through, the two S vacancies disappeared. This indicates that the influence between the crack tip and defects in materials is two-way rather than one-way. Vacancies trigger the path deviation of the crack tip due to the structural incoherence, and in turn, the stress field concentrated around the crack front gives rise to the migration of vacancies. Therefore, an accurate prediction on the deflection position of a crack could be complex, as it is not simply determined by the location of a static vacancy but is governed by a dynamic process involving a mutual effect between the vacancy and the crack front. To confirm the crack tip as the dominant factor for the migration of these two S vacancies and exclude the impact from the EB radiation, I monitored another four S vacancies situated away from the crack path (marked by green circles in **Figure 7.7**d), where the stress field is reduced. All of them kept unmoved after the crack propagated through this region (**Figure 7.7**e). MD Simulations with 1% S vacancies under the same loading condition (**Figure C3**) show different crack propagation compared to pristine MoS_2 (**Figure 7.4**b), in agreement with the experimental results.

In addition, stress concentrated at the crack tip induces lattice distortions, causing the regularly stacked double S atoms in the (001) crystal orientation to split (**Figure 7.7**g,h and **Figure C3**a,b). However, there is no obvious lattice reconstruction in the tip region. The crack typically propagates by directly unzipping the Mo-S bond (marked by A and B in **Figure 7.7**h) perpendicular to the tearing path along the zigzag direction. Once the crack tip passes, the distortion in the bonding is reduced, but with some of the S atoms on the S-terminated edge lost or reconstructed to out-of-plane positions.

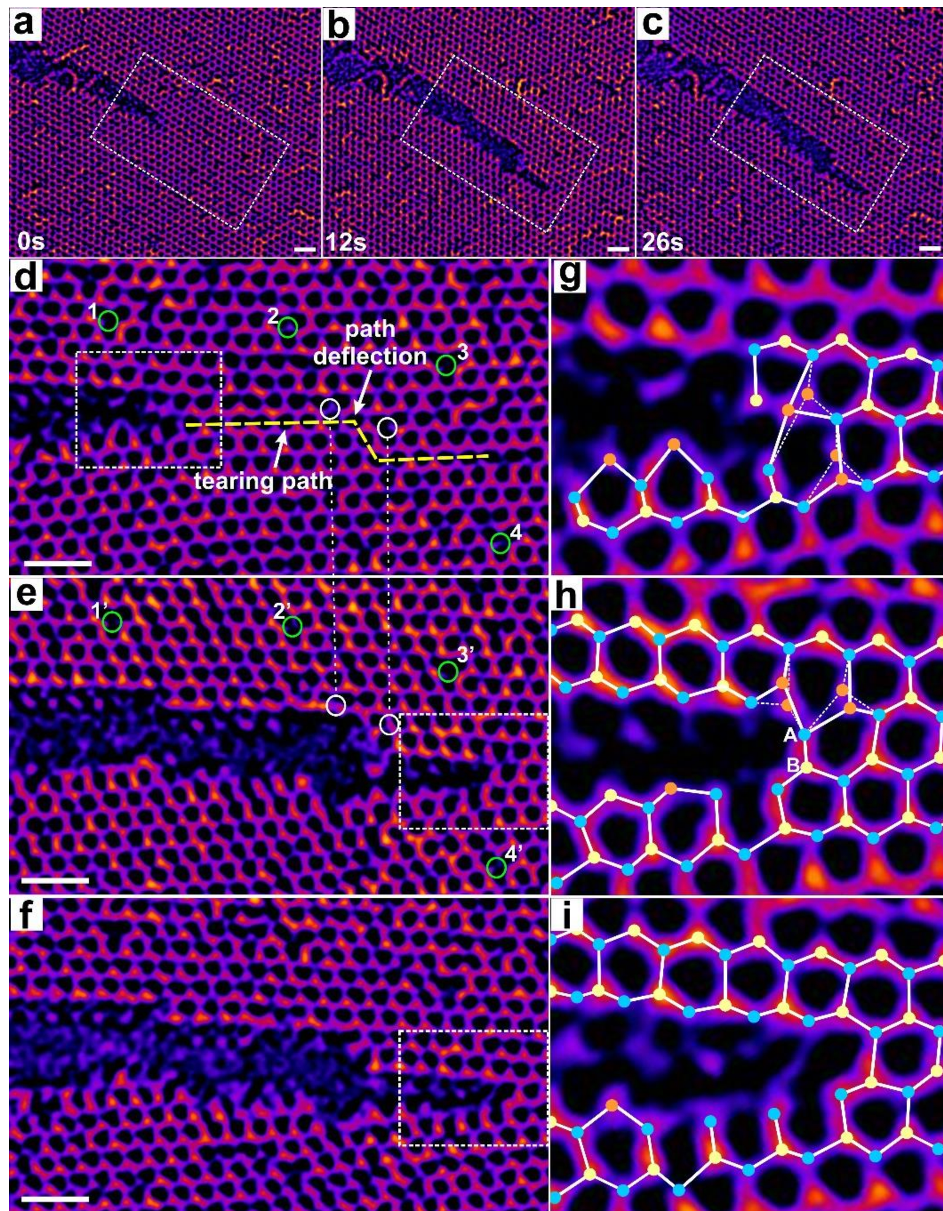

Figure 7.7. Time series of AC-TEM images showing *in-situ* dynamics of MoS_2 crack propagation in a mildly defective region. (a–c) Time series of AC-TEM images showing crack movement through a mildly-defective region, having a low concentration of S vacancies. (d–f) AC-TEM images showing the detailed propagation of the crack tip, marked in the region of the white dashed boxes in panel a, b and c, respectively. The white circles in (d) indicate two S vacancies close to the crack path. However, these two vacancies disappeared after the crack tip passes through, as two locations where sitting S vacancies were replaced by regular stacked double S atoms, marked by two white circles in (e). The yellow dashed line in panel d represents the tearing path of the crack front with a white arrow indicating the path deflection point, situating between two S vacancies. The green circles numbered from 1 to 4 are used to show four S vacancy defects located farther away from the tearing path, compared to those two vacancies marked by white circles. Their locations in (e) are labelled by green circles with corresponding numbers from 1' to 4', respectively. (g–i) AC-TEM images of

the crack tip region marked in white boxes in (d–f), respectively, with atomic models overlaid. The blue, yellow and orange circles represent the single Mo atom, double S atoms and the single S atom, respectively. All scale bars are 1 nm.

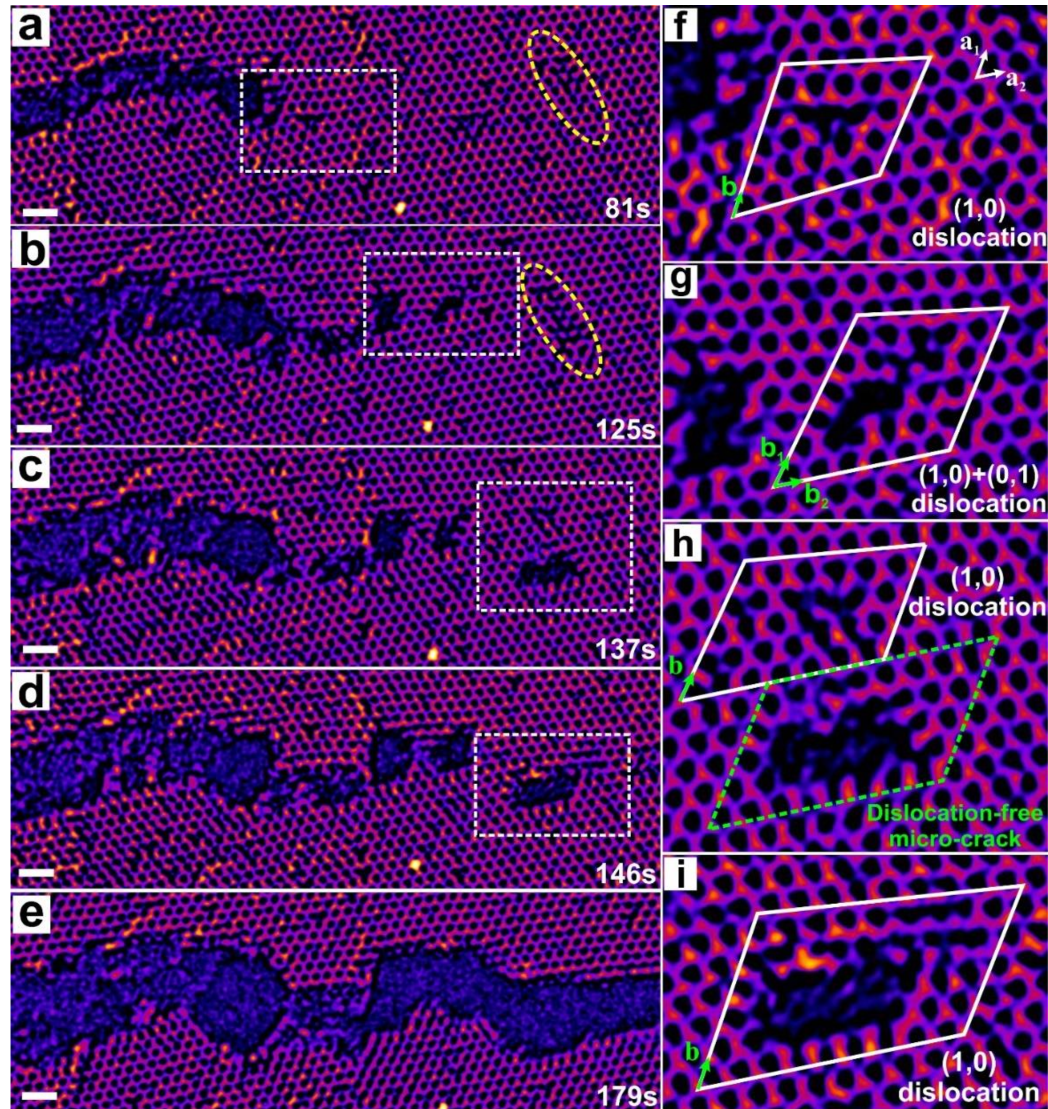

Figure 7.8. Time series of AC-TEM images showing the *in-situ* crack propagation within a moderately defective MoS_2 region containing an increased number of vacancy defect. (a–e) Time series of AC-TEM images of crack propagation across an area with a medium concentration of S vacancies, showing the creation of dislocations and micro-cracks ahead of the crack tip marked by white dashed rectangles. The yellow ellipses in (a,b) show the aggregation of some S vacancies into line defects, which subsequently evolve into dislocation pools in (c) as the crack tip approaches. (f–i) AC-TEM images of regions marked in white dashed boxes in (a–d), respectively. Dislocations with corresponding Burgers' vectors, labelled by green arrows, are shown by drawing Burgers' circuits in white. Dislocation-free micro-crack is marked by green dashed lines. All scale bars are 1 nm.

Increasing the vacancy defect concentration in front of a crack tip results in distinctly different crack propagation behaviour. Instead of the cleavage of lattice planes along zigzag directions, the crack front emits dislocations and micro-cracks ahead of the tip with small regions of dislocation-free lattice trapped in between (**Figure 7.8**a-e). Simulations show similar dislocation formation when increasing S vacancy density up to 20% (**Figure C4**a-e). The Burgers vector of the dislocation region shows two types, (1,0) dislocation and (1,0) + (0,1) dislocation, constructed from two $|b(1,0)| = 3.1$ Å dislocations of (1,0) and (0,1) (**Figure 7.8**f-i).(*193*) All these dislocation forms can be identified in the simulation snapshots at the crack tip as shown in **Figure C4**f-i for moderately defective samples. The generation of dislocations blunted the crack tip compared to the fracture front having atomic sharpness in **Figure 7.2** and **Figure 7.7**, making the crack perform in a more ductile fashion. A fracture velocity of ~0.07 nm/s in this moderately defective region is the lowest speed measured, compared to the pristine and mildly defective regions. It could be attributed to the creation of dislocations and micro-cracks ahead of the crack tip, as well as a frequent shift of the crack direction. The shielding effect of dislocations and micro-cracks could partly protect the crack tip from the surrounding stress, rendering the crack front to be arrested temporarily until it splits the trapped lattice in between. Additionally, the continuous creation of dislocations ahead of the crack front decreases the vacancy density in this region (comparing **Figure 7.8**a with **Figure 7.8**d,e), indicating that the dislocations are partly generated by the aggregation of vacancy defects. Furthermore, large-area dislocation pools are formed by the coalescence of small dislocation cores with dislocation-free micro-crack (**Figure 7.8**h,i). All of these features indicate an increased level of plastic deformation in defective monolayer MoS_2, which results in a 'brittle-to-ductile' transition of the crack mode.

7.2.3 Fracture Toughness Calculation of Defective Monolayer MoS_2

Using MD simulations, it was found that the defects in MoS_2 beyond a critical density can generate a strong collective effect to delay the propagation of atomic crack tip and such mechanism is not shown in graphene. **Figure 7.10**a schematically shows that randomly distributed S vacancy defects beyond 10% in MoS_2 aggregate to form line defects that are distinctly different to the vacancy aggregates in graphene, for which increasing vacancy density results in dislocation pairs and then finally small holes. This result is supported by the observation that the application of EB dose to a MoS_2 in AC-TEM results in vacancies aggregating to form line defects (**Figure 7.9**). The computational simulations of MoS_2 (**Figure 7.10**b) and graphene (**Figure 7.10**c) show that the line defects in MoS_2 helps to guide and deflect the crack in propagation but not for the small holes and dislocation in graphene. Such mechanism contributes to the enhanced energy release rate (G_C) and fracture toughness (K_{IC}) for defected MoS_2 but not for graphene (**Figure 7.10**d,e). It is noted that our calculations for graphene fracture agree with previous experimental and simulation results.(*188*, *194*) Surprisingly, the fracture toughness for mildly and moderately defective MoS_2 can exceed that of graphene, **Figure 7.10**e. This is attributed to the way in which the atomically sharp crack tips interact with the line defects in MoS_2 compared to graphene.

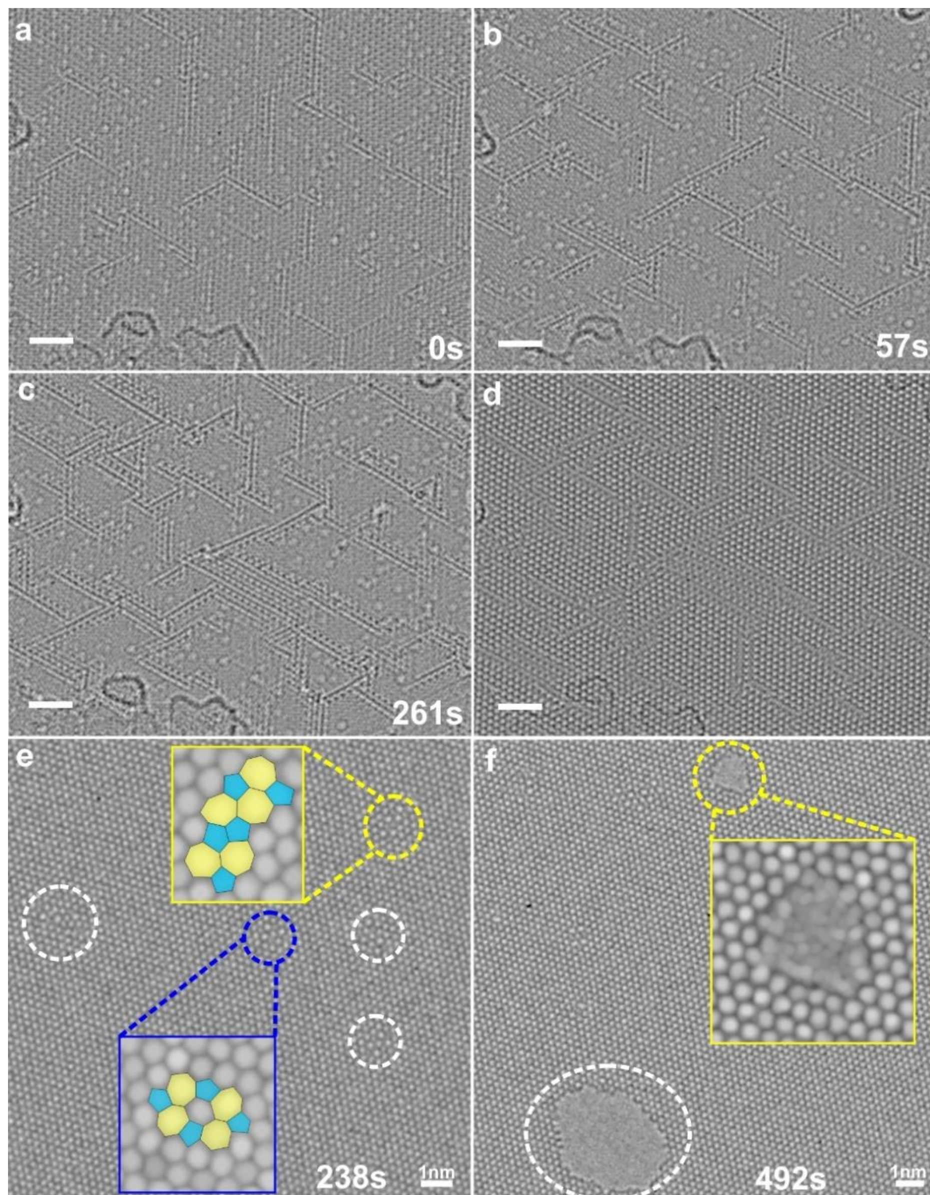

Figure 7.9. Structure evolution comparison between monolayer MoS_2 and graphene under a continuous electron beam irradiation. (a-c) AC-TEM images showing the configuration evolution of monolayer MoS_2 under the same electron dose as that I used when imaging the crack propagation. I applied a nonstandard defocus value rather than the ‘optimal’ Scherzer focus to ‘filter’ the pristine MoS_2 but highlight the defect structures like vacancies and line defects. (d) AC-TEM image taking under the standard defocus value close to the Scherzer focus, which proves that those highlighted configurations in (a–c) are vacancies and line defects rather than dislocation pools. Scale bar: 2nm. (e-f) AC-TEM images showing the generation of vacancy clusters, dislocation pairs and small holes on graphene under a prolonged EB illumination, which is different from the lattice evolution on monolayer MoS_2, where S vacancies are prone to aggregating into line defect networks.

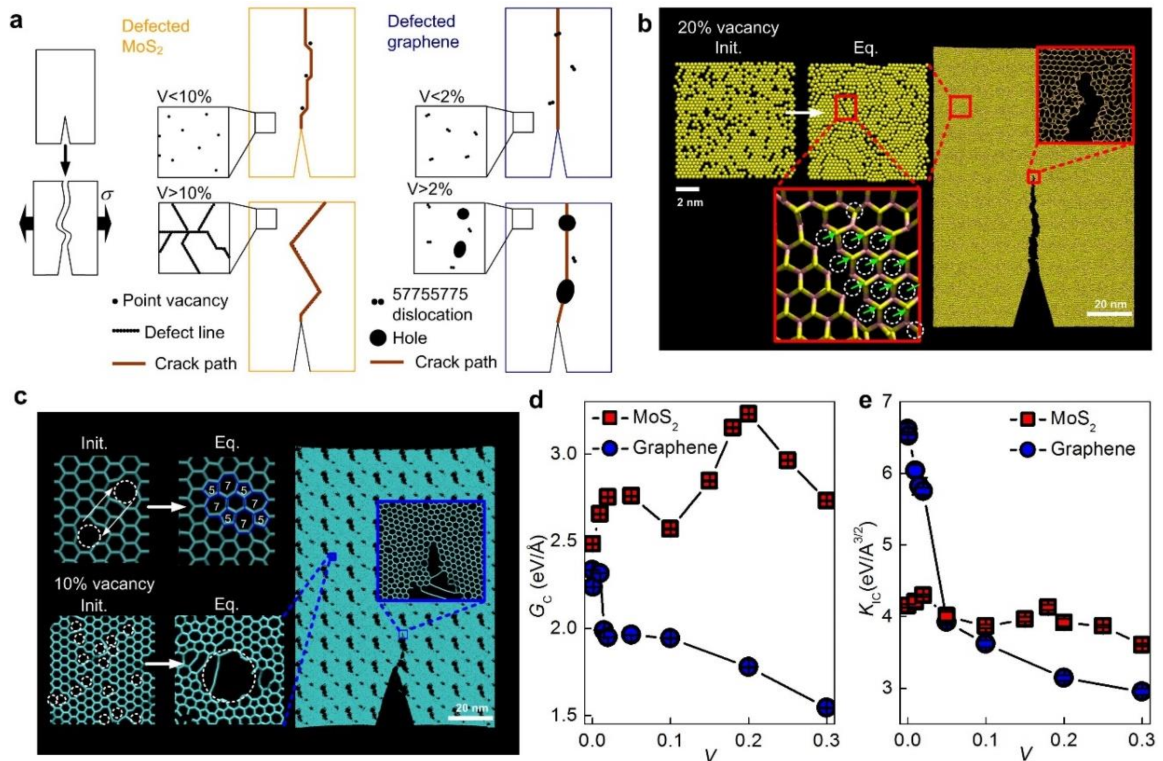

Figure 7.10. The enhanced fracture toughness of defected MoS_2 and its molecular mechanism. (a) Schematic shows that the tensile loading force to material samples was applied on the left and right boundaries until their total failure in the computational simulations. Fracture of defected MoS_2 with different vacancy density (V) is featured by the deflected crack pathway which is very different from what is seen in graphene. The crack path associates with the conformation of defects at equilibrium as vacancies in MoS_2 can aggregate and form a defect network composed of lines to guide the crack propagation. (b) The simulation snapshots of a defected MoS_2 sample with initially randomly distributed defects with V=20% before and after equilibration, which shows the merging of vacancies and forming of a defect network. The defect network deflects the crack pathway during fracture. (c) The simulation snapshots of a defected graphene sample with initially randomly distributed defects with V=10% before and after equilibration, while two neighbouring vacancies can be healed by forming a 57755775 dislocation, more vacancies form holes instead. The crack pathway in graphene is not significantly deflected. (d–e) The comparison of the energy release rate (G_C, panel d) as the energy release of unit length of the 2D material during fracture and fracture toughness (K_{IC}, panel e) as a function of vacancy density for MoS_2 and graphene, which shows MoS_2 has a higher energy release rate and an superior fracture toughness to graphene once mildly or moderately defected.

7.3 Conclusion

In summary, the findings enable validation of many theoretical and computational studies that form the foundation of fracture mechanics, but which were previously too difficult to observe at the single atom level in thick materials. Crack tips remained atomically sharp during propagation and in dislocation nucleation. The atomically sharp crack does not have infinitely large stress at the tip because the interactions between defects and crack tip can lead to deflections, crack blunting and plastic yielding by rearranging of the defects. Increasing the density of defects in MoS_2 leads to enhanced fracture toughness, not observed in graphene, as crack tips become blunt and the propagation speed reduces dramatically, which is associated with increased fracture toughness.

Chapter 8 Conclusion and Outlook

8.1 Conclusion

Monolayer MoS_2, which has an ultra-thin layered structure and a direct bandgap of 1.9 eV, holds potential applications in nanoelectronics, optoelectronics and flexible devices.(*9*) It also provides possibilities to control the spin and valley degree of freedom due to its broken inversion symmetry and a strong spin-orbital coupling, making it as a promising material for spintronic and valleytronic devices.(*8*) The widespread use of this material is based upon establishing a scalable, low-cost and environmentally-friendly production method, which enables the achievement of high-quality, large-area monolayer MoS_2 with big grain sizes and homogeneous thickness. CVD may open up an avenue to realize these goals, since it has been proven to be effective in the fabrication of graphene.

My first task is to establish a growth strategy capable of producing monolayer MoS_2. MoO_3 and S powder are utilized as precursors with independent temperature control profiles. The CVD system is artificially designed to generate a sharp spatial gradient of gaseous MoO_3 on the SiO_2/Si substrate, which both increases the synthesis flexibility and provides a platform to explore the impact of this factor on the MoS_2 growth. High-quality monolayer MoS_2 domains are obtained using this hydrogen-free, atmospheric pressure CVD (APCVD) approach, verified by a host of characterizations, including SEM, AFM, Raman and PL

spectroscopy. A regular spatial-dependent shape evolution of MoS_2 domains from triangular to hexagonal geometries is also observed, which is explained by the local changes in the Mo:S ratio of precursors (1:>2, 1:2, and 1:<2) and its influence on the kinetic growth dynamics of edges. These progress naturally pushes my synthesis research into the second stage, *i.e.*, optimizing the method to increase the coverage area, growth uniformity and continuity. This task is implemented by two primary modifications on the CVD setup, which enhances the temporal and the spatial homogeneity of the precursor feed-stock on the substrate surface. One optimization is to separate two precursors (MoO_3 and S powder) by adding an inner quartz tube. It stabilises the supply of both gaseous precursors into the reaction zone throughout the growth by avoiding the gradual quench of the MoO_3 powder by the S vapour. The second improvement is to vertically orient the substrate, which drastically alleviates the spatial concentration gradient on the substrate and may passivate the growth sensitivity on the mixture uniformity level of precursor vapours by a switch of the rate-limiting step. Centimetre-scale monolayer MoS_2 films with a grain size of 10-20 μm are gained. Apart from these achievements, a systematic study is carried out to investigate a range of synthesis parameters on the product, including the heating temperature of the MoO_3 powder, the temperature of the growth substrate and the flow rate of the Ar carrier gas. All the knowledge accumulated in this section (Chapter 4) provides an in-depth understanding of the CVD method of monolayer MoS_2 growth and establishes a practical CVD synthesis strategy that has potential to be expanded to the 4-inch quartz tube.

The second part of my work is motivated by the pursuit of preserving the intrinsic properties of CVD-grown monolayer MoS_2 better. This is realized by changing the growth substrate from the 3D amorphous SiO_2 to the 2D CVD-grown, continuous multilayer h-BN films, which can also maintain the overall 2D nature of the vertical heterostructures. Four types of specimens (MoS_2 grown on h-BN films, MoS_2 grown on SiO_2 substrates, MoS_2

transferred on h-BN films, MoS_2 transferred on SiO_2 substrates) are studied to show their variations on the built-in strain and the doping level. The information is obtained primarily through the analysis about the in-plane and out-of-plane vibrational modes in Raman spectroscopy of MoS_2 and the recombination ratio between the neutral exciton and trion in PL spectroscopy. It is found that direct CVD-grown MoS_2 crystals on the h-BN film suffer smaller lattice strain and lower doping. It also possesses cleaner interfaces to ensure a high-quality interlayer contact. The results in this section (Chapter 5) provides a simple and versatile fabrication method of 2D MoS_2/h-BN vertical heterostructures, which has potential to be generalized to create other TMDs/h-BN hybrid structures. The merits of h-BN films on sustaining the pristine properties of monolayer MoS_2 has also been manifested, making it promising in the substrate application in nanoelectronics and optoelectronics.

The third part of my investigation relies on the atomic resolving ability of AC-TEM. It not only empowers me to build up a bridge between the material's atomic configuration and its properties, but also can serve as a highly controllable fine probe to modify the material through defect engineering. It is found that S vacancies can be generated by employing AC-TEM under 80 kV. S vacancies migrate and aggregate into line defects along the zig-zag direction, rendering remarkable lattice compression in the armchair orientation. Lattice distortion of line defects in various length and width is quantitatively studied, which provides accurate structure models to conduct a convincible property prediction by theoretical calculations. DFT calculation shows that the bandgap of the line defect in monolayer MoS_2 decreases as its width broadens, making it perform as a 1D metallic channel embedded in the pristine semiconducting monolayer MoS_2. These results present an avenue for the top-down fabrication of components with distinct electronic properties in the 2D material. If keeping enhancing the electron dose to the monolayer MoS_2, brittle facture happens, showing the crack propagation led by an atomically sharp tip predominantly along

the energetic favourable zigzag direction. Sparse vacancy defects are found to trigger the crack deflection, while an increased defect density induces a brittle to ductile transition of the fracture behaviour due to plastic deformation of lattice structures through vacancy migration and reconstruction. Large-area molecular dynamic simulations are carried out, showing that the toughness of defective MoS_2 surpasses that of graphene because of interactions between the crack front and the vacancy clusters. These results indicate monolayer 2D materials as an ideal platform for the fundamental research on fracture mechanics, which can provide atomic scale details conducive to the insight into crack mechanisms.

To sum up, the thesis covers three broad sections: (1) establishing versatile APCVD methods to produce centimetre-scale, high-quality, continuous monolayer MoS_2 films with big grain sizes on SiO_2/Si substrate, and having insights into the growth mechanism; (2) developing an all APCVD method to fabricate 2D MoS_2/h-BN vertical heterostructures, and proving its main advantageous in built-in lattice strain and doping level by studying the vibrational and optical properties through Raman and PL spectroscopy; and (3) investigating the atomic level defects and fracture behaviours of monolayer MoS_2 by operating AC-TEM.

8.2 Outlook

My PhD work can develop along three different directions. First is to upgrade the large-area growth of uniform monolayer MoS_2 films to the 4-inch size CVD system, thus satisfying the industrial requirements on the productivity. To realize this goal, low-pressure CVD (LPCVD) method deserves to be investigated, as it may switch the rate-limiting step from the mass transfer in the APCVD to the surface diffusion/reaction process, thus alleviating the negative impact from the spatial non-uniformity of precursor vapours. This method may excel at achieving large-area, continuous monolayer films with uniform thickness compared with the method of orienting the substrate perpendicular to the mass

flux of precursor vapours in APCVD (section 4.2), as the latter could suffer from the inhomogeneous growth caused by the turbulence especially around the substrate edges. Apart from modifying synthesis recipes, a thorough understanding about the growth mechanism is highly desirable. Many questions need to be answered, including (1) whether the CVD growth of monolayer MoS_2 is the 'absorption–surface reaction' process or the 'gas phase reaction–precipitation' one; (2) what roles do the MoO_3 and S precursors play, respectively, in the MoS_2 nucleation and growth stages; (3) what the detailed chemical reaction procedure is between Mo-based and S-based species absorbed on the substrate surface to form MoS_2, such as the cleavage of Mo-O bonds, and how it impacts the growth kinetics; (4) can the monolayer MoS_2 growth be self-limited through a careful design of the synthesis strategy or a special choice of the substrate; (5) how to experimentally determine the rate-limiting step of the MoS_2 growth, which involves multi-steps, including the mass transport of precursor vapours, absorption/desorption of precursor molecules on the substrate, surface diffusion of absorbed molecules and the surface chemical reaction process; and (6) how the commonly-encountered impurities in either the precursor powder or in the carrier gas (*e.g.* H_2O and O_2) impact the growth results, product quality and experiment reproducibility, *etc*. To solve these questions, a series of controllable experiments and a range of *in-situ* and *ex-situ* characterizations are required to track the real-time growth procedure.

The second direction is related to the fabrication of 2D vertical heterostructures. An important question which has not been fully answered in my research on the MoS_2/h-BN heterostructures in Chapter 5 is what the microscopic interaction is between the surface of various substrates (*e.g.* SiO_2, h-BN) and the monolayer MoS_2 and how it influences the achievement of the electronic-grade 2D materials. In addition, most research accomplished in the field of 2D vertical heterostructures utilized 2D layered materials, such as graphene,

h-BN and TMDs, as fundamental building blocks to generate new structures for tailoring material's properties. Given the limited species of layered materials, further evolution could rely on expanding the 2D building block library from layered materials to non-layered materials. Challenges may lie in how to obtain the 2D form of non-layered materials, and choosing a suitable 2D layered material as the template could be conducive to both their stabilization and epitaxial growth.

The third direction is to deepen the understanding about the atomic configuration of MoS_2 and to try establishing a bridge between the microscopic structure of MoS_2 with its growth strategy and the material's property. Many topics can be investigated, including (1) resolving the boundary structure between two merged grains with different levels of the crystal orientation mismatch, checking whether two grain boundaries realize the atomic stitching or overlap with each other followed by an *in-situ* measurement on the electric property at the grain boundary; (2) linking different polymorphs of as-grown MoS_2 revealed by HRTEM with its synthesis conditions, *etc.* In addition, improving the manipulation ability on the MoS_2 lattice by employing the state-of-the-art STEM would also be of particular interest, which may help tailor the material property through the modification on the lattice periodicity,

Appendix A

Supporting Information of Chapter 5

A.1. CVD synthesis and transfer of h-BN films

The growth of few-layer h-BN films were performed using an APCVD method with a copper catalyst (Cu, 25µm, Alfa Aesar).(*195*) Two separated furnaces were used to independently control the evaporation temperature of the precursor, ammonia borane, and the growth temperature on the substrate. Five milligrams of ammonia borane powder (≥97%, Sigma Aldrich) and a copper foil with the size of 1cm by 1cm were loaded into the centre of two furnaces, respectively. Before the growth of h-BN, the copper was annealed at 1,000 ℃ for 60 min with 555 sccm of argon and hydrogen mixed gas (~0.35% hydrogen) to larger the grain size of copper and smooth the substrate surface. The h-BN growth was carried out with the typical temperatures for the precursor and the substrate being ~80 ℃ and ~1,000 ℃, respectively, under the flow rate of 80 sccm (~22% hydrogen and 78% argon). The growth lasted for 40 minutes followed by fast cooling of the sample by removing it from the hot-zone of the furnace under the protection of the argon and hydrogen gas mixture. **Figure A1**a shows the SEM image of the CVD-grown continuous h-BN film on the substrate of copper *via* the aforementioned method. The Raman spectrum, where the characteristic peak is

centred at ~1365 cm^{-1}, indicates the film thickness to be multilayer (**Figure A1**b). **Figure A1**b,c give a typical AFM measurement, showing the thickness of the h-BN film is ~ 3nm after transferring it on the SiO_2/Si substrate.

For the transfer process of CVD-grown h-BN film from copper (Cu) to the SiO_2/Si substrate, the surface of the as-grown h-BN/Cu sample was first spin-coated with a thin film of poly (methyl methacrylate) (PMMA) followed by floating it on the ~0.1 mol/L ammonium persulfate [$(NH_4)_2S_4O_8$] solution to etch Cu substrate away. The PMMA/h-BN film was transferred into the deionized water for 3 times before loading it onto the central area of a bare SiO_2/Si substrate. The h-BN/SiO_2/Si sample was first air-dried overnight and then baked at ~180°C for 15 minutes to ensure good interface contact between h-BN and the SiO_2 surface. Finally, PMMA was washed off with acetone at 40°C for 3h.

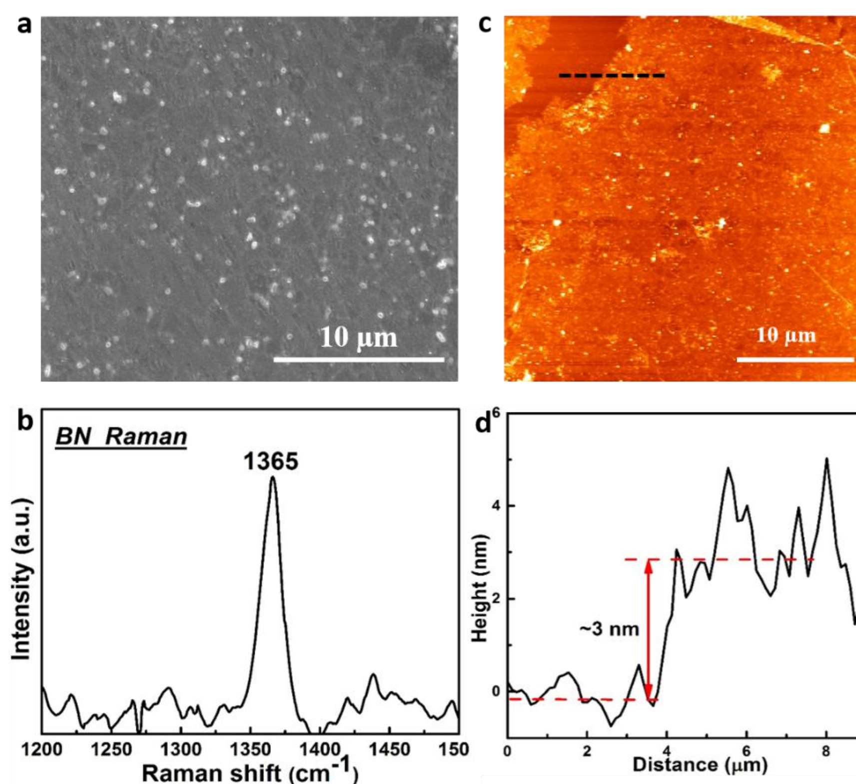

Figure A1. (a) Typical SEM image of the CVD-grown h-BN film on the substrate of copper. (b) Raman spectrum of the h-BN film after transferring it onto the SiO_2/Si substrate. (c,d) AFM image of h-BN film transferred on the SiO_2/Si substrate and corresponding height profile taken across the black dash line in panel c.

A.2. AFM measurements of monolayer MoS_2 grown on h-BN and on SiO_2 and discussion on the h-BN surface roughness change before and after MoS_2 growth

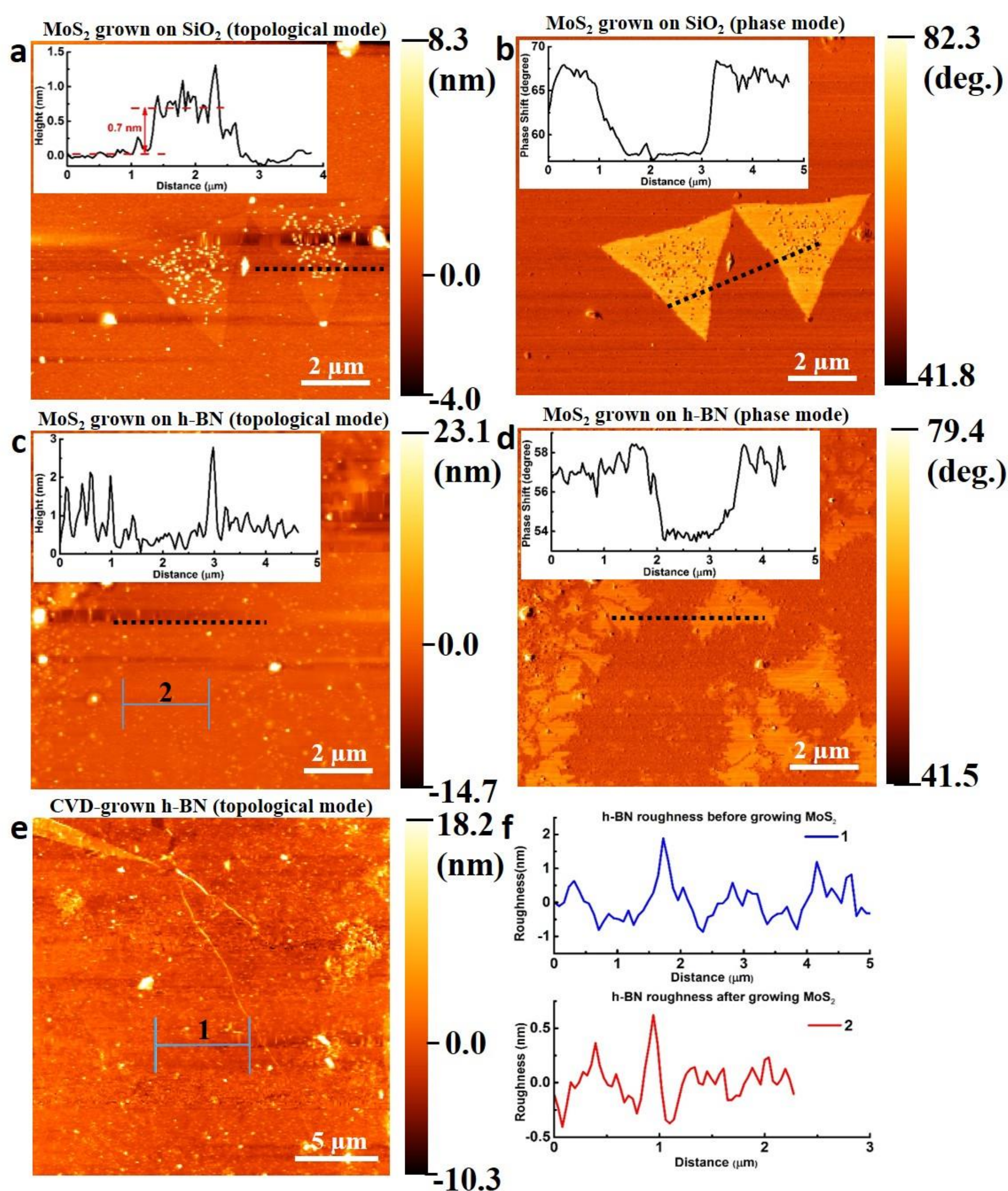

Figure A2. (a-d) AFM images of MoS_2 grown on SiO_2 and on h-BN films, respectively. Panel a and c were measured under topological mode, while b and d were under phase mode. The insets show the surface height profiles or phase shift curves along the corresponding black dashed lines in each image. (e) AFM image of CVD-grown continuous multilayer h-BN films transferred on the SiO_2 surface before MoS_2 growth. (f) Surface roughness profiles for h-BN films before and after growing MoS_2, which were taken across the blue straight lines marked by 1 and 2 in panel e and d, respectively.

We did AFM measurements of monolayer MoS_2 grown on h-BN and compared them with MoS_2 grown on SiO_2. Under topological mode, the outline of MoS_2 domains is much more detectable when they are grown on SiO_2 than on h-BN films (**Figure A2** (a) and (c)). This is further convinced by the height profiles taken along corresponding black dashed lines in each image. For MoS_2 grown on SiO_2, the domain thickness is shown to be ~0.7 nm, which is consistent with that of MoS_2 monolayers. However, for MoS_2 grown on h-BN, we are unable to read out the MoS_2 thickness, because it is covered up by the height fluctuations of h-BN film surface. Even though monolayer MoS_2 on h-BN is invisible using topological mode, thanks to the elasticity difference among materials, under phase mode, the coverage regions of MoS_2 on h-BN can be seen (**Figure A2**(d)), since the AFM tip vibration has a phase change of ~3 degrees when moving from h-BN to MoS_2:h-BN heterostructures surface. The phase mode measurement is also applicable to detect MoS_2 on SiO2 (**Figure A2**(b)). Another interesting phenomenon is that the surface roughness of h-BN was decreased after experiencing the CVD growth procedure of MoS_2 on it. **Figure A2**(e) is the AFM image of transferred CVD-grown continuous h-BN films before the growth of MoS_2. By measuring the roughness profiles along the blue straight lines marked by 1 and 2 in panel e and c, which correspond to h-BN surface before and after MoS_2 growth, respectively, it was found that the h-BN surface roughness before MoS_2 growth is ~3-4 times higher than that after MoS_2 growth. The average roughness of curve 1 is 0.3-0.4 nm, while for curve 2, it is ~0.1nm. The roughness curves were measured using the software of Gwyddion with a line width of 40 pixels. This indicates that the MoS_2 CVD growth procedure can, to a certain extent, enhance the surface flatness of h-BN. However, the transferred h-BN film surface roughness after MoS_2 CVD growth is still higher than that of the bare SiO_2/Si substrate, which is measured to be ~0.03nm in average. This could be attributed to the nature of flexibility of 2D h-BN films.

Appendix B

Supporting Information of Chapter 6

B.1. Bond length measurement on DFT-calculated SV and DV atomic models with and without the consideration on the existence of S vacancies around

As depicted in **Figure B1**a,b, based on the DFT calculation, the generation of DV will induce the shrinkage of the Mo-Mo atomic distances from 3.12 Å to 2.75 Å, yielding a contraction percentage of around 12%. Moreover, the lattice compression between double Mo atoms are equal along three directions when there is no other SVs around. However, if taking the presence of neighbouring, randomly distributed SVs into consideration, the contraction ratio along different lattice orientations varies, being consistent with experimental observations in **Figure 6.2**j, yielding 2.80, 2.75, 2.60 Å, respectively, as shown in **Figure B1**c,d. This indicates that presence of other SVs could exert anisotropic influence on the lattice configuration of DV. **Figure B1**e–h show the DFT-calculated atomic models and the corresponding multislice TEM image simulations of SV with and without the consideration on neighbouring SVs. It can be seen that the generation of SV triggers negligible Mo-S bond contraction at the point defect site, yielding a compression ratio of around 1.1%, which agrees well with the experimental observation in **Figure 6.2**i. Moreover,

similar with the case in DV, the random-distributed SVs around the central SV causes the inhomogeneous lattice contraction along three armchair directions.

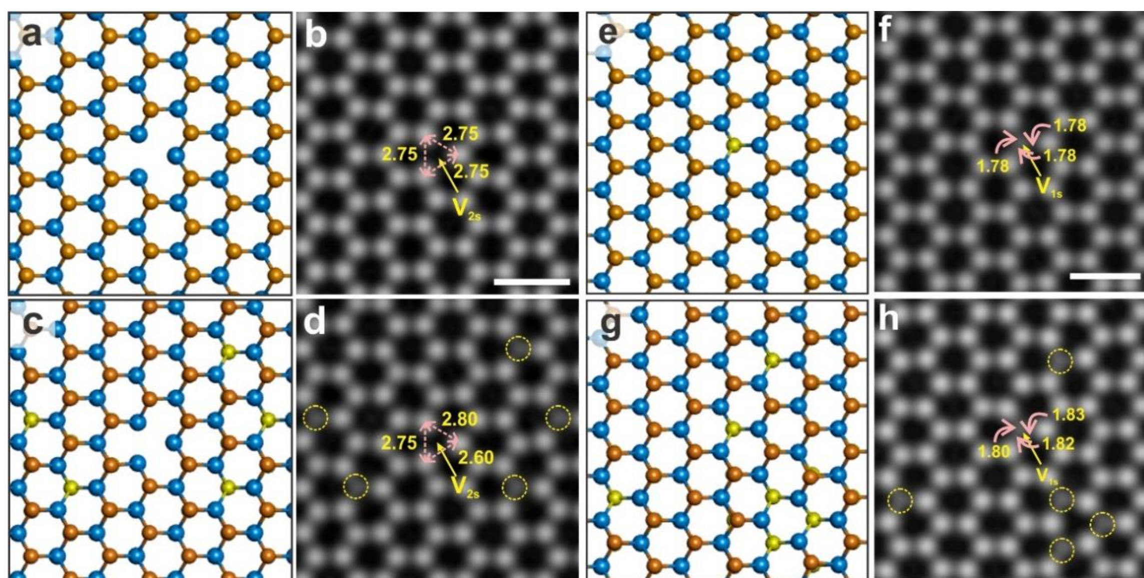

Figure B1. (a,c) DFT-calculated atomic models for DV with and without the consideration on surrounding SVs, respectively. (b,d) Multislice TEM image simulations based on the atomic model shown in panel a and c, respectively. The Mo-Mo interatomic distances in the absence and presence of neighbouring SVs are measured by drawing the intensity line profiles. (e,g) DFT-calculated atomic models for SV with and without the consideration on surrounding SVs, respectively. (f,h) Multislice TEM image simulations based on the atomic model shown in panel a and c, respectively. The Mo-S atomic distances in the absence and presence of neighbouring SVs are measured by drawing the intensity line profiles. The unit for each value is Angstrom. Scale bar corresponds to 0.5 nm.

B.2. Atomic model showing one possible 1SVL structure with a residual line of single S atoms sitting at different atomic planes.

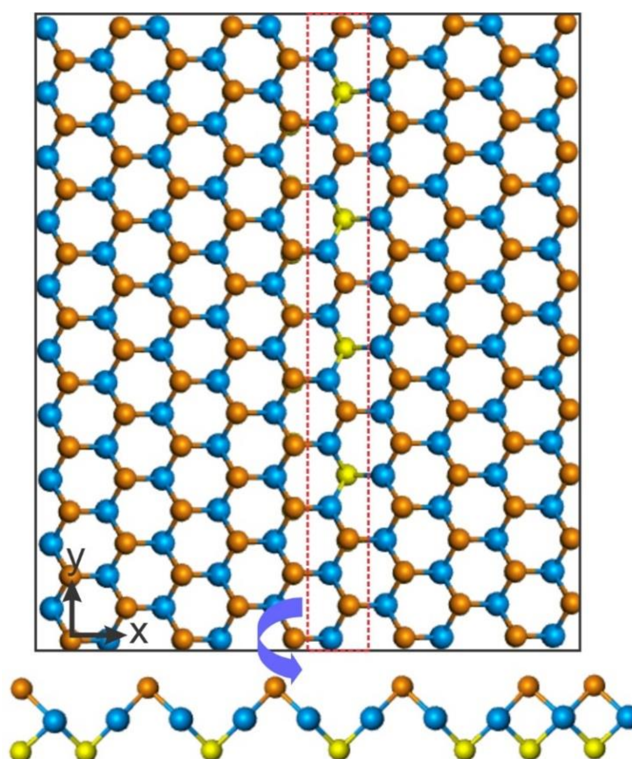

Figure B2. Atomic model showing one possible 1SVL structure having a residual line of single S atoms constructed in an up-down-up-down configuration. The top panel is the atomic model in the projection view, where blue, orange and yellow spheres represent Mo atom, single S atom in the top lattice plane and the single S atom in the bottom lattice plane, respectively. The bottom panel is the atomic model seen from the x direction at 1SVL, which reveals the up-down-up-down arrangement of single S atoms at the line defect. DFT calculation reveals that such lattice arrangement having single S atoms in the same line sitting at different atomic planes is more energy unfavourable than the atomic structure shown in **Figure 6.4**e.

B.3. Detailed locations of taking intensity line profiles on 1SVL, 2SVL and 3SVL in different lengths

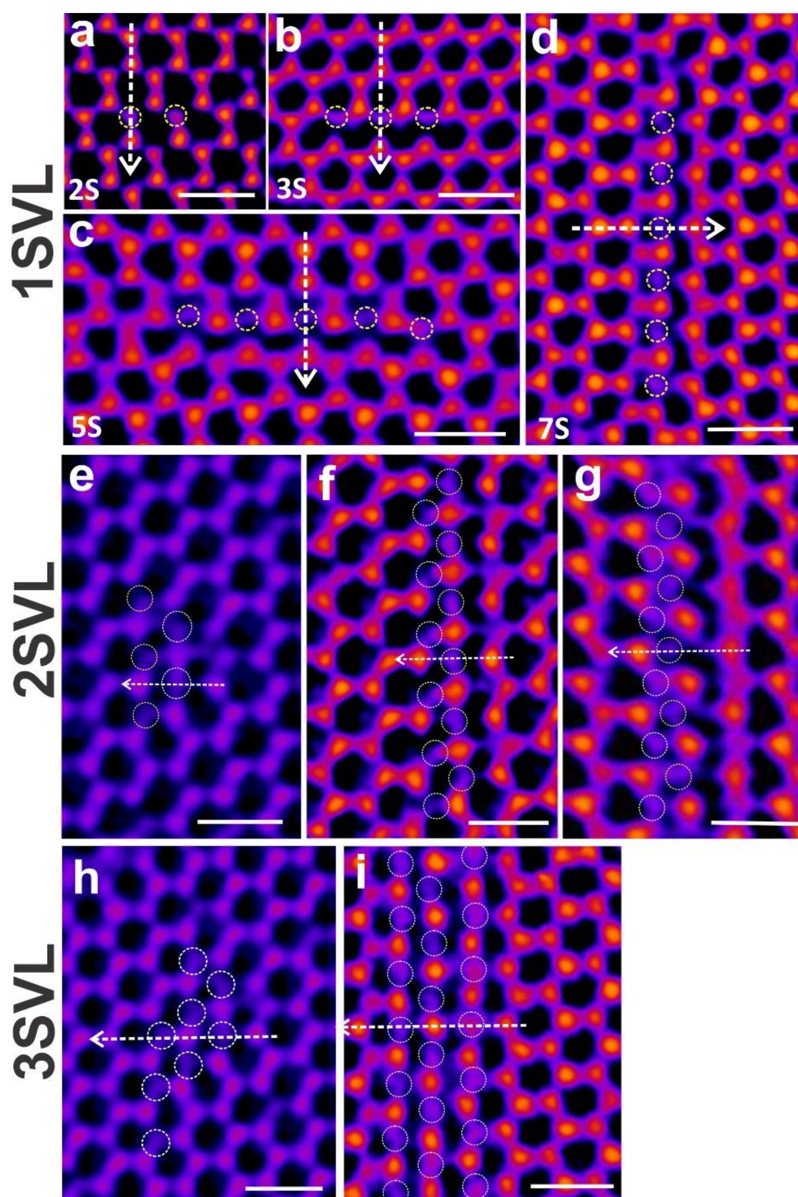

Figure B3. (a–d) AC-TEM images of 1SVL in different lengths, shown in **Figure 6.4**a–d, respectively. White arrows indicate the exact measurement locations of boxed intensity line profiles shown in **Figure 6.4**g. (e–g) AC-TEM images of 2SVL in different lengths and types, shown in **Figure 6.3**f, **Figure 6.6**a and **Figure 6.6**e, respectively. White arrows indicate the exact measurement locations of boxed intensity line profiles shown in figure 5m, corresponding to short type 1 2SVL, long type 1 2SVL and type 2 2SVL, respectively. (h,i) AC-TEM images of 3SVL in different lengths, shown in **Figure 6.3**g and **Figure 6.7**d, respectively. White arrows indicate the exact measurement locations of boxed intensity line profiles shown in **Figure 6.7**g, corresponding to short-3SVL, long-3SVL, respectively. Scale bar corresponds to 0.5 nm in all panels.

B.4. AC-TEM images for 2D displacement and strain maps

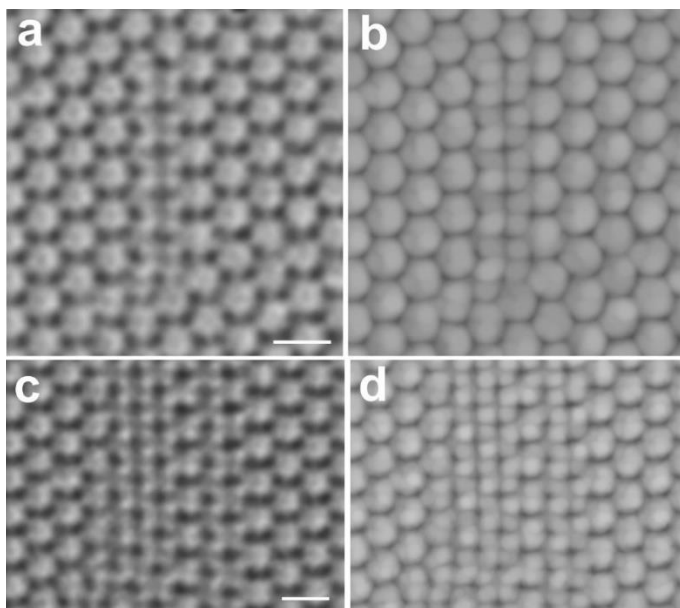

Figure B4. (a,c) AC-TEM images of type 1 2SVL and 7SVL used for the generation of 2D displacement and strain maps in **Figure 6.8**. (b,d) Maximum-filtered AC-TEM images corresponding to panel a and c, respectively, which show atom positions more clearly. All scale bars correspond to 0.5 nm.

B.5. Bond length change at line defects

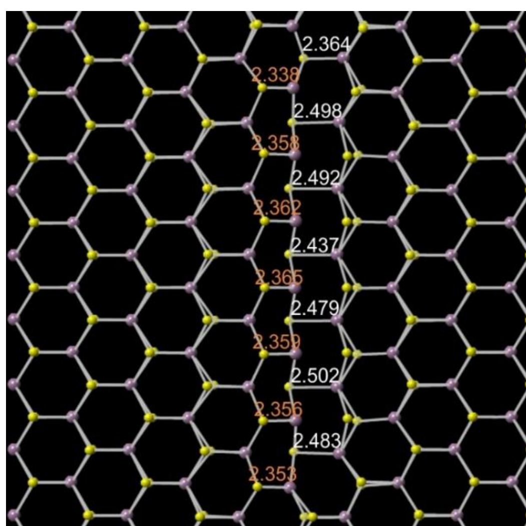

Figure B5. DFT-calculated MoS_2 lattice structure containing type 1 2SVL. The Mo-S bond lengths in the defective region are labelled. The standard Mo-S in the pristine lattice is 2.383 Å.(*196*) It shows that the bond length variation at line defects do not exceed 5% compared with the pristine Mo-S bond. The pink and yellow spheres represent Mo and S atoms, respectively.

B.6. Discussion on the displacement and strain maps

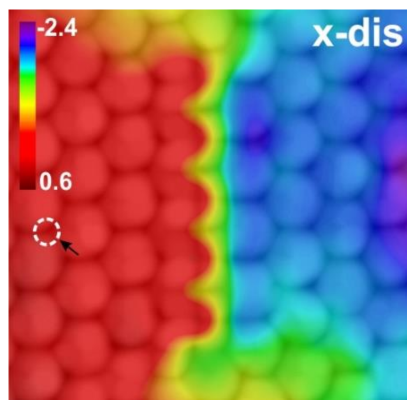

Figure B6. 2D displacement map in the x direction of type 1 2SVL. The TEM image used here is the same as that for **Figure 6.8**(i)a. The reference point is marked by a white circles together with a black arrow beside it.

The 2D displacement maps in **Figure 6.8** are generated by first identifying the precise positions of atoms from the AC-TEM images having sulphur vacancy lines and then subtracting them from their expected locations in a pristine MoS_2 lattice. The strain maps are generated through first doing the scattered interpolant on the displacement map by applying the method of natural neighbour interpolation, and then calculating the strain between adjacent interpolating points. The 'scatteredinterpolant' function together with the 'meshgrid' function in the Matlab software are able to transform the displacement values in a hexagonal lattice into a meshgrid format, which facilitates the drawing of 2D contour plot or 3D surface plot. The colour of the displacement map indicates the absolute displacement values at different sites, which is related to the reference point chosen. However, the lattice strain is revealed by the displacement gradient on the displacement map rather than the absolute displacement values. The sharper the colour changes in the displacement map, the higher the strain will be. Therefore, the strain does not depend on the reference point I choose. To better confirm this, I did a comparison experiment on the generation of the displacement map in the x direction for the same AC-TEM image by choosing different reference points.

In **Figure 6.8**(i)a, I originally chose one single Mo atom on the 2SVL as the reference point, where I think the displacement at this atom is zero compared with a pristine MoS_2 lattice. I can choose an arbitrary atom as the reference point and get very similar displacement map. As shown in **Figure B6**, I chose an atom in the pristine area which is indicated by the white circle as the reference point and obtained the corresponding displacement map. The colour gradient is very similar as **Figure 6.8**(i)a. The only difference is the absolute displacement value for each atom, as this value is determined by the reference point. This indicates that the choice of the reference point will not affect the displacement gradient, thus having no influence on the strain calculation. The reason why choosing a single S atom in the 2SVL as the reference point rather than an arbitrary atom in the lattice is because this can make the colour scale of the displacement map to be symmetric, which is from -1.5Å to 1.5Å. It will be easier to understand the relative movement direction of atoms around the line defects.

In addition to the continuous displacement and strain maps shown in **Figure 6.8**(i), I have also drawn the 2D scattered displacement and strain maps without doing interpolations. As shown in **Figure B7**a,b, the discrete displacement values of each atom in the x and y direction of the AC-TEM image are revealed by the spots' colours, respectively. The 2D scattered strain maps are generated by calculating the difference between the displacement values at two adjacent atomic positions, divided by the distance between these two atoms. For example, to determine $\Delta Ux/\Delta x$, I can pick two horizontally adjacent atoms numbered by 1 and 2 from the 2D displacement map of U_x in **Figure B7**a, and then calculate $\{U_x(2)-U_x(1)\}/\{x(2)-x(1)\}$ to get $\Delta Ux/\Delta x$ at the location marked by 1 in **Figure B7**c. Similarly, $\Delta Ux/\Delta x$ at location 2 in **Figure B7**c are produced by calculating $\{U_x(3)-U_x(2)\}/\{x(3)-x(2)\}$ based on **Figure B7**a. To obtain $\Delta Ux/\Delta y$, I can pick two vertically adjacent atoms in the same line numbered by 1 and 2' in Figure S14a, and then calculate $\{U_x(2')-U_x(1)\}/\{y(2')-y(1)\}$ to get $\Delta Ux/\Delta y$ in location 1' in Figure S14e. Similarly, $\Delta Ux/\Delta y$ at location 2' in

Figure B7e is produced by calculating {U_x(3')-U_x (2')}/{y(3')-y(2')} based on **Figure B7**a. $\Delta Uy/\Delta x$ and $\Delta Uy/\Delta y$ can be obtained by applying the same calculation method for **Figure B7**c and e on the 2D scattered displacement map of U_y, respectively. I have also drawn the scattered displacement and strain maps corresponding to the 7SVL example in **Figure 6.8**(ii), as shown in **Figure B8**. The 2D scattered strain maps show good consistency with the continuous contour maps in **Figure 6.8**, indicating the validity of our strain map generation in the main text.

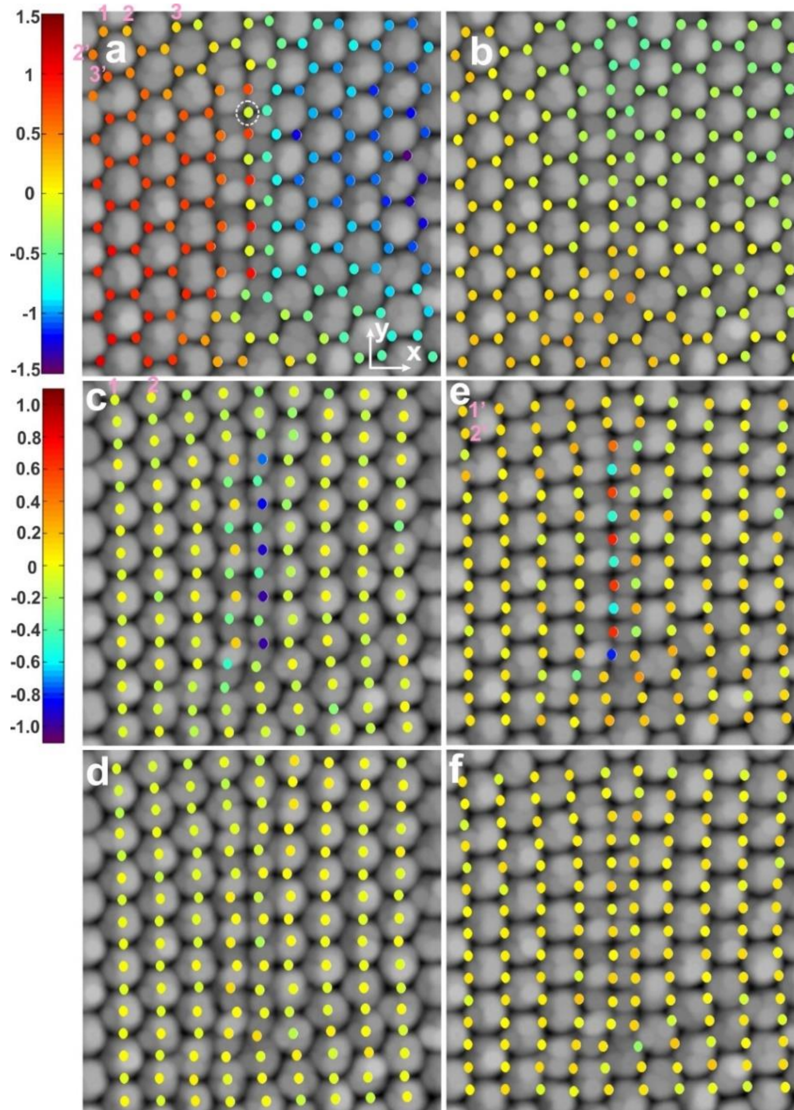

Figure B7. (a,b) 2D scattered displacement maps of type 1 2SVL in the x and y direction (U_x and U_y), respectively. The colour scale is ± 1.5Å. The reference point is the same as that in figure 7(i)a, which is marked by a white dashed circle. (c-f) 2D scattered strain maps of $\Delta Ux/\Delta x$, $\Delta Uy/\Delta x$, $\Delta Ux/\Delta y$ and $\Delta Uy/\Delta y$, respectively. The color scale is ±1.1.

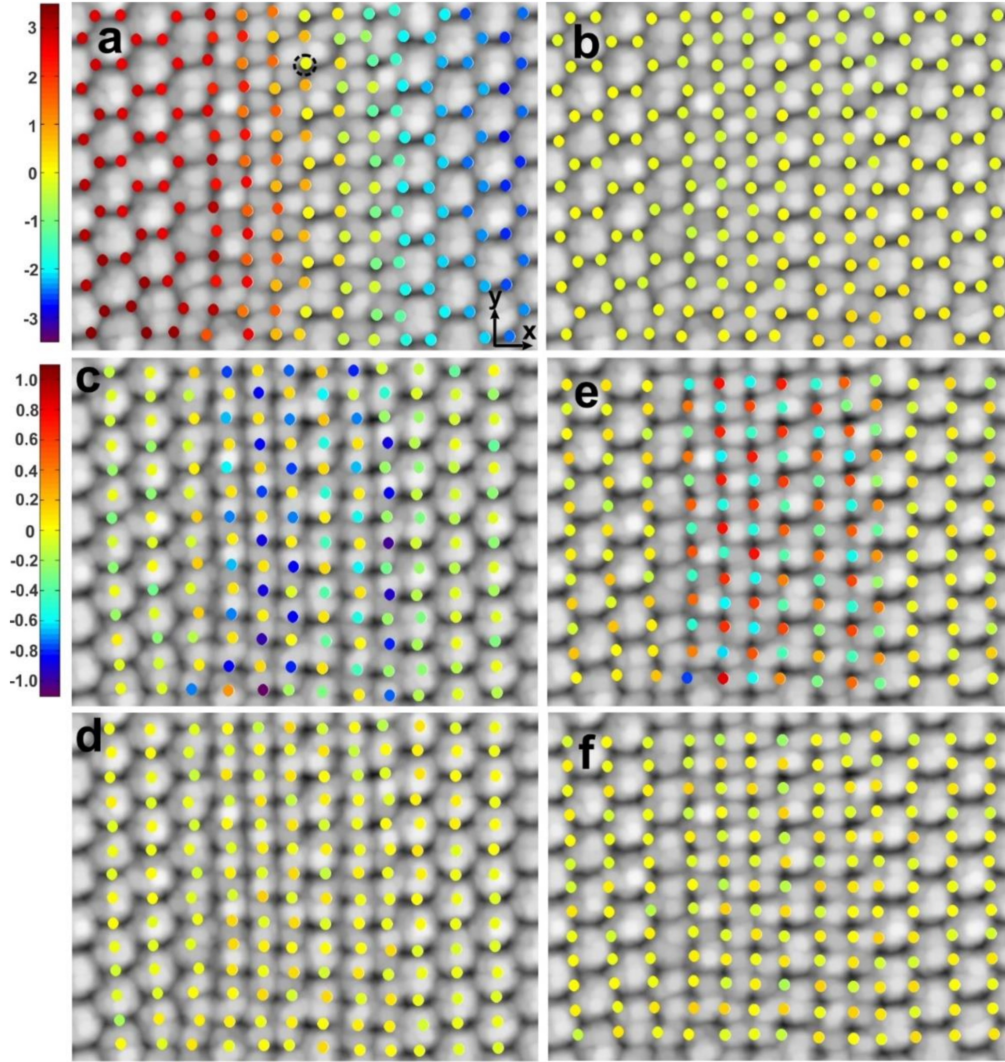

Figure B8. (a,b) 2D scattered displacement maps of 7SVL in the x and y direction (U_x and U_y), respectively. The colour scale is ± 3.5Å. The reference point is the same as that in Figure 7(ii)a, which is marked by a black dashed circle. (c-f) 2D scattered strain maps of $\Delta Ux/\Delta x$, $\Delta Uy/\Delta x$, $\Delta Ux/\Delta y$ and $\Delta Uy/\Delta y$, respectively. The color scale is ±1.1.

The precision of the atomic positions in MoS_2 is ~±20 pm. This is evaluated by measuring the atom positions of the same TEM image several independent times and calculating the average difference for each atom position. This error is the main source of the errors in the displacement and strain maps. Based on the error propagation in the displacement and strain functions, I can evaluate that the errors in the displacement and strain maps are ~±20 pm and ~±0.2, respectively.

B.7. DFT-calculated band structures of line defects from 5SVL to 8SVL

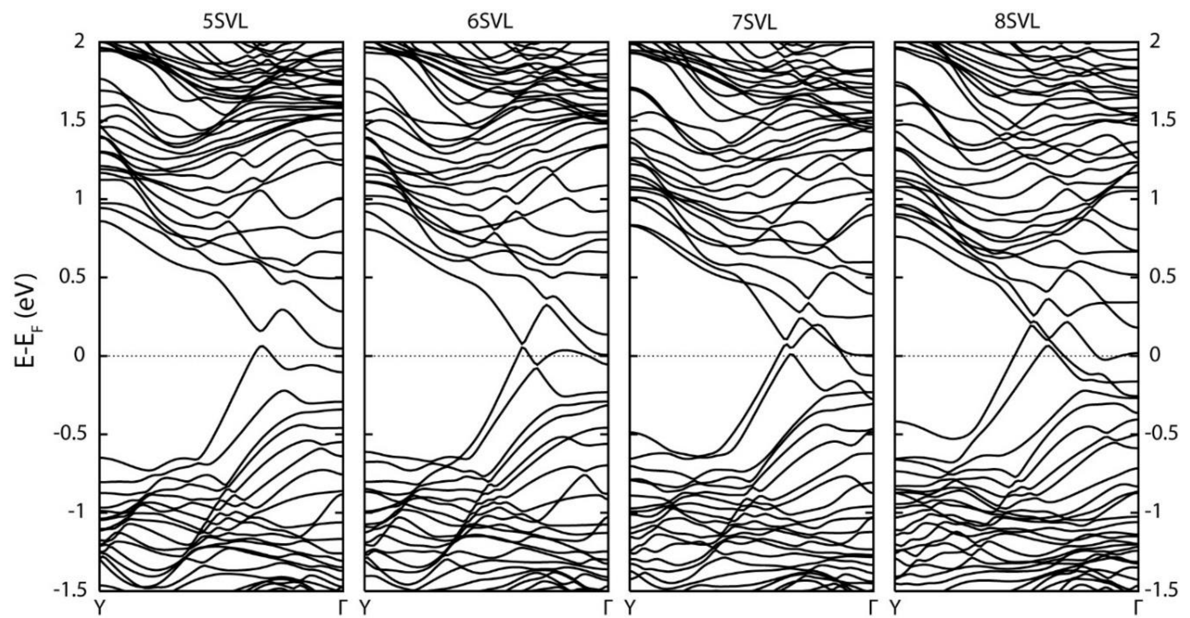

Figure B9. Band structures of line defects from 5SVL to 8SVL, respectively, performing metallic properties.

Appendix C

Supporting Information of Chapter 7

C.1. Methods of resolving the lattice structure of MoS_2 around the torn edges

For annular dark-field (ADF) imaging in a scanning transmission electron microscope (STEM) the image contrast is directly related to the atomic number of the atoms, allowing an easy way of chemical identification for different elements in a sample.(*23*) In phase contrast TEM imaging of a binary elementary system, such as MoS_2 monolayers, it is more complicated. As depicted in **Figure C1**a, image simulations on the atomic model of pristine monolayer MoS_2 show that the intensity ratio between single Mo atom (Mo) and double stacked S atoms (2S) is dependent on many factors, including the defocus values and the temporal coherence of the electron beam, denoted as defocus spread. This hinders the ability to distinguish Mo from 2S by simply comparing the contrast intensity from atomic columns. However, there is another feasible approach to identify different elements in monolayer MoS_2, which is to find a sulphur vacancy as the reference point and deduce the species of other atoms around it one by one. Sulphur vacancies are preferentially created by 80kV electron beam irradiation. **Figure C1**b shows how to identify the element type of atoms on a torn edge of MoS_2 monolayers. I initially find two mono-sulphur vacancies (V_s) close to

the edge, where the atom intensity is prominently lower than either the Mo or 2S sites. Subsequently, as Mo and 2S are known to arrange alternatively, I will be able to deduce species of all the other atoms around vacancies and know the element of the edge atoms. This method is both easy and accurate. Firstly, since the monolayer MoS_2 is relatively sensitive to the electron beam irradiation, under the accelerating voltage of 80 kV, it is always easy to find some sulphur vacancies as the reference points in the imaging area. Secondly, it has been reported that single Mo vacancies are hard to find in CVD-grown monolayer MoS_2 samples,(*29*) because the S atoms around it will become prone to sputtering once it is generated. There is a low possibility of misinterpretation for element types for each atom using this method. In addition, I can increase the judgement accuracy by choosing multiple S vacancies as different reference points and deducing the atom type in the same area by starting the counting of atoms from various reference points.

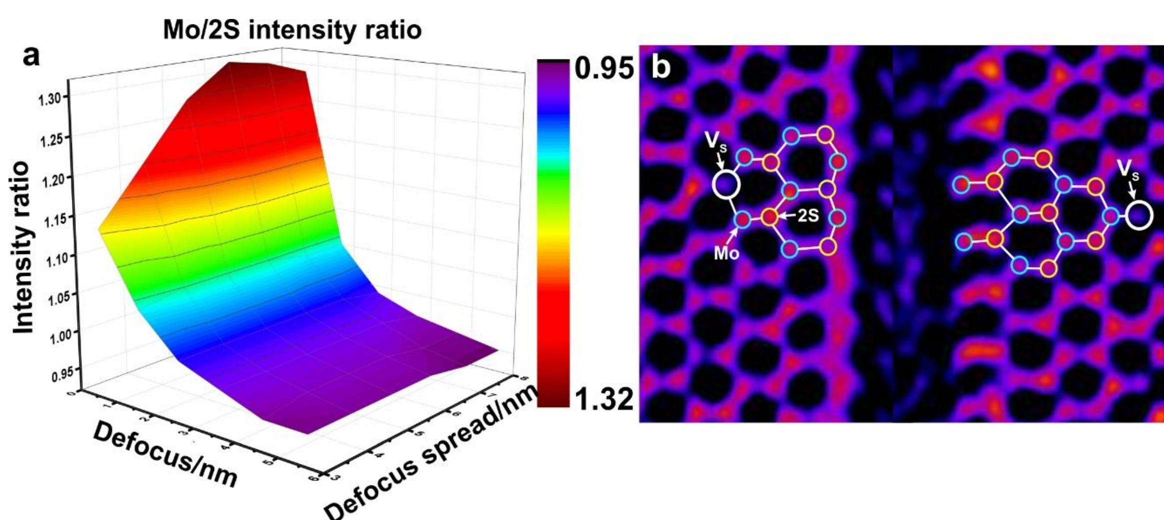

Figure C1. (a) 3D plot showing the dependence of the Mo/2S intensity ratio in the AC-TEM on the parameters of defocus (nm) and defocus spread (nm) by performing a series of simulations on the atomic model of pristine monolayer MoS_2. (b) AC-TEM image showing cracked MoS_2 edges with white circles highlighting the mono-sulphur vacancies as reference points, as well as blue and yellow circles representing Mo and 2S sites, respectively.

In order to better confirm whether the outermost S atoms on the ‘Klein-edge-like’(*192*) Mo-terminated edge are lost or moving to more out-of-plane locations. I conducted multi-

slice simulations using different atomic models having various edge structures created in Accelry Discovery Studio Visualizer software with appropriate supercells and compared their contrast at the same near-edge region with the raw AC-TEM image. **Figure C2**a,d are AC-TEM images in gray showing the right part of the brittle torn edge in **Figure 7.3**a with a magnified view, which is the same as the right part of **Figure 7.3**b. A boxed line profile(*197*) was conducted in the region marked in the yellow dashed rectangle in **Figure C2**b to show the contrast variation (**Figure C2**k). **Figure C2**c–f show atomic models of four possible edge structures. Each of them show the case of having both the top and bottom S atoms lost, having the bottom S atoms lost and the top S atoms move to places above the MoS_2 lattice plane, having the top S atoms lost and the bottom S atoms move to places below the MoS_2 plane, and having no S atoms on the edge lost but both the top and the bottom S atoms move to out-of-plane places, respectively. The upper parts show the top views of the atomic models, while of the bottom parts show the side views. **Figure C2**g–j are multi-slice simulation images based on the corresponding atomic models **Figure C2**c–f, respectively. The defocus spread and the defocus values are chosen to be 5.5 nm and 3 nm based on the analysis of the TEM image resolution. **Figure C2**l–o are the boxed line profiles showing the contrast variation across the region in yellow boxes for each simulation image. Compared with the boxed line profile of the AC-TEM image in panel m and n, which corresponds to the edge atomic model that has both the top and bottom S atoms lost, has the best match based on the contrast variation on the edge. Therefore, it can be confirmed that the brittle torn edge configuration shown in panel d corresponds to the atomic model in panel e, where the outermost S atoms on both the top and the bottom planes are lost, leaving ‘Klein-edge-like’ Mo-terminations.

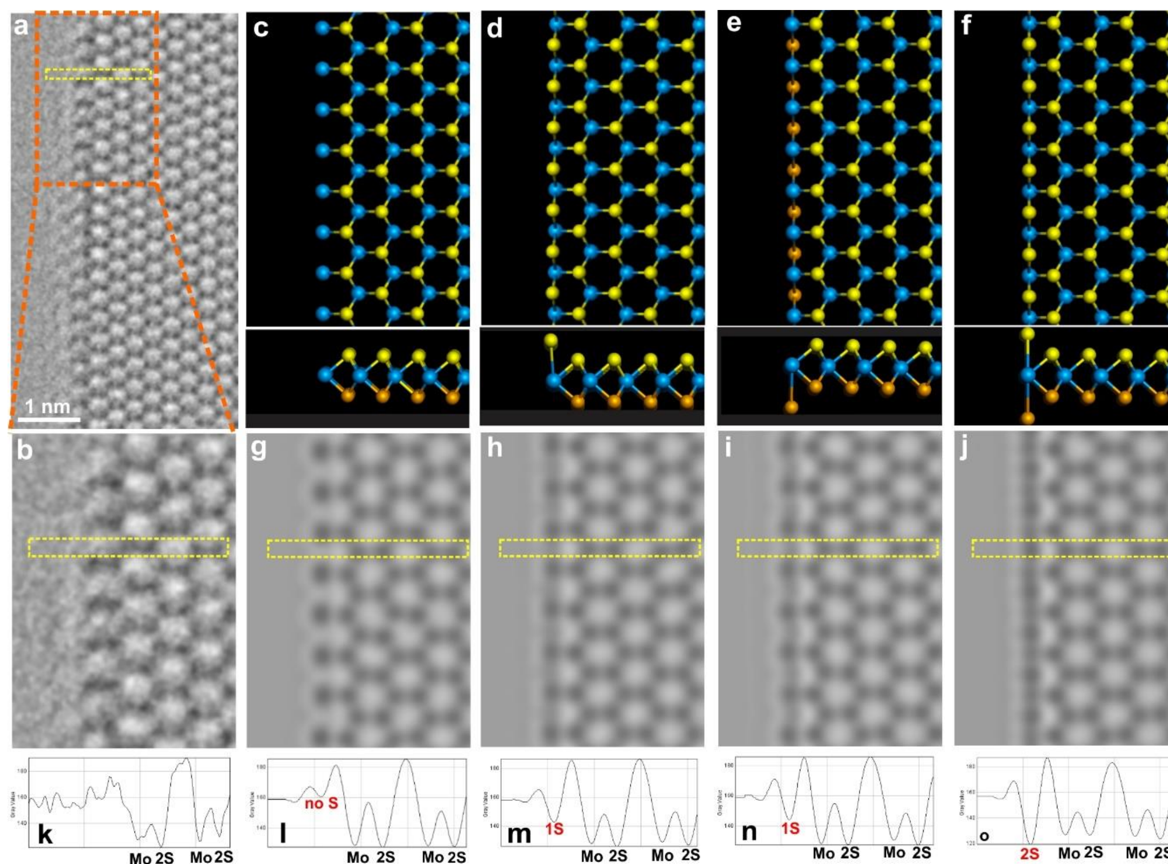

Figure C2. (a) AC-TEM image of one side of the long and straight zigzag edges, which is the right part of **Figure 7.3**b. (b) Magnified view of the structure of the MoS_2 edge from the region indicated by the orange dashed box in panel c. (c–f) Atomic models of four possible edge configurations. Each of them is having both the top and bottom S atoms lost, having the bottom S atoms lost and the top S atoms move to places above the MoS_2 lattice plane, having the top S atoms lost and the bottom S atoms move to places below the MoS_2 plane, and having no S atoms on the edge lost but both the top and the bottom S atoms move to out-of-plane places, respectively. The upper parts show the top views of the atomic models, while the bottom parts show the side views. (g–j) Multislice image simulations of the edge structure based on corresponding atomic models shown in panel e-h, respectively. (k–o) Boxed line profile analysis across the edge region shown in yellow dashed boxed in panel d, i-l, respectively.

C.2. MD simulation of monolayer MoS_2 crack propagation in a mildly defective region

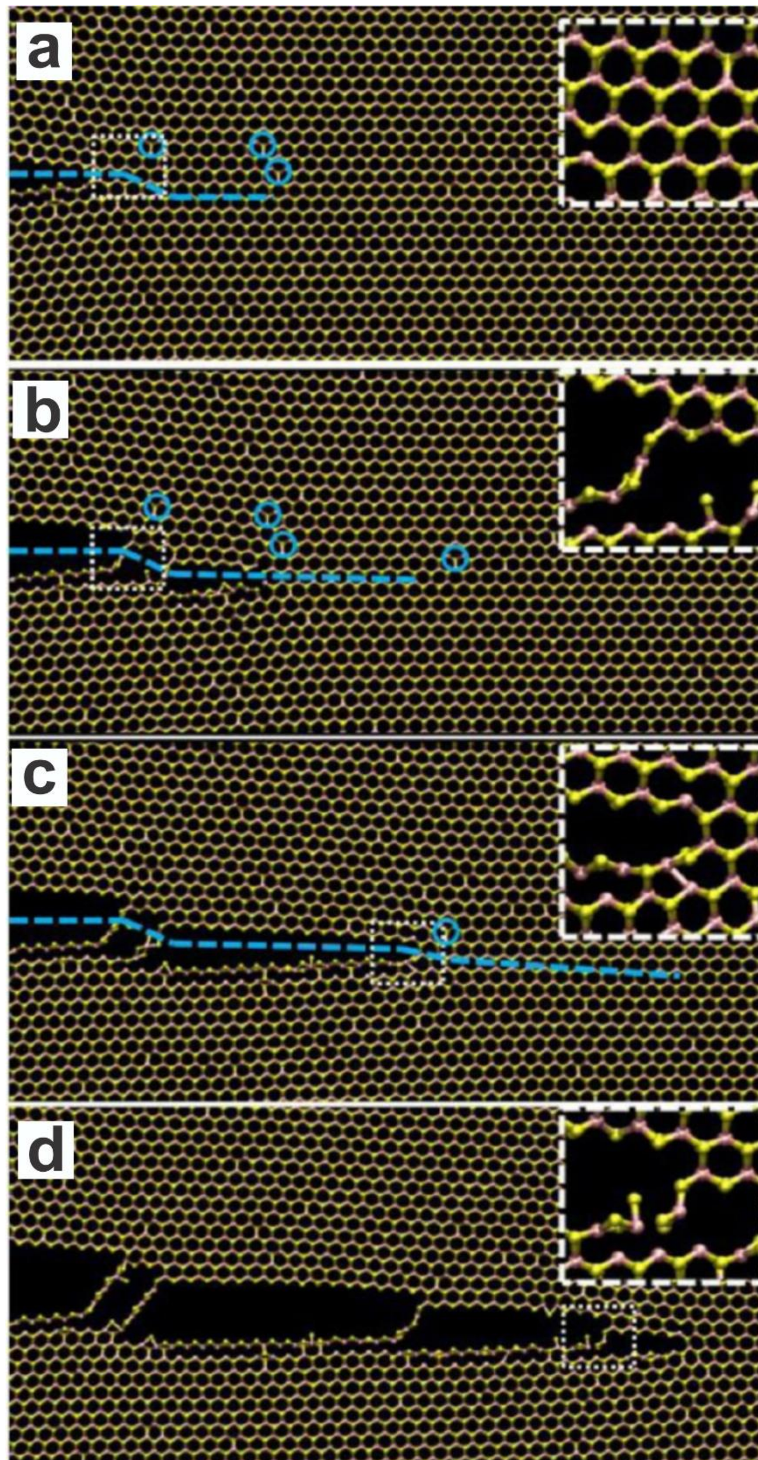

Figure C3. Simulation snapshots of the crack propagation in a MoS_2 model with 1% S atom missing, showing the crack pathway is deflected by the defects near the crack tip.

C.3. MD simulation of monolayer MoS_2 crack propagation in a moderately defective region

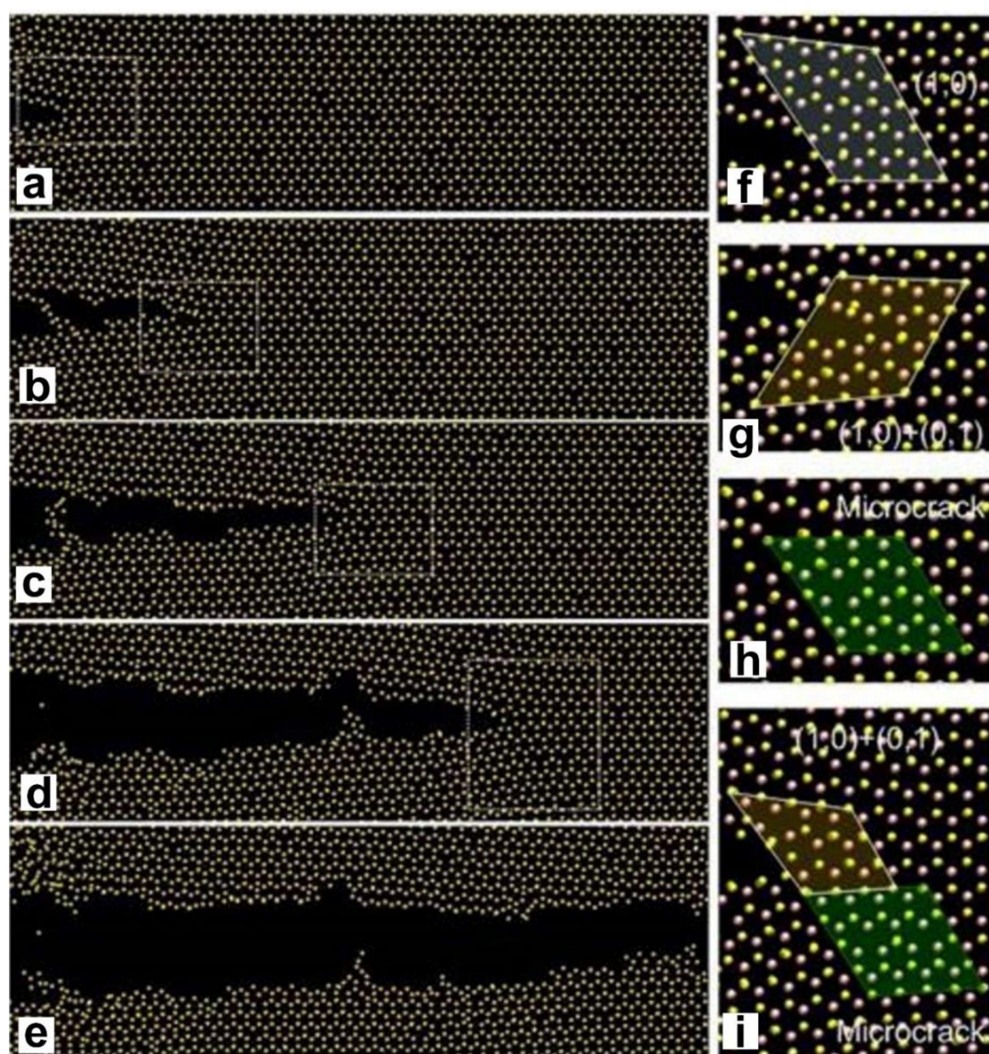

Figure C4. Simulation snapshots of the crack propagation in a MoS_2 model with 20% S atom missing, showing various types of dislocations form at the crack tip. The dislocations interact with the crack propagation by deflecting the crack path and making the crack tip less sharp than material samples with lower defect rates.

References

1. A. K. Geim, K. S. Novoselov, The rise of graphene. *Nat. Mater.* **6**, 183–191 (2007).
2. H. Wang, H. Yuan, S. Hong, Y. Cui, Physical and chemical tuning of two-dimensional transition metal dichalcogenides. *Chem. Soc. Rev.* **44**, 2664–2680 (2015).
3. A. A. Tedstone, D. J. Lewis, P. O'Brien, Synthesis, properties, and applications of transition metal-doped layered transition metal dichalcogenides. *Chem. Mater.* **28**, 1965–1974 (2016).
4. X. Duan, C. Wang, A. Pan, R. Yu, X. Duan, Two-dimensional transition metal dichalcogenides as atomically thin semiconductors : opportunities and challenges. *Chem. Soc. Rev.* **44**, 8859–8876 (2015).
5. M. Chhowalla *et al.*, The chemistry of two-dimensional layered transition metal dichalcogenide nanosheets. *Nat. Chem.* **5**, 263–275 (2013).
6. D. Deng *et al.*, Catalysis with two-dimensional materials and their heterostructures. *Nat. Nanotechnol.* **11**, 218–230 (2016).
7. D. Jariwala, V. K. Sangwan, L. J. Lauhon, T. J. Marks, M. C. Hersam, Emerging device applications for semiconducting two-dimensional transition metal dichalcogenides. *ACS Nano* **8**, 1102–1120 (2014).
8. J. R. Schaibley *et al.*, Valleytronics in 2D materials. *Nat. Rev. Mater.* **1**, 16055 (2016).
9. R. Ganatra, Q. Zhang, Few layer MoS_2: A promising layered semiconductor. *ACS Nano* **8**, 4074–4099 (2014).
10. B. Radisavljevic, A. Radenovic, J. Brivio, V. Giacometti, A. Kis, Single-layer MoS_2 transistors. *Nat. Nanotechnol.* **6**, 147–150 (2011).
11. K. F. Mak, K. He, J. Shan, T. F. Heinz, Control of valley polarization in monolayer MoS_2 by optical helicity. *Nat. Nanotechnol.* **7**, 494–498 (2012).
12. K. F. Mak, K. L. McGill, J. Park, P. L. McEuen, The valley Hall effect in MoS_2 transistors. *Science* **344**, 1489–1492 (2014).
13. D. Merki, X. Hu, Recent developments of molybdenum and tungsten sulfides as hydrogen evolution catalysts. *Energy Environ. Sci.* **4**, 3878–3888 (2011).
14. Y. Yu *et al.*, Layer-dependent electrocatalysis of MoS_2 for hydrogen evolution. *Nano Lett.* **14**, 553–558 (2014).
15. H. Li *et al.*, Activating and optimizing MoS_2 basal planes for hydrogen evolution through the formation of strained sulphur vacancies. *Nat. Mater.* **15**, 48–53 (2015).
16. S. Li *et al.*, Edge-enriched 2D MoS_2 thin films grown by chemical vapor deposition for enhanced catalytic performance. *ACS Catal.* **7**, 877–886 (2017).
17. J. Deng *et al.*, Triggering the electrocatalytic hydrogen evolution activity of inert two-dimensional MoS_2 surface *via* single-atom metal doping. *Energy Environ. Sci.* **8**, 1594–1601 (2015).
18. H. S. S. R. Matte *et al.*, MoS_2 and WS_2 analogues of graphene. *Angew. Chem. Int. Ed. Engl.* **49**, 4059–4062 (2010).
19. I. Song, C. Park, H. C. Choi, Synthesis and properties of molybdenum disulphide: from bulk to atomic layers. *RSC Adv.* **5**, 7495–7514 (2015).
20. J. Yan *et al.*, Stacking-dependent interlayer coupling in trilayer MoS_2 with broken inversion symmetry. *Nano Lett.* **15**, 8155–8161 (2015).
21. M. Xia *et al.*, Spectroscopic signatures of AA' and AB stacking of chemical vapor deposited bilayer MoS_2. *ACS Nano* **9**, 12246–12254 (2015).
22. Y.-C. Lin, D. O. Dumcenco, Y.-S. Huang, K. Suenaga, Atomic mechanism of the semiconducting-to-metallic phase transition in single-layered MoS_2. *Nat. Nanotechnol.* **9**, 391–396 (2014).

23. O. L. Krivanek *et al.*, Atom-by-atom structural and chemical analysis by annular dark-field electron microscopy. *Nature* **464**, 571–574 (2010).
24. A. Yan *et al.*, Identifying different stacking sequences in few-layer CVD-grown MoS_2 by low-energy atomic-resolution scanning transmission electron microscopy. *Phys. Rev. B* **93**, 041420 (2016).
25. M. Kan *et al.*, Structures and phase transition of a MoS_2 monolayer. *J. Phys. Chem. C*. **118**, 1515–1522 (2014).
26. Y. Cheng, A. Nie, Q. Zhang, L. Gan, R. Shahbazian-yassar, Origin of the phase transition in lithiated molybdenum disulfide. *ACS Nano* **8**, 11447–11453 (2014).
27. R. Kappera *et al.*, Phase-engineered low-resistance contacts for ultrathin MoS_2 transistors. *Nat. Mater.* **13**, 1128–1134 (2014).
28. A. N. Enyashin *et al.*, New route for stabilization of 1T-WS_2 and MoS_2 phases. *J. Phys. Chem. C*. **115**, 24586–24591 (2011).
29. W. Zhou *et al.*, Intrinsic structural defects in monolayer molybdenum disulfide. *Nano Lett.* **13**, 2615–2622 (2013).
30. J. Hong *et al.*, Exploring atomic defects in molybdenum disulphide monolayers. *Nat. Commun.* **6**, 6293 (2015).
31. H. Qiu *et al.*, Hopping transport through defect-induced localized states in molybdenum disulphide. *Nat. Commun.* **4**, 2642 (2013).
32. H.-P. Komsa *et al.*, Two-dimensional transition metal dichalcogenides under electron irradiation: Defect production and doping. *Phys. Rev. Lett.* **109**, 035503 (2012).
33. X. Liu *et al.*, Top-down fabrication of sub-nanometre semiconducting nanoribbons derived from molybdenum disulfide sheets. *Nat. Commun.* **4**, 1776 (2013).
34. R. Zan *et al.*, Control of radiation damage in MoS_2 by graphene encapsulation. *ACS Nano* **7**, 10167–10174 (2013).
35. H.-P. Komsa, S. Kurasch, O. Lehtinen, U. Kaiser, A. V. Krasheninnikov, From point to extended defects in two-dimensional MoS_2: Evolution of atomic structure under electron irradiation. *Phys. Rev. B* **88**, 035301 (2013).
36. S. Najmaei *et al.*, Vapour phase growth and grain boundary structure of molybdenum disulphide atomic layers. *Nat. Mater.* **12**, 754–759 (2013).
37. A. M. van der Zande *et al.*, Grains and grain boundaries in highly crystalline monolayer molybdenum disulphide. *Nat. Mater.* **12**, 554–561 (2013).
38. J. Lin, S. T. Pantelides, W. Zhou, Vacancy-induced formation and growth of inversion domains in transition-metal dichalcogenide monolayer. *ACS Nano* **9**, 5189–5197 (2015).
39. F. Banhart, J. Kotakoski, A. V. Krasheninnikov, Structural defects in graphene. *ACS Nano* **5**, 26–41 (2011).
40. S. A. Han, R. Bhatia, S.-W. Kim, Synthesis, properties and potential applications of two-dimensional transition metal dichalcogenides. *Nano Converg.* **2**, 17 (2015).
41. P. D. Fleischauer, J. R. Lince, P. A. Bertrand, R. Bauer, Electronic structure and lubrication properties of molybdenum disulfide: a qualitative molecular orbital approach. *Langmuir* **5**, 1009–1015 (1989).
42. C. Lu, G. Li, J. Mao, L.-M. Wang, E. Y. Andrei, Bandgap, mid-gap states, and gating effects in MoS_2. *Nano Lett.* **14**, 4628–4633 (2014).
43. S. Z. Butler *et al.*, Progress, challenges, and opportunities in two-dimensional materials beyond graphene. *ACS Nano* **7**, 2898–2926 (2013).
44. A. Splendiani *et al.*, Emerging photoluminescence in monolayer MoS_2. *Nano Lett.* **10**, 1271–5 (2010).

45. J. K. Ellis, M. J. Lucero, G. E. Scuseria, The indirect to direct band gap transition in multilayered MoS_2 as predicted by screened hybrid density functional theory. *Appl. Phys. Lett.* **99**, 261908 (2011).
46. K. F. Mak, C. Lee, J. Hone, J. Shan, T. F. Heinz, Atomically thin MoS_2: A new direct-gap semiconductor. *Phys. Rev. Lett.* **105**, 136805 (2010).
47. A. Ramasubramaniam, Large excitonic effects in monolayers of molybdenum and tungsten dichalcogenides. *Phys. Rev. B* **86**, 115409 (2012).
48. T. Cheiwchanchamnangij, W. R. L. Lambrecht, Quasiparticle band structure calculation of monolayer, bilayer, and bulk MoS_2. *Phys. Rev. B* **85**, 205302 (2012).
49. H. Komsa, A. V Krasheninnikov, Effects of confinement and environment on the electronic structure and exciton binding energy of MoS_2 from first principles. *Phys. Rev. B* **86**, 241201 (2012).
50. M. Ye, D. Winslow, D. Zhang, R. Pandey, Y. Yap, Recent advancement on the optical properties of two-dimensional molybdenum disulfide (MoS_2) thin films. *Photonics* **2**, 288–307 (2015).
51. P. Tonndorf *et al.*, Photoluminescence emission and Raman response of monolayer MoS_2, $MoSe_2$, and WSe_2. *Opt. Express* **21**, 4908–4916 (2013).
52. N. Alidoust, G. Bian, S. Xu, Observation of monolayer valence band spin-orbit effect and induced quantum well states in MoX_2. *Nat. Commun.* **5**, 4673 (2014).
53. J. D. Lin *et al.*, Electron-doping-enhanced trion formation in monolayer molybdenum disulfide functionalized with cesium carbonate. *ACS Nano* **8**, 5323–5329 (2014).
54. S. Mouri, Y. Miyauchi, K. Matsuda, Tunable photoluminescence of monolayer MoS_2 *via* chemical doping. *Nano Lett.* **13**, 5944–5948 (2013).
55. K. F. Mak *et al.*, Tightly bound trions in monolayer MoS_2. *Nat. Mater.* **12**, 207–211 (2013).
56. W. S. Yun, S. W. Han, S. C. Hong, I. G. Kim, J. D. Lee, Thickness and strain effects on electronic structures of transition metal dichalcogenides: 2H-MX_2 semiconductors (M = Mo, W; X = S, Se, Te). *Phys. Rev. B* **85**, 033305 (2012).
57. E. Scalise, M. Houssa, G. Pourtois, V. Afanas, A. Stesmans, Strain-induced semiconductor to metal transition in the two-dimensional honeycomb structure of MoS_2. *Nano Res.* **5**, 43–48 (2012).
58. J. Feng, X. Qian, C. Huang, J. Li, Strain-engineered artificial atom as a broad-spectrum solar energy funne. *Nat. Photonic*. **6**, 866–872 (2012).
59. H. J. Conley *et al.*, Bandgap engineering of strained monolayer and bilayer MoS_2. *Nano Lett.* **13**, 3626–3630 (2013).
60. S. Manzeli, A. Allain, A. Ghadimi, A. Kis, Piezoresistivity and strain-induced band gap tuning in atomically thin MoS_2. *Nano Lett*. **15**, 5330–5335 (2015).
61. L. M. Xie, Two-dimensional transition metal dichalcogenide alloys: preparation, characterization and applications. *Nanoscale* **7**, 18392–18401 (2015).
62. D. Lloyd *et al.*, Band gap engineering with ultralarge biaxial strains in suspended monolayer MoS_2. *Nano Lett.* **16**, 5836–5841 (2016).
63. K. P. Dhakal *et al.*, Confocal absorption spectral imaging of MoS_2: optical transitions depending on the atomic thickness of intrinsic and chemically doped MoS_2. *Nanoscale* **6**, 13028–13035 (2014).
64. J. Mann *et al.*, 2-Dimensional transition metal dichalcogenides with tunable direct band gaps: $MoS_{2(1-x)}Se_{2x}$ monolayers. *Adv. Mater.* **26**, 1399–1404 (2014).
65. S. Tongay *et al.*, Broad-range modulation of light emission in two-dimensional semiconductors by molecular physisorption gating. *Nano Lett.* **13**, 2831–2836 (2013).

66. A. Kutana, E. S. Penev, B. I. Yakobson, Engineering electronic properties of layered transition-metal dichalcogenide compounds through alloying. *Nanoscale* **6**, 5820–5825 (2014).
67. Z. Wang *et al.*, Chemical vapor deposition of monolayer $Mo_{1-x}W_xS_2$ crystals with tunable band gaps. *Sci. Rep.* **6**, 21536 (2016).
68. M. Buscema, G. A. Steele, H. S. J. van der Zant, A. Castellanos-Gomez, The effect of the substrate on the Raman and photoluminescence emission of single-layer MoS_2. *Nano Res.* **7**, 561–571 (2014).
69. K.-G. Zhou *et al.*, Raman modes of MoS_2 used as fingerprint of van der Waals interactions. *ACS Nano* **8**, 9914–9924 (2014).
70. C. Lee *et al.*, Anomalous lattice vibrations of single- and few-layer MoS_2. *ACS Nano* **4**, 2695–2700 (2010).
71. B. Chakraborty *et al.*, Symmetry-dependent phonon renormalization in monolayer MoS_2 transistor. *Phys. Rev. B*. **85**, 161403 (2012).
72. Y. Y. Hui *et al.*, Exceptional tunability of band energy in a compressively strained trilayer MoS_2 sheet. *ACS Nano* **7**, 7126–7131 (2013).
73. H. Li *et al.*, From bulk to monolayer MoS_2: evolution of Raman scattering. *Adv. Funct. Mater.* **22**, 1385–1390 (2012).
74. X. Wang, H. Feng, Y. Wu, L. Jiao, Controlled synthesis of highly crystalline MoS_2 flakes by Chemical Vapor Deposition. *J. Am. Chem. Soc.* **135**, 5304−5307 (2013).
75. W. Zhang *et al.*, High-gain phototransistors based on a CVD MoS_2 monolayer. *Adv. Mater.* **25**, 3456–3461 (2013).
76. K. Liu *et al.*, Elastic properties of chemical-vapor-deposited monolayer MoS_2, WS_2, and their bilayer heterostructures. *Nano Lett.***14**, 5097−5103 (2014).
77. S. Bertolazzi, J. Brivio, A. Kis, Stretching and breaking of ultrathin MoS_2. *ACS Nano* **5**, 9703–9709 (2011).
78. A. Castellanos-Gomez *et al.*, Elastic properties of freely suspended MoS_2 nanosheets. *Adv. Mater.* **24**, 772–775 (2012).
79. J. Pu *et al.*, Highly flexible MoS_2 thin-film transistors with ion gel dielectrics. *Nano Lett.* **12**, 4013–4017 (2012).
80. T. Li, Ideal strength and phonon instability in single-layer MoS_2. *Phys. Rev. B* **85**, 235407 (2012).
81. H. Li *et al.*, Fabrication of single- and multilayer MoS_2 film-based field-effect transistors for sensing NO at room temperature. *Small* **8**, 63–67 (2012).
82. K.-G. Zhou, N.-N. Mao, H.-X. Wang, Y. Peng, H.-L. Zhang, A mixed-solvent strategy for efficient exfoliation of inorganic graphene analogues. *Angew. Chem. Int. Ed. Engl.* **50**, 10839–10842 (2011).
83. Z. Zeng *et al.*, Single-layer semiconducting nanosheets: high-yield preparation and device fabrication. *Angew. Chem. Int. Ed. Engl.* **50**, 11093–11097 (2011).
84. C. N. R. Rao, A. Nag, Inorganic analogues of graphene. *Eur. J. Inorg. Chem.* **2010**, 4244–4250 (2010).
85. C. Gong *et al.*, Metal contacts on physical vapor deposited monolayer MoS_2. *ACS Nano* **7**, 11350–11357 (2013).
86. S. Wu *et al.*, Vapor–solid growth of high optical quality MoS_2 monolayers with near-unity valley polarization. *ACS Nano* **7**, 2768–2772 (2013).
87. Y. Zhan, Z. Liu, S. Najmaei, P. M. Ajayan, J. Lou, Large-area vapor-phase growth and characterization of MoS_2 atomic layers on a SiO_2 substrate. *Small* **8**, 966–971 (2012).
88. M. R. Laskar *et al.*, Large area single crystal (0001) oriented MoS_2. *Appl. Phys. Lett.* **102**, 252108 (2013).

89. Y.-C. Lin *et al.*, Wafer-scale MoS_2 thin layers prepared by MoO_3 sulfurization. *Nanoscale* **4**, 6637–6641 (2012).
90. K.-K. Liu *et al.*, Growth of large-area and highly crystalline MoS_2 thin layers on insulating substrates. *Nano Lett.* **12**, 1538–1544 (2012).
91. Y.-H. Lee *et al.*, Synthesis of large-area MoS_2 atomic layers with chemical vapor deposition. *Adv. Mater.* **24**, 2320–2325 (2012).
92. Y.-H. Lee *et al.*, Synthesis and transfer of single-layer transition metal disulfides on diverse surfaces. *Nano Lett.* **13**, 1852–1857 (2013).
93. X. Ling *et al.*, Role of the seeding promoter in MoS_2 growth by chemical vapor deposition. *Nano Lett.* **14**, 464–472 (2014).
94. J. Zhang *et al.*, Scalable growth of high-quality polycrystalline MoS_2 monolayers on SiO_2 with tunable grain sizes. *ACS Nano* **8**, 6024–6030 (2014).
95. Q. Ji *et al.*, Epitaxial monolayer MoS_2 on mica with novel photoluminescence. *Nano Lett.* **13**, 3870–3877 (2013).
96. Y. Yu *et al.*, Controlled scalable synthesis of uniform, high-quality monolayer and few-layer MoS_2 films. *Sci. Rep.* **3**, 1866 (2013).
97. K. Kang *et al.*, High-mobility three-atom-thick semiconducting films with wafer-scale homogeneity. *Nature* **520**, 656–660 (2015).
98. D. A. . King, D. P. Woodruff, Growth and Properties of Ultrathin Epitaxial Layers. *Elsevier* (1997).
99. S. Bhaviripudi, X. Jia, M. S. Dresselhaus, J. Kong, Role of kinetic factors in chemical vapor deposition synthesis of uniform large area graphene using copper catalyst. *Nano Lett.* **10**, 4128–4133 (2010).
100. S. Wang *et al.*, Shape evolution of monolayer MoS_2 crystals grown by chemical vapor deposition. *Chem. Mater.* **26**, 6371–6379 (2014).
101. C. Kastl *et al.*, The important role of water in growth of monolayer transition metal dichalcogenides. *2D Mater.* **4**, 21024 (2017).
102. W. Chen *et al.*, Oxygen-assisted chemical vapor deposition growth of large single-crystal and high-quality monolayer MoS_2. *J. Am. Chem. Soc.* **137**, 15632–15635 (2015).
103. M. K. Dobkin, D.M., Zuraw, Principles of chemical vapor deposition. *Springer Sci. Bus. Media* (2003).
104. Y. Xu, X.-T. Yan, Chemical vapour deposition: an integrated engineering design for advanced materials. *Springer-Verlag London* (2010).
105. Y. Shi *et al.*, Van der Waals epitaxy of MoS_2 layers using graphene as growth templates. *Nano Lett.* **12**, 2784–2791 (2012).
106. Y.-C. Lin *et al.*, Direct synthesis of van der Waals solids. *ACS Nano* **8**, 3715–3723 (2014).
107. M. Okada *et al.*, Direct chemical vapor deposition growth of WS_2 atomic layers on hexagonal boron nitride. *ACS Nano* **8**, 8273–8277 (2014).
108. A. Yan *et al.*, Direct growth of single- and few-layer MoS_2 on h-BN with preferred relative rotation angles. *Nano Lett.* **15**, 6324–6331 (2015).
109. J. A. Miwa *et al.*, Van der Waals epitaxy of two-dimensional MoS_2 graphene heterostructures in ultrahigh vacuum. *ACS Nano* **9**, 6502–6510 (2015).
110. Y. Gong *et al.*, Vertical and in-plane heterostructures from WS_2/MoS_2 monolayers. *Nat. Mater.* **13**, 1135–1142 (2014).
111. S. Wang, X. Wang, J. H. Warner, All chemical vapor deposition growth of MoS_2:h-BN vertical van der Waals heterostructures. *ACS Nano* **9**, 5246–5254 (2015).
112. Z. Y. Al Balushi *et al.*, Two-dimensional gallium nitride realized *via* graphene encapsulation. *Nat. Mater.* **15**, 1166–1171 (2016).

113. Q. Chen, K. He, A. W. Robertson, A. I. Kirkland, J. H. Warner, Atomic structure and dynamics of epitaxial 2D crystalline gold on graphene at elevated temperatures. *ACS Nano* **10**, 10418–10427 (2016).
114. G. Algara-Siller, O. Lehtinen, A. Turchanin, U. Kaiser, Dry-cleaning of graphene. *Appl. Phys. Lett.* **104**, 153115 (2014).
115. J. H. Warner, N. P. Young, A. I. Kirkland, G. A. D. Briggs, Resolving strain in carbon nanotubes at the atomic level. *Nat. Mater.* **10**, 958–962 (2011).
116. D. Abanin, L. Levitov, Conformal invariance and shape-dependent conductance of graphene samples. *Phys. Rev. B* **78**, 035416 (2008).
117. L. Fan *et al.*, Topology evolution of graphene in chemical vapor deposition, a combined theoretical/experimental approach toward shape control of graphene domains. *Nanotechnology* **23**, 115605 (2012).
118. M. Amani *et al.*, Electrical performance of monolayer MoS_2 field-effect transistors prepared by chemical vapor deposition. *Appl. Phys. Lett.* **102**, 193107 (2013).
119. J. J. De Yoreo, P. G. Vekilov, Principles of crystal nucleation and growth. *Rev. Mineral. Geochemi*. **54**, 57–93 (2003).
120. C. de M. Donegá, Nanoparticles: workhorses of nanoscience. *Springer* (2014).
121. A. Govind Rajan, J. H. Warner, D. Blankschtein, M. S. Strano, Generalized mechanistic model for the chemical vapor deposition of 2D transition metal dichalcogenide monolayers. *ACS Nano* **10**, 4330–4344 (2016).
122. V. Senthilkumar, L. Tam, Y. Kim, Y. Sim, Direct vapor phase growth process and robust photoluminescence properties of large area MoS_2 layer. *Nano Res.* **7**, 1759–1768 (2014).
123. J. Jeon *et al.*, Layer-controlled CVD growth of large-area two-dimensional MoS_2 film. *Nanoscale* **7**, 1688–1695 (2015).
124. Y. Rong *et al.*, Controlled preferential oxidation of grain boundaries in monolayer tungsten disulfide for direct optical imaging. *ACS Nano* **9**, 3695–3703 (2015).
125. Y.-H. Lee *et al.*, Synthesis of large-area MoS_2 atomic layers with chemical vapor deposition. *Adv. Mater.* **24**, 2320–2325 (2012).
126. S. L. Li *et al.*, Quantitative raman spectrum and reliable thickness identification for atomic layers on insulating substrates. *ACS Nano* **6**, 7381–7388 (2012).
127. A. K. Geim, I. V Grigorieva, Van der Waals heterostructures. *Nature* **499**, 419–25 (2013).
128. L. Britnell *et al.*, Field-effect tunneling transistor based on vertical graphene heterostructures. *Science* **335**, 947–50 (2012).
129. T. Georgiou *et al.*, Vertical field-effect transistor based on graphene-WS_2 heterostructures for flexible and transparent electronics. *Nat. Nanotechnol.* **8**, 100–103 (2013).
130. W. J. Yu *et al.*, Highly efficient gate-tunable photocurrent generation in vertical heterostructures of layered materials. *Nat. Nanotechnol.* **8**, 952–958 (2013).
131. R. Cheng *et al.*, Electroluminescence and photocurrent generation from atomically sharp WSe_2/MoS_2 heterojunction p-n diodes. *Nano Lett.* **14**, 5590–5597 (2014).
132. A. V Kretinin *et al.*, Electronic properties of graphene encapsulated with different two-dimensional atomic crystals. *Nano Lett.* **14**, 3270–3276 (2014).
133. S. J. Haigh *et al.*, Cross-sectional imaging of individual layers and buried interfaces of graphene-based heterostructures and superlattices. *Nat. Mater.* **11**, 764–767 (2012).
134. Z. Liu *et al.*, Direct growth of graphene/hexagonal boron nitride stacked layers. *Nano Lett.* **11**, 2032–2037 (2011).
135. G. W. Shim *et al.*, Large-area single-layer $MoSe_2$ and its van der Waals heterostructures. *ACS Nano* **8**, 6655–6662 (2014).

136. X. Zhang *et al.*, Vertical heterostructures of layered metal chalcogenides by van der Waals epitaxy. *Nano Lett.* **14**, 3047–3054 (2014).
137. C. R. Dean *et al.*, Boron nitride substrates for high-quality graphene electronics. *Nat. Nanotechnol.* **5**, 722–726 (2010).
138. W. Gannett *et al.*, Boron nitride substrates for high mobility chemical vapor deposited graphene. *Appl. Phys. Lett.* **98**, 242105 (2011).
139. R. V Gorbachev *et al.*, Hunting for monolayer boron nitride: optical and Raman signatures. *Small* **7**, 465–468 (2011).
140. C. Rice *et al.*, Raman-scattering measurements and first-principles calculations of strain-induced phonon shifts in monolayer MoS2. *Phys. Rev. B* **87**, 081307 (2013).
141. L. Yang *et al.*, Lattice strain effects on the optical properties of MoS_2 nanosheets. *Sci. Rep.* **4**, 5649 (2014).
142. X. Lu *et al.*, Large-area synthesis of monolayer and few-layer $MoSe_2$ films on SiO_2 substrates. *Nano Lett.* **14**, 2419–2425 (2014).
143. D. Lloyd *et al.*, Band gap engineering with ultralarge biaxial strains in suspended monolayer MoS_2. *Nano Lett.* **16**, 5836–5841 (2016).
144. J. Zabel *et al.*, Raman spectroscopy of graphene and bilayer under biaxial strain: Bubbles and balloons. *Nano Lett.* **12**, 617–621 (2012).
145. Y. Cai, J. Lan, G. Zhang, Y.-W. Zhang, Lattice vibrational modes and phonon thermal conductivity of monolayer MoS_2. *Phys. Rev. B* **89**, 035438 (2014).
146. H. J. Conley *et al.*, Bandgap engineering of strained monolayer and bilayer MoS_2. *Nano Lett.* **13**, 3626–3630 (2013).
147. N. Mao, Y. Chen, D. Liu, J. Zhang, L. Xie, Solvatochromic effect on the photoluminescence of MoS_2 monolayers. *Small* **9**, 1312–1315 (2013).
148. W. Bao, X. Cai, D. Kim, K. Sridhara, M. S. Fuhrer, High mobility ambipolar MoS_2 field-effect transistors: Substrate and dielectric effects. *Appl. Phys. Lett.* **102**, 042104 (2013).
149. S. Ghatak, A. N. Pal, A. Ghosh, Nature of electronic states in atomically thin MoS_2 field-effect transistors. *ACS Nano* **5**, 7707–7712 (2011).
150. S. Sahoo, A. P. S. Gaur, M. Ahmadi, R. S. Katiyar, Temperature-dependent Raman studies and thermal conductivity of few-layer MoS_2. *J. Phys. Chem. C.* **117**, 9042–9047 (2013).
151. S. Najmaei, Z. Liu, P. M. Ajayan, J. Lou, Thermal effects on the characteristic Raman spectrum of molybdenum disulfide (MoS_2) of varying thicknesses. *Appl. Phys. Lett.* **100**, 013106 (2012).
152. J. S. Ross *et al.*, Electrical control of neutral and charged excitons in a monolayer semiconductor. *Nat. Commun.* **4**, 1474 (2013).
153. D. M. Sim *et al.*, Controlled doping of vacancy-containing few-layer MoS_2 *via* highly stable thiol-based molecular chemisorption. *ACS Nano* **9**, 12115–12123 (2015).
154. S. B. Desai *et al.*, Strain-induced indirect to direct bandgap transition in multilayer WSe_2. *Nano Lett.* **14**, 4592–4597 (2014).
155. L. Liu, M. Qing, Y. Wang, S. Chen, Defects in graphene: Generation, healing, and their effects on the properties of graphene: A review. *J. Mater. Sci. Technol.* **31**, 599–606 (2015).
156. Y.-C. Lin *et al.*, Three-fold rotational defects in two-dimensional transition metal dichalcogenides. *Nat. Commun.* **6**, 6736 (2015).
157. A. Azizi *et al.*, Dislocation motion and grain boundary migration in two-dimensional tungsten disulphide. *Nat. Commun.* **5**, 4867 (2014).
158. F. Börrnert *et al.*, Programmable sub-nanometer sculpting of graphene with electron beams. *ACS Nano* **6**, 10327–10334 (2012).

159. A. W. Robertson *et al.*, Spatial control of defect creation in graphene at the *Nanoscale Nat. Commun.* **3**, 1144 (2012).
160. H. Liu *et al.*, Dense network of one-dimensional midgap metallic modes in monolayer $MoSe_2$ and their spatial undulations. *Phys. Rev. Lett.* **113**, 066105 (2014).
161. K. He, G.-D. Lee, A. W. Robertson, E. Yoon, J. H. Warner, Hydrogen-free graphene edges. *Nat. Commun.* **5**, 3040 (2014).
162. H. I. Rasool *et al.*, Conserved atomic bonding sequences and strain organization of graphene grain boundaries. *Nano Lett.* **14**, 7057–7063 (2014).
163. Q. Chen *et al.*, Atomic evel distributed strain within graphene divacancies from bond rotations. *ACS Nano* **9**, 8599–8608 (2015).
164. S. Lebègue, O. Eriksson, Electronic structure of two-dimensional crystals from ab initio theory. *Phys. Rev. B* **79**, 115409 (2009).
165. S. Bhattacharyya, A. K. Singh, Semiconductor-metal transition in semiconducting bilayer sheets of transition-metal dichalcogenides. *Phys. Rev. B* **86**, 075454 (2012).
166. J. Lin *et al.*, Flexible metallic nanowires with self-adaptive contacts to semiconducting transition-metal dichalcogenide monolayers. *Nat. Nanotechnol.* **9**, 436–442 (2014).
167. M. J. Buehler, H. Gao, Dynamical fracture instabilities due to local hyperelasticity at crack tips. *Nature* **439**, 307–310 (2006).
168. A. J. Pons, A. Karma, Helical crack-front instability in mixed-mode fracture. *Nature* **464**, 85–89 (2010).
169. D. H. Warner, W. A. Curtin, S. Qu, Rate dependence of crack-tip processes predicts twinning trends in f.c.c. metals. *Nat. Mater.* **6**, 876–881 (2007).
170. J. R. Kermode *et al.*, Low-speed fracture instabilities in a brittle crystal. *Nature* **455**, 1224–1227 (2008).
171. A. Livne, E. Bouchbinder, I. Svetlizky, J. Fineberg, The near-tip fields of fast cracks. *Science* **327**, 1359–1363 (2010).
172. S. Hénaux, F. Creuzet, Crack tip morphology of slowly growing cracks in glass. *J. Am. Ceram. Soc.* **83**, 415–417 (2000).
173. M. J. Buehler, A. C. T. Van Duin, W. A. Goddard, Multiparadigm modeling of dynamical crack propagation in silicon using a reactive force field. *Phys. Rev. Lett.* **96**, 095505 (2006).
174. K. H. Nam, I. H. Park, S. H. Ko, Patterning by controlled cracking. *Nature* **485**, 221–224 (2012).
175. D. Wang *et al.*, Where, and how, does a nanowire break? *Nano Lett.* **7**, 1208–1212 (2007).
176. F. Cleri, S. Yip, D. Wolf, S. Phillpot, Atomic-scale mechanism of crack-tip plasticity: Dislocation nucleation and crack-tip shielding. *Phys. Rev. Lett.* **79**, 1309–1312 (1997).
177. E. Bitzek, J. R. Kermode, P. Gumbsch, Atomistic aspects of fractures. *Int. J. Fract.* **191**, 13–30 (2015).
178. L. Liu, J. Wang, S. K. Gong, S. X. Mao, Atomistic observation of a crack tip approaching coherent twin boundaries. *Sci. Rep.* **4**, 4397 (2014).
179. C. W. Zhao, Y. M. Xing, Nanoscale experimental study of a micro-crack in silicon. *Phys. B Condens. Matter*. **403**, 4202–4204 (2008).
180. R. Goswami, C. S. Pande, Investigations of crack-dislocation interactions ahead of mode-III crack. *Mater. Sci. Eng. A*. **627**, 217–222 (2015).
181. A. Litorowicz, Identification and quantification of cracks in concrete by optical fluorescent microscopy. *Cem. Concr. Res.* **36**, 1508–1515 (2006).
182. E. Guilloteau, H. Charrue, F. Creuzet, The direct observation of the core region of a propagating fracture crack in glass. *Europhys. Lett.* **34**, 549–554 (1996).

183. M. A. L. Marques, H. E. Troiani, M. Miki-Yoshida, M. Jose-Yacaman, A. Rubio, On the breaking of carbon nanotubes under tension. *Nano Lett.* **4**, 811–815 (2004).
184. A. Barreiro, F. Börrnert, M. H. Rümmeli, B. Büchner, L. M. K. Vandersypen, Graphene at high bias: Cracking, layer by layer sublimation, and fusing. *Nano Lett.* **12**, 1873–1878 (2012).
185. N. Alem *et al.*, Atomically thin hexagonal boron nitride probed by ultrahigh-resolution transmission electron microscopy. *Phys. Rev. B* **80**, 155425 (2009).
186. Z. Zhang, A. Kutana, B. I. Yakobson, Edge reconstruction-mediated graphene fracture. *Nanoscale* **7**, 2716–2722 (2015).
187. S. S. Terdalkar *et al.*, Nanoscale fracture in graphene. *Chem. Phys. Lett.* **494**, 218–222 (2010).
188. G. Jung, Z. Qin, M. J. Buehler, Molecular mechanics of polycrystalline graphene with enhanced fracture toughness. *Extrem. Mech. Lett.* **2**, 52–59 (2015).
189. G. López-Polín, J. Gómez-Herrero, C. Gómez-Navarro, Confining crack propagation in defective graphene. *Nano Lett.* **15**, 2050–2054 (2015).
190. K. Kim *et al.*, Ripping graphene: Preferred directions. *Nano Lett.* **12**, 293–297 (2012).
191. R. Jack, D. Sen, M. J. Buehler, Graphene nanocutting through nanopatterned vacancy defects. *J. Comput. Theor. Nanosci.* **7**, 354–359 (2010).
192. K. He *et al.*, Extended Klein edges in graphene. *ACS Nano* **8**, 12272–12279 (2014).
193. O. V. Yazyev, S. G. Louie, Topological defects in graphene: Dislocations and grain boundaries. *Phys. Rev. B* **81**, 195420 (2010).
194. P. Zhang *et al.*, Fracture toughness of graphene. *Nat. Commun.* **5**, 3782 (2014).
195. R. Y. Tay *et al.*, A systematic study of the atmospheric pressure growth of large-area hexagonal crystalline boron nitride film. *J. Mater. Chem. C.* **2**, 1650–1657 (2014).
196. E. S. Kadantsev, P. Hawrylak, Electronic structure of a single MoS_2 monolayer. *Solid State Commun.* **152**, 909–913 (2012).
197. J. H. Warner *et al.*, Dislocation-driven deformations in graphene. *Science* **337**, 209–212 (2012).